Quantitative Fault Tolerant Control Design for a Hydraulic Actuator with a Leaking Piston Seal

by

Mark Karpenko

A thesis
presented to the University of Manitoba
in fulfilment of the
thesis requirement for the degree of
Doctor of Philosophy

Department of Mechanical and Manufacturing Engineering
The University of Manitoba
Winnipeg, Manitoba, Canada

© Mark Karpenko, September 2008

THE UNIVERSITY OF MANITOBA

FACULTY OF GRADUATE STUDIES

*****

COPYRIGHT PERMISSION

Quantitative Fault Tolerant Control Design for a Hydraulic Actuator with a Leaking Piston Seal

BY

Mark Karpenko

A Thesis/Practicum submitted to the Faculty of Graduate Studies of The University of Manitoba in partial fulfillment of the requirement of the degree

Of

Doctor of Philosophy

Mark Karpenko © 2008

Permission has been granted to the University of Manitoba Libraries to lend a copy of this thesis/practicum, to Library and Archives Canada (LAC) to lend a copy of this thesis/practicum, and to LAC's agent (UMI/ProQuest) to microfilm, sell copies and to publish an abstract of this thesis/practicum.

This reproduction or copy of this thesis has been made available by authority of the copyright owner solely for the purpose of private study and research, and may only be reproduced and copied as permitted by copyright laws or with express written authorization from the copyright owner.

Abstract

Hydraulic actuators are complex fluid power devices whose performance can be degraded in the presence of system faults. In this thesis a linear, fixed-gain, fault tolerant controller is designed that can maintain the positioning performance of an electrohydraulic actuator operating under load with a leaking piston seal and in the presence of parametric uncertainties. Developing a control system tolerant to this class of internal leakage fault is important since a leaking piston seal can be difficult to detect, unless the actuator is disassembled. The designed fault tolerant control law is of low-order, uses only the actuator position as feedback, and can: (*i*) accommodate nonlinearities in the hydraulic functions, (*ii*) maintain robustness against typical uncertainties in the hydraulic system parameters, and (*iii*) keep the positioning performance of the actuator within prescribed tolerances despite an internal leakage fault that can bypass up to 40% of the rated servovalve flow across the actuator piston. Experimental tests verify the functionality of the fault tolerant control under normal and faulty operating conditions.

The fault tolerant controller is synthesized based on linear time-invariant equivalent (LTIE) models of the hydraulic actuator using the quantitative feedback theory (QFT) design technique. A numerical approach for identifying LTIE frequency response functions of hydraulic actuators from acceptable input-output responses is developed so that linearizing the hydraulic functions can be avoided. The proposed approach can properly identify the features of the hydraulic actuator frequency response that are important for control system design and requires no prior knowledge about the asymptotic behavior or structure of the LTIE transfer functions.

A distributed hardware-in-the-loop (HIL) simulation architecture is constructed that enables the performance of the proposed fault tolerant control law to be further substantiated, under realistic operating conditions. Using the HIL framework, the fault tolerant hydraulic actuator is operated as a flight control actuator against the

real-time numerical simulation of a high-performance jet aircraft. A robust electrohydraulic loading system is also designed using QFT so that the in-flight aerodynamic load can be experimentally replicated. The results of the HIL experiments show that using the fault tolerant controller to compensate the internal leakage fault at the actuator level can benefit the flight performance of the airplane.

Acknowledgments

First and foremost, I would like to express my deepest thanks and most sincere appreciation to my advisor Dr. Nariman Sepehri, whose continued encouragement, support, and guidance made the completion of this thesis possible. I also wish to express my gratitude to the members of my advisory committee, Dr. S. Onyshko and Dr. U. D. Annakkage for their constructive criticisms and invaluable suggestions, which undoubtedly improved the quality of the work.

My thanks also go to Dr. I. M. Horowitz, founder of QFT and former Winnipegger, as well as Dr. C. H. Houpis for encouraging me to further explore the potentials of QFT for practical control system design. Financial support provided by the Natural Sciences and Engineering Research Council of Canada (NSERC) and the University of Manitoba Faculty of Graduate Studies is also gratefully acknowledged.

Finally, my heartfelt appreciation goes to all of those who helped me to persist and find the strength to keep slowly chipping away at my research over the past number of years. To all the members of the Fluid Power Research and Experimental Robotics Lab, thanks for your suggestions, technical support, camaraderie, and tomfoolery. To Mr. Farshid Najafi, thanks for all the coffee, interesting conversation, and ideas we exchanged as we worked towards our degrees. I will always remember all the fun we had putting together the *bugs*. To my parents, thank you for a lifetime of support and for instilling in me an appreciation and stubbornness for working hard. Last but not least, thank you Christy for standing by me through *all* of the ups and downs that go into completing a Ph.D. "*Our journey of a thousand miles begins with this single step*" – *Chinese proverb.*

Contents

Abstract i

Acknowledgments iii

List of Tables vii

List of Figures viii

Nomenclature xiii

1 Introduction **1**

1.1 Problem Statement 1

1.2 Relevant Background 3

1.3 Objectives of this Research 8

1.4 Thesis Outline 9

2 Hydraulic Actuation System **12**

2.1 Applications 12

2.2 Valve Controlled Ram 14

2.3 Common Faults 16

2.4 Experimental Setup 20

2.5 Mathematical Modeling 25

2.5.1 Nonlinear Model 25

2.5.2 Model Validation 29

2.6 Summary 37

3 Quantitative Feedback Theory **38**

3.1 Background 39

3.2 Review of QFT Design Technique 42

3.2.1 Linear Time Invariant Plants 42

3.2.2 Extension to Nonlinear Plants 50

3.3 Equivalent LTI Modeling of Hydraulic Actuators 54

3.3.1 Acceptable System Responses 54

3.3.2 Small-Signal Approach 57

3.3.3 LTI-Equivalent Approach 63

3.4 Summary 74

4 Controller Design **75**

4.1 Problem Setup 76

4.2 Controller Design for Normal Operation 81

4.2.1 Design Details 82

4.2.2 Experimental Results 99

4.2.3 Performance in Presence of Internal Leakage Fault 104

4.3 Design of Fault Tolerant Controller 108

4.3.1 Design Details 108

4.3.2 Experimental Results 123

4.4 Summary 128

5 Hardware-in-the-Loop Simulator **129**

5.1 Simulator Architecture 130

5.2 Description of Flight Model 135

5.3 Robust Force Control of Loading Actuator 138

5.4 Demonstration of HIL Simulator 157

5.5 Summary 163

6 Hardware-in-the-Loop Experiments **164**

6.1 Description of Tests 164

6.2 Results 168

6.2.1 Bank-to-Bank Reversals 168

6.2.2 Roll Maneuver 177

6.3 Summary 185

7 Concluding Remarks **186**

7.1 Contributions 186

7.2 Future Work 190

References **191**

A Hydraulic Actuator Inverse Model **201**

B Table of Hinge Moment Coefficients **203**

List of Tables

2.1 List of nominal system parameters of fault emulation circuit. 30
2.2 List of nominal system parameters of loading actuator. 31

3.1 Typical specifications on closed-loop performance for QFT design. . . 45
3.2 Servovalve operating points. 61
3.3 LTIE transfer functions obtained using Golubev's method. 65
3.4 LTIE transfer functions estimated from frequency response functions. 73

4.1 Ranges and nominal values of uncertain hydraulic actuator parameters. 81
4.2 Closed-loop magnitude variations using controllers A and B. 92

5.1 Implemented control surface deflection limits. 138
5.2 Parametric uncertainty considered in force control system design. . . 143

B.1 Table of hinge moment coefficients 203

List of Figures

2.1 Range of operation of hydraulic actuators. 13

2.2 Operation of a typical valve controlled hydraulic flight actuator. . . . 15

2.3 Schematic of hydraulic test bench. 22

2.4 Experimental hardware for producing internal leakage fault. 23

2.5 Flexible coupling for connecting two experimental hydraulic actuators. 24

2.6 Schematic of hydraulic actuator for mathematical modeling. 25

2.7 Examples of worn actuator rod seals. 28

2.8 Predicted and measured position for fault emulator actuator model validation test. 33

2.9 Predicted and measured velocity for fault emulator actuator model validation test. 34

2.10 Predicted and measured load pressure for fault emulator actuator model validation test. 34

2.11 Predicted and measured position for loading actuator model validation test. 36

2.12 Predicted and measured velocity for loading actuator model validation test. 36

2.13 Predicted and measured load pressure for loading actuator model validation test. 37

3.1 Two degree of freedom control system. 40

3.2 Example QFT templates at several frequencies. 44

3.3 Example QFT bounds. 48

3.4 Example QFT bounds and nominal loop transmission. 49

3.5 Example design bounds on prefilter frequency response. 49

3.6 Nonlinear and equivalent linear feedback systems. 50
3.7 Typical acceptable hydraulic actuator input-output responses. 56
3.8 Hydraulic load lines superimposed over a plot of nonlinear servovalve flow curves. 60
3.9 Equivalent small-signal position responses of hydraulic actuator. . . . 62
3.10 Bode plots of small-signal transfer functions. 63
3.11 Responses of LTIE transfer functions obtained by Golubev's method. 66
3.12 Bode plots of LTIE transfer functions obtained by Golubev's method. 67
3.13 Bode plots of LTIE frequency response ratios. 71
3.14 Bode plots of LTIE transfer functions estimated from frequency response ratios. 72
3.15 Responses of LTIE transfer function estimates. 73

4.1 Two degree of freedom feedback control system around hydraulic actuator. 76
4.2 Acceptable unit step responses for design of QFT position controller. 77
4.3 Variation in hinge moment coefficient as a function of control surface deflection. 79
4.4 Acceptable plant input-output responses for normal operation. 83
4.5 Computed frequency response ratios for normal operation. 83
4.6 Templates of set $\mathcal{P}_e$ for normal actuator operation. 84
4.7 QFT bounds for normal operation. 86
4.8 Inverted Nichols chart showing contours of constant closed-loop sensitivity. 89
4.9 QFT bounds and nominal loop transmissions for normal operation. . 91
4.10 Bode magnitudes of two controllers designed for normal operation. . . 92
4.11 Envelope of closed-loop frequency responses for normal operation. . . 94
4.12 Envelope of closed-loop tracking magnitudes for normal operation. . . 95
4.13 Simulated position responses for control system A under normal operation. 97
4.14 Simulated position responses for control system B under normal operation. 98
4.15 Experimental step responses against a 30 kN/m spring (control system A). 100

4.16 Experimental step responses with different environment stiffnesses (control system A). 101
4.17 Experimental step responses against a 30 kN/m spring (control system B). 102
4.18 Experimental step responses with different environment stiffnesses (control system B). 103
4.19 Experimental step responses in presence of internal leakage fault (control system A). 106
4.20 Experimental step responses in presence of internal leakage fault (control system B). 107
4.21 Acceptable plant input-output responses in presence of internal leakage fault. 109
4.22 Computed frequency response ratios in presence of internal leakage fault. 111
4.23 Templates of set $\mathcal{P}_e$ in presence of internal leakage fault. 112
4.24 Comparison of plant template boundaries for normal and faulty operation. 113
4.25 QFT bounds for fault tolerant control. 114
4.26 Two candidate loop transmissions for fault tolerant control. 115
4.27 QFT bounds and fault tolerant loop transmission with relaxed stability margins. 118
4.28 Envelope of closed-loop frequency responses using fault tolerant controller. 120
4.29 Simulated position responses for fault tolerant control system under normal operation. 121
4.30 Comparison of simulated step responses using fault tolerant control system under normal operation and in presence of leakage fault. . . . 122
4.31 Experimental step responses against a 30 kN/m spring using fault tolerant controller under normal operation. 124
4.32 Experimental step responses with different environment stiffnesses using fault tolerant controller. 125
4.33 Experimental step responses using fault tolerant controller in presence of internal leakage fault. 126
4.34 Experimental step responses using fault tolerant controller in presence of slowly increasing internal leakage. 127

5.1 Overview of hardware-in-the-loop flight simulator. 131

5.2 Hydraulic test bench configuration. 134
5.3 Block diagram of experimental hydraulic actuator control system implementation. 135
5.4 Aircraft body coordinate system. 136
5.5 Variation in control surface hinge moment coefficient. 139
5.6 Block diagram of QFT control system around loading actuator. . . . 140
5.7 Time histories of acceptable plant input-output responses for force control design. 142
5.8 Bode plots of loading actuator frequency response. 144
5.9 Templates of set $\mathcal{P}_e$ for force control system design. 145
5.10 QFT bounds and nominal loop transmission of force control system. . 147
5.11 Schematic of augmented force control system. 149
5.12 Magnitude plots for filter design. 150
5.13 Simulated step responses of closed-loop force control system. 152
5.14 Simulated closed-loop force regulating errors resulting from flight actuator movement. 153
5.15 Experimental performance of force control system against a fixed environment. 155
5.16 Experimental performance of augmented force control system against a moveable environment. 156
5.17 Results of angle of attack control experiment 158
5.18 Elapsed CPU time versus simulation time pertaining to angle of attack pull-up experiment. 160
5.19 Results of 360° roll experiment. 162

6.1 Input command and typical bank angle response for bank-to-bank reversal maneuver. 166
6.2 Input command and typical roll response for 360° roll maneuver. . . . 167
6.3 Bank-to-bank reversals using benchmark controller A under normal operation. 170
6.4 Bank-to-bank reversals using benchmark controller A for increasing internal leakage. 172
6.5 Bank-to-bank reversals using fault tolerant controller for increasing internal leakage. 175

6.6 Roll maneuver using benchmark controller A under normal operation. 179
6.7 Roll maneuver using benchmark controller A for increasing internal leakage. 181
6.8 Roll maneuver using fault tolerant controller for increasing internal leakage. 183

Nomenclature

Parameters and Variables

A	piston annulus area (m^2)
β_h	effective bulk modulus of hydraulic fluid (Pa)
C_v	servovalve coefficient of discharge
d	actuator viscous damping coefficient (N·sec/m)
F_a	actuator force (N)
F_C	Coulomb friction (N)
F_f	friction force (N)
F_L	external load force (N)
F_s	static friction (N)
k	load stiffness (N/m)
k_c	stiffness of flexible coupling (N/m)
k_v	servovalve spool position gain (m/V, m/mA)
K_v	servovalve flow gain $\left(\sqrt{m^3/kg}\right)$
K_1, K_2, K_{12}	turbulent leakage coefficients $\left(m^3/sec/\sqrt{Pa}\right)$
K_{1f}, K_{2f}	linearized servovalve flow coefficients (m^2/sec)
K_{1p}, K_{2p}	linearized flow-pressure coefficients (m^3/sec/Pa)
L	length of actuator stroke (m)
m	mass of piston, rods and load (kg)
P_1, P_2	pressures on each side of piston (Pa)
P_L	load pressure (Pa)
P_s	supply pressure (Pa)
P_r	tank pressure (Pa)
ρ_{oil}	density of hydraulic oil (kg/m^3)
σ_0, σ_1	parameters of LuGre friction model
u	control valve input signal (V, mA)
x_p	actuator position (m)
v_p	actuator velocity (m/sec)
x_v	servovalve spool position (m)
x_{vm}	maximum servovalve spool displacement (m)
v_s	Stribeck velocity (m/sec)
v_v	velocity of servovalve spool (m/sec)
Q_1, Q_2	servovalve control flows (m^3/sec)
q_1, q_2	actuator external leakage flows (m^3/sec)

q_{12}	actuator internal leakage flow (m^3/sec)
w	servovalve orifice area gradient (m^2/m)
V_1, V_2	volumes of each cylinder half (m^3)
$\bar{V}_1$, $\bar{V}_2$	volumes of connecting lines (m^3)
ω_v	equivalent servovalve natural frequency (rad/sec)
ζ_v	equivalent servovalve damping ratio
$\bar{q}$	free-stream dynamic pressure (Pa)
ρ_a	density of air (kg/m^3)
V_T	airspeed (m/sec)
S	control surface area (m^2)
$\bar{c}$	control surface mean aerodynamic chord (m)
l_h	length of control surface linkage (m)
C_h	hinge moment coefficient
θ	control surface angle of incidence (deg)
δ	control surface deflection (deg)
α	angle of attack (deg)
β	sideslip angle (deg)
F_c	commanded force (N)
δ_c	commanded deflection (deg)

Transfer Functions

G	controller
F	prefilter
L	loop transmission
P	linear time-invariant plant
$\mathcal{P}$	set of linear time-invariant plants
P_H	small-signal hydraulic actuator dynamics
P_e	linear time-invariant equivalent plant
$\mathcal{P}_e$	set of linear time-invariant equivalent plants
P_V	servovalve spool dynamics
S	sensitivity function
T	system transfer function
$\mathcal{T}$	set of system transfer functions
T_L	lower tracking bound
T_U	upper tracking bound
W	nonlinear plant mapping
$\mathcal{W}$	set of nonlinear plant mappings

Subscripts

h	horizontal tail
a	aileron
r	rudder
nom	nominal
o	operating point

Abbreviations

EBM	effective bulk modulus
FTC	fault tolerant control
HIL	hardware-in-the-loop
LTI	linear time-invariant
LTIE	linear time-invariant equivalent

Chapter 1

Introduction

1.1 Problem Statement

Hydraulic actuation systems are used in many applications ranging from robotics and aerospace to mining and construction. Hydraulic servos are often cited for their reliability [1] and controllability [2], as compared to other actuator types. However, the performance of these complex systems can become degraded when the system components begin to wear or malfunction. For example, a problem with a pump may occur suddenly and cause changes in the pressure of the hydraulic fluid supply. This can alter the control valve flow characteristics and may cause the actuator to stall against the load. Other common faults in hydraulic systems include internal and external fluid leakages [3, 4], fluctuation of the effective fluid bulk modulus due to air or water contamination [5, 6], changes in actuator friction characteristics due to seal or component wear [3,5] and servovalve malfunctions [7]. Any of these faults can deteriorate the performance of a hydraulic system and potentially lead to the loss of important functions, which in turn, can impair safety.

Motivated by the desire to increase levels of safety, reliability, and availability of hydraulic systems, there has been an increasing interest in developing suitable meth-

ods for fault diagnosis (FD) and fault tolerant control (FTC) of fluid power systems. Over the last two decades, a great deal of research has been done on the development of FD techniques for hydraulic actuators. Many of the available techniques for FD in fluid power systems can be grouped into one of three broad categories: (*i*) model-based approaches [4–6, 8–12], (*ii*) approaches based on feature pattern recognition and classification [3, 13–17], and (*iii*) knowledge-based approaches [18–23]. Irrespective of the approach used, the main objective of FD is to signal the occurrence of a fault and identify the cause of the diminishing performance or loss of functionality. Fault diagnosis is therefore a supervisory process that can do little to maintain the performance of the system in the presence of a fault. FTC systems, on the other hand, strive to retain the performance of the system within safe and acceptable limits, and maintain its functionality in the event of a fault.

Compared to the body of work on FD for hydraulic actuators, however, comparatively little work has been directed to the development of FTC systems for hydraulic servomechanisms. Only a small subset of the common actuator faults has been studied [24], despite the potential benefits of fault tolerant fluid power systems in many applications. In particular, the design of an FTC algorithm to overcome a class of hydraulic pump faults leading to reduced supply pressure was documented in [25]. Switching and fixed-gain fault tolerant compensators for a hydraulic positioning system with a partially failed actuator piston seal were presented in [26, 27]. Clearly, additional development is needed in this area.

To further advance fault tolerant control technology for hydraulic actuators beyond the present state-of-the-art, several issues need to be addressed. First, the fault tolerant fluid power control systems cited above were developed based on small-signal models of the hydraulic actuator. However, the use of linearization for controller design may be inappropriate since small-signal assumptions are often violated during the operation of hydraulic systems [28]. This problem could be further aggravated by faults. Therefore, other methodologies for modeling hydraulic actuators, which

are not subject to small-signal assumptions, need to be investigated. An important aspect of control system design for fluid power systems that should be accounted for when developing fault tolerant compensators, is robustness against inherent system nonlinearities and parameter uncertainties. Some of the work cited above has not considered this requirement. Finally, to gain insight into how fault tolerant fluid power systems will function and interact in the field, fault tolerant hydraulic actuators should be tested under operating conditions that incorporate the dynamics of the complex engineering systems in which the actuators are embedded.

1.2 Relevant Background

Over the years, many approaches have been documented to design feedback systems for controlling the position, velocity, and force output of hydraulic actuators. Yet, the design of feedback controls for hydraulic actuators remains a challenging task. This statement is true, even in the absence of faults, when all of the components making up the system are functioning normally. A detailed survey of the fluid power control literature revealed that the main problems to be addressed during control system design arise from a number of non-idealities associated with the various system components. Some of these difficulties include:

1. The presence of a lightly damped resonant mode in the frequency response between the valve spool displacement and the position of the actuator.
2. Changes in the characteristics of the resonant mode in different parts of the stroke due to the compressibility of hydraulic fluid.
3. The presence of friction in the actuator.
4. A nonlinear relationship between pressure and flow in the valve.
5. Ignorance of, or uncertainty in, the particular values of the parameters that characterize the performance of the system.

Much of the initial work on feedback control of hydraulic actuators [2, 29, 30] was concerned with improving the damping of the troublesome resonant mode in the hydraulic frequency response as well as investigating the application of simple compensation schemes to improve the transient response of the closed-loop system. It was observed early on that the damping of the hydraulic resonance is worst, and the natural frequency lowest, when the actuator is centered in the cylinder and the valve is operating around the null position [2]. Thus, typical control system designs were carried out for these worst-case conditions, by linearizing the nonlinear dynamic equations around a particular system operating point with the actuator at mid-stroke.

Early investigations also acknowledged actuator friction as a problem complicating control system design. Friction in a hydraulic actuator results primarily from the seals installed between dynamic surfaces. Friction is a complicated natural phenomenon and its degrading effects, with respect to control system performance, are well known. In a position servo, for example, Coulomb friction causes steady state positioning errors, while viscous friction can result in tracking lags [31]. In hydraulic systems, the presence of Coulomb friction has also been observed to cause limit-cycle oscillations [2] and undesirable stick-slip motion [32]. Many articles have been devoted to the development of effective friction compensation schemes for hydraulic actuators. Some recent examples include [32–34]. While friction compensation techniques can improve system performance, the necessity to employ friction compensation at all, seems to depend greatly on the particular system under study and the closed-loop performance requirements that must ultimately be obtained.

Another challenge in designing feedback controls for hydraulic actuators, is the nonlinear relationship between pressure and flow in the valve. Since the flow of hydraulic fluid through the valve varies nonlinearly with the actuator load pressure, the dynamic response of the actuator can change significantly with the load [28]. Consequently, control laws that have been designed by linearizing the dynamic equations around a particular operating point may fail to perform properly if the operating

point changes quickly during the normal operation of the system.

In addition to compensating for valve nonlinearities, effective controllers for hydraulic actuators must also be able to cope with variations in the other parameters that influence the system performance. For example, the effective bulk modulus of the hydraulic fluid[1] varies with temperature and pressure [35]. Changes in the valve flow characteristics can also occur over time due to wear of the valve spool. Parametric uncertainties considered in the controller design must also include the uncertainty in any other system parameter whose value cannot be established exactly, for example the actuator viscous damping coefficient.

In the literature, the design of control laws that retain closed-loop performance and stability in the presence of variations in the load and other parametric uncertainties have been carried out using a number of adaptive [36–40], nonlinear [41–47], and robust control techniques such as LQG [48, 49], H_∞ [50–54], and quantitative feedback theory (QFT) [55–59]. Essentially all of this work has been directed at developing effective controls for fluid power systems in the absence of faults. Designing FTCs for hydraulic actuators presents an additional challenge: The fault tolerant controller must also have the capacity to either desensitize the feedback loop or adapt to uncertainties arising from changes in system dynamics that occur due to faults. This gives rise to two possible approaches for FTC design, namely active and passive approaches [60].

In the active approach, the control strategy is modified on-line in order to compensate the effect of faults. The adaptive control approaches cited above fall into this category, along with switching and gain-scheduling controllers, which select a control law from an *a priori* designed set based on the condition of the system. Adaptive controls have been shown to be effective at accommodating normal variations in hydraulic system parameters such as the supply pressure or fluid bulk modulus [61] and

[1]The effective bulk modulus describes the compressibility of the hydraulic fluid and takes into account the flexibility actuator cylinder and fluid lines as well as any air or water entrainment in the fluid.

can potentially be applied as fault tolerant controls. However, adaptive systems often require significant instrumentation for implementation. Switching and gain-scheduled controls, on the other hand, must rely on additional supervisory systems that evaluate and report the condition of the system.

Passive FTC, on the other hand, uses robust control techniques to synthesize a fixed-gain control law that ensures insensitivity to changes in the plant dynamics for a predefined selection of faults. Using robust techniques it is often the case that good steady state and transient performance can be obtained using only the controlled variable as feedback. This is attractive from the perspective of practical implementation [62]. Moreover, with the passive approach, fault tolerant control action can be realized without the need for additional diagnostics algorithms. As far as FTC strategies based on robust control concepts are concerned, the few fault tolerant control strategies for fluid power systems that have been documented in the literature were designed using quantitative feedback theory [25–27].

Quantitative feedback theory (QFT) [63] is a well-established approach for designing robust control systems that must function in the presence of bounded plant parametric uncertainty, such as the uncertainties introduced by faults. The technique has been used to solve a wide range of difficult control problems ranging from automated welding processes [64] to full-envelope flight control [65]. The basic idea behind the approach, which was originally developed for uncertain linear plants [66], is to first characterize the parametric uncertainties in the plant dynamics as *templates* on the Nichols chart[2]. The templates are then used, along with prescribed tolerances on the desired closed-loop performance, for example closed-loop stability and reference tracking performance, to derive point-by-point bounds on the system loop transmission function. Finally a fixed-gain controller, that guarantees the closed-loop performance of the system for all the plants in the uncertain set, is synthesized by manipulating the shape of the loop transmission to satisfy the bounds in a point-wise

[2]A plot of the open-loop magnitude on the ordinate and the open-loop phase on the abscissa.

fashion.

QFT has been extended to design controllers around nonlinear plants, such as hydraulic actuators, by recasting the effects of the inherent system nonlinearities as additional parametric uncertainties against which the control system must be robust. The effects of system nonlinearities can be captured for QFT design by: (*i*) linearizing the plant (small-signal assumptions must hold), or (*ii*) employing the concept of restricted device equivalence, also known as LTI-equivalence (LTIE) [67]. A third technique also exists, whereby the effects of the nonlinearities are recast as a set of equivalent disturbances [68]. However, this approach can be difficult to apply to practical engineering systems owing to the difficulties associated with separating the equivalent disturbances from the original nonlinear plant.

The first paper to document the design of a fault tolerant hydraulic actuator using QFT is the work of Niksefat and Sepehri [25], which developed a position controller that could compensate for malfunctioning position sensors and a class of hydraulic pump failures. The design utilized small-signal theory to derive the representative plant transfer functions and considered uncertainty in some of the other systems parameters. Experiments demonstrated the ability of the QFT fault tolerant control to maintain the closed-loop performance under reduced hydraulic supply pressure arising from a hydraulic pump failure and in the presence of increased sensor noise. However, the actuator was only operated in the small-signal regime and the system performance for large signals was not verified.

Karpenko and Sepehri [26] applied QFT to design a fault tolerant position control for a hydraulic actuator to compensate for a faulty actuator piston seal, which causes internal leakage of hydraulic fluid across the actuator piston. As in [25], small-signal theory was employed in [26] to derive a linearized model of the hydraulic system under study. To solve the FTC problem, a set of QFT controllers was designed and then scheduled to generate the appropriate control action based on an on-line estimate of the severity of the internal leakage fault. In a follow up work [27], the same authors

employed QFT to design a passive, fixed-gain, controller to compensate the internal leakage fault and eliminate the reliance of the controller on the scheduling algorithm. A significant shortcoming of [26,27] is that control system robustness to uncertainties normally present in hydraulic systems was not considered as part of the control system design.

1.3 Objectives of this Research

The primary objective of this research is to develop and test a robust, fault tolerant, position control law for an electrohydraulic actuator operating in the presence of an internal leakage fault and other parametric uncertainties. The internal leakage fault allows hydraulic oil to be bypassed across the actuator piston, which can degrade the positioning performance of the actuator and impair the ability of the ram to control the load. Since no fluid is lost from the hydraulic circuit, internal leakage can be difficult to detect unless the actuator is disassembled or tested using an advanced diagnostics algorithm, such as the one given in [4]. Moreover it is possible, within the physical limitations of the hydraulic system, to design a control law that can maintain the closed-loop positioning performance within prescribed tolerances despite the internal leakage fault. QFT is applied to synthesize a fixed-gain, model-based, linear fault tolerant control law that:

1. Compensates the nonlinear hydraulic actuator dynamics.
2. Maintains the positioning performance of the electrohydraulic actuator within prescribed tolerances despite an internal leakage fault that can bypass approximately 40% of the rated servovalve flow across the actuator piston.
3. Is robust against typical uncertainty in the hydraulic system parameters including a 20% reduction in the hydraulic supply pressure, $\pm 50\%$ variation in the hydraulic bulk modulus, and 20% uncertainty in the viscous damping coefficient.
4. Is of low-order and uses only the actuator position as feedback.

To achieve these requirements, a fundamental challenge that must be overcome is translating the nonlinear hydraulic functions into an equivalent LTI form. Several methods, besides small signal analysis, have been proposed for accomplishing this task. However, they can be cumbersome to apply in a practical design scenario and improvement is needed in this area. Therefore, a secondary goal of this research is to develop an efficient procedure for computing LTIE frequency response functions from acceptable input-output data that can properly identify the features of the hydraulic actuator frequency response, which are important for control system design.

The final objective of this thesis is to implement a hardware-in-the-loop (HIL) simulation architecture that can be utilized to objectively test the performance of the experimental fault tolerant control system under operating conditions that incorporate the dynamics of a complex engineering system. The application area of interest is aircraft flight control where hydraulic actuators are used to position aerodynamic surfaces. In this application, the experimental hydraulic actuator must exhibit good transient performance for a wide range of command inputs and in the presence of a highly uncertain aerodynamic load. Since flight actuator faults can impact the maneuverability of the aircraft and potentially give rise to unsafe operating conditions, demonstrating the ability of the fault tolerant controller to maintain the performance of the faulty flight actuator under realistic in-flight operating conditions is crucial.

1.4 Thesis Outline

The thesis consists of seven chapters and two appendices. Chapter 2 presents a description of the electrohydraulic actuator system under study. A comprehensive review of typical faults in fluid power systems is given and a specially designed hydraulic test bench that is capable of emulating different kinds of system faults is described. The state-of-the-art test bench employs a secondary hydraulic ram as a loading actuator to generate realistic dynamic loading conditions. To build numerical

simulations of each experimental actuator, a detailed and general nonlinear mathematical model of a servovalve controlled actuator is derived from first principles. The nonlinear models, which are validated by open-loop testing, are used as a basis for control system synthesis and evaluation in subsequent chapters.

Chapter 3 presents an overview of the QFT design technique and how, using the concept of LTI equivalence, it can be extended for control system synthesis around uncertain nonlinear plants. Chapter 3 also examines several different approaches for evaluating the equivalent LTI frequency response functions for the hydraulic actuator under study. A numerical procedure for constructing the equivalent LTI frequency response functions directly from the actuator input-output data is proposed. The approach, which is based on numerical integration of the continuous-time Fourier integral, is a crucial element for developing the QFT-based fault tolerant controller.

A QFT position controller is designed in chapter 4 based on a set of equivalent LTI frequency response functions that consider only the normal operation of the hydraulic actuator. This is done to establish a benchmark against which the structure and performance of the fault tolerant controller can be compared. The set of equivalent LTI frequency response functions is then extended to account for the dynamic uncertainty introduced by the internal leakage fault. A fixed-gain fault tolerant control law, which can overcome the effects of the internal leakage fault, is then designed. The performance of the developed controllers is evaluated throughout the chapter by nonlinear simulation studies as well as experimental tests.

Chapter 5 describes the architecture of a hardware-in-the-loop (HIL) simulation framework that has been developed to further evaluate the performance of the fault tolerant control system under operating conditions that incorporate the dynamics of a complex engineering system. Using the HIL simulator, the fault tolerant hydraulic actuator can be exercised against the numerical simulation of a modern high-performance jet aircraft. A QFT-based electrohydraulic loading system is also designed and the overall functionality of the HIL simulator is demonstrated by the

results of several HIL simulation examples.

In chapter 6, the HIL simulator is used to further substantiate the efficacy of the designed fault tolerant controller within the context of a realistic flight control application. The complex interaction between the functionality of the experimental flight actuator and the flight performance of the aircraft is also examined within two different flight maneuvers. It is shown that the fault tolerant controller, by properly compensating the effects of the internal leakage fault, can keep the airplane from entering into an undesirable flight regime.

The contributions of this thesis are summarized in chapter 7, along with some suggestions for future research. The appendices contain information that is ancillary to the body of the thesis. Appendix A details an inverse modeling scheme for hydraulic actuators that was developed previously in [59]. The inverse model is used to solve the actuator input-output data that is required for control system synthesis. Appendix B provides a listing of data, adapted from [69], that are required in the HIL simulation model to compute the aerodynamic load force command that drives the hydraulic loading actuator.

Chapter 2

Hydraulic Actuation System

This chapter begins by describing typical applications and basic operational principles of the valve controlled hydraulic actuator under study. A review of the common faults in hydraulic actuation systems is presented in section 2.3. Section 2.4 provides a brief description of the experimental system upon which the controller developments will be tested. The specially designed hydraulic test bench has the capability to emulate a number of common actuator faults and a secondary hydraulic ram can be employed as a dynamic loading actuator to increase the fidelity of experimentation. A detailed and general nonlinear mathematical model of the experimental valve controlled actuator is derived and validated in section 2.5. The model captures the effects of the actuator internal leakage fault as an adjustable parameter and is an essential element for completing the design of the QFT-based fault tolerant controller.

2.1 Applications

Hydraulic actuators see widespread use in a variety of different applications where large power to weight ratios and fast response times are required, such as in aircraft flight control. Hydraulic actuators are also able to hold a load indefinitely without causing the excessive generation of heat, as is usually the case with electromechanical actuators [41]. This makes hydraulic drives excellent candidates for powering robots

as well as manufacturing and other machinery. Typical capabilities of hydraulic actuators are shown in Figure 2.1.

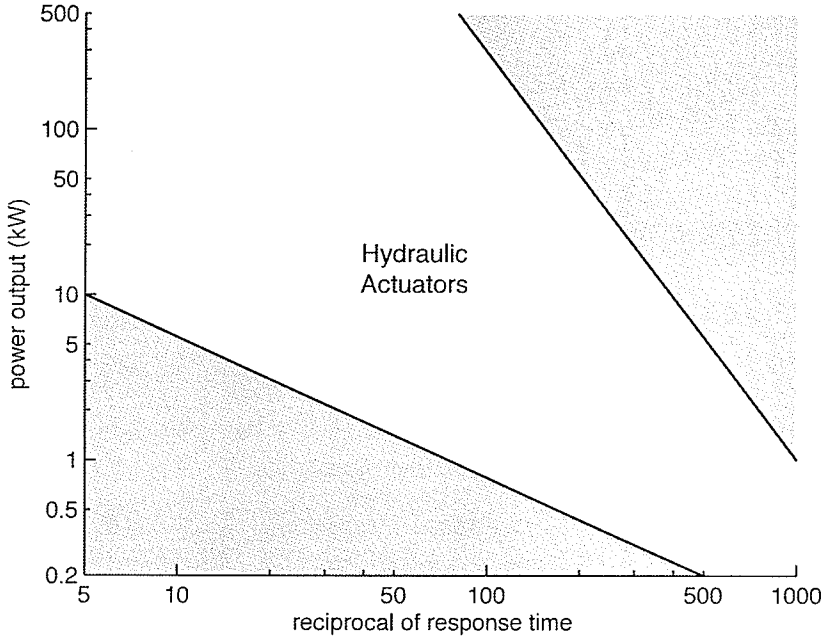

Figure 2.1: Range of power output and control response time for hydraulic actuators (Reproduced from [70] in modified form.)

Perhaps one of the earliest applications of compressed oil actuators was to position warship guns in 1906 [71]. From this point on, the development of fluid power technology continued, in order to satisfy demands for performance that was difficult or impossible to obtain by any other technology [72]. Hydraulic actuators were being integrated into machine tool design by 1925 [73], and began to see use in aviation to power flight surfaces by the 1940s [74]. Due to the need for precise control over the hydraulic system output in these applications, the development of hydraulic servo technology was also advanced during this period. Much of the pioneering work in fluid power control was completed at the Servomechanisms Laboratory at the Massachusetts Institute of Technology culminating in the text *Fluid Power Control* [72]. Herbert E. Merritt, whose focus was on the improvement of hydraulic machine tool

drives, published his classic fluid power text in the late 1960s [2]. Merritt's book is referenced in nearly every research paper written since 1967 and is still used by fluid power designers and students alike [75].

Despite a great deal of academic attention in the first part of the 20th century, an examination of conference proceedings and journal papers of the late 1960s to early 1980s reveals a comparatively low level of activity with regard to research on fluid power drives [61]. Indeed, most of the technological developments during this period have been proprietary, rather than open and general [76]. Today, fluid power research has once again increased in popularity owing to advances in control systems technology as well as the availability and extraordinary computational power of personal and embedded computers. Some of the most common contemporary application areas for fluid power actuators continue to include agriculture, forestry, manufacturing, mining, robotics, construction, material handling, motion and load simulators, as well as aerospace. In many of these applications, the valve controlled hydraulic ram remains the prime mover of choice.

2.2 Valve Controlled Ram

A typical valve controlled hydraulic actuator, applied to position a flight surface, is shown in Figure 2.2 [1,77]. The system consists of a fluid reservoir, which contains hydraulic fluid kept at a low pressure as well as a variable displacement pump that supplies the high-pressure port of a flow control valve. The oil pressure at the valve is typically held at a nominally constant pressure between 17 and 21 MPa (2500 to 3000 psi). Usually, the type of valve employed for hydraulic flight actuation is a nozzle-flapper servovalve with force feedback. The valve controls the flow of fluid to and from the actuator, which consists of two cylindrical chambers separated by a movable piston. In the actuator, elastomeric or metallic seals are used between

dynamic surfaces to prevent hydraulic fluid from leaking across the piston or out to the atmosphere. The control surface is connected to the piston through the actuator rod and a linkage that converts the linear motion of the actuator to the angular deflection of the control surface.

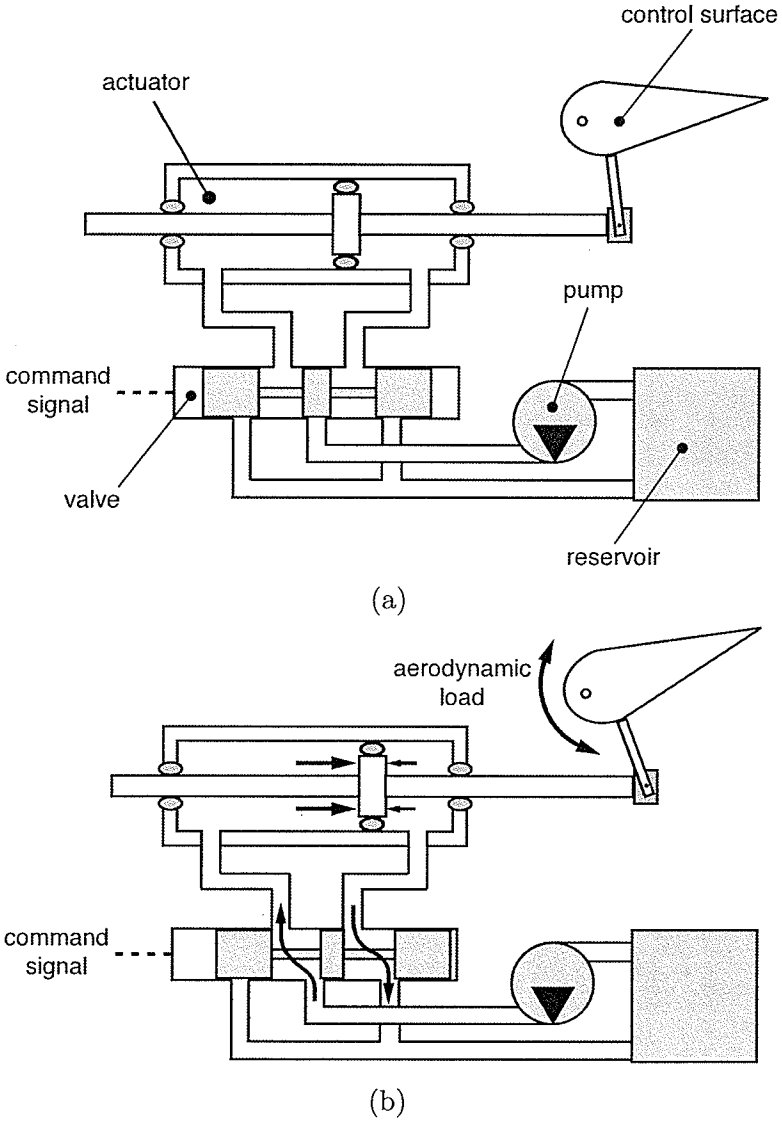

Figure 2.2: Operation of a typical valve controlled hydraulic flight actuator: (a) system components; (b) actuator motion against aerodynamic load for rightward valve spool displacement.

In order to position the control surface, electrical command signals originating from the flight control computer are used to modulate the position of the valve spool. In a nozzle-flapper servovalve, a torque-motor is used to drive a hydraulic amplifier, which in turn, positions the main valve spool. The motion of the valve spool opens one cylinder half to the high-pressure supply, while venting the other to the tank. A pressure imbalance is created across the piston as hydraulic fluid is metered in and out of the actuator halves by the throttling action of the valve (see Figure 2.2b). This imbalance enables the piston to move the control surface against the aerodynamic load, which is created by the distribution of air pressure acting on the surface.

2.3 Common Faults

There are many different faults that can affect the performance of a valve controlled ram. One of the most common problems is the leakage of hydraulic fluid from the fittings and lines that connect the various system components. Hydraulic fluid may also leak across dynamic seals placed between moving parts. Fluid leakages may be classified as *external* or *internal*, depending upon whether the hydraulic fluid is lost to the atmosphere or is simply displaced to another location within the hydraulic circuit. One type of internal leakage fault is the leakage of fluid across the actuator piston seal that closes the gap between the moveable piston and the cylinder wall. As the actuator ages, it is normal for the cylinder bore and the seal material to become worn. This wear may be accelerated by particles of debris that become trapped between the piston and cylinder wall if the hydraulic fluid becomes contaminated due to ineffective filtration or improper maintenance.

As the amount of wear increases, more fluid is allowed to flow across the piston and between the cylinder halves. Although no fluid is lost from the circuit, the dynamic performance of the system is affected since only a portion of the flow delivered to

the actuator is available to move the piston against the load. Leakage across the piston introduces a flow deadband, which can lead to servoing errors, and increases the overall damping of the actuator. These effects are intensified as the size of the leakage grows. A typical piston seal fault can allow over 30% of the flow through the control valve to be bypassed across the piston [15, 16].

Wear and age can also lead to external leakage of hydraulic fluid from the actuator rod seals. Leaking rod seals also tend to increase the damping of the system, giving rise to a more sluggish transient response. Similar effects on the performance of the system can result from external leakages due to supply line failures or improperly installed hydraulic fittings. In extreme cases, it is possible that nearly the entire volume of the fluid supplied to the circuit by the valve will be lost. If the problem is not corrected, the actuator will lose the ability to control the load. Wear of the actuator cylinder and the seals also changes the friction characteristics of the actuator, which can affect the dynamic performance of the system. A 10% change in the viscous damping coefficient of the actuator can be an indication of excessive actuator friction Skormin [5], and signify a potential problem with the actuator seals.

Degradation in the performance of the variable displacement piston pump (VDP) that supplies the high-pressure hydraulic fluid to the system is usually caused by air, water, and particle contamination of the hydraulic fluid [9]. Accelerated wear of pump components also causes excessive internal fluid leakage and an accompanying increase in friction between pump components. These effects worsen, the further the clearances within the unit fall from the original design tolerances. Since the pump must work harder to generate the required hydraulic pressure and flow rate, the overall efficiency of the power supply decreases in the presence of these faults. In addition, there exists a dynamic coupling between the output pressure of the VDP and the magnitude of the pump internal leakage [78]. Thus, the ability of the VDP to maintain the desired supply pressure or flow rate during sudden changes in the demand for fluid is affected by the magnitude of the fluid leakage within the pump.

Since the hydraulic fluid is used to lubricate the pump mechanism, some fluid leakage is normal, but is usually less than 5% of the rated flow capacity of the unit. The performance of the pump begins to degrade when internal leakage rates increase by 10 to 20% above normal [9].

On most commercially available power supplies, the pump supply pressure is set using a pressure relief valve. In order to maintain the nominal pressure of the hydraulic fluid, the relief valve is used to bypass excess fluid to the tank or to de-stroke the hydraulic pump. In the event of a malfunction in the pressure relief valve, the pump pressure can increase or decrease from normal or may oscillate (hunt) around the nominal value. A reduction in the supply pressure reduces the flow capabilities of the valve and can therefore impact the dynamic performance of a servoactuator. A reduced supply pressure also reduces the efficiency of actuator power transfer to the load and can cause the actuator to stall. Aside from a malfunctioning pressure relief valve, leaking supply lines or partial blockage of high-pressure filters can also cause an overall decrease in supply pressure. The nominal supply pressure can also fluctuate with the demand for fluid if a hydraulic accumulator has failed. If the supply pressure increases above nominal, closed-loop servo systems may become unstable due to the accompanying increase in the control valve flow gain. Typical studies [3, 6] seem to indicate that typical hydraulic pump failures can cause variations in the nominal supply pressure on the order of ± 30 %. In severe cases, the supply pressure may be reduced to less than 40% of the nominal value [25].

Another common fault in hydraulic systems is the change in the effective bulk modulus (EBM) of the hydraulic fluid that occurs when the fluid becomes contaminated. Since the EBM is associated with the hydraulic stiffness of the actuator, any change in the nominal EBM can affect the ability of the actuator to work against a load. When the EBM decreases, so does the hydraulic stiffness, which impacts the ability of the actuator to attenuate the effects of load disturbances. During the normal operation of a fluid power system some variation in the value of the EBM can

be expected due to fluctuations in the fluid temperature and pressure[1]. The normal range of the bulk modulus parameter is relatively insensitive to particle contamination of the fluid. Therefore, significant deviations of the EBM from the normal range are generally the result of air or water contamination. Aeration of the fluid, which may be caused by external leakages or by improper maintenance procedures, can cause the EBM to decrease by up to 20% [9]. The accumulation of water in the hydraulic fluid, on the other hand, increases the EBM since the density of water is larger than that of petroleum based hydraulic fluids. A 10% increase in the EBM above normal can be an indicator of water contamination [9].

In many applications, filtration devices are installed at various locations in the hydraulic circuit in order to trap any particles of debris that are carried in the fluid. As the filters become blocked with debris, they begin to restrict the fluid flow around the circuit. This affects system dynamics by reducing the supply pressure and increasing the tank back-pressure, which alters the flow characteristics of the valve. Blocked filter elements can also raise the temperature of the hydraulic fluid causing the EBM to drift outside of its normal range. In addition, increased fluid temperatures can cause premature seal wear. If the flow restriction occurs in the tank return line, the increase in backpressure can damage the servovalve by rupturing the flexure tube that connects the flapper to the torque motor. Therefore, restrictions due to filter blockages often cause the occurrence of other faults within the fluid power circuit.

Mechanical faults in the servovalve, such as wear or scoring of the valve spool and bushing, can also impact the performance of a fluid power system by increasing valve internal leakage and altering the valve friction characteristics. Similar to the leakage of fluid across the actuator piston, increased servovalve leakage adds to the system damping and can lead to servoing errors. Increased friction between the valve spool and bushing can affect the spool position response time and influence the overall

[1]The bulk modulus of standard hydraulic fluids decreases at a rate of approximately 6.2 MPa/°C, and increases at a rate of 0.1 MPa/MPa [79].

accuracy of servovalves [80]. In addition, the accuracy of servovalves can also be influenced by a damaged or worn feedback spring (conventional nozzle-flapper types), by faulty spool position feedback sensors (modern servovalves), or by electrical failures in the primary valve stages (i.e. torque motor or feedback electronics).

Faults in any of the other feedback sensors that relay quantitative information about the hydraulic actuator states can also influence the performance of a closed-loop hydraulic system. Typical faults associated with sensors are sensor gain drift, which leads to measurements inconsistent with the original calibration, and sensor malfunctions. Malfunctioning sensors may have an intermittent or noisy output signal or no output signal at all.

Of all the hydraulic actuator faults described above, fluid leakages are among the most troublesome. Internal fluid leakages, such as leakage across the actuator piston seal, can be especially problematic. Part of the reason for this is the fact that internal leakage is difficult to detect without dismantling the actuator, or analyzing the performance of the system using advanced diagnostics algorithms. Therefore the problem, which can impair the ability of the actuator to control the load, may go unnoticed until system maintenance is performed. Since internal fluid leakage can also generate heat, the fault can impact important system parameters, such as the effective bulk modulus. This can further degrade the performance of the hydraulic system, making the development of a fault tolerant controller that can maintain the performance of the hydraulic system a nontrivial design task, which deserves further attention.

2.4 Experimental Setup

In order to facilitate studies on fault tolerant control of fluid power systems, a specialized test rig that has the capacity to experimentally emulate a faulty fluid power system was designed. A schematic of the experimental test rig is shown in Figure 2.3. The test rig consists of two independent hydraulic circuits that can

interact with one another. Referring to Figure 2.3, the actuator on the left has been outfitted with a number of additional hardware elements that enable the various faults described in section 2.3 to be created experimentally. Hereafter, the left side actuator will be referred to as the fault emulator actuator. The second hydraulic ram, installed on the right side of the test bench is used as a loading actuator. The purpose of the loading ram is to interact with the fault emulator actuator in order to create a dynamic load for the fault emulator circuit to operate against. Both fluid power circuits are mounted to a reinforced steel table and are supplied with filtered hydraulic fluid from a common hydraulic power supply. The hydraulic power supply utilizes a pressure compensated variable-displacement piston type pump and is capable of delivering hydraulic fluid at a maximum pressure of 21 MPa (3000 psi) and a maximum rate of 59 L/min (15.5 GPM).

The fault emulator circuit is built around a main actuator driven by a Moog D765 nozzle-flapper servovalve. The main actuator is a double-rod type with a 610 mm (24 in.) stroke, a 38.1 mm (1.5 in.) bore and 25.4 mm (1 in.) diameter rods. The D765 is high-performance servovalve with a nominal 2 msec rise time and a flow capacity of 34 L/min (9 GPM) at 21 MPa (3000 psi) supply pressure. To create an internal fluid leakage across the actuator piston, the actuator fault under study in this work, fluid is bypassed across the piston using plumbing that directly connects the two cylinder halves. The internal leakage flow rate is set by an adjustable needle valve and is measured using a gear-type positive-displacement flow meter. The experimental setup for producing the internal leakage fault is shown in Figure 2.4. A more detailed description of the capabilities of the fault emulation circuit and a discussion on how the other actuator faults have been implemented in hardware is presented elsewhere in reference [24].

The loading actuator consists of a double-rod actuator driven by a Moog 31 series nozzle-flapper servovalve. The servovalve can deliver fluid to the system at a rate of 26 L/min (7 GPM) when operated at 21 MPa (3000 psi) nominal supply pressure.

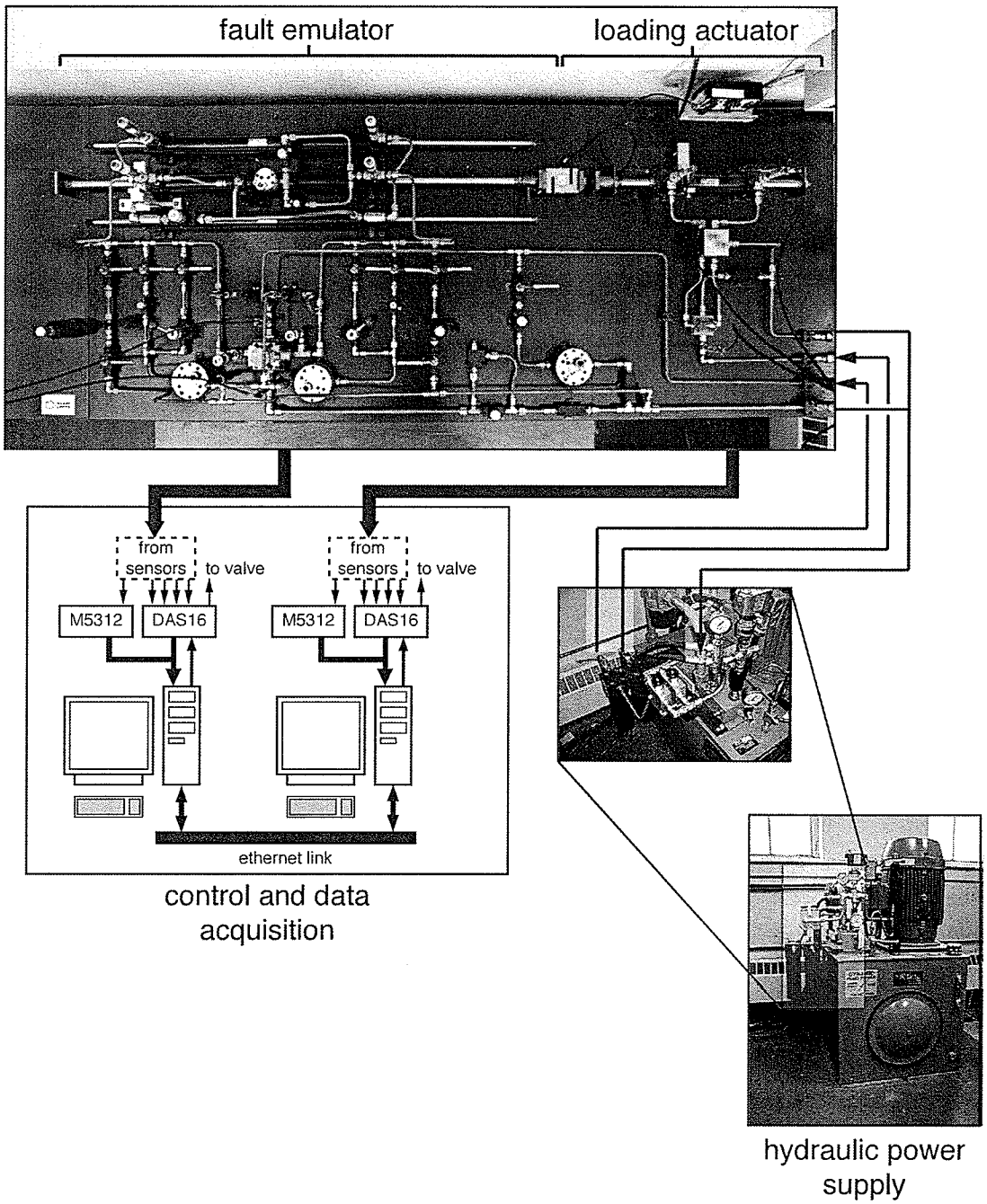

Figure 2.3: Schematic of hydraulic test bench.

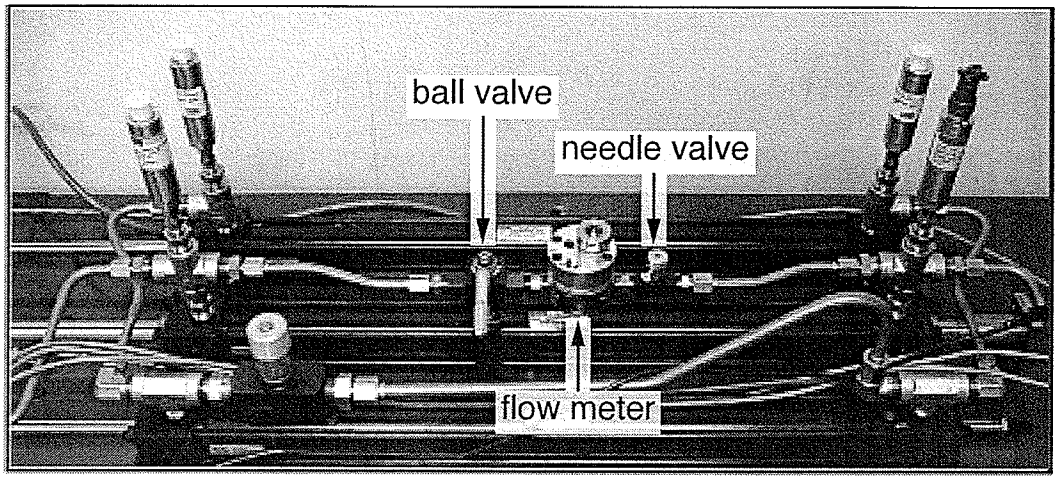

Figure 2.4: Experimental hardware for producing internal leakage fault.

The valve has a nominal 1.5 msec rise time. The loading actuator has a 7.5 kN operational range and is identical to the main actuator of the fault simulation circuit, with the exception of a shorter 203 mm (8 in.) stroke.

In order to decrease the stiffness of the joint between the two hydraulic actuators, a special flexible coupling, which acts nearly as a pure stiffness, was designed. A photograph of the coupling is shown in Figure 2.5. The coupling is built from a number of die compression springs that have been arranged in such a way that both tensile and compressive loads can be transmitted between the rams, by compressing one bank of springs or the other. The nominal stiffness of the flexible joint can be adjusted anywhere between 150 and 1500 kN/m by adding or removing pairs of springs. The actual force transmitted between the rams is measured using a 22 kN (5000 lb) load cell.

Modifying the stiffness of the joint between the two actuators effectively alters the gain of the force control loop implemented around the loading actuator. Reducing the gain has a stabilizing effect [81] and makes it easier to design the force control law. However, a necessary tradeoff is a reduction in the achievable force bandwidth [82]. Therefore, to a certain extent, the stiffness of the joint must be compatible with the

bandwidth of the load force to be replicated. This point will be further elaborated on in chapter 5.

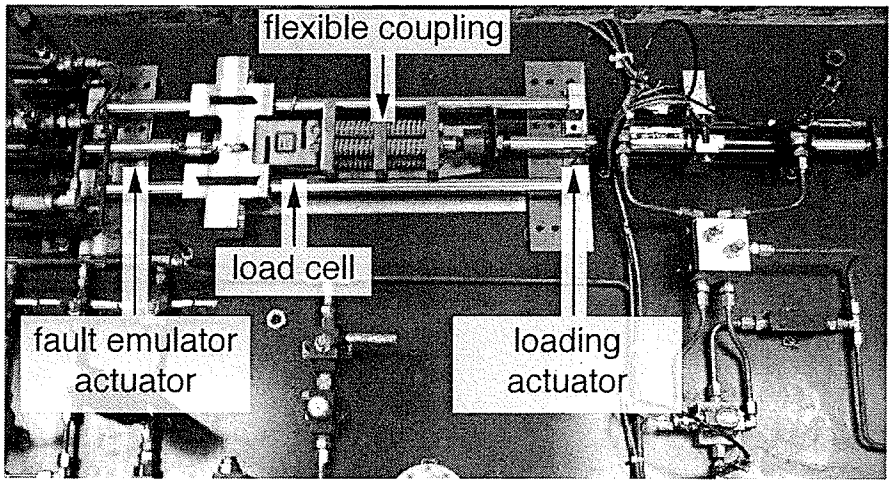

Figure 2.5: Flexible coupling for connecting two experimental hydraulic actuators.

The hydraulic test bench is completed by a computerized control and data acquisition system comprised of two desktop computers, each equipped with a DAS16F input-output board and a M5312 24-bit quadrature incremental encoder card. Using two computers allows each hydraulic circuit to be controlled by a dedicated processor. The DAS16F boards are used to digitize all relevant sensing instruments with the exception of the optical position encoders, which are interfaced directly to the appropriate quadrature card. The D765 servovalve of the fault simulation circuit is driven directly by the analog outputs of one DAS16F board operating as a voltage source. The voltage outputs of the other DAS16F board are conditioned by a Moog N121-132 servocontroller operating in open-loop mode to generate a suitable command current to drive the Moog 31 valve.

2.5 Mathematical Modeling

2.5.1 Nonlinear Model

A schematic of a servovalve controlled hydraulic actuator for mathematical modeling is shown in Figure 2.6. The mathematical model relating the control input, u, to the output variable, which may be the actuator position, x_p, or the actuator force, F_a, depends on the dynamics of the valve spool, the nonlinear flows through the valve control ports, the deformation and compressibility flows, as well as the Newtonian mechanics of the piston motion.

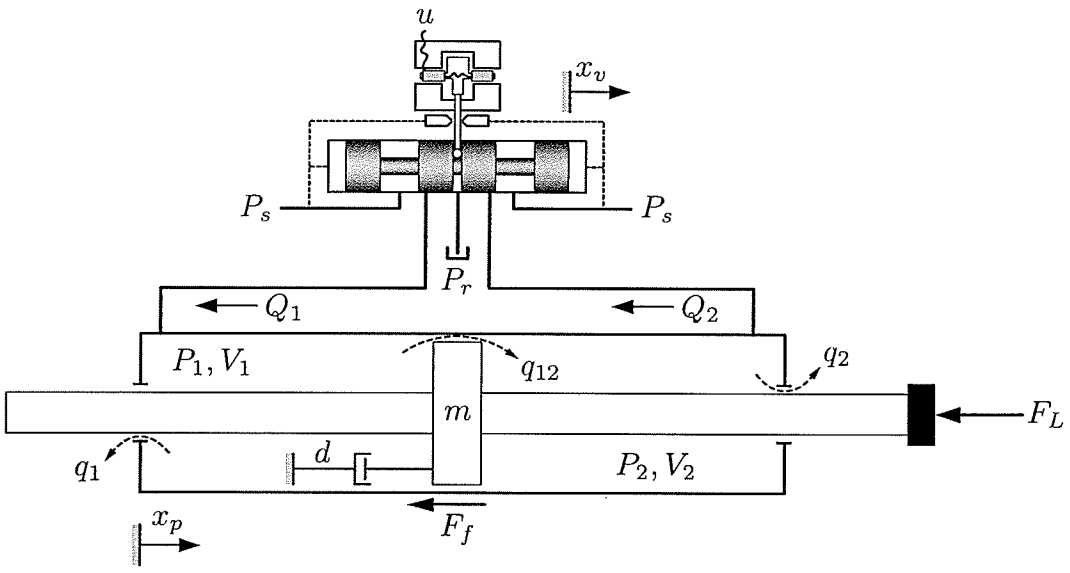

Figure 2.6: Schematic of hydraulic actuator for mathematical modeling.

For a two-stage flapper-nozzle servovalve, the relationship between the input current and the position of the valve spool is nonlinear. However, in the design of hydraulic servosystems, detailed analysis of the non-ideal valve characteristics is generally not required [83]. For the purpose of control system design, the servovalve spool dynamics are often approximated using linear transfer function models that capture

the main characteristics of the valve dynamics in the low frequency range [26, 41, 59]. Here, a second-order model was selected to approximate the dynamics of the servovalve spool position. A second-order lag representation is generally adequate for the design of position servos since the servovalve frequency response is well approximated to the point where the phase lag of the real valve is $-90°$ [83]. The relationship position of the valve spool, x_v, and the current, u, applied to the torque motor is

$$x_v = -\frac{1}{\omega_v^2}\ddot{x}_v - \frac{2\zeta_v}{\omega_v}\dot{x}_v + k_v u \tag{2.1}$$

where k_v is the valve spool position gain and parameters ω_v and ζ_v are the natural frequency and damping ratio that best represent the servovalve magnitude and phase characteristics in the low frequency range. The values of the second-order model parameters can be estimated relatively easily from valve frequency response curves given in manufacturers' catalogs.

For a valve with a critically-lapped spool having matched and symmetrical orifices, control flows Q_1 and Q_2 follow the turbulent orifice equation [2]. The nonlinear governing equations can be written in the following compact form

$$Q_1 = K_v w x_v \sqrt{\frac{P_s - P_r}{2} + \frac{x_v}{|x_v|}\left(\frac{P_s + P_r}{2} - P_1\right)} \tag{2.2}$$

$$Q_2 = K_v w x_v \sqrt{\frac{P_s - P_r}{2} + \frac{x_v}{|x_v|}\left(P_2 - \frac{P_s + P_r}{2}\right)} \tag{2.3}$$

In equations (2.2) and (2.3), $K_v = C_v\sqrt{\frac{2}{\rho_{oil}}}$ is the valve flow gain, which depends on orifice coefficient of discharge, C_v, and the density, ρ_{oil}, of the hydraulic fluid. Parameter w is the width of the rectangular port cut into the valve bushing through which the fluid flows. The supply and tank pressures are denoted by P_s and P_r, respectively, while variables P_1 and P_2 refer to the hydraulic pressures in each of the actuator cylinders.

The continuity equations for compressible fluid volumes describe the time rate of change of the pressure in each actuator chamber. The continuity equation considers both the deformation and compressibility flows and can be written for each cylinder half as [2]:

$$\dot{P}_1 = \frac{\beta_h}{Ax_p + \bar{V}_1}(Q_1 - q_1 - q_{12} - A\dot{x}_p) \tag{2.4}$$

$$\dot{P}_2 = \frac{\beta_h}{A(L - x_p) + \bar{V}_2}(-Q_2 - q_2 + q_{12} + A\dot{x}_p) \tag{2.5}$$

In equations (2.4) and (2.5), A is the annulus areas of the piston, q_1 and q_2 are the external leakage flows from each cylinder half, and q_{12} is the internal leakage flow across the actuator piston. Parameter β_h denotes the effective bulk modulus of the hydraulic fluid. The volumes of oil contained in the connecting lines between the servovalve and the actuator are given by $\bar{V}_1$ and $\bar{V}_2$. The length of the actuator stroke is denoted by L.

Unless leakage flows are purposefully introduced into the actuator, for example to improve the system damping [79], variables q_1, q_2 and q_{12} can be considered to be null for a normally functioning ram. However, when any of the actuator seals fail or begin to wear, the leakage of hydraulic fluid across the dynamic sealing surfaces can become significant. A couple of damaged actuator rod seals are shown in Figure 2.7. From these illustrations, it is evident that the leakage flow paths across failed seals are highly irregular and have complex geometries. Consequently, it is assumed that the leakage flows caused by faulty actuator seals can be described using the turbulent orifice equation. Assuming the external leakage flows are vented directly to the atmosphere the actuator leakage rates are given by the following equations

$$q_1 = K_1\sqrt{P_1} \tag{2.6}$$

$$q_2 = K_2\sqrt{P_2} \tag{2.7}$$

$$q_{12} = K_{12}\sqrt{|P_1 - P_2|}\text{sgn}(P_1 - P_2) \tag{2.8}$$

where K_1, K_2, and K_{12} are the turbulent leakage coefficients whose values depend on the severity of the leakage fault. In (2.8), the sign function has been included in order to accommodate the directionality of the leakage flow, which depends on the sign of pressure difference $(P_1 - P_2)$.

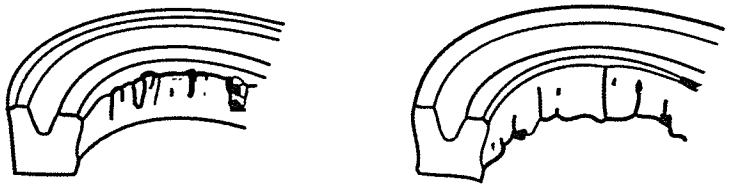

(a) (b)

Figure 2.7: Examples of worn actuator rod seals from a manufacturers' catalog [84]: (a) scarring due to particulate fluid contamination; (b) extrusion due to extreme pressure.

In order to complete the mathematical model of the hydraulic servoactuator, the Newtonian mechanics governing the motion of the actuator are now considered. By carrying out a force balance on the piston, it is found that the motion of the actuator can be described by the following equation

$$m\ddot{x}_p + d\dot{x}_p = F_a - F_L - F_f \tag{2.9}$$

In (2.9), m is the combined mass of the piston, actuator rods and load, and parameter d is the equivalent viscous damping coefficient, which describes the combined effect of the viscous friction between the piston and the cylinder walls and the damping of the load. Force $F_a = A\,(P_1 - P_2)$ is the force generated by the actuator, while force F_L refers to the external load disturbance that must ultimately be rejected at the plant output. The force acting between the piston and the cylinder walls due to friction is denoted by F_f.

Equations (2.1) to (2.3) and (2.4) to (2.9) can now be assembled to form a non-

linear model of the entire hydraulic actuator in the state space

$$\dot{x}_p = v_p \tag{2.10a}$$

$$\dot{v}_p = \frac{1}{m}\left(AP_1 - AP_2 - dv_p\right) - \frac{1}{m}F_d \tag{2.10b}$$

$$\dot{P}_1 = \frac{\beta_h}{Ax_p + \bar{V}_1}\left[K_v w x_v \sqrt{\frac{P_s - P_r}{2} + \frac{x_v}{|x_v|}\left(\frac{P_s + P_r}{2} - P_1\right)}\right. \tag{2.10c}$$

$$\left. -K_1\sqrt{P_1} - K_{12}\sqrt{|P_1 - P_2|}\,\mathrm{sgn}(P_1 - P_2) - Av_p\right] \tag{2.10d}$$

$$\dot{P}_2 = \frac{\beta_h}{A(L - x_p) + \bar{V}_2}\left[-K_v w x_v \sqrt{\frac{P_s - P_r}{2} + \frac{x_v}{|x_v|}\left(P_2 - \frac{P_s + P_r}{2}\right)}\right. \tag{2.10e}$$

$$\left. -K_2\sqrt{P_2} + K_{12}\sqrt{|P_1 - P_2|}\,\mathrm{sgn}(P_1 - P_2) + Av_p\right] \tag{2.10f}$$

$$\dot{x}_v = v_v \tag{2.10g}$$

$$\dot{v}_v = -{\omega_v}^2 x_v - 2\zeta_v\omega_v v_v + k_v{\omega_v}^2 u \tag{2.10h}$$

The nonlinear state equations (2.10) are valid for both extending and retracting strokes and the states v_p and v_v refer to the velocities of the piston and the valve spool. The output variable for position control is x_p and the two system inputs are the control valve command signal, u, and the total disturbing force $F_d = F_L + F_f$. Furthermore, state equations (2.10) directly capture the effects of the actuator internal and external leakage faults as adjustable model parameters.

2.5.2 Model Validation

Using nonlinear state equations (2.10), a numerical simulation model was implemented for each hydraulic circuit, to facilitate control system design and analysis. The numerical values of the model parameters, for each actuator, were identified wherever possible from available manufacturers' data. However, some parameter values had to be estimated by comparing nonlinear simulation results with experimental

data. The nominal system parameters identified for each actuator are summarized in Tables 2.1 and 2.2. Standard values [2] for the effective bulk modulus and mass density of hydraulic fluid are reported.

Table 2.1: List of nominal system parameters of fault emulation circuit, under normal operation.

Parameter	Symbol	Value
supply pressure	P_s	≤ 17 MPa
tank pressure	P_r	< 0.25 MPa
mass of piston, rods and load	m	12.3 kg
static friction	F_s	800 N
Coulomb friction	F_C	250 N
Stribeck velocity	v_s	0.08 m/sec
LuGre bristle-spring constant	σ_0	2×10^5 N/m
LuGre bristle-damping constant	σ_1	240 N·sec/m
viscous damping coefficient	d	250 N·sec/m
piston annulus area	A	6.33 cm^2
actuator stroke	L	609.6 cm
line volumes	$\bar{V}_1, \bar{V}_2$	88.7 cm^3
hydraulic fluid density	ρ_{oil}	847 kg/m^3
fluid bulk modulus	β_h	689 MPa
servovalve discharge coefficient	C_v	0.6
servovalve flow gain	K_v	2.92×10^{-2} m$^{3/2}/\sqrt{\text{kg}}$
maximum valve spool displacement	x_{vm}	± 0.2794 mm
servovalve orifice area gradient	w	20.75 mm^2/mm
servovalve spool position gain	k_v	0.0279 mm/V
servovalve natural frequency	ω_v	175 Hz
servovalve damping ratio	ζ_v	0.65

Table 2.2: List of nominal system parameters of loading actuator.

Parameter	Symbol	Value
supply pressure	P_s	$\leq$ 17 MPa
tank pressure	P_r	$<$ 0.25 MPa
mass of piston, rods and load	m	3.8 kg
static friction	F_s	750 N
Coulomb friction	F_C	200 N
Stribeck velocity	v_s	0.09 m/sec
LuGre bristle-spring constant	σ_0	2×10^5 N/m
LuGre bristle-damping constant	σ_1	660 N·sec/m
viscous damping coefficient	d	250 N·sec/m
piston annulus area	A	6.33 cm^2
actuator stroke	L	203.2 cm
line volumes	$\bar{V}_1, \bar{V}_2$	14.7 cm^3
hydraulic fluid density	ρ_{oil}	847 kg/m^3
fluid bulk modulus	β_h	689 MPa
servovalve discharge coefficient	C_v	0.6
servovalve flow gain	K_v	2.92×10^{-2} m$^{3/2}/\sqrt{\text{kg}}$
maximum valve spool displacement	x_{vm}	$\pm$0.315 mm
servovalve orifice area gradient	w	13.21 mm^2/mm
servovalve spool position gain	k_v	0.0315 mm/V
servovalve natural frequency	ω_v	150 Hz
servovalve damping ratio	ζ_v	0.9

To investigate whether the simulation models derived for each actuator adequately represent the behavior of the real fluid power systems, several open-loop validation tests were performed on each ram. In one set of experiments a sinusoidal input signal was applied to the valve. The supply pressure was set to 17.2 MPa (2500 psi) and each hydraulic circuit was run independently. The time histories of the actuator position and the actuator cylinder pressures were recorded. The nominal sampling rate was 1.3 kHz. A suite of numerical simulations was then carried out for comparison. Since the actuators were run in the absence of any external load, the friction force was the dominant load acting on the piston. Therefore, to properly compare the experimental and simulated results, the actuator friction force had to be estimated. The friction force was computed in the simulations using a LuGre friction model [85]. The LuGre model views the mechanism of friction in terms of a bristle model and computes the friction force as

$$F_f = \sigma_0 z + \sigma_1 \dot{z} \tag{2.11}$$

where σ_0 and σ_1 are parameters. State, z, is required to model the frictional dynamics as defined by the following differential equation

$$\dot{z} = \dot{x}_p - \sigma_0 \frac{|\dot{x}_p|}{F_C + (F_s - F_C)e^{-(\dot{x}_p/v_s)^2}} z \tag{2.12}$$

In (2.12), F_s is the stiction force, F_C is the magnitude of the Coulomb friction, and v_s is the Stribeck velocity [85]. The effect of viscous friction has already been incorporated into the system model (see state equations 2.10), and is therefore not accounted for in (2.12). It must be emphasized that actuator friction, which can pose a serious challenge to achieving good performance in some applications, will not be included in the control system development since friction effects cannot be incorporated easily into the QFT synthesis procedure. Nonetheless, as will be seen later, neglecting friction does not adversely affect the closed-loop performance of the QFT control systems developed in this work.

The experimental and simulation results for one fault emulator validation test are compared in Figures 2.8 through 2.10. In the test, a harmonic command signal (1 Hz frequency and 5 V peak-to-peak amplitude) was applied to the valve. During the test, the value of the hydraulic supply pressure was observed to fluctuate between 16.5 and 17.3 MPa (2400 to 2510 psi), indicating that the system supply pressure may need to be considered as an uncertain model parameter for control system design. The return line pressure never exceeded 232 kPa (35 psi). Therefore, in the numerical simulation, fluctuations in the supply pressure were accounted for using the experimentally measured values. The return line gage pressure was considered to be zero.

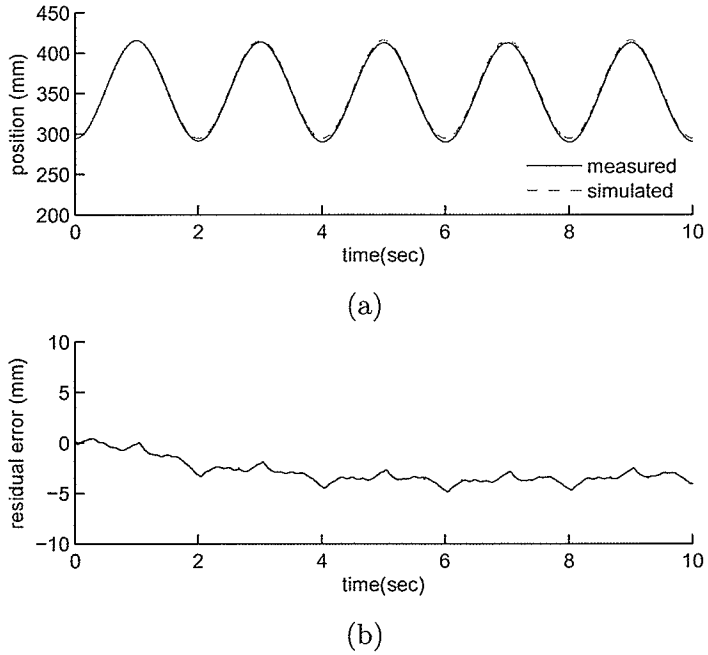

Figure 2.8: Predicted and measured position for fault emulator actuator model validation test: (a) actuator position; (b) residual error.

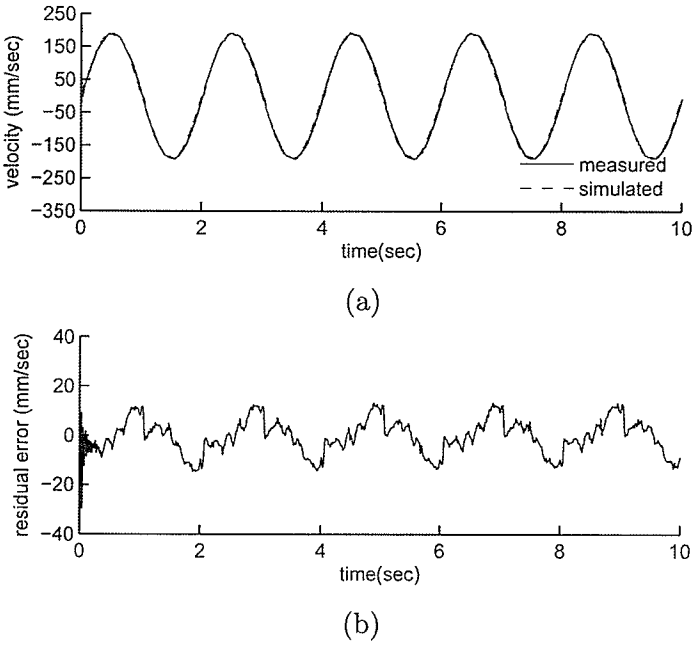

Figure 2.9: Predicted and measured velocity for fault emulator actuator model validation test: (a) actuator velocity; (b) residual error.

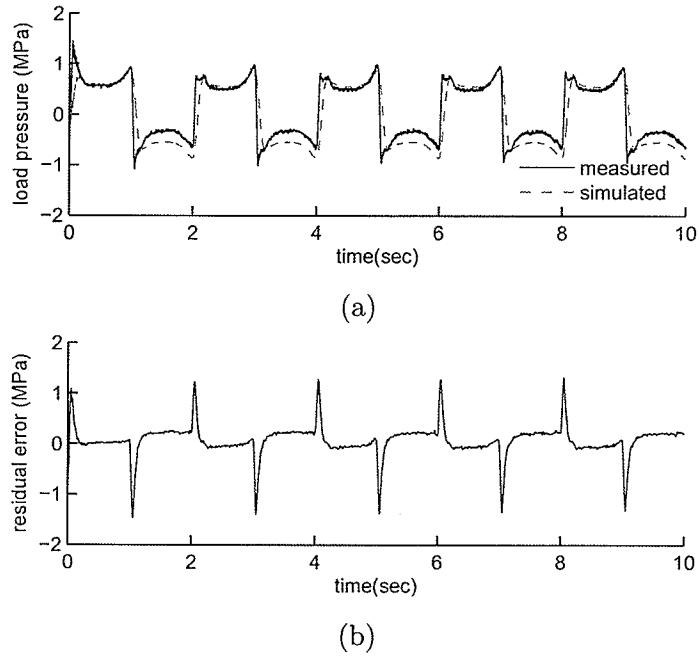

Figure 2.10: Predicted and measured load pressure for fault emulator actuator model validation test: (a) load pressure; (b) residual error.

The measured and model-predicted motion of the actuator is shown in Figure 2.8 along with the residual estimation error. It is observed that the nonlinear actuator model predicts the displacement of the ram with a good degree of accuracy. The average residual position error is about 2%. The actuator velocity, shown in Figure 2.9 was also adequately predicted by the numerical simulation model, as evidenced by the trace of the residual velocity error. The experimental actuator velocity was computed *a posteri* from the experimental position data using linear regression analysis and a 20 sample moving window. With respect to the actuator load pressures, $(P_1 - P_2)$, the average residual error was around 10% (see Figure 2.10).

A similar 1 Hz harmonic motion test was carried out for the loading actuator. Figures 2.11 through 2.13 show the experimental and simulation results. For the test, the amplitude of the control current applied to the servovalve was 9 mA peak-to-peak. As before, fluctuations in the hydraulic supply pressure were observed in the experiment and were accounted for in the simulation using the recorded experimental data. Referring to Figures 2.11 through 2.13, good overall agreement is observed between the experimental and simulated results. Residual errors pertaining to the actuator position and load pressure were less than 2% and 5%, respectively. In another set of open-loop experiments, step inputs of various magnitudes and duration were applied to each hydraulic system. When the experimental responses were compared to the results obtained from the numerical simulation models, good agreement was again noted.

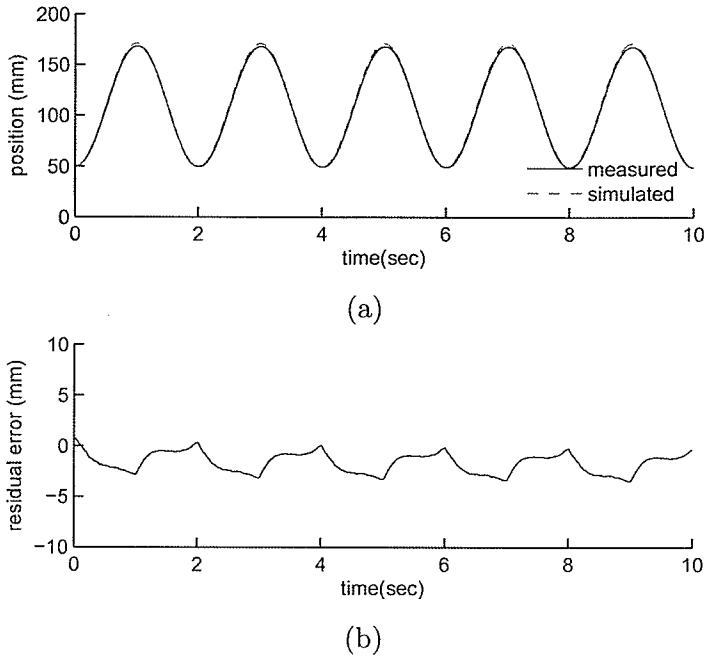

Figure 2.11: Predicted and measured position for loading actuator model validation test: (a) actuator position; (b) residual error.

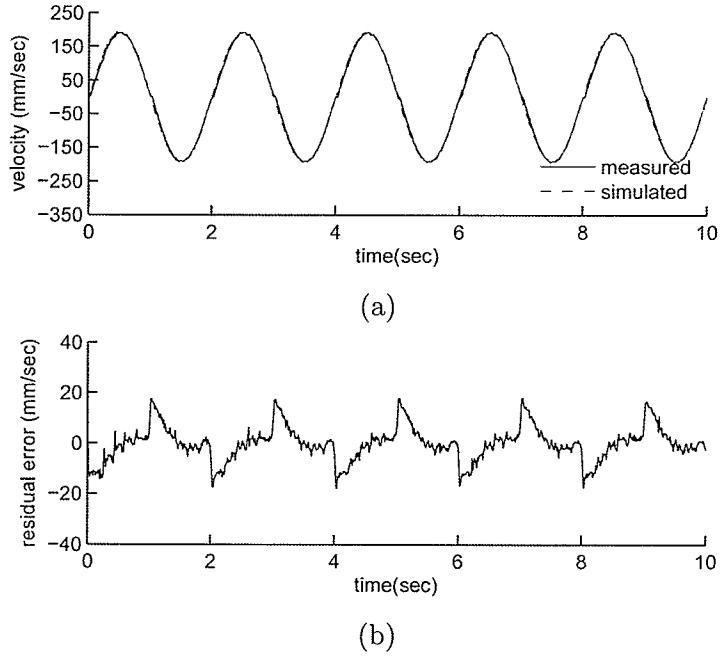

Figure 2.12: Predicted and measured velocity for loading actuator model validation test: (a) actuator velocity; (b) residual error.

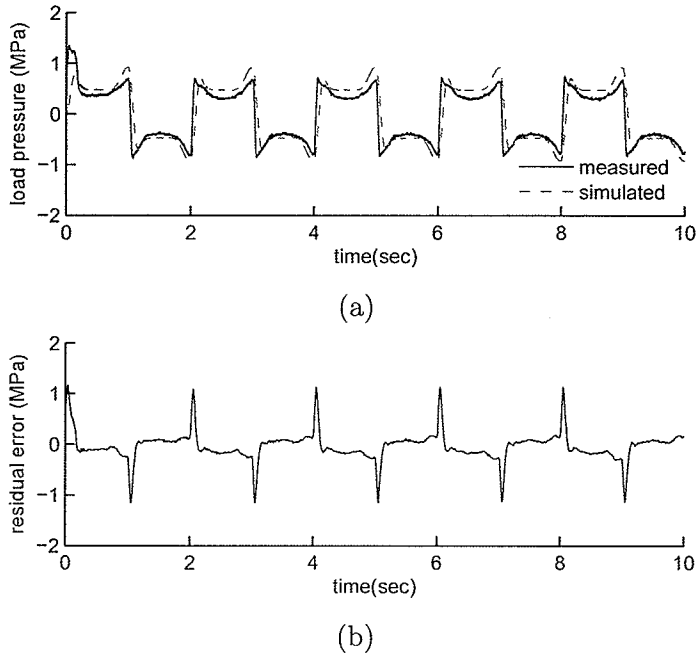

Figure 2.13: Predicted and measured load pressure for loading actuator model validation test: (a) load pressure; (b) residual error.

2.6 Summary

This chapter described the operational principles of valve controlled hydraulic actuators and presented a comprehensive review of common faults that can impair the performance of this type of system. The potential effects of the identified faults on the performance of fluid power systems were also discussed, in a qualitative fashion. Details of the experimental system upon which the controller developments of this work will be tested were given. Finally, a general and nonlinear model of the experimental hydraulic actuator was derived and validated. The model captures the effects of the actuator internal leakage fault as an adjustable parameter and is an essential element for completing the design of the QFT-based fault tolerant controller. The model will also be employed for developing a robust force controller for the electrohydraulic loading actuator.

Chapter 3

Quantitative Feedback Theory

This chapter presents an overview of the quantitative feedback theory (QFT) design technique [66] that is used for control system synthesis. The classical two degree of freedom feedback control problem is reviewed in section 3.1 followed by a demonstration of QFT design procedure in section 3.2. A simple design example, around a parametrically uncertain linear time-invariant (LTI) plant, is given first. Extension of the QFT methodology for control system design around nonlinear plants, such as hydraulic actuators, is discussed next. The basic idea behind QFT design for nonlinear systems is to replace the nonlinear plant by a set LTI transfer functions which is equivalent to the original nonlinear system with respect to a set of acceptable plant outputs [86]. Control system development is then executed for the system represented by the set of equivalent LTI transfer functions. Two approaches for translating nonlinear plant dynamics into an equivalent LTI form are available. The first, which is very popular amongst engineers, is to employ small-signal analysis to linearize the nonlinear system equations about an operating point. The second approach employs the concept of restricted device equivalence [63], where the equivalent LTI function is found by evaluating the transforms of the actuator input-output signals and taking their ratio, in the frequency domain. This is called the LTI-equivalent (LTIE) approach [87]. Section 3.3 shows that small-signal analysis, in general, fails to properly describe the hydraulic actuator dynamics, thus making the LTIE approach more

attractive for QFT synthesis of hydraulic actuator control systems. A numerical procedure for computing the LTIE frequency response of hydraulic actuators, which is a crucial step in the control design process, is developed.

3.1 Background

The block diagram of a typical two degree of freedom control system is shown in Figure 3.1. It is desired to formulate a linear time invariant (LTI) prefilter $F(s)$ to shape reference input, r, and a controller $G(s)$ to drive the plant $P(s) \triangleq P_1(s)P_2(s)$. Both the controller and the prefilter must work together to ensure that the value of controlled output, y, tracks the reference input within some prescribed tolerance and in a stable fashion. It is also the role of control law $G(s)$ to maintain these objectives in the presence of several additional nonideal inputs, d_i, d_o and n that can perturb the value of the output. With reference to Figure 3.1, signal d_i is a disturbing signal that enters the plant internally and d_o is a disturbance that acts directly on the plant output. Nuisance signal n refers to the measurement noise associated with the feedback sensor that monitors the value of the plant output. Since the plant is presently assumed to be LTI, the value of the closed-loop output can be obtained easily by superposition:

$$Y(s) = \left\{\frac{Y(s)}{R(s)}\right\} R(s) - \left\{\frac{Y(s)}{D_i(s)}\right\} D_i(s) - \left\{\frac{Y(s)}{D_o(s)}\right\} D_o(s) - \left\{\frac{Y(s)}{N(s)}\right\} N(s) \quad (3.1)$$

In (3.1), the s-notation implies Laplace transformation, i.e. $Y(s) = \mathcal{L}\{y(t)\}$, and the rational functions $\{\cdot\}$ represent the transfer functions between each input and output, Y.

The important system transfer functions can be written as follows, in terms of loop transmission $L = GP$:

$$\frac{Y}{R} = F\frac{L}{1+L} \quad (3.2)$$

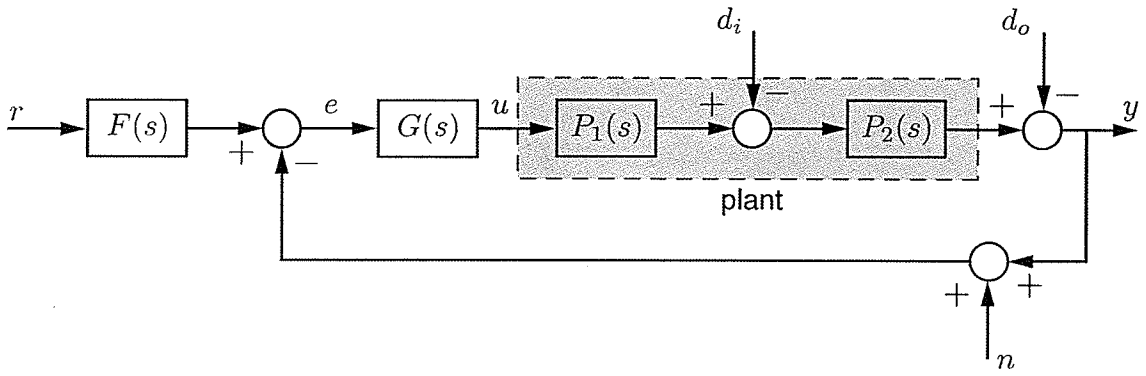

Figure 3.1: Two degree of freedom control system.

$$\frac{Y}{D_i} = \frac{P_2}{1+L} \tag{3.3}$$

$$\frac{Y}{D_o} = \frac{1}{1+L} \tag{3.4}$$

$$\frac{Y}{N} = \frac{L}{1+L} \tag{3.5}$$

Upon inspection of transfer functions (3.2) to (3.5), it can be seen that the two available degrees of freedom, namely functions F and L, allow the tracking and regulating functions of the closed-loop control system to be synthesized independently. The regulating function of the control loop is realized by designing $G = \frac{L}{P}$ to make the Bode magnitude of the loop transmission large in the low frequency range $0 \leq \omega \leq \omega_c$, where ω_c is the gain-crossover frequency[1]. Designing G so that $|L| \gg 1$ reduces the effects of disturbances by decreasing the magnitude of the sensitivity function, $S = \frac{1}{1+L}$. Thus, one of the primary uses of feedback is to better attenuate the effects of immeasurable disturbance inputs [88]. In addition, using G to make L large, results in $\frac{Y}{R} = F\frac{L}{1+L} \approx F$ at low frequencies. Hence, the reference tracking performance of the

[1]The gain-crossover frequency, ω_c, is defined as the frequency where $|L(j\omega_c)| = 1$.

closed-loop system is defined primarily by the response of prefilter F.

Another important advantage of closing the loop is a reduction in the sensitivity of the system output to uncertainties in the values of the system parameters. Such uncertainty can result from measurement errors, the effects of plants nonlinearities, or the occurrence of faults in the system. Horowitz [63,88] has shown that the variation in the nominal system transfer function, $T_{\text{nom}} = F\frac{GP_{\text{nom}}}{1+GP_{\text{nom}}}$, due to large-scale changes in the parameters of the plant, i.e. large-scale sensitivity S_P^T, can be written as follows:

$$S_P^T \triangleq \frac{\Delta T/T_{\text{nom}}}{\Delta P/P_{\text{nom}}} = \frac{\frac{T-T_{\text{nom}}}{T}}{\frac{P-P_{\text{nom}}}{P}} = \frac{1-\frac{T_{\text{nom}}}{T}}{1-\frac{P_{\text{nom}}}{P}} = \frac{1-\frac{P_{\text{nom}}/P+L_{\text{nom}}}{1+L_{\text{nom}}}}{1-\frac{P_{\text{nom}}}{P}} = \frac{1}{1+L_{\text{nom}}} \tag{3.6}$$

Referring to the right hand side of (3.6), it is observed that designing G to make $|L| \gg 1$ in the low frequency range not only improves the regulating properties of the closed-loop system, but also reduces the overall variation in the system transfer function due to plant parametric uncertainty[2].

From the above discussion, it is evident that the amount of feedback used to improve system performance should be related to the prescribed tolerances on the closed-loop performance and also to the amount of uncertainty in the plant. This philosophy is followed in QFT, where the primary objective of the controller design

[2]The price that must be paid for these benefits of feedback is explained by a fundamental constraint on the nature of sensitivity function, S, in the context of LTI feedback control systems. This constraint is known as Bode's integral theorem [89], or the equality of positive and negative feedback areas [63]:

$$\int_0^\infty \ln|S(j\omega)|d\omega = 0 \tag{3.7}$$

Equation (3.7) states that if $|S| < 1$ over some frequency range, such as when $|L|$ is large, there must exist another frequency range where $|S| > 1$ in order to satisfy the integral. Since in most practical feedback control systems $|S| < 1$ up to the crossover frequency, (3.7) implies that the sensitivity must be greater than unity in the high frequency range where $|L|$ is small. In other words, closing the feedback loop around the plant simply shifts the region of high loop sensitivity from the low frequency range to the high frequencies [90]. It is therefore important to reduce $|L|$ as quickly as possible for frequencies above the gain-crossover to limit the band of frequencies over which $|S| > 1$. This practice ensures that the controller bandwidth, one measure of the cost of feedback, can be kept to a practicable minimum and reduces, as much as possible, the sensitivity of the system to high frequency noise, resonant modes, and unmodeled high frequency dynamics which are amplified when $|S| > 1$.

process is to economize the cost of feedback associated with reducing the system sensitivity to plant parametric uncertainty. The goal is to design G with the least amount of gain-bandwidth necessary to satisfy the desired closed-loop performance specifications [66]. QFT thus establishes a quantitative link between dynamic uncertainty, closed-loop performance requirements, and the amount of compensation necessary to meet the design objectives. QFT synthesis is carried out in the frequency domain by shaping the nominal loop transmission, L, to satisfy point-wise design bounds on sensitivity reduction, and by designing prefilter, F, in a way that the prescribed closed-loop performance specifications are satisfied for each plant in the uncertain set. A properly designed QFT control system therefore exhibits *robust performance* with respect to the prescribed control objectives [91].

3.2 Review of QFT Design Technique

This section presents an overview of the QFT design technique. The synthesis procedure is demonstrated by following a simple design example for an uncertain LTI plant. Two approaches for extending the QFT design methodology to accommodate nonlinear plants, such as hydraulic actuators are also described.

3.2.1 Linear Time Invariant Plants

QFT control system design around an uncertain LTI plant is carried out by completing the following steps:

1. Establish bounds on each of the uncertain model parameters and compute the variation in the frequency response of the uncertain plant. The locus describing overall variation in the open-loop magnitude and phase at a given angular frequency is called a QFT template.

2. Define a set of acceptable closed-loop performance tolerances in the frequency domain.

3. Compute a set of point-wise bounds on nominal loop transmission L to guide the design of compensator G. Shaping L to satisfy the design bounds guarantees

that the prescribed closed-loop performance can be achieved over the entire range of plant uncertainty described by the templates.

4. Synthesize prefilter F to further shape the reference tracking response.
5. Verify the design by simulations and/or experiments.

The various steps in the QFT design process are now elaborated on by following a typical design example. Consider the following LTI plant:

$$P(s) = \frac{K}{s(s^2 + 2\zeta\omega_n s + \omega_n^2)} \tag{3.8}$$

The parametric uncertainty associated with the plant transfer function (3.8) is as follows: $K \in [1, 100]$, $\omega_n^2 \in [8, 125]$, and $\zeta \in [0.63, 0.93]$. These parameter uncertain ranges were selected arbitrarily. However, in practice the uncertainty in each plant parameter must be determined by considering: (i) the accuracy with which the plant parameters can be measured, (ii) how the characteristics of the plant components vary over time or under different operating conditions, (iii) how faults can influence the plant dynamics, and (iv) the effects of any inherent system nonlinearities.

Once the ranges of the plant parametric uncertainties have been established, the plant templates can be determined. Templates of (3.8) are shown in Figure 3.2 at a number of selected frequencies, ω. Only the sizes of the templates are important in the QFT design process as their positions relative to one another will be manipulated during loop shaping by adjusting the frequency response of G. Therefore, in Figure 3.2, the templates are shown side-by-side for comparison. The size of each template in the vertical direction corresponds to the overall variation in the open-loop gain of the plant, while the size of each template in the horizontal direction depicts the overall variation in the open-loop phase angle. The shapes of the templates can be obtained most easily by first discretizing the uncertainty range of each parameter and then computing the frequency response for various combinations of the uncertain plant parameters (see §9.2 of [92]). The plant templates are then determined, at each

frequency of interest, by finding the boundary of the set of magnitude-phase points (see template for $\omega = 0.5$ in Figure 3.2).

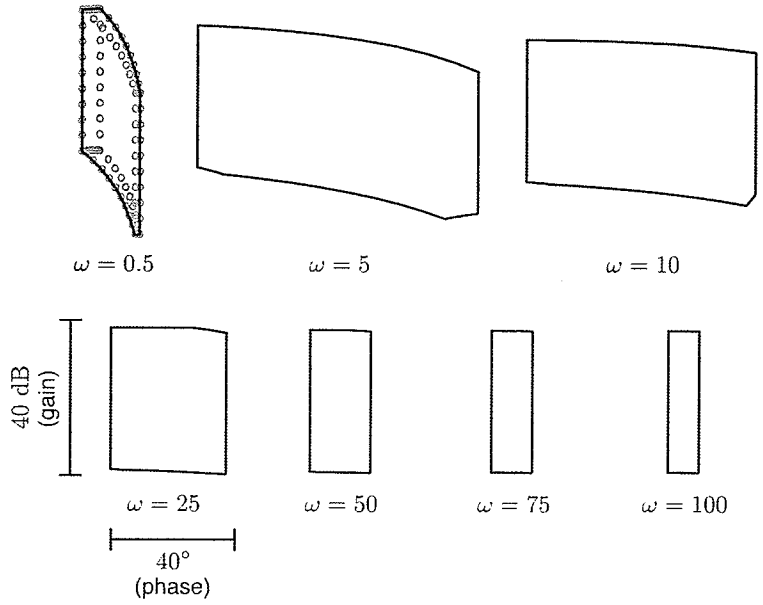

Figure 3.2: Templates of uncertain plant (3.8) at selected frequencies, ω (rad/sec). The entire set of computed magnitude-phase points are shown for $\omega = 0.5$ rad/sec, for reference.

Using the plant templates, QFT bounds are determined next to guide the shaping of the nominal loop transmission, $L = GP_{\text{nom}}$ on the Nichols chart. The QFT bounds are derived, at each design frequency, from a set of prescribed tolerances on closed-loop performance. Specifications on closed-loop regulating performance for QFT design are written as frequency domain inequalities built from classical time domain specifications such as rise-time, settling time, and maximum overshoot [92]. Several QFT design inequalities are summarized in Table 3.1 [93]. In Table 3.1, constraints Λ are frequency dependent bounds on the Bode magnitude. Notation $\mathcal{P}$ has been used to emphasize the fact that the inequality must be satisfied for *all* of the plants in the uncertain set.

Closed-loop reference tracking performance is specified in QFT by defining two frequency dependent functions whose magnitude difference describes the amount of

Table 3.1: Typical specifications on closed-loop performance for QFT design [93] (see Figure 3.1 for nomenclature).

Specification	Design Inequality
robust stability margins	$\left\|\frac{Y}{RF}\right\| = \left\|\frac{G\mathcal{P}}{1+G\mathcal{P}}\right\| \leq \Lambda_M$
plant internal disturbance attenuation	$\left\|\frac{Y}{D_i}\right\| = \left\|\frac{\mathcal{P}_2}{1+G\mathcal{P}}\right\| \leq \Lambda_{Di}(\omega)$
plant output disturbance attenuation	$\left\|\frac{Y}{D_o}\right\| = \left\|\frac{1}{1+G\mathcal{P}}\right\| \leq \Lambda_{Do}(\omega)$
control effort/noise minimization	$\left\|\frac{-U}{N}\right\| = \left\|\frac{G}{1+G\mathcal{P}}\right\| \leq \Lambda_N(\omega)$

variation in the system transfer function that is permissible at each design frequency. Lower and upper bounds are necessary because it is impossible to specify a single acceptable system function $T = F\frac{GP}{1+GP}$ for all plants in set $\mathcal{P}$. The QFT design specification for reference tracking is written as [63]:

$$|T_L(j\omega)| \leq \left|F(j\omega)\frac{G(j\omega)\mathcal{P}(j\omega)}{1+G(j\omega)\mathcal{P}(j\omega)}\right| \leq |T_U(j\omega)| \tag{3.9}$$

Specification (3.9) implies that the closed-loop frequency responses should be enveloped from above and below by frequency dependent functions $T_U(j\omega)$ and $T_L(j\omega)$, respectively. Bounds T_U and T_L are typically derived from model system responses in the time domain [94]. Referring to (3.9) it is evident that the task of satisfying the reference tracking specification is divided between the controller, G, and the prefilter, F. However, the design of prefilter F can be decoupled from the design of controller

G by rewriting inequality (3.9) as follows [93]:

$$\log|T_L(j\omega)| - \log\left|\frac{G(j\omega)\mathcal{P}(j\omega)}{1+G(j\omega)\mathcal{P}(j\omega)}\right|_{\min} \leq \log|F(j\omega)| \tag{3.10}$$

and

$$\log|F(j\omega)| \leq \log|T_U(j\omega)| - \log\left|\frac{G(j\omega)\mathcal{P}(j\omega)}{1+G(j\omega)\mathcal{P}(j\omega)}\right|_{\max} \tag{3.11}$$

Together (3.10) and (3.11) imply that a prefilter, $F(j\omega)$, exists if the following inequality holds [93]:

$$\Delta\log\left|\frac{G\mathcal{P}}{1+G\mathcal{P}}\right| \triangleq \log\left|\frac{G\mathcal{P}}{1+G\mathcal{P}}\right|_{\max} - \log\left|\frac{G\mathcal{P}}{1+G\mathcal{P}}\right|_{\min} \leq \log\frac{|T_U|}{|T_L|} \tag{3.12}$$

It is apparent, upon inspection of (3.12), that the role of controller G is to reduce the variation in the magnitudes of set $\frac{G\mathcal{P}}{1+G\mathcal{P}}$ to an amount less than the specified tolerances. The objective of prefilter F, on the other hand, is to shape the tracking responses of the closed-loop system such that they all lie within the specified lower and upper tracking bounds. Note that because transfer function F is not embedded within the feedback loop, the filtering effect of F does not change the value of $\Delta\log\left|\frac{G\mathcal{P}}{1+G\mathcal{P}}\right|$. Consequently, prefilter F can be designed after synthesis of the feedback controller has been completed.

Returning now to the QFT design example, the following typical specifications on the closed-loop performance are considered:

Closed-loop tracking:

$$\left|\frac{200}{(s+1)(s+2)(s+10)^2}\right| \leq \left|F\frac{GP}{1+GP}\right| \leq \left|\frac{2(s+5)}{s^2+2.8s+10}\right| \quad \forall P\in\mathcal{P} \tag{3.13}$$

Closed-loop stability:

$$\left|\frac{GP}{1+GP}\right| \leq 1.2 \quad \forall P\in\mathcal{P} \tag{3.14}$$

Closed-loop disturbance attenuation:

$$\left|\frac{1}{1+GP}\right| \leq 1.4 \quad \forall P \in \mathcal{P} \tag{3.15}$$

The lower and upper reference tracking bounds in (3.13) were obtained in the usual way as the Laplace transforms of the unit step responses of a model second-order system [92]. Additional poles and zeros were added to increase the allowable variations in the closed-loop transfer function in the high frequency range, where the benefits of feedback are negligible [88]. Closed-loop stability specification (3.14) ensures that magnitude peaks in the closed-loop transfer functions will never enter the 1.6 dB M-circle on the Nichols chart. This guarantees 5.3 dB and 49° gain and phase margins, respectively. Similarly, the disturbance rejection specification (3.15) guarantees that the peak closed-loop sensitivity always remains less than 2.9 dB.

QFT bounds, $\mathcal{B}(\omega)$, pertaining to the prescribed closed-loop tolerances were solved using the numerical technique described in [95]. Several $\mathcal{B}(\omega)$ are shown in Figure 3.3. The Nichols locus of the uncompensated nominal plant, $P_{\text{nom}}(j\omega)$, is also shown for reference. As shown in Figure 3.3, there are two types of QFT bounds: (i) open bounds, that are single valued functions of the phase angle and (ii) closed bounds which encircle the critical $(-180°, 0\text{ dB})$ point. The nominal loop must be shaped by adjusting the frequency response of the controller so that $L = GP_{\text{nom}}$ can be positioned in the acceptable region, i.e. on or above the open bounds and outside of the closed bounds.

Loop shaping is carried out manually on the Nichols chart or in an automated fashion using one of several available techniques [96–99]. A nominal loop shape, which solves the example design problem, is shown in Figure 3.4. The transfer function of the controller is obtained as the ratio, $G = \frac{L}{P_{\text{nom}}}$:

$$G(s) = \frac{1.67 \times 10^{10}(s+3.5)(s+5)(s+80)}{(s+30)(s+1500)(s^2+2200s+4\times 10^6)} \tag{3.16}$$

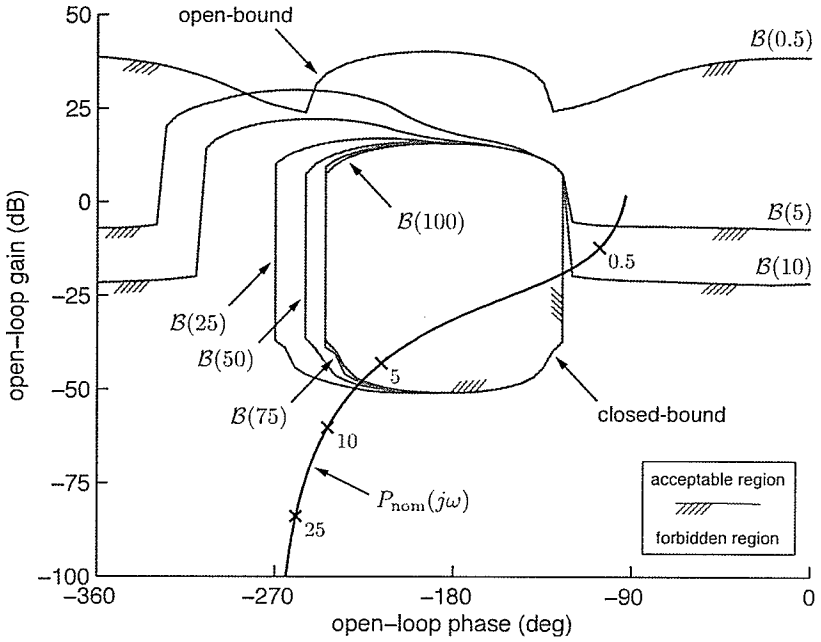

Figure 3.3: Example QFT bounds, $\mathcal{B}(\omega)$, and Nichols locus of uncompensated nominal plant, $P_{\text{nom}}(j\omega)$.

To complete the design, prefilter F was synthesized to ensure the closed-loop reference tracking responses all fall within the prescribed specifications (3.13). To design F, logarithmic differences $\left(\log|T_L| - \log\left|\frac{GP}{1+GP}\right|_{\min}\right)$ and $\left(\log|T_U| - \log\left|\frac{GP}{1+GP}\right|_{\max}\right)$ are plotted as a function of frequency, ω. These curves form lower and upper design bounds on $|F(j\omega)|$ as shown in Figure 3.5 [92]. Using the design bounds, the transfer function of a suitable prefilter can be determined using straight-line Bode approximations within the bounding envelope. The transfer function of the prefilter is:

$$F(s) = \frac{15}{(s+3)(s+5)} \tag{3.17}$$

After functions $G(s)$ and $F(s)$ have been determined, the last step in the QFT design process is to check the design by simulating the closed-loop system for as many of the plants in set $\mathcal{P}$ as possible.

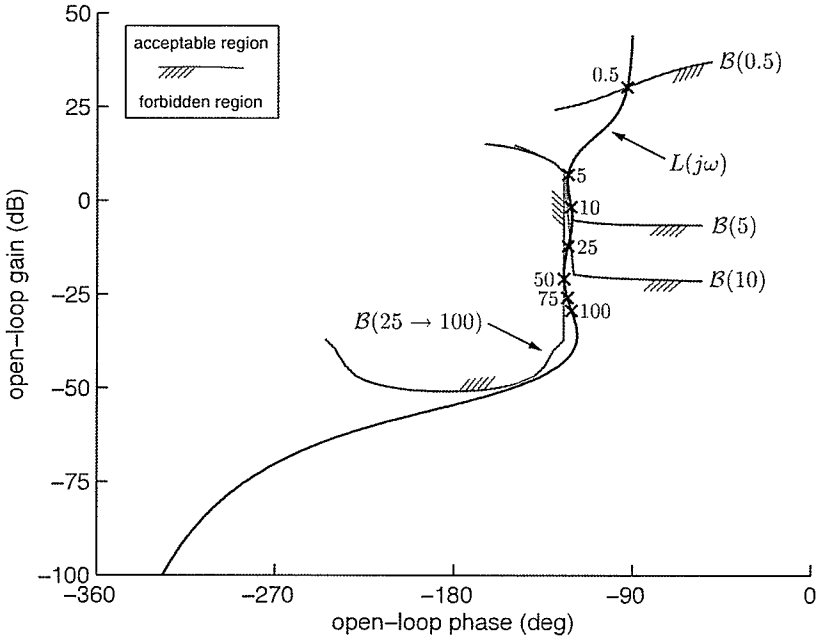

Figure 3.4: Example QFT bounds, $\mathcal{B}(\omega)$, and nominal loop transmission, $L(j\omega)$.

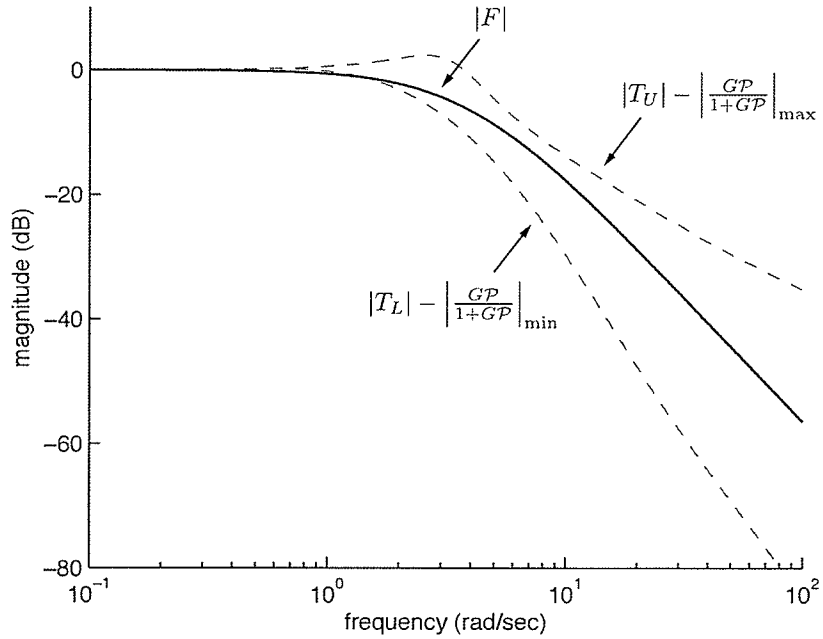

Figure 3.5: Example design bounds on prefilter frequency response.

3.2.2 Extension to Nonlinear Plants

The block diagram of a two degree of freedom QFT control structure employed to close the loop around a nonlinear plant, W, is shown in Figure 3.6. Due to parametric uncertainty there exists a set of nonlinear plants denoted as $\mathcal{W} = \{W\}$. The objective of the QFT design procedure is to synthesize fixed-gain prefilter, F, and control law, G, so that the closed-loop system around plant set, $\mathcal{W}$ (Figure 3.6a), behaves like the LTI feedback system shown in Figure 3.6b. This objective is accomplished by identifying a set of equivalent LTI transfer functions, $P = \{\mathcal{P}\}$, between plant input, u, and output, y, that represent the dynamics of the uncertain nonlinear plant. A proof, based on Schauder's fixed-point theorem, that the compensating functions which solve the equivalent LTI control problem are also valid for the original nonlinear control problem is presented in §11.5 of reference [63].

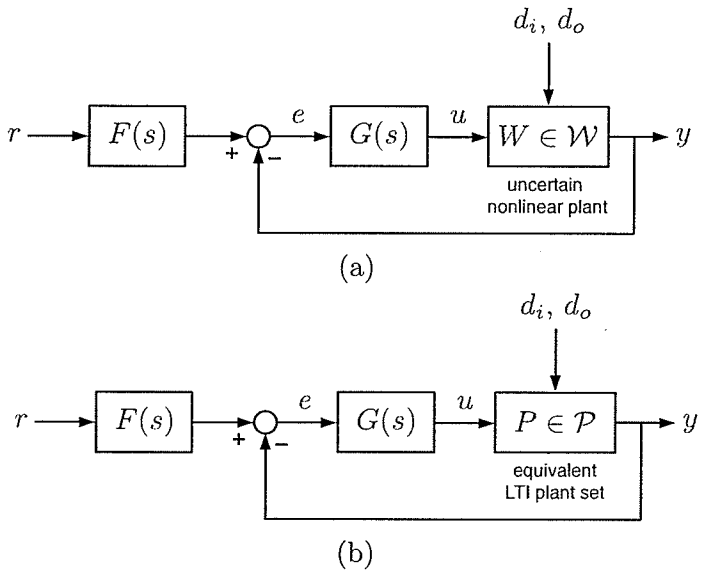

Figure 3.6: Nonlinear and equivalent linear feedback systems: (a) original feedback system around uncertain nonlinear plant set, $\mathcal{W}$; (b) equivalent linear feedback system with each $W \in \mathcal{W}$ replaced by an equivalent linear time invariant (LTI) plant, $P \in \mathcal{P}$.

Derivation of the equivalent LTI plant set can be carried out by following one of two approaches. The first approach, which is well-understood by engineers, is

small-signal analysis [100] that characterizes nonlinear behavior by linearizing the plant about an operating point. Using the small-signal approach, the effects of plant nonlinearities are captured as additional parameter uncertainties in the small-signal transfer function model of the original nonlinear plant. The set of linearized transfer functions can be used to carry out the QFT control design process.

Strictly speaking, the synthesis technique described in section 3.2.1 can only make rigorous guarantees on the performance of the closed-loop control system if the parameters of the plant remain fixed during periods of signal processing [66]. Therefore, small-signal analysis may not be suitable for systems where the operating point changes rapidly during the transient response [93]. The extent to which the small-signal approach is valid for QFT design around nonlinear systems, is therefore related to the sensitivity of the feedback structure to the rate of change in the system operating point[3]. Often, parameter variations can be tolerated without any ill-effects if the rate of variation is slow as compared to the bandwidth of the closed-loop system [88]. In such cases, the small-signal approach for QFT control design around nonlinear plants can be applied with satisfactory results (see [25, 65, 101, 102] for examples).

A more rigorous approach for recasting the nonlinear dynamics of plant set $\mathcal{W}$ into a set of equivalent LTI functions relies on the notion of *restricted device equivalence* [63]. The LTI-equivalent (LTIE) transfer function, $P_e(s)$, is the transfer function that produces the same output, y, as the nonlinear plant, W, when driven by the same input signal, $\hat{u}$. Since the plant is nonlinear, the equivalence between P_e and W is

[3]Some comments on the sensitivity of feedback systems to the rate of parameter variations can be found in §8.15 and §8.16 of reference [88]. It is noted in this text that the maximum allowable rate of parameter variation, for which a feedback design based on the fixed parameter assumption remains approximately correct, is on the order of the reciprocal of the closed-loop bandwidth. This result is based on the argument that time-varying parameters can be considered as disturbances which are related to the speed of parameter variation. Since feedback is effective for disturbances whose bandwidths are within the order of the system bandwidth, the effects of fast variations in the system parameters (within the system bandwidth) should be reasonably attenuated. However, the applicability of this assertion must be checked in order confirm the efficacy of the design. If the design is found to be unsatisfactory, then it may be required to employ a linear time-varying description of the plant dynamics.

restricted to the special case where the input signal is $\hat{u}$. Therefore, different $P_e(s)$ is required to describe the behavior of each $W \in \mathcal{W}$ when different $u(t)$ are considered. However unlike small-signal models, LTIE transfer functions can accurately represent large signal responses. To appreciate this fundamental difference between LTIE and small-signal transfer functions, consider the following example.

Let W, represent a nonlinear plant whose output, $y(t)$, is related to a command input, $u(t)$, by the following first-order differential equation

$$W \triangleq \dot{y} + k_1 y^2 = k_2 u \tag{3.18}$$

where k_1 and k_2 are uncertain system parameters. Suppose that it is desired to design the control system around (3.18), using the structure shown in Figure 3.6a, such that the closed-loop reference tracking responses follow a model second-order function, $T = \frac{Y}{R} = \frac{a^2}{(s+a)^2}$, with variable a. For $r(t) = M$, the desired output of the nonlinear plant is

$$y(t) = \mathcal{L}^{-1}\left\{\frac{M}{s} \cdot \frac{a^2}{(s+a)^2}\right\} = M\left(1 - e^{-at} - ate^{-at}\right) \tag{3.19}$$

Squaring and taking the Laplace transform of the right hand side of (3.19) gives

$$\mathcal{L}\{y^2(t)\} = \frac{2M^2a^4(3s+4a)}{s(s+a^2)(s+2a)^3} \tag{3.20}$$

The Laplace transform of the input signal, $u(t)$, associated with the desired response can be written from (3.18) as

$$U(s) = \frac{1}{k_2}sY(s) + \frac{k_1}{k_2}\mathcal{L}\{y^2(t)\} = \frac{1}{k_2}\frac{Ma^2}{(s+a)^2} + \frac{k_1}{k_2}\frac{2M^2a^4(3s+4a)}{s(s+a^2)(s+2a)^3} \tag{3.21}$$

From (3.21), it follows that

$$P_e(s) = \frac{Y(s)}{U(s)} = \frac{k_2(s+2a)^3}{s(s+2a)^3 + 2k_1Ma^2(3s+4a)} \tag{3.22}$$

LTIE transfer function (3.22) is the restricted transfer function that reproduces the response of the nonlinear plant, W, for the special case that $y(t) = M\left(1 - e^{-at} - ate^{-at}\right)$.

Function $P_e(s)$ is structurally different than the small-signal representation of the nonlinear system, which is given as

$$P(s) = \frac{Y(s)}{U(s)} = \frac{k_2}{s + 2k_1 y_o} \tag{3.23}$$

where parameter y_o represents the system operating point. The additional poles and zeros of the LTIE function enables (3.22) to represent the large signal response of nonlinear system (3.18) using a fixed parameter structure. Therefore, LTIE representation of nonlinear plants allows QFT to be applied in a rigorous fashion to systems whose small-signal operating points are strongly time-varying over the transient response interval.

The LTIE approach can be applied to the nonlinear synthesis problem of Figure 3.6a in the following way [63]: First, a family of outputs, $\mathcal{Y} = \{y(t)\}$, is defined to represent acceptable responses of the closed-loop system for different reference inputs, $\mathcal{R} = \{r(t)\}$. If they are known in advance, the set of possible disturbance inputs, $\mathcal{D} = \{d_i(t), d_o(t)\}$, should also be considered for each $r \in \mathcal{R}$. Next, the set of plant drive signals, $\mathcal{U} = \{u(t)\}$, that generate each $y \in \mathcal{Y}$, are solved for every member of uncertain nonlinear plant set $\mathcal{W}$. The drive signals are computed as $u(t) = W^{-1}y(t)$, where W^{-1} denotes the inverse dynamics of the nonlinear plant. Finally the ratio of Laplace transforms, is evaluated to obtain the LTIE transfer function $P_e(s) = \frac{\mathcal{L}\{y(t)\}}{\mathcal{L}\{u(t)\}}$, for each input-output signal pair. The remainder of the QFT design follows the procedure outlined in section 3.2.1

3.3 Equivalent LTI Modeling of Hydraulic Actuators

In this section, the applicability of small-signal and restricted device equivalence concepts are examined towards expressing the nonlinear dynamics of valve controlled hydraulic actuators as a set of equivalent LTI functions. An advantage of using the small-signal approach for modeling the hydraulic actuator is that the transfer function description of the actuator dynamics is analytic. Therefore, it is relatively straightforward to determine lower and upper bounds on the operating point dependent transfer function parameters. However as discussed previously, it is necessary to check whether the operating point remains fixed during the transient response of the actuator. If the operating point drifts, the fluid power system may fail to perform as expected when the QFT controller is implemented. LTIE models, on the other hand, are established directly from acceptable hydraulic actuator input-output data. Thus, it is possible to represent both small and large signal responses with fixed-gain structures. The LTIE approach can therefore more rigorously translate the original nonlinear hydraulic actuator dynamics into an equivalent LTI form.

3.3.1 Acceptable System Responses

To obtain a set of equivalent LTI models for a hydraulic actuator, whether by small-signal analysis or by the LTIE approach, a set of acceptable input-output responses must be first solved from the nonlinear system model. To do this, a typical family of output responses is defined as

$$\mathcal{X}_p^a(s) = \mathcal{R}(s)\mathcal{T}(s) \tag{3.24}$$

where $X_p^a(s) \in \mathcal{X}_p^a(s)$ is the acceptable position response to the reference command $R(s) \in \mathcal{R}(s)$. A typical reference command is a step, $r(t) = M$. $\mathcal{T}(s) = \{T(s)\}$ is the set of acceptable closed-loop system functions, which map each reference input

to an output response in set $\mathcal{X}_p^a(s)$. A simple description of system function $T(s)$ for a hydraulic actuator is

$$T(s) = \frac{\left(\frac{s}{\lambda}+1\right)}{\left(\frac{s}{p_1}+1\right)\left(\frac{s}{p_2}+1\right)\left(\frac{s^2}{\omega_p^2}+\frac{2\zeta_p}{\omega_p}s+1\right)} \tag{3.25}$$

In (3.25), the locations of the transfer function poles are fixed to set the main characteristics of the actuator response. Some variation in the output of the hydraulic actuator is inevitable due to the system nonlinearities and parametric uncertainties. The acceptable range of variation in the closed-loop responses can therefore be regulated by adjusting parameter λ. Figure 3.7a shows the time histories of typical acceptable position responses. The response curves were generated for step commands of magnitude $M = 5$, 25, and 50 mm by using (3.25) with $p_1 = 15$, $p_2 = 20$, $\zeta_p = 1.0$, $\omega_p = 85^2$, and $\lambda \in [12, 33]$.

Once the acceptable output set has been defined, the time history of the input signal (servovalve displacement) required to drive the ram the along the acceptable closed-loop trajectory needs to be calculated. A suitable procedure for computing the inverse dynamics of the hydraulic actuator has already been developed in [62] and is outlined in Appendix A. This method was used to compute the time history of the servovalve spool displacement shown in Figure 3.7b. The nominal parameter values of the fault emulator actuator (see Table 2.1), were used to obtain the plots, under the assumption that the load acting on the ram is stiffness dominant, i.e. $F_L(t) = kx_p^a(t)$. Together, the time histories of the valve spool displacements and corresponding actuator position responses form input-output pairs that can be used to identify equivalent LTI models of the hydraulic actuator. Many more signal pairs are normally required for control system synthesis to ensure that the nonlinear actuator dynamics are adequately represented over the operational envelope of the system.

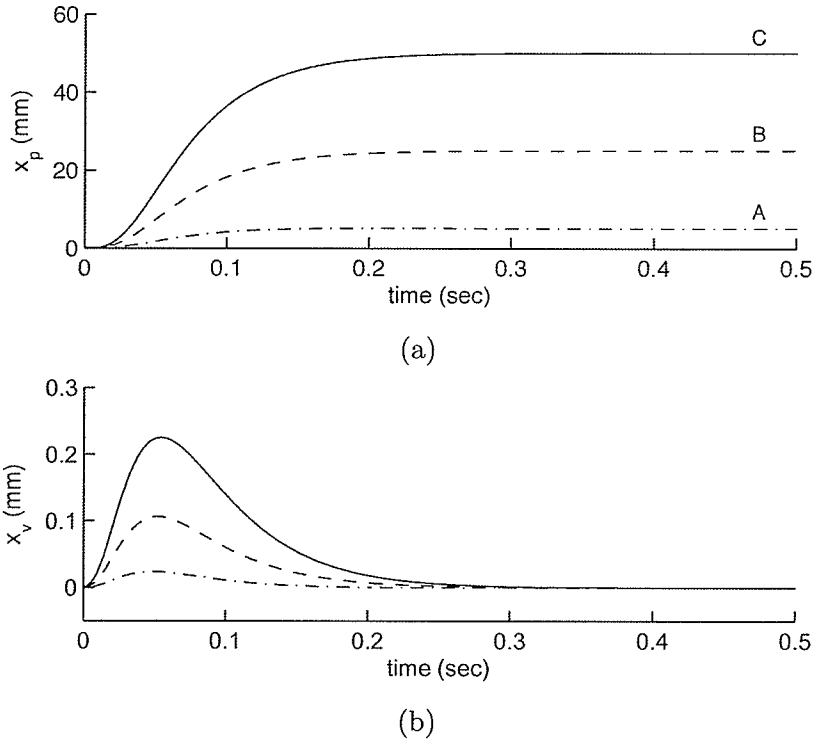

Figure 3.7: Typical acceptable hydraulic actuator input-output responses obtained using (3.25): (a) actuator position responses (output); (b) servovalve spool displacements (input).

3.3.2 Small-Signal Approach

The hydraulic actuator small-signal transfer function that relates changes in the valve spool displacement, x_v, to changes in the actuator position, x_p, is derived by linearizing the equations describing the servovalve control flows. Expanding equations (2.2) and (2.3) using a truncated Taylor series around operating point, o, gives the linearized servovalve flows as

$$\begin{aligned} Q_1 &= K_v w x_v \sqrt{\frac{P_s - P_r}{2} + \frac{x_v}{|x_v|}\left(\frac{P_s + P_r}{2} - P_1\right)} \\ &\approx Q_{1o} + \frac{\partial Q_1}{\partial x_v}(x_v - x_{vo}) + \frac{\partial Q_1}{\partial P_1}(P_1 - P_{1o}) \\ &\approx Q_{1o} + K_{1f}(x_v - x_{vo}) - K_{1p}(P_1 - P_{1o}) \end{aligned} \tag{3.26}$$

$$\begin{aligned} Q_2 &= K_v w x_v \sqrt{\frac{P_s - P_r}{2} + \frac{x_v}{|x_v|}\left(P_2 - \frac{P_s + P_r}{2}\right)} \\ &\approx Q_{2o} + \frac{\partial Q_2}{\partial x_v}(x_v - x_{vo}) + \frac{\partial Q_2}{\partial P_2}(P_2 - P_{2o}) \\ &\approx Q_{2o} + K_{2f}(x_v - x_{vo}) + K_{2p}(P_2 - P_{2o}) \end{aligned} \tag{3.27}$$

In (3.26) and (3.27), partial derivatives $\frac{\partial Q}{\partial x_v}$ are known as the valve flow gains and partial derivatives $\frac{\partial Q}{\partial P}$ are called the flow-pressure coefficients [2].

For an equal area ram driven by a matched and symmetrical valve with $P_r = 0$, the pressure in one cylinder half rises above $\frac{P_s}{2}$ while the pressure in the other cylinder half decreases below $\frac{P_s}{2}$ by roughly the same amount [2]. Thus for an extending stroke, the individual cylinder pressures are $P_1 \approx \frac{1}{2}(P_s + P_L)$ and $P_2 \approx \frac{1}{2}(P_s - P_L)$, where $P_L = P_1 - P_2$ is the load pressure. Due to the relationship between P_1 and P_2, it is quite often the case that $K_{1f} \approx K_{2f}$ and $K_{1p} \approx K_{2p}$ [2]. The valve coefficients can therefore be written in terms of the operating point load pressure as follows:

$$K_f = K_v w \sqrt{\frac{1}{2}\left(P_s - \frac{x_{vo}}{|x_{vo}|} P_{Lo}\right)} \tag{3.28}$$

$$K_p = \frac{K_v w |x_{vo}|}{\sqrt{2\left(P_s - \frac{x_{vo}}{|x_{vo}|} P_{Lo}\right)}} \tag{3.29}$$

Using (3.26) through (3.29), the small-signal state equations from input, x_v, to output, x_p, are now derived from the nonlinear hydraulic actuator model (see section 2.5) by considering each state to be a perturbation from the nominal operating point value, i.e. $\Delta x_v = x_v - x_{vo}$. The linearized state equations are

$$\begin{aligned}
\Delta \dot{x}_p &= \Delta v_p \\
\Delta \dot{v}_p &= \frac{1}{m}\left(A\Delta P_1 - A\Delta P_2 - d\Delta v_p\right) - \frac{1}{m}\Delta F_L \\
\Delta \dot{P}_1 &= \frac{\beta_h}{V_{1o}}\left[K_{1f}\Delta x_v - K_{1p}\Delta P_1 - A\Delta v_p\right] \\
\Delta \dot{P}_2 &= \frac{\beta_h}{V_{2o}}\left[-K_{2f}\Delta x_v - K_{2p}\Delta P_2 + A\Delta v_p\right]
\end{aligned} \tag{3.30}$$

In (3.30), cylinder volumes V_{1o} and V_{2o} are assumed to be constant operating point dependent parameters.

Substituting $F_L = k\Delta x_p$ into (3.30) the linearized state equations can be reduced to obtain the equivalent small-signal transfer function model of the hydraulic actuator. The transfer function between relating changes in the servovalve spool displacement, $\Delta X_v(s)$, to changes in the actuator position, $\Delta X_p(s)$, is

$$P_H(s) = \frac{\Delta X_p(s)}{\Delta X_v(s)} = \frac{\beta_h A K_f\left[(V_{1o} + V_{2o})s + 2AK_p\right]}{(ms^2 + ds + k)\,D(s) + \beta_h A^2(V_{1o} + V_{2o})s^2 + 2\beta_h^2 A^2 K_p s} \tag{3.31}$$

with

$$D(s) = V_{1o}V_{2o}s^2 + \beta_h K_p(V_{1o} + V_{2o})s + 2\beta_h^2 K_p \tag{3.32}$$

To use small-signal transfer function (3.31) for control system synthesis, the values of the servovalve flow and flow-pressure coefficients need to be evaluated at different operating points. A method for identifying the servovalve operating points, which

lends itself well to graphical interpretation, is the load locus technique [72]. The idea is to superimpose a plot of the hydraulic load line over a plot of the nonlinear servovalve flow curves. The load line defines the relationship between the load pressure needed to drive the mechanical load and the necessary load flow of hydraulic oil to the actuator. On the load locus plot, the servovalve operating point can be identified by the intersections of the load line and the valve flow curves [28].

The time history of the load pressure required to position the actuator against the load is

$$P_L(t) = \frac{1}{A}\left[m\ddot{x}_p^a(t) + d\dot{x}_p^a(t) + kx_p^a(t)\right] \tag{3.33}$$

The corresponding load flow, $Q_L = \frac{Q_1+Q_2}{2}$, of hydraulic oil through the servovalve is given by

$$Q_L(t) = \frac{1}{2\beta_h}\left[\dot{P}_1(t)\{Ax_p^a(t) + \bar{V}_1\} - \dot{P}_2(t)\{A(L - x_p^a(t)) + \bar{V}_2\}\right] + A\dot{x}_p^a(t) \tag{3.34}$$

Since it has already been assumed that $P_1 \approx \frac{1}{2}(P_s + P_L)$ and $P_2 \approx \frac{1}{2}(P_s - P_L)$, the cylinder pressure derivatives are $\dot{P}_1 \approx \frac{\dot{P}_L}{2}$ and $\dot{P}_2 \approx -\frac{\dot{P}_L}{2}$. Therefore, (3.34) can be rewritten in an approximate form

$$\begin{aligned} Q_L(t) &\approx \frac{1}{2\beta_h}\left[\frac{\dot{P}_L(t)}{2}\{Ax_p^a(t) + \bar{V}_1\} - \left(-\frac{\dot{P}_L(t)}{2}\right)\{A(L - x_p^a(t)) + \bar{V}_2\}\right] + A\dot{x}_p^a(t) \\ &\approx \frac{AL + \bar{V}_1 + \bar{V}_2}{2\beta_h}\dot{P}_L(t) + A\dot{x}_p^a(t) \end{aligned} \tag{3.35}$$

where term $(AL + \bar{V}_1 + \bar{V}_2)$ is the total volume of both cylinder halves including the volumes of the connecting lines between the cylinder and the servovalve.

Using (3.33) and (3.35), a plot of Q_L versus P_L can be constructed for each acceptable hydraulic actuator response under consideration. The load lines pertaining to the example actuator responses of Figure 3.7 are shown in Figure 3.8. Referring to

locus C, the load line is traversed as indicated by the arrowhead from the initial state at the origin, point 'a', to the steady-state, point 'j'. The actuator state changes similarly for the other load loci. At each location where the load lines intersect the valve pressure-flow curves, the servovalve operating point can be graphically evaluated by reading the operating point valve spool displacement, x_{vo}, and the operating point load pressure, P_{Lo}, and solving for the valve coefficients.

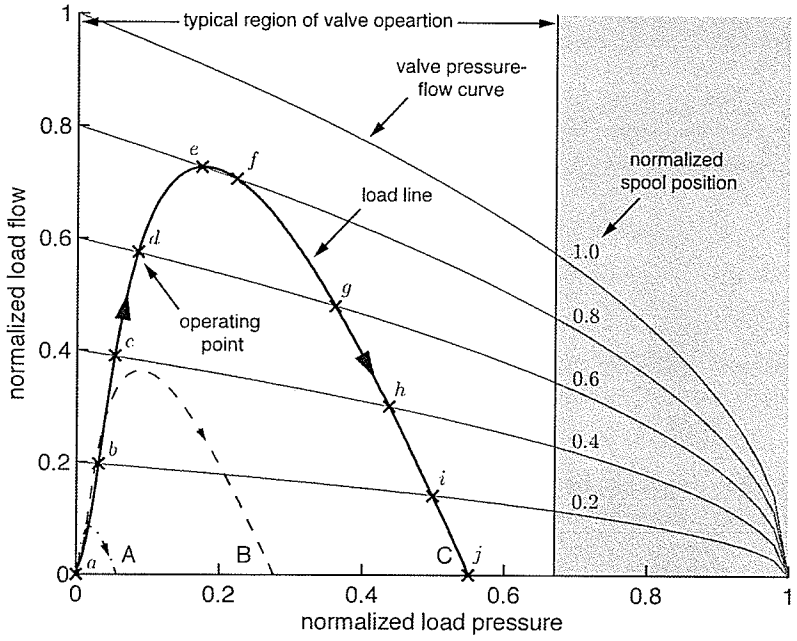

Figure 3.8: Example hydraulic load lines showing graphical determination of servovalve operating points for typical actuator position responses.

Table 3.2 reports the servovalve flow coefficients, K_f and K_p, corresponding to load line C in Figure 3.8. Referring to the tabulated data, it is observed that the servovalve flow gain is reduced by about 33% from 1.8 to 1.2 m^2/sec. The value of the servovalve flow-pressure coefficient, which increases in proportion to the servovalve spool displacement, reaches a peak value of approximately 1.3×10^{-11} m^3/Pa·sec at operating point 'f' before decreasing again to zero in the steady-state. Clearly, the valve coefficients are strongly time-varying over the transient response interval. A

similar result is observed for load line B. On the other hand, for load line A, the variation in the value of K_f is less than 3% and the peak value of the flow-pressure coefficient is an order of magnitude less than the peak value reported in Table 3.2.

Table 3.2: Servovalve operating points pertaining to hydraulic load line C in Figure 3.8.

point	time (sec)	$x_{vo} \times 10^5$ (m)	P_{Lo} (MPa)	K_f (m^2/sec)	$K_p \times 10^{11}$ (m^3/Pa·sec)
a	0.0	0.00	0.00	1.78	0.00
b	0.015	0.53	0.52	1.75	0.28
c	0.023	1.08	0.91	1.73	0.58
d	0.032	1.68	1.48	1.70	0.90
e	0.050	2.23	3.00	1.61	1.26
f	0.059	2.23	3.84	1.57	1.30
g	0.089	1.66	6.26	1.42	1.07
h	0.113	1.12	7.54	1.33	0.77
i	0.149	0.55	8.61	1.26	0.40
j	>0.346	0.00	9.48	1.19	0.00

Figure 3.9 shows the response of transfer function (3.31) when the values of K_f and K_p vary over time as in Table 3.2 and when the values of K_f and K_p are fixed. As is seen, the small-signal model with time-varying parameters can accurately reproduce the transient response, while the fixed-gain models cannot. Therefore, unless the region of operation of the servovalve is suitably restricted, as for load line A, small-signal analysis may not be suitable for design of the QFT control system.

Bode plots of the small-signal transfer functions at the operating points listed in Table 3.2 are shown in Figure 3.10. It is observed that the linearization process introduces a significant amount of dynamic uncertainty in the low frequency range $\omega < 10$ rad/sec. This is a result of the fact that some of the small-signal models, for example the model corresponding to operating point 'f', are type 0 since $K_p \neq 0$ during part of the system transient. However, since the servovalve meters flow, it must close when the position error is zeroed. Thus, the actuator always physically behaves as a type 1 system and the actual low frequency uncertainty is much smaller than

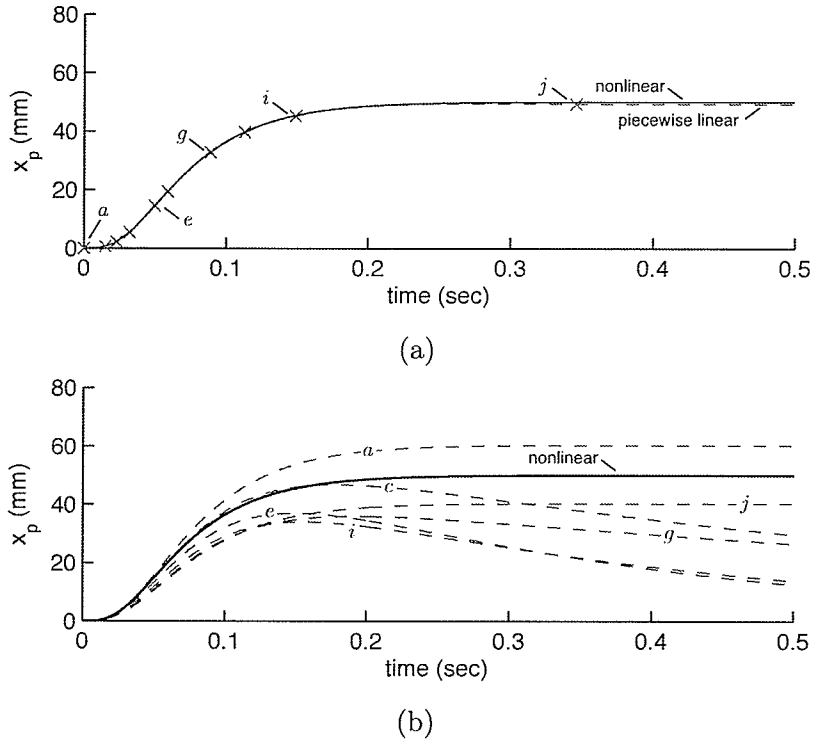

Figure 3.9: Comparison between nonlinear position response C and responses of equivalent small-signal models: (a) response for time-varying K_f and K_p (data points correspond to updates of linearized valve coefficients); (b) response for fixed values of K_f and K_p.

the amount predicted by the set of equivalent small-signal models. Since QFT relates the amount of feedback required at each frequency to the amount of uncertainty in the plant dynamics, the controller will be constrained to make the magnitude of the loop transmission unnecessarily large in the low frequency range. The result is an overdesigned and conservative control system that uses much more feedback gain than is actually required to solve the robust control problem.

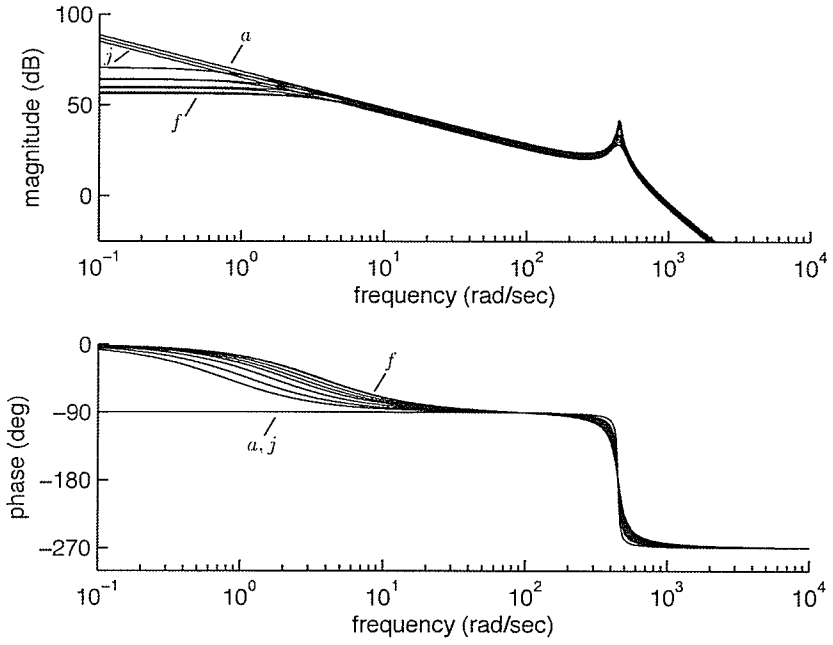

Figure 3.10: Bode plots of small-signal transfer functions pertaining to load line C in Figure 3.8.

3.3.3 LTI-Equivalent Approach

To identify LTIE models of the hydraulic actuator in the frequency domain, it is necessary to evaluate the ratios of Laplace transforms, $P_H(j\omega) = \frac{\mathcal{L}\{x_p(t)\}}{\mathcal{L}\{x_v(t)\}} = \frac{\hat{X}_p(j\omega)}{\hat{X}_v(j\omega)}$, of acceptable time-domain input-output data. Due to the complexity of the nonlinear hydraulic functions, it is not possible to compute these transforms analytically. Instead, each transformation must be carried out numerically. Two methods for ac-

complishing this task are detailed in this section. The first is an existing approach, which has been applied before for LTIE identification of hydraulic actuators, but has several drawbacks that will be elaborated on. The second approach is a procedure that has not previously been applied to identify hydraulic actuator LTIE models.

Existing Approach – Golubev's Method

One approach for computing LTIE frequency response $P_H(j\omega) = \frac{\hat{X}_p(j\omega)}{\hat{X}_v(j\omega)}$ has been developed by Golubev and Horowitz [86]. The method allows least-squares estimates of the LTIE transfer function coefficients to be calculated by repeated integration of the plant input-output data. Golubev's method was originally derived as a tool for QFT synthesis using a frequency domain error criterion. The technique can, however, be developed more straightforwardly in the time domain [103]. For the hydraulic actuator under study, the LTIE equivalent system can be described in the time domain by the following ordinary differential equation, which assumes zero initial conditions

$$b_n x_p^{(n)}(t) + b_{n-1} x_p^{(n-1)}(t) + \ldots + b_0 x_p(t) = a_0 x_v(t) + \ldots + a_m x_v^{(m)}(t) \qquad (3.36)$$

where $x_p^{(j)}(t) = \frac{d^j}{dt^j} x_p(t)$. Each side of (3.36) is integrated n-times to get

$$b_n x_p(t) = -b_{n-1} x_p^{(-1)}(t) - \ldots - b_0 x_p^{(-n)}(t) + a_0 x_v^{(-n)}(t) + \ldots + a_m x_v^{(-n+m)}(t) \qquad (3.37)$$

The integrals in (3.37) are computed from samples of signals x_p and x_v taken at time instants t_k $(k = 1, 2, \ldots, N)$. For example, using the trapezoidal rule, $x_p^{(-r)}(t_k) = x_p^{(-r)}(t_{k-1}) + \frac{h}{2}\left[x_p^{(-r+1)}(t_k) + x_p^{(-r+1)}(t_{k-1})\right]$, where h is the sampling interval.

Assuming $b_n = 1$, a least-squares problem is then assembled to solve unknown

system coefficients a_i and b_j as follows

$$\left[\sum_{k=1}^{N}\phi(t_k)\phi^T(t_k)\right]\{b_0,\ldots,b_{n-1},a_0,\ldots,a_m\}^T=\left\{\sum_{k=1}^{N}\phi(t_k)x_p(t_k)\right\} \tag{3.38}$$

where $\phi(t_k)=\left[-x_p^{(-n)}(t_k),\ldots,-x_p^{(-1)}(t_k),x_v^{(-n)}(t_k),\ldots,x_v^{(-n+m)}(t_k)\right]$. Golubev's method thus allows the LTIE transfer function to be evaluated by taking the Laplace transform of (3.36), and inserting the values of a_i and b_j solved from (3.38).

Golubev's method was applied to estimate a LTIE transfer function for each of the hydraulic actuator input-output signal pairs shown in Figure 3.7. The results are summarized in Table 3.3, along with the sampling intervals h and data record lengths N that were used to form systems (3.38). The ability of the identified LTIE transfer functions to reproduce the original nonlinear position responses is shown in Figure 3.11a. As is seen, the results are indistinguishable. Referring to Figure 3.11b, the modeling error (difference between the nonlinear and LTIE response) is less than 1%.

Table 3.3: LTIE transfer function estimates obtained using Golubev's method.

case	h (sec)	N	LTIE transfer function
A	5×10^{-5}	600	$P_A(s)=\dfrac{5.27\times10^8}{s(s^2+19.3s+2.0\times10^5)}$
B	5×10^{-5}	4200	$P_B(s)=\dfrac{5.52\times10^8(s+55.0)(s+156.8)}{s(s+64.2)(s+144.9)(s^2+35.2s+2.1\times10^5)}$
C	1×10^{-4}	2100	$P_C(s)=\dfrac{5.18\times10^8(s+48.6)(s+122.0)}{s(s^2+8.9s+2.0\times10^5)(s^2+161.3s+6.8\times10^3)}$

Bode plots of the identified LTIE transfer functions are shown in Figure 3.12. It is observed that the LTIE transfer functions properly capture two of the important features of the hydraulic actuator behavior. The first is the inherent integration characteristic of the ram in the low frequency range, $\omega < 10$ rad/sec. The second feature is the resonant mode in the high frequency range, $\omega = 500$ rad/sec, that results from the interaction between the load mass and the compressibility of the hydraulic

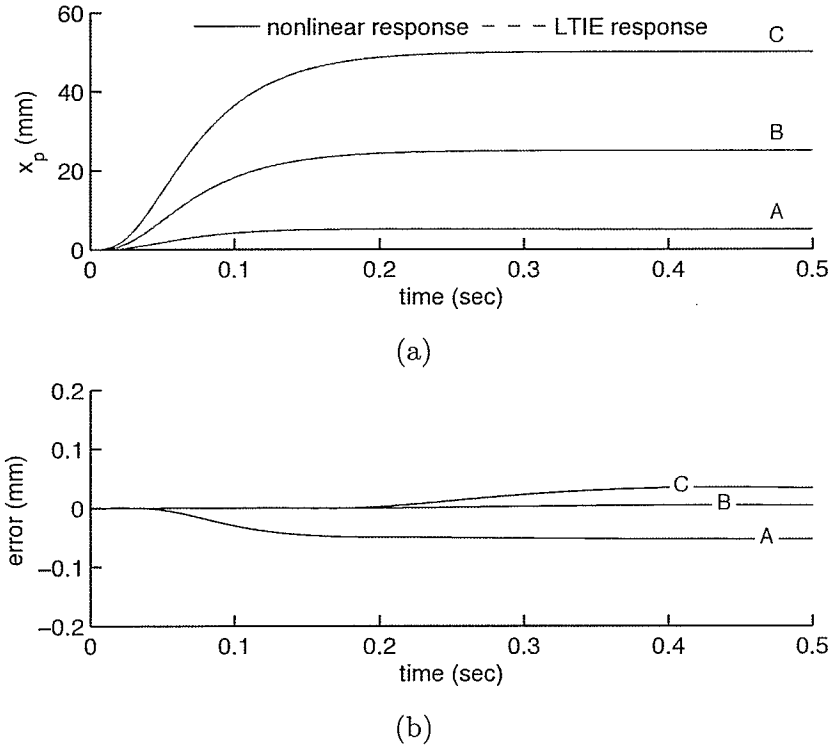

Figure 3.11: Comparison between nonlinear position responses and responses of LTIE transfer functions obtained by Golubev's method: (a) position response; (b) modeling error.

oil. Proper identification of the resonant mode is important for control system design since the resonance peaks occur when the phase lag is 180° and thus tend to limit the achievable gain margin. As expected, the identified LTIE transfer functions for large input commands have more complex structures than the small-signal transfer function. The additional transfer function elements are necessary to account for the large signal effects, which could not be properly represented by the fixed parameter small-signal models.

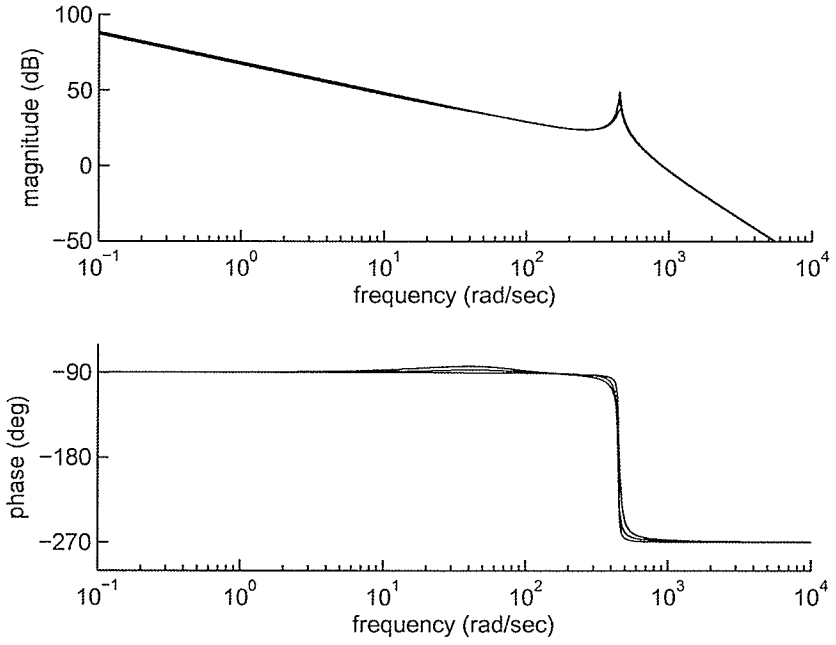

Figure 3.12: Bode plots of LTIE transfer functions obtained by Golubev's method.

In spite of the desirable features of Golubev's method cited above, several drawbacks of the approach for hydraulic actuator model identification are noted below:

1. The algorithm was found to be quite sensitive to the sampling interval, h, and the length of the data record, N, used to assemble the least-squares system (3.38). If parameters h and N were chosen incorrectly, the algorithm was observed to generate transfer functions with unstable poles and zeros. This behavior has also been observed by others [59, 104] and could be related to the ill-conditioning of the least-squares system.

2. The length of the data record, N, used in the approximation plays an important role in determining the frequency range over which the transfer function estimate is most accurate. Parameter N had to be set small in order to properly identify the actuator resonance. However, selecting N small was observed to decrease the accuracy of the transfer function approximation in the low-frequency range. This suggests that difficulties may be encountered when applying Golubev's method to systems having both slow and fast dynamic modes as in hydraulic actuators with internal leakage.

3. To obtain good transfer function fits using small N, prior information about the asymptotic behavior of the transfer function had to be inserted into the model. For example, parameter b_0 in (3.38) had to be set to zero to force the LTIE transfer function to have a pole at the origin.

4. There is no way to decide, *a priori*, the orders of the numerator and denominator polynomials that give the best fit of the time-domain data, even if the excess of poles over zeros is known. The polynomial degrees can only be determined by trail-and-error. This makes the application of the approach tedious, if not unmanageable, in a practical design scenario.

New Approach – Fourier Transformation

A different approach that can be used to compute LTIE frequency response, $P_H(j\omega) = \frac{\hat{X}_p(j\omega)}{\hat{X}_v(j\omega)}$, which has not been applied to hydraulic actuators is Fourier transformation. An advantage of Fourier transformation over Golubev's method is that the frequency response functions (magnitudes and phase angles) of the LTIE plants can be obtained directly without the need to solve a rational transfer function. Fourier transformation can therefore improve the efficiency of the LTIE modeling process, the most time consuming aspect of the QFT design process. In this section, a simple numerical procedure for evaluating the Fourier transforms of the hydraulic actuator input-output pairs is developed.

The frequency response function $\hat{X}_p(j\omega)$ can be found from its relation to signal $x_p(t)$ by the one-sided Laplace integral

$$\hat{X}_p(j\omega) = \lim_{\sigma \to 0} \int_0^\infty x_p(\tau) e^{-(\sigma + j\omega)t} d\tau \tag{3.39}$$

subject to $\sigma > 0$. Mopsik [105] has pointed out that, in the sense of the limit, (3.39) can be evaluated as a Fourier integral

$$\hat{X}_p(j\omega) = \int_0^\infty x_p(\tau)e^{-j\omega\tau}d\tau \tag{3.40}$$

From a numerical perspective, (3.40) should be considered as a sum of three components [105]

$$\hat{X}_p(j\omega) = I_1 + I_2 + I_3 = \int_0^h x_p(\tau)e^{-j\omega\tau}d\tau + \int_h^T x_p(\tau)e^{-j\omega\tau}d\tau + \int_T^\infty x_p(\tau)e^{-j\omega\tau}d\tau \tag{3.41}$$

In (3.41), h refers to the fixed sampling interval and T denotes the end of the finite interval over which the sampled $x_p(t)$ data are available. The second term in sum (3.41) is the only component of the indefinite integral that can be obtained directly. The frequency band over which the numerical approximation to (3.40) is valid is therefore limited to the interval [105]

$$\frac{1}{T} < \omega < \frac{1}{h} \tag{3.42}$$

Restriction (3.42) is necessary because at high frequencies, $\omega > \frac{1}{h}$, term I_1 is typically dominant and it is difficult to evaluate I_1 due to the oscillatory nature of the integrand [106]. However, for frequencies $\omega \ll \frac{1}{h}$, the contribution of component I_1 becomes small. At the other end of the spectrum ($\omega < \frac{1}{T}$) term I_3 can become dominant, but the value of I_3 can only be estimated since signal $x_p(t)$ is truncated at time T.

If the Fourier integral is truncated after the hydraulic system has reached steady-state, restriction $\omega > \frac{1}{T}$ can be removed since the value of $x_p(t)$ will be constant for $t \geq T$. Therefore, term I_3 can be computed exactly, i.e. $I_3 = x_p(T)\frac{e^{-j\omega T}}{j\omega}$. Alternatively, one can work with time derivative $\dot{x}_p(t) = \mathcal{L}^{-1}\{sX_p(s)\}$. In the steady-state $\dot{x}_p(t) = 0$ for $t \geq T$ making $I_3 \equiv 0$ in (3.41). The required frequency response

function $\hat{X}_p(j\omega)$ can then be recovered as $\hat{X}_p(j\omega) = \frac{\hat{\dot{X}}_p(j\omega)}{j\omega}$ (see §12.2 of reference [88]).

A similar approach can be taken to evaluate the frequency responses, $\hat{X}_v(j\omega)$, of the actuator input signal. In the case where there is fluid leakage between the actuator cylinders the steady-state servovalve spool displacement will be non-zero. Time derivative $\dot{x}_v(t)$ should therefore be used for the computation of $\hat{X}_v(j\omega)$. The time history of $\dot{x}_v(t)$ can be computed from $x_v(t)$ by finite differences or by setting $u(t) = \frac{x_v}{k_v}$ and simulating the servovalve state equations.

In light of the above discussion, an estimate of the frequency response function for signal $x_p(t)$ can be evaluated by computing the truncated Fourier integral

$$\hat{X}_p(j\omega) = \int_h^T x_p(\tau) e^{-j\omega\tau} d\tau \tag{3.43}$$

Calculation of the transcendental integrand in (3.43) is carried out by first subdividing the integration interval $(0, T]$ into N panels of length h. Then, by assuming term $x_p(\tau)$ is constant over each panel and by using a Filon-like approach [107] along with Euler's formula, (3.43) can be rewritten as

$$\hat{X}_p(j\omega) = \frac{1 - \cos(\omega h) + j\sin(\omega h)}{j\omega} \sum_{k=0}^{N-1} x_p(kh)[\cos(\omega kh) - j\sin(\omega kh)] \tag{3.44}$$

The sum in (3.44) bears resemblance to the discrete Fourier transform and can be computed efficiently using the fast-Fourier transform (FFT). However, (3.44) offers improved accuracy over the FFT since the multiplicative factor corrects for the error introduced by the FFT assumption that terms '$\cos(\omega h)$' and '$\sin(\omega h)$' are constant over the integration interval. Thus, (3.44) gives the advantage that the accuracy of the Fourier integration depends primarily on the smoothness of signal $x_p(t)$ [108].

Equation (3.44) was applied to evaluate the LTIE frequency response functions for the $x_v(t)$–$x_p(t)$ signal pairs shown in Figure 3.7. Bode plots of the identified LTIE frequency response ratios, $P_H(j\omega) = \frac{\hat{X}_p(j\omega)}{\hat{X}_v(j\omega)}$, are shown in Figure 3.13. As can be seen,

the proposed numerical procedure properly identified the low frequency integration characteristic of the ram as well as the resonant mode in the high frequency range. Moreover, the LTIE frequency response ratios obtained by Fourier transformation are quite similar to the ones identified using Golubev's method. However, an important advantage of the Fourier transformation approach is that the LTIE frequency response function can be arrived at without the need to make assumptions on the structure of the LTIE transfer function.

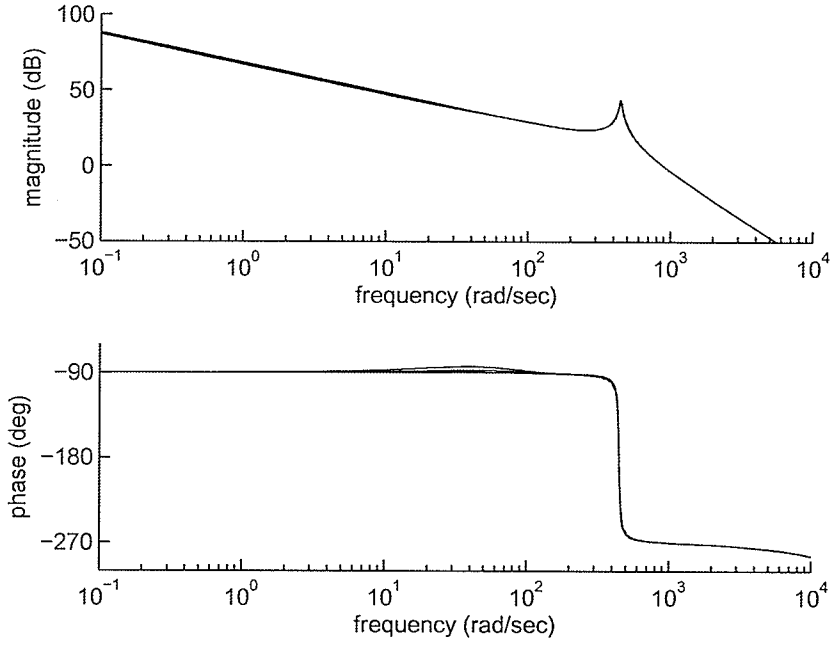

Figure 3.13: Bode plots of LTIE frequency response functions, $\frac{\hat{X}_p(j\omega)}{\hat{X}_v(j\omega)}$, obtained by Fourier transformation approach.

To confirm that the identified LTIE frequency responses accurately reflect behavior of the nonlinear hydraulic actuator, a transfer function was estimated for each $\frac{\hat{X}_p(j\omega)}{\hat{X}_v(j\omega)}$ ratio. The LTIE transfer function has the following general rational form:

$$P(j\omega) \triangleq \frac{\hat{X}_p(j\omega)}{\hat{X}_v(j\omega)} = \frac{A_0 + A_1(j\omega) + \ldots + A_{m-1}(j\omega)^{m-1} + A_m(j\omega)^m}{B_0 + B_1(j\omega) + \ldots + B_{n-1}(j\omega)^{n-1} + (j\omega)^n}, \quad m \leq n \tag{3.45}$$

Coefficients A_i and B_j in (3.45) were found by minimizing, in a least squares sense, the error

$$E = \sum_{k=1}^{K} \left\| \frac{A(j\omega_k)}{B(j\omega_k)} - \frac{\hat{X}_p(j\omega_k)}{\hat{X}_v(j\omega_k)} \right\|^2 \tag{3.46}$$

where K refers to the total number of discrete frequencies considered in the estimate [109]. The identified LTIE transfer functions are listed in Table 3.4 and their frequency responses are shown in Figure 3.14. The position response of each estimated LTIE transfer function is demonstrated in Figure 3.15. As can be seen, the models can accurately predict the behavior of the hydraulic actuator to within 0.5%. Thus, the Fourier transformation approach developed in this section can be applied for QFT control systems design around hydraulic actuators.

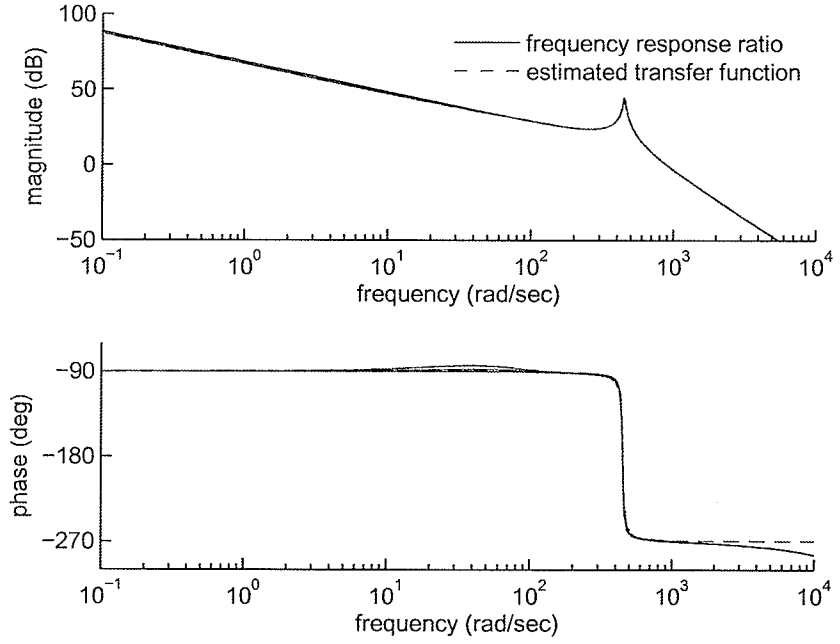

Figure 3.14: Bode plots of LTIE transfer functions estimated from frequency response ratios.

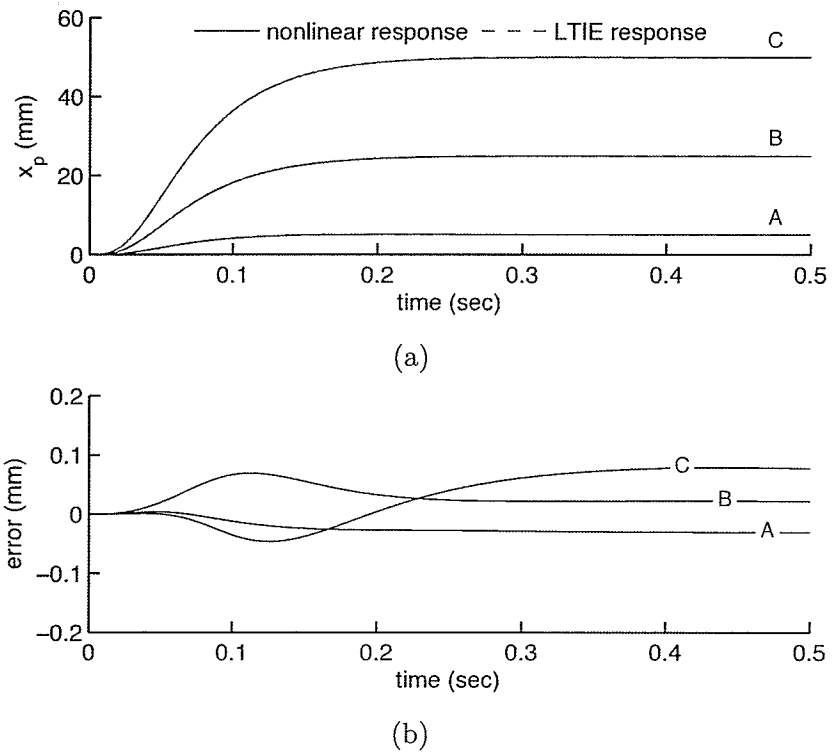

Figure 3.15: Comparison between nonlinear position responses and responses of LTIE transfer function estimates: (a) position response; (b) modeling error.

Table 3.4: LTIE transfer functions estimated from frequency response ratios $\frac{\hat{X}_p(j\omega)}{\hat{X}_v(j\omega)}$.

case	LTIE transfer function estimate
A	$P_A(s) = \dfrac{5.31 \times 10^8}{s(s^2 + 18.3s + 2.0 \times 10^5)}$
B	$P_B(s) = \dfrac{5.21 \times 10^8 (s^2 + 134.1s + 6.1 \times 10^3)}{s(s^2 + 15.3s + 2.0 \times 10^5)(s^2 + 131.2s + 6.5 \times 10^3)}$
C	$P_C(s) = \dfrac{5.24 \times 10^8 (s + 40.0)(s^2 + 178.5s + 1.7 \times 10^4)}{s(s + 51.9)(s^2 + 14.5s + 2.0 \times 10^5)(s^2 + 167.5s + 1.5 \times 10^4)}$

3.4 Summary

The goal of the first part of this chapter was to familiarize the reader with the QFT synthesis technique that will be employed to close the loop around the hydraulic actuator under study. A simple QFT design example was first carried out, around a parametrically uncertain LTI plant, to demonstrate the details of the approach. Then it was shown how QFT can be extended for control system development around an uncertain nonlinear system. The approach involves replacing the nonlinear plant dynamics, for different input signals, by an equivalent set of LTI transfer functions. Two approaches for recasting the nonlinear plant dynamics into an equivalent LTI form are available: (*i*) small-signal analysis and (*ii*) LTIE modeling. It was demonstrated that fixed-parameter small-signal models are generally inadequate to properly describe the transient response of hydraulic actuators. Moreover, it was observed that small-signal analysis can introduce more uncertainty than is necessary to characterize the nonlinear actuator dynamics. The LTIE modeling approach, on the other hand, enables large signal hydraulic actuator responses to be accurately characterized using a fixed-gain structure, and is therefore a more appropriate choice for fluid power control system development. A numerical procedure for directly evaluating the LTIE hydraulic actuator frequency response from acceptable input-output data, a crucial step in the control system design process, was also developed.

Chapter 4

Controller Design

This chapter presents the development of the QFT position control system for closing the loop around the fault emulator actuator. The end goal is to synthesize a low-order fixed-gain, fault tolerant, control law that can maintain the position tracking performance within prescribed tolerances despite the internal leakage of hydraulic fluid across the actuator piston. The control system is designed to achieve closed-loop performance similar to that of a typical electrohydraulic flight control actuator. Section 4.1 is devoted to formulating the position control problem which includes: (*i*) establishing the acceptable closed-loop position response envelope, (*ii*) establishing a representation of the aerodynamic load that must be overcome by the actuator, and (*iii*) defining the system uncertainty against which the position controller should be robust. In section 4.2, the QFT synthesis technique is employed to design a benchmark control system that considers only the normal operation of the hydraulic actuator. It is shown that two different control structures can be used to solve the benchmark control problem, and that the optimal control structure, in terms of minimizing the controller gain, is a non-integrating proportional type. The benchmark control problem is also solved using a higher-gain integrating controller structure, which is used as a basis for developing the fixed-gain fault tolerant controller in section 4.3. The overall performance of each designed position control system, and the ability of the fault tolerant controller to properly compensate the internal leakage

fault are demonstrated by nonlinear simulations and experimental tests.

4.1 Problem Setup

Acceptable Response Envelope

A block diagram of the two degree of freedom closed-loop position control system to be designed around the hydraulic actuator is shown in Figure 4.1. The envelope of acceptable closed-loop position responses, which the control system should generate, was derived by considering the transfer function model that describes the closed-loop dynamics of a modern hydraulic flight actuator [56]:

$$\frac{X_p^a(s)}{X_p^c(s)} = \frac{14.9 \times 10^6}{(s+20.2)(s+144.8)(s^2+105.1s+71.4^2)} \tag{4.1}$$

where $X_p^c(s)$ and $X_p^a(s)$ are the commanded and actual flight actuator positions, respectively.

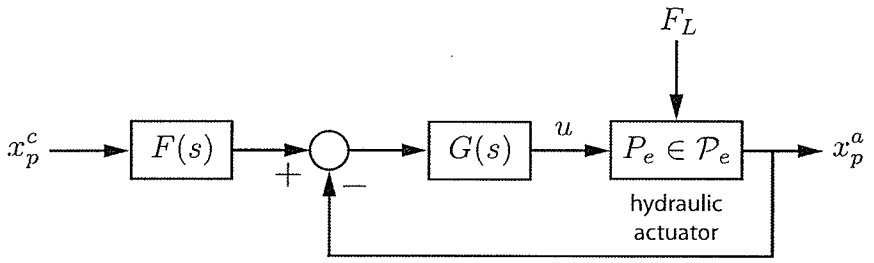

Figure 4.1: Two degree of freedom feedback control system around hydraulic actuator.

Due to the effects of the nonlinear hydraulic functions, uncertainties in the parameters of the hydraulic actuator and the internal leakage fault, some deviation from target system function (4.1) is inevitable. However by using feedback, it is possible to keep the closed-loop position responses within an envelope that is reasonably close to the target response. The acceptable closed-loop response envelope is defined by

the following fourth order transfer function:

$$T(s) = \frac{X_p^a(s)}{X_p^c(s)} = \frac{21.68 \times 10^5 \, (s/\lambda + 1))}{(s+15)(s+20)(s+85)^2}, \quad \lambda \in [14, 33] \tag{4.2}$$

Several unit step responses of (4.2) are shown in Figure 4.2 along with the unit step response of (4.1) for comparison. As can be seen, the actuator position responses within the selected acceptable envelope closely follow the target response given by (4.1).

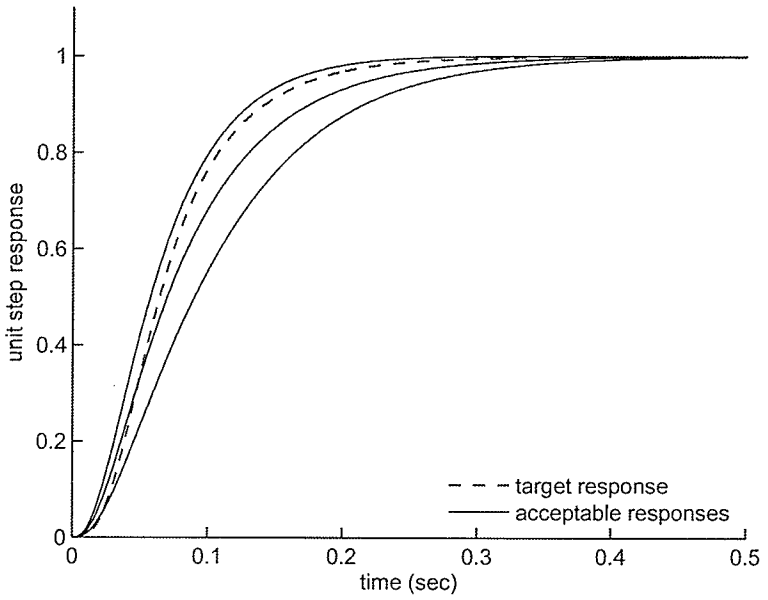

Figure 4.2: Acceptable unit step responses using linear model (solid lines) for design of QFT position controller and unit step response of typical flight control actuator (dashed line).

Description of the Load

In a flight control application, the dominant load force acting on the hydraulic actuator is the force resulting from the aerodynamics of the flight surface. The load force,

F_L, can be calculated from the following equation [110]:

$$F_L = \frac{\bar{q}S\bar{c}}{l_h} C_h(\theta, \delta) \tag{4.3}$$

In (4.3), $\bar{q} = \frac{1}{2}\rho_a V_T^2$ refers to the free-stream dynamic pressure, which is a function of the density of air, ρ_a, and the airspeed, V_T, of the aircraft. Therefore, the magnitude of the load force changes with height and speed. Parameter S denotes the area of control surface and $\bar{c}$ refers to the control surface mean aerodynamic chord. The equivalent length of the moment arm, which translates the linear motion of the actuator into rotation of the control surface about the hinge, is denoted by l_h. Coefficient C_h is the hinge moment coefficient, which is a nonlinear function of the control surface angle of incidence, θ, and the control surface displacement, δ.

Considering pitching motion of the aircraft, (4.3) can be recast in an approximate transfer function form [111]

$$F_L(s) \approx \frac{\bar{q}S\bar{c}}{l_h} \{C_{h,\alpha}\alpha(s) + C_{h,\delta_h}\delta_h(s)\} = \frac{\bar{q}S\bar{c}}{l_h} \left\{ C_{h,\alpha} \frac{\alpha(s)}{\delta_h(s)} + C_{h,\delta_h} \right\} \delta_h(s) \tag{4.4}$$

where $C_{h,\alpha}$ and C_{h,δ_h} represent the components of the hinge moment coefficient related to the angle of attack, α, and the deflection of the horizontal tail, δ_h, respectively. Transfer function $\frac{\alpha(s)}{\delta_h(s)}$ denotes to the short-period approximation of the aircraft longitudinal response [74].

For a modern jet aircraft, such as the F16, the bandwidth of the short-period response is about 5 rad/sec [74], which is much smaller than the 20 rad/sec bandwidth of the flight actuator. Consequently, the aerodynamic disturbing load can be considered to have a slow component arising from the pitching response of the aircraft and a quick component related directly to the motion of the flight actuator. Assuming that the aircraft angle of attack remains roughly constant during flight actuator motion,

(4.4) can be further approximated as

$$F_L(s) \approx \frac{\bar{q}S\bar{c}}{l_h} C_{h,\delta_h} \delta_h(s) + F_o \tag{4.5}$$

Referring to (4.5), term $F_o = \frac{\bar{q}S\bar{c}}{l_h} C_{h,\alpha}\alpha$ is the constant load force associated with the orientation of the aircraft. The behavior of variable term $\frac{\bar{q}S\bar{c}}{l_h} C_{h,\delta_h}\delta_h(s)$ can be interpreted from typical plots of coefficient C_{h,δ_h}, such as those shown in Figure 4.3. With reference to Figure 4.3, it is observed that changes in the value of the hinge moment coefficient, and therefore the changes in the actuator load for fixed α, are approximately proportional to the displacement of the control surface. The plots show this to be true over a wide range of control surface motion. However, for control surfaces that exhibit nonlinear behavior, such as curve b in Figure 4.3, the constant of proportionality can change depending on the region of control surface operation.

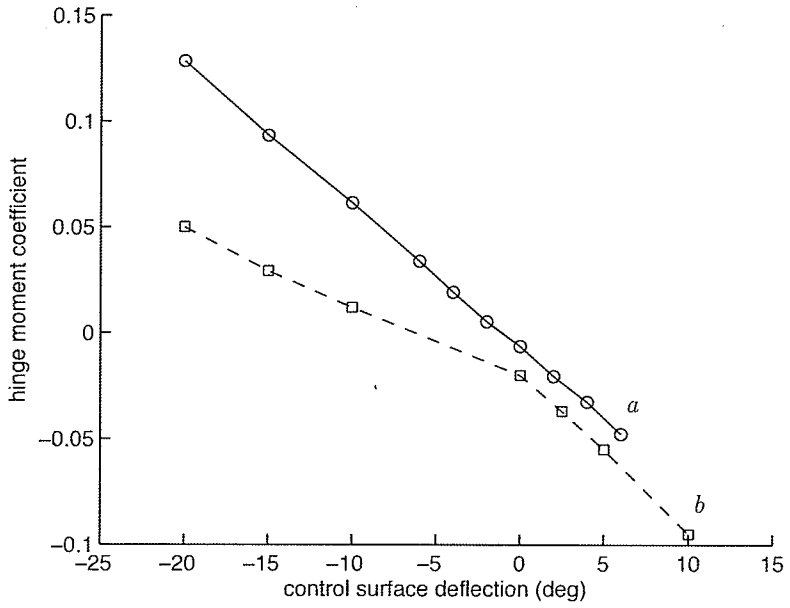

Figure 4.3: Typical variations in hinge moment coefficients as a function of control surface deflection. (Data for curves a and b are for $\alpha = 2°$ and were obtained from Figure 13a of [69] and from Figure 6.23 of [110], respectively.)

Using (4.5), the complex nature of the aerodynamic load force can be decomposed, for design of the position control system, as a simple stiffness dominant load

$$F_L(t) = kx_p(t) + F_o \tag{4.6}$$

where it has been assumed that $\delta \propto x_p$. In (4.6), a variable stiffness, $k \in [1, 60]$ kN/m, and an uncertain preload, $F_o \in [0, 4.4]$ kN, are used to account for different operating points in the aircraft flight envelope. The overall ranges of these parameters were selected to be compatible with the actuator hardware implemented on the experimental test bench.

Actuator Parameter Uncertainty

Even in the absence of system faults, normal variations and/or uncertainties in the values of the hydraulic system parameters can impact the dynamic response of the actuator and degrade the closed-loop performance. Therefore, parametric uncertainties should be explicitly considered in the control system design process. The uncertain hydraulic system parameters and the ranges used in the development of the position controller are summarized in Table 4.1. The considered parameter uncertainty is in line with other research work, for example [44, 57], which is focused on the design of robust control systems around healthy hydraulic actuators.

In Table 4.1, the range of variation in the supply pressure was established by operating the hydraulic test bench and observing the fluctuations that occur when the pump must adapt to changes in the demand for fluid. Since the cut-off frequency of the Moog D765 servovalve is about an octave above the natural frequency of the actuator resonant mode, only the nominal values of ω_v and ζ_v were considered in the control system design. In a design where the control valve dynamics and the actuator resonant mode occur in a similar frequency range, the variation in ω_v and ζ_v that can result from changes in the strength of the input signal should be accounted for.

Table 4.1: Ranges and nominal values of uncertain hydraulic actuator parameters.

Uncertain Parameter	Value		
	min	nominal	max
P_s (MPa)	13.8	17.2	18.6
m (kg)	11.0	12.3	13.5
d (N·sec/m)	200	250	300
β_h (MPa)	345	689	1030
$k_v \times 10^5$ (m/V)	2.51	2.79	3.07
F_o (kN)	0	0	4.4
k (kN/m)	1	30	60

4.2 Controller Design for Normal Operation

In this section, QFT is applied to design a benchmark position controller for the experimental hydraulic actuator under normal operation, which does not consider the effects of the internal leakage fault. The controller will, however, be designed for robust operation against the uncertainties listed in Table 4.1. It is shown that the benchmark position control problem can be solved using two different controller structures. The first is a non-integrating structure that allows the near optimal control law to be designed, in terms of minimizing the controller gain. The second is a higher-gain integrating structure that is used as a basis for developing the fault tolerant controller in the next section. Details on the design execution are given in section 4.2.1 and the experimental performance of the benchmark control systems is demonstrated in section 4.2.2 for normal operation. The manner in which the internal leakage fault impairs the performance of the benchmark control laws is examined in section 4.2.3.

4.2.1 Design Details

Step 1: LTI Equivalent Plant Set, $\mathcal{P}_e$

Using (4.2), the family of acceptable closed-loop position responses, $\mathcal{X}_p^a = \{X_p^c T\}$, was generated for the set of command inputs, $\mathcal{X}_p^c$, consisting of steps from 5 to 50 mm in magnitude. The acceptable output response set is shown in Figure 4.4a. The envelope (shaded area) and some typical examples of the plant drive signals required to generate the acceptable position responses are shown in Figure 4.4b. The servovalve spool displacements were solved by simulating the inverse model of the hydraulic actuator (see Appendix A) over the extreme ranges of the parameter and load uncertainties listed in Table 4.1. Approximately 3500 different plant cases were considered.

The frequency responses of each $x_v(t)$–$x_p(t)$ pair were computed next, using the Fourier transformation approach developed in section 3.3.3. The envelope of the set of frequency response ratios, $\frac{\hat{X}_p(j\omega)}{\hat{X}_v(j\omega)}$, is shown in Figure 4.5 along with some typical examples of the computed frequency response curves. Referring to Figure 4.5, it is observed that the identified frequency responses capture the important characteristics of the hydraulic actuator behavior including the low frequency integration characteristic and the actuator resonant mode in the high frequency range.

Templates of the identified LTIE plant set, $\mathcal{P}_e$, were determined by multiplying ratios $\frac{\hat{X}_p(j\omega)}{\hat{X}_v(j\omega)}$ with the frequency response of the servovalve, $P_V(j\omega)$. Templates of $\mathcal{P}_e = \left\{P_V \frac{\hat{X}_p}{\hat{X}_v}\right\}$, for different frequencies ω (rad/sec), are shown side-by-side in Figure 4.6 to facilitate comparison. The sizes and shapes of the templates describe, in terms of open-loop gain and phase variations on the Nichols chart, the changes in the dynamics of the hydraulic actuator that are attributable to: (i) the nonlinearity introduced by the hydraulic functions, and (ii) the considered uncertainty in the hydraulic system parameters and load (see Table 4.1). A few comments about the nature of the LTIE plant templates are now given.

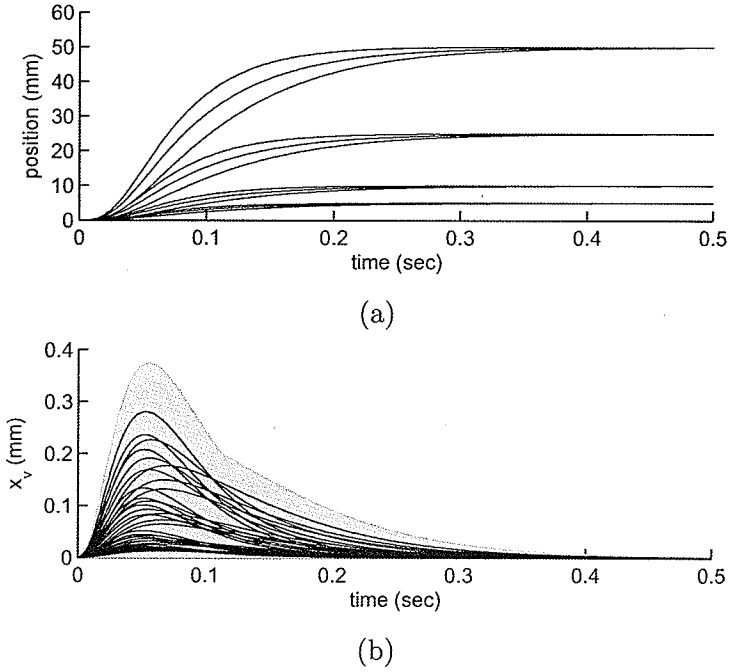

Figure 4.4: Time histories of acceptable plant input-output responses for normal operation of hydraulic actuator: (a) acceptable position responses (output); (b) envelope (shaded area) and typical examples of valve spool displacements (input).

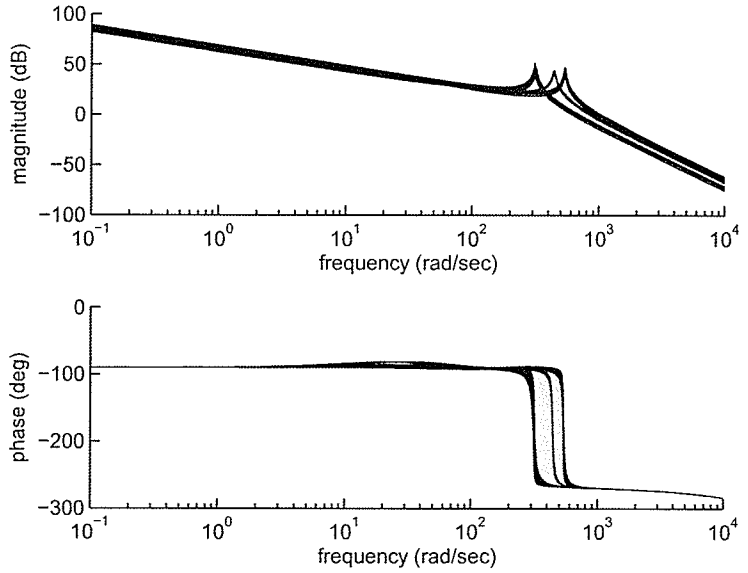

Figure 4.5: Envelope (shaded area) and examples of computed frequency response ratios, $\frac{\hat{X}_p(j\omega)}{\hat{X}_v(j\omega)}$, for normal operation.

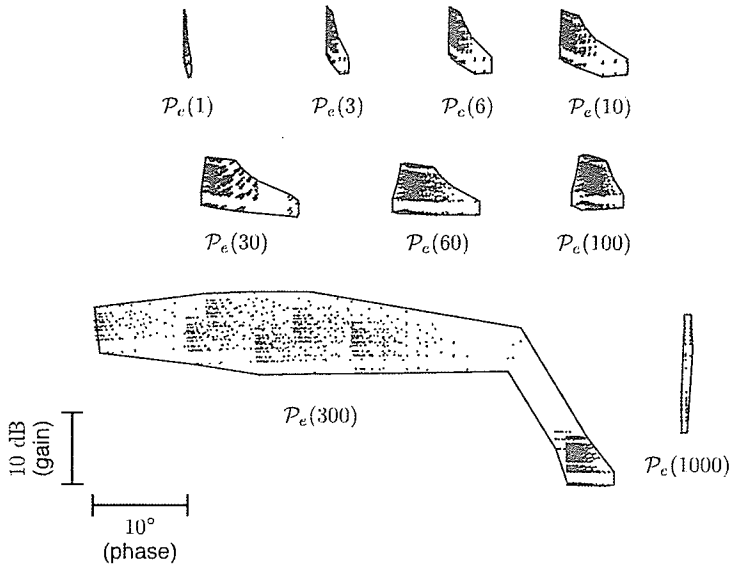

Figure 4.6: Templates of LTIE plant set, $\mathcal{P}_e$, for normal operation of hydraulic actuator at selected frequencies, ω (rad/sec).

At low frequencies, $\omega < 10$, the templates are close to vertical lines and the amount of phase variation in the plant is small (less than 5°). This is due to the fact that only the gain of the plant is affected by the system nonlinearities and parameter uncertainties. In the mid frequency band, $10 \leq \omega \leq 100$, the widths of the templates increase, primarily due to the effects of the servovalve spool motion away from the null position. The plant templates are biggest around the actuator resonant frequency, $300 \leq \omega \leq 700$ rad/sec. The large template sizes result from the relationship between the characteristics of the resonant mode and the uncertainty in the actuator mass, viscous damping coefficient, and hydraulic fluid bulk modulus (see template for $\omega = 300$ rad/sec). The changes in the cylinder volumes that occur as the actuator is stroked also influences the template size around the resonant frequency. Beyond 800 rad/sec, the template widths begin to decrease and the template points again merge into vertical lines.

Step 2: Nominal Loop Shaping a Prefilter Design

Using the templates of plant set $\mathcal{P}_e$, the next step in the QFT design process is to synthesize functions $F(s)$ and $G(s)$ in Figure 4.1. The objective is to design $F(s)$ and $G(s)$ such that $T = \frac{X_p^a}{X_p^c} = F\frac{GP_e}{1+GP_e}$ lies within the set $\mathcal{T} = \frac{\mathcal{X}_p^a}{\mathcal{X}_p^c}$ for all $P_e \in \mathcal{P}_e$.

To accomplish this objective, the controller and prefilter were designed to satisfy two tolerances on the closed-loop performance. The first design requirement is the tolerance on the closed-loop reference tracking response that must be satisfied for all plants in set $\mathcal{P}_e$:

$$|T_L| \leq \left| F\frac{GP_e}{1+GP_e} \right| \leq |T_U| \tag{4.7}$$

where

$$T_L(s) = \frac{12 \times 10^6}{(s+15)(s+20)(s+200)^2} \tag{4.8}$$

$$T_U(s) = \frac{28.6(s+10.5)}{(s+15)(s+20)} \tag{4.9}$$

$T_L(s)$ and $T_U(s)$ are lower and upper bounding functions whose step responses form an envelope encompassing the acceptable hydraulic actuator response set $\mathcal{X}_p^a$.

To ensure robust stability of the closed-loop system, a specification was also prescribed on the peak value of the closed-loop magnitude

$$\left| \frac{GP_e}{1+GP_e} \right| \leq 1.2 \text{ dB}, \quad \forall P_e \in \mathcal{P}_e \tag{4.10}$$

Inequality (4.10) is equivalent to specifying 5.4 dB and 50° gain/phase margins for the closed-loop system. These margins will give 20% overshoot in the system step response, which is slightly greater than the allowable amount fixed by upper tracking bound (4.9). The overshoot will be reduced later to a level compatible with the prescribed tracking bounds by the design of prefilter, $F(s)$. Since (4.10) also indirectly sets an upper limit on the peak sensitivity of the closed-loop system, no additional disturbance attenuation specification was made.

The QFT design specifications (4.7) and (4.10) were used together with the identified templates of $\mathcal{P}_e$, to formulate the QFT design bounds on the nominal loop transmission, $L = GP_{e,\text{nom}}$, and the prefilter, $F(s)$. The QFT bounds were solved using the numerical procedure documented in [95]. To reduce computation time, only plant magnitude-phase points lying on the template boundaries were used to calculate the bounds. Only the template boundaries need to be considered since the design specifications will be satisfied automatically for any magnitude-phase points lying inside the template perimeter [112]. The QFT bounds, $\mathcal{B}(\omega)$, are shown in Figure 4.7, at a number of important design frequencies.

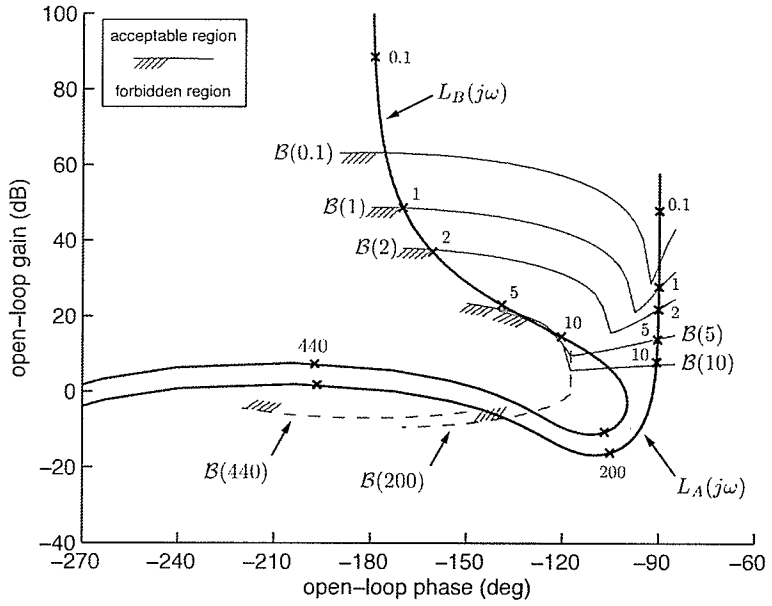

Figure 4.7: QFT bounds, $\mathcal{B}(\omega)$, and two example loop transmissions that are inadequate to solve the benchmark position control problem. ($L_A(j\omega)$ shaped using a proportional controller with $K_p = 325$ V/m; $L_B(j\omega)$ shaped using a proportional-integral controller with $K_i = 3500$ V/m·sec and $K_p = 610$ V/m.)

Figure 4.7 also shows two example loop transmissions that were designed in an attempt to solve the position control problem. The first loop transmission, L_A, corresponds to a proportional (P) controller cascaded in series with the nominal plant. The proportional gain has to be set to $K_p = 325$ V/m in order to satisfy the low-

frequency position tracking bounds, $\mathcal{B}(0.1)$ through $\mathcal{B}(10)$. However, implementing this value of proportional gain results in an unstable closed-loop system as evidenced by the violation of closed-loop stability bound $\mathcal{B}(440)$ and by the negative nominal gain margin, i.e. the magnitude of the loop transmission is greater than 0 dB when the phase angle is $-180°$. The second loop transmission, L_B, was designed by using a proportional-integral (PI) controller in series with the nominal plant. In order to satisfy the position tracking bounds, the controller gains were set to $K_i = 3500$ V/m·sec and $K_p = 610$ V/m. Referring to Figure 4.7, it is observed that L_B also violates bound $\mathcal{B}(440)$ and is closed-loop unstable.

Figure 4.7 illustrates clearly that conventional P and PI control laws are inadequate to solve the benchmark position control problem. It is impossible to make $|L(j\omega)|$ large enough to satisfy the position tracking bounds, $\mathcal{B}(0.1)$ through $\mathcal{B}(10)$, and at the same time realize acceptable stability margins. The main obstacle to the controller design is the lightly damped hydraulic actuator resonant mode, which gives sharp magnitude peaking in the actuator frequency response. Since the magnitude peaks occur when the actuator phase angle is about $-180°$ (see Figure 4.5), the resonance severely limits the achievable gain margin.

There are several different approaches that can be applied to alleviate the stability degrading effect of the actuator resonance. One approach is to introduce damping electronically by using a minor loop feedback arrangement. In this approach, high-pass filtered load pressure or piston acceleration measurements are employed as secondary control inputs to the servovalve [29, 30]. However, implementing the minor loop feedback requires additional instrumentation and can, in some circumstances, decrease the dynamic stiffness of the ram or intensify the effect of load disturbances having high frequency components [113]. A narrow-band filter in series with the controller can also be used to modify the characteristics of the hydraulic resonance [63,79]. Here, the idea is to exploit the magnitude-phase characteristics of the narrow-band filter to cancel the actuator complex poles and replace them by another pole pair

with more desirable characteristics. A problem associated with this approach is the fact that the resonant poles can never be cancelled exactly. This is especially true when the locations of the complex poles drift, due to parameter uncertainty. As a result of the inexact cancellation, some plants in the uncertain set may still exhibit poor stability properties when the feedback loop is closed.

In this work, a third approach, which was inspired by [114], is used to address the problematic resonant mode and improve the gain margin. The design philosophy is to use the phase characteristics of the controller to reposition the resonant peaks in a way that exploits the geometry of the Nichols chart, in particular the contours of constant closed-loop sensitivity. Recall from chapter 3 that the sensitivity of the closed-loop system, $S = \frac{1}{1+L}$, determines how disturbances affect the plant output. Several contours of constant closed-loop sensitivity are shown in Figure 4.8, which is known as the inverted Nichols chart [91]. As can be seen, the contours divide the inverted Nichols chart into two different regions. The first is the region of sensitivity amplification, $|S > 1|$, indicated by the shaded area in Figure 4.8. Outside the shaded area, $|S < 1|$. It is reasonable to place the actuator resonant peaks in a region of low sensitivity, for example by shaping the loop transmission so that $\angle L \approx -360°$ at the resonant frequency. Doing this reduces the influence of the actuator resonant mode on the gain margin, and has the desirable effect of improving the closed-loop disturbance response by reducing the sensitivity at the resonant frequency.

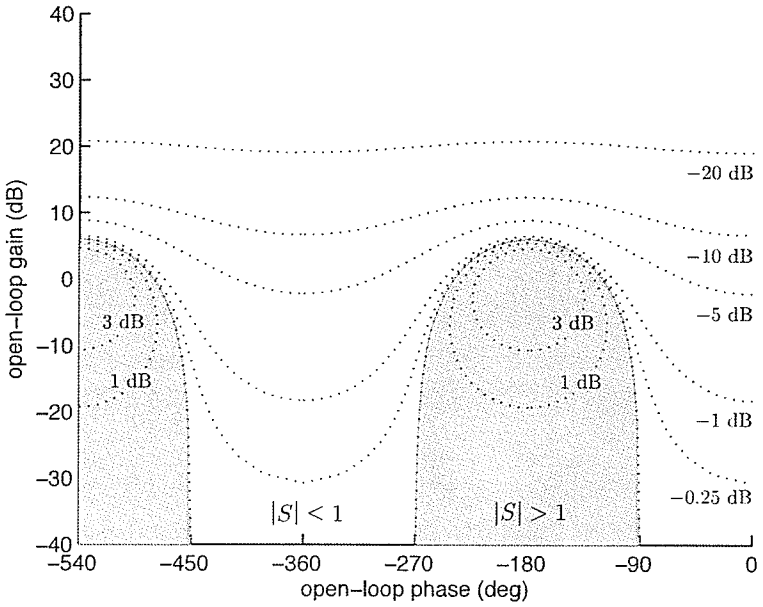

Figure 4.8: Inverted Nichols chart showing contours of constant closed-loop sensitivity as well as regions of sensitivity amplification, $|S| > 1$ (shaded area), and sensitivity attenuation, $|S| < 1$.

Figure 4.9a shows two loop transmissions that have been shaped, using the design concept described above, to properly satisfy the QFT bounds. The compensator corresponding to loop transmission $L_A(j\omega)$ is solved as the ratio $\frac{L_A(j\omega)}{P_{e,\text{nom}}}$ and has the following transfer function:

$$G_A(s) = \frac{2.76 \times 10^6 (s + 25)}{(s + 16)(s^2 + 108s + 120^2)} \tag{4.11}$$

Controller (4.11) was built from the P-control structure shown in Figure 4.7 and will be referred to hereafter as benchmark controller A. To design controller A, the proportional loop gain was first adjusted to satisfy $\mathcal{B}(1)$. Next, a lag filter formed by pole zero pair, $\frac{(s+25)}{(s+16)}$, was implemented to pull L slightly to the left in order to satisfy the other tracking bounds. Finally, an underdamped complex pole pair was added to roll off the high frequency controller gain and introduce the necessary phase lag to move the resonance peaks left and into the region of low sensitivity on the inverted

Nichols chart (see Figure 4.9b). Since $L_A(j\omega)$ passes through the minima in the QFT bounds, the loop shape is near optimal in terms of minimizing the controller gain.

The other loop transmission, $L_B(j\omega)$ in Figure 4.9, uses an integrating control structure. To shape the loop, the integral gain was first increased to position the loop transmission above bound $\mathcal{B}(1)$ and a zero was placed at $s = -5$ to give a PI controller. The closed-loop system was then stabilized by adding an underdamped complex pole pair with damping ratio $\zeta = 0.45$ and natural frequency $\omega_p = 250$ rad/sec. This also moved the resonance peaks into the low sensitivity region on the gain-phase chart. A lag filter was designed to further shape the loop transmission around the stability margins. The following control law, solved as the ratio $\frac{L_B(j\omega)}{P_{e,\text{nom}}}$, was obtained after some iteration

$$G_B(s) = \frac{3.21 \times 10^7 (s+4.7)(s+42)}{s(s+29)(s^2+225s+250^2)} \tag{4.12}$$

Henceforth, controller (4.12) will be referred to as benchmark controller B.

The Bode magnitudes of each designed controller are shown in Figure 4.10. Referring to Figure 4.10, it is clear that the non-integrating controller, controller A, solves the position control problem with a lower overall gain. Thus, controller A would be attractive in applications where it is desired to minimize the effect of sensor noise, for example, when a linear variable differential transformer (LVDT) is used to measure the position of the hydraulic actuator. Also, the lower overall gain of control system A enables the QFT bounds to be satisfied with the least amount of design conservatism. This is evidenced by Table 4.2, which summarizes the closed-loop magnitude variations, $\left|\frac{GP_e}{1+GP_e}\right|_{\max} - \left|\frac{GP_e}{1+GP_e}\right|_{\min}$, associated with each designed control law at several selected frequencies. The prescribed tolerances are also reported. Table 4.2 shows that both the designed control systems are capable of reducing the closed-loop magnitude variations to less than the values specified. Table 4.2 also shows that using controller A, the closed-loop magnitude variations closely follow the prescribed amounts. On the other hand, controller B reduces the closed-loop magnitude varia-

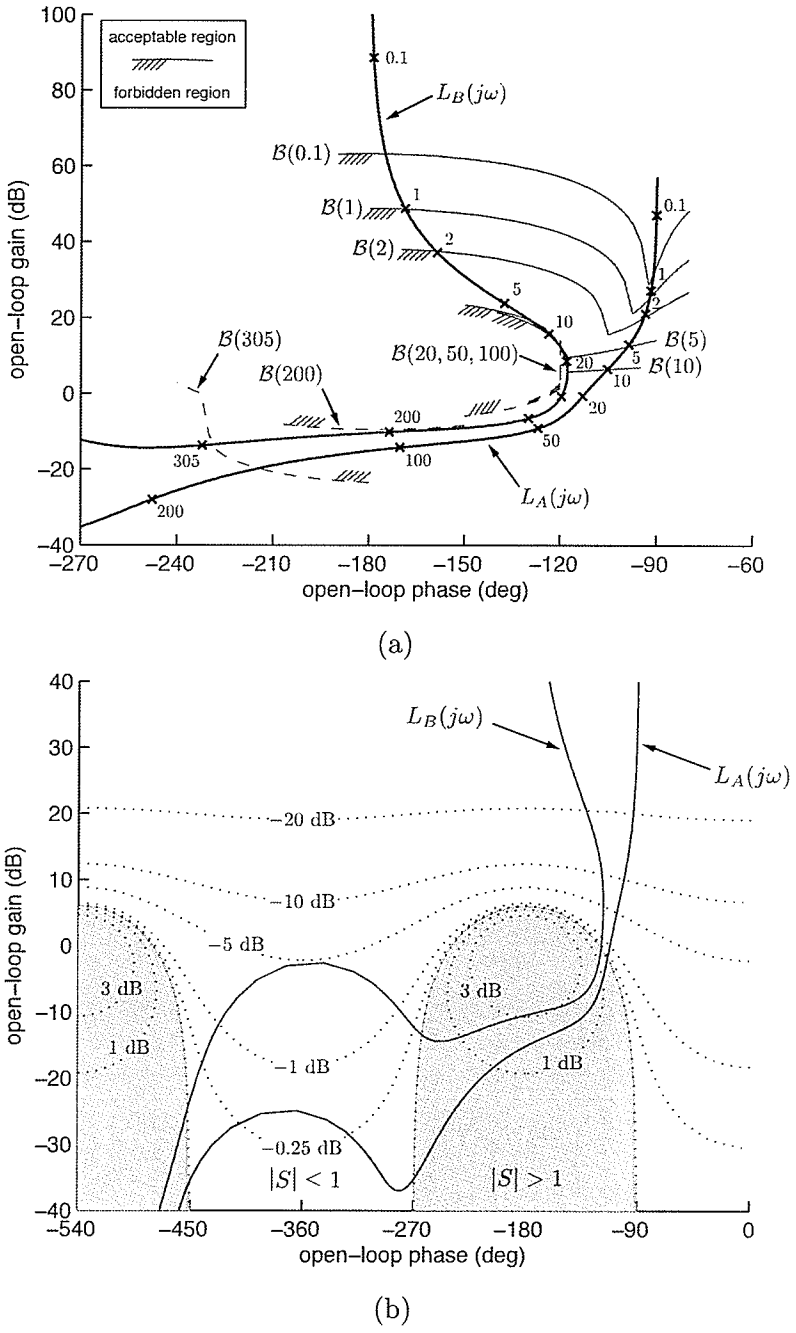

Figure 4.9: QFT bounds, $\mathcal{B}(\omega)$, and two designed loop transmissions: (a) loop shapes that satisfy QFT bounds; (b) loop transmissions on inverted Nichols chart. Legend: $L_A(j\omega)$ – loop transmission using a non-integrating controller structure; $L_B(j\omega)$ – loop transmission using an integrating controller structure.

tions much more than the design specifications dictate. This overdesign can increase the susceptibility of the control loop to noise and is a necessary cost associated with the use of an integrating control structure.

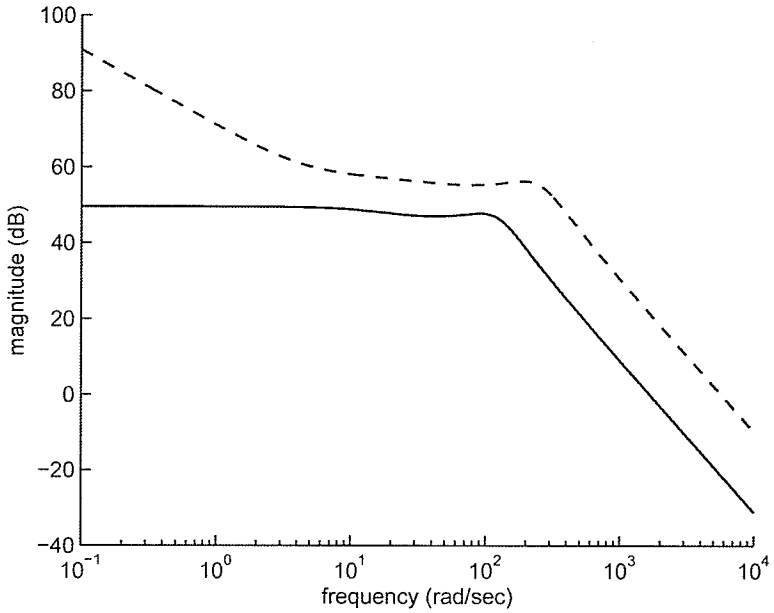

Figure 4.10: Bode magnitudes of controller A (solid line) and controller B (dashed line).

Table 4.2: Closed-loop magnitude tolerances and actual variation obtained using controllers A and B at selected frequencies.

Frequency	Closed-Loop Magnitude Variation		
(rad/sec)	tolerance	using $G_A(s)$	using $G_B(s)$
1	0.05	0.03	0.05
3	0.35	0.30	0.33
5	0.90	0.82	0.58
10	2.83	2.85	0.58
30	9.82	8.19	3.59

Prefilters were designed next to shape the frequency responses of each closed-loop system so that they all lie within the specified tracking envelope. Further manipulation of the tracking responses is necessary since shaping the loop transmission only guarantees that the overall magnitude variation in set $\frac{G\mathcal{P}_e}{1+G\mathcal{P}_e}$ is less than the allowable amount, at each design frequency. Following the synthesis procedure outlined in section 3.2.1, a suitable prefilter for control system A was found to be

$$F_A(s) = \frac{100}{s+100} \tag{4.13}$$

The transfer function of the prefilter for control system B is

$$F_B(s) = \frac{23(s+13)}{(s+7.5)(s+40)} \tag{4.14}$$

Step 3: Controller Verification

Before testing the designed control systems on the experimental test bench, it is prudent to verify that the closed-loop systems indeed meet the specified performance requirements. To confirm each design, several different checks were made. First, the closed-loop frequency responses $\left|\frac{G\mathcal{P}_e}{1+G\mathcal{P}_e}\right|$ were evaluated over the extreme values of parameter uncertainty considered in the design. This was done to check whether the stability margin specification (4.10) is satisfied for the entire plant set $\mathcal{P}_e$. The results are shown in Figure 4.11 for both of the designed control systems. Referring to Figure 4.11, the magnitude peaks in $\left|\frac{G\mathcal{P}_e}{1+G\mathcal{P}_e}\right|$ are observed never to exceed the 1.2 dB design specification. The magnitudes of the closed-loop tracking responses, shown in Figure 4.12 for each designed control system, were also computed. Figure 4.12 confirms that the envelope of tracking transfer functions $\left|F\frac{G\mathcal{P}_e}{1+G\mathcal{P}_e}\right|$ falls within the prescribed lower and upper tracking bounds.

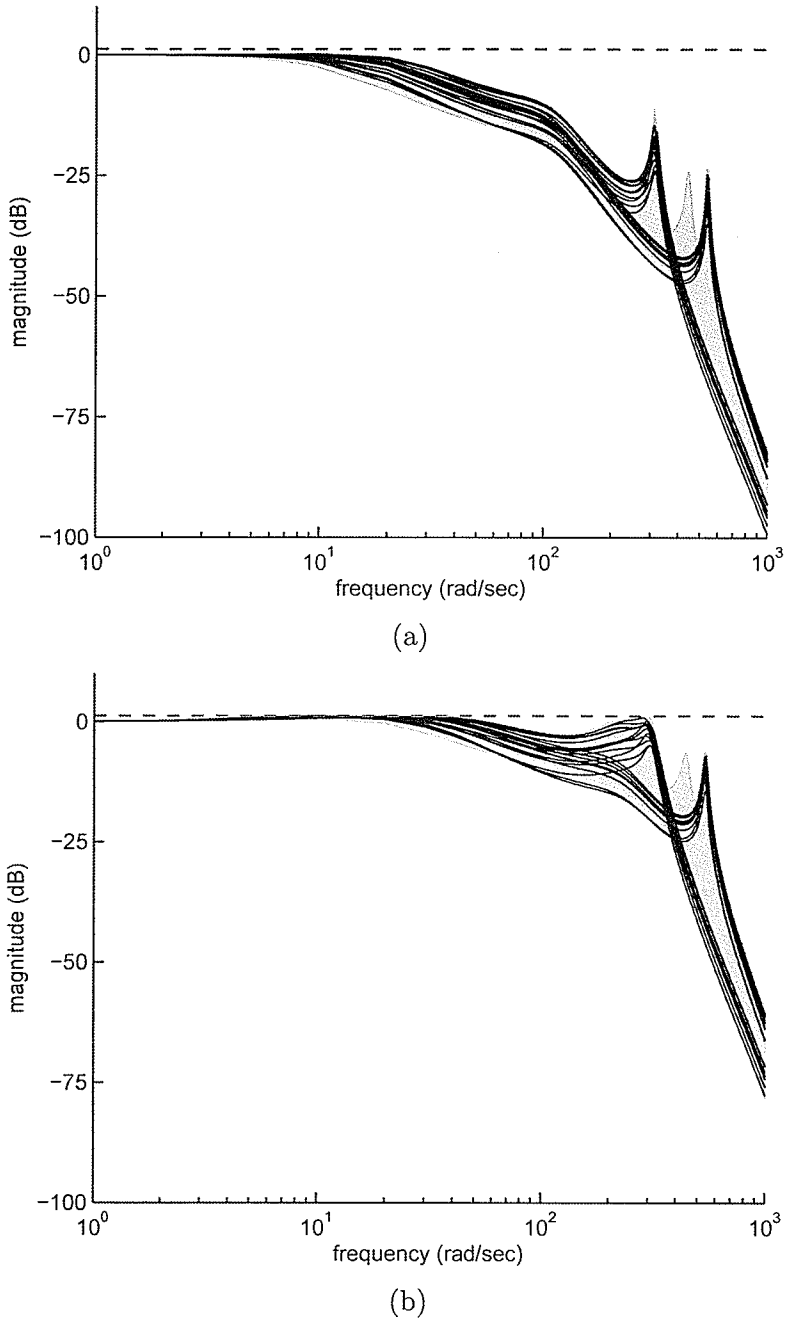

Figure 4.11: Envelope (shaded area) and examples of closed-loop frequency responses, $\left|\frac{GP_e}{1+GP_e}\right|$, over range of parameter uncertainty: (a) control system A; (b) control system B. Dashed line indicates design specification on closed-loop magnitude peaks.

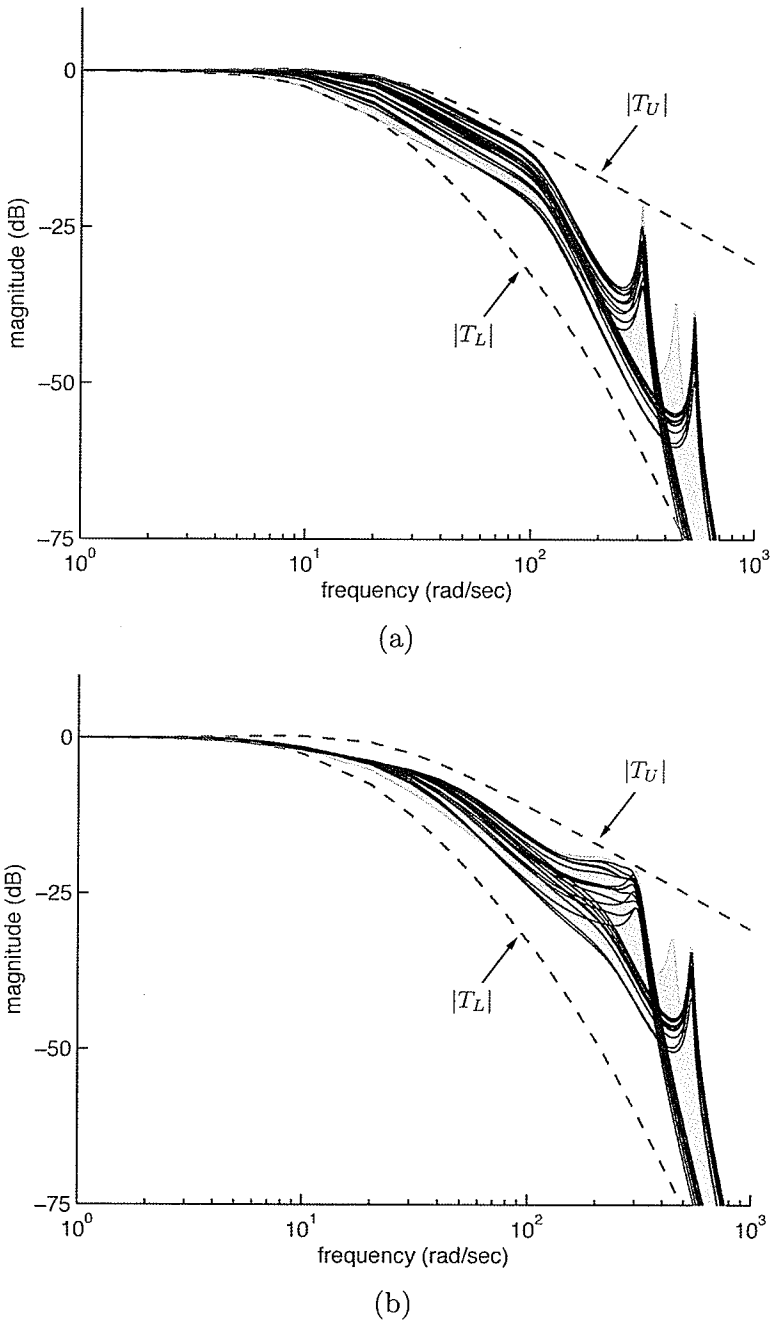

Figure 4.12: Envelope (shaded area) and examples of closed-loop tracking responses, $\left|F\frac{GP_e}{1+GP_e}\right|$, over range of parameter uncertainty: (a) control system A; (b) control system B. Dashed lines indicate lower and upper tracking bounds.

To test the time domain performance of the designed control systems, several hundred nonlinear simulations were performed using extreme combinations of the uncertain system parameters listed in Table 4.1. Different step commands ranging from 5 to 50 mm were simulated for each uncertain parameter combination. Normalized step responses are shown for control system A in Figure 4.13a. The acceptable step response envelope formed by the time responses of (4.8) and (4.9) is also shown as the shaded area for reference. As shown in Figure 4.13a, the step responses all fall between the lower and upper tracking bounds, which further confirms the validity of the control system design. Moreover, the step responses are observed to nearly fill the acceptable response envelope. This indicates that the amount of controller gain used to satisfy the design specifications is near optimal and is very well matched to the amount of uncertainty in the plant. Referring to Figure 4.13b, which shows the control signals pertaining to the nonlinear simulations, it is observed that the closed-loop positioning system makes good use of the available plant capacity. The control value just begins to saturate at 10 V for the large 50 mm step commands.

The time domain performance of control system B was also evaluated by nonlinear simulations. The results are shown in Figure 4.14 for the same combinations of uncertain parameters and reference commands as in Figure 4.13. Figure 4.14a shows that the normalized step responses fall well within the prescribed acceptable envelope. However, in comparison to Figure 4.13a it is observed that the overall range of variation in the step responses is much smaller. This is a direct result of the conservatism and overdesign inherent in higher-gain control system B. The control signals pertaining to the nonlinear simulations are shown in Figure 4.14b. As with controller A, saturation of the control valve input is observed for some of the large 50 mm step commands.

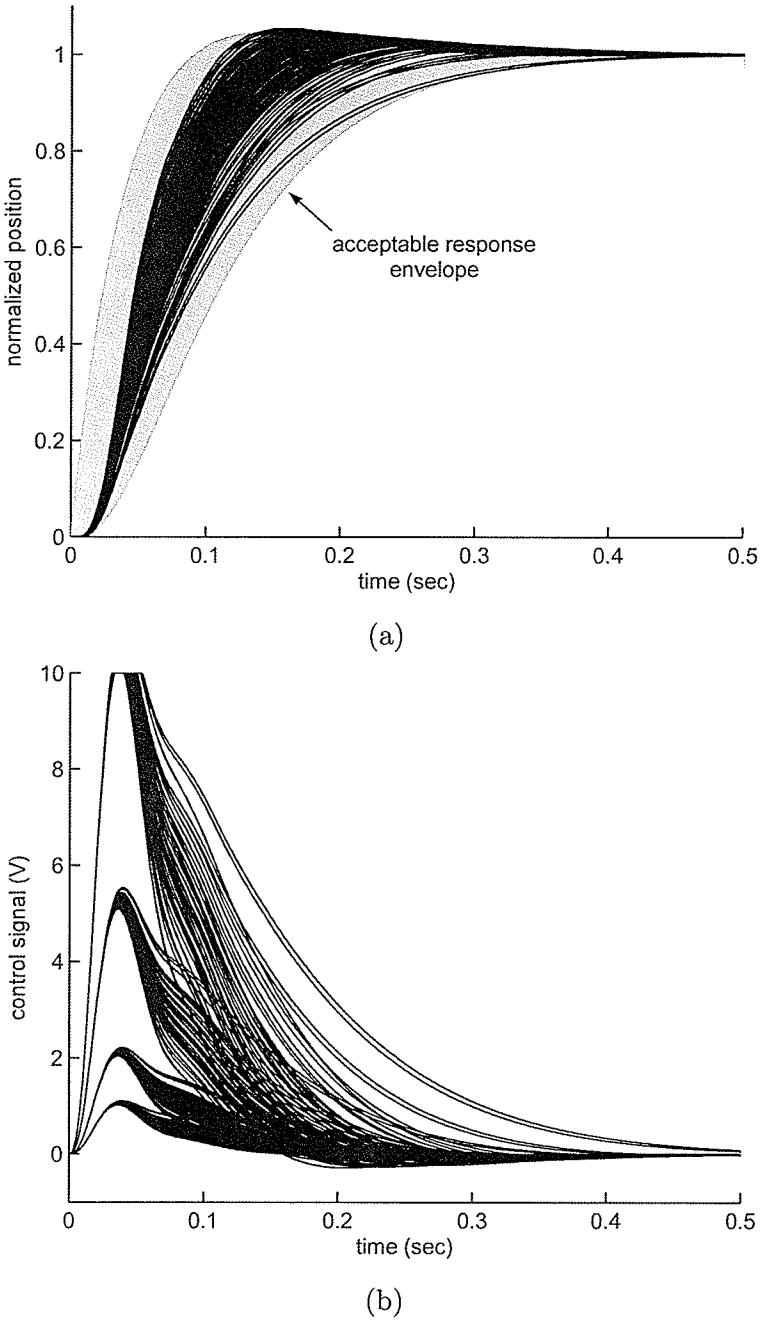

Figure 4.13: Representative normalized closed-loop step responses for non-integrating control system A (nonlinear simulations): (a) normalized positions; (b) control signals.

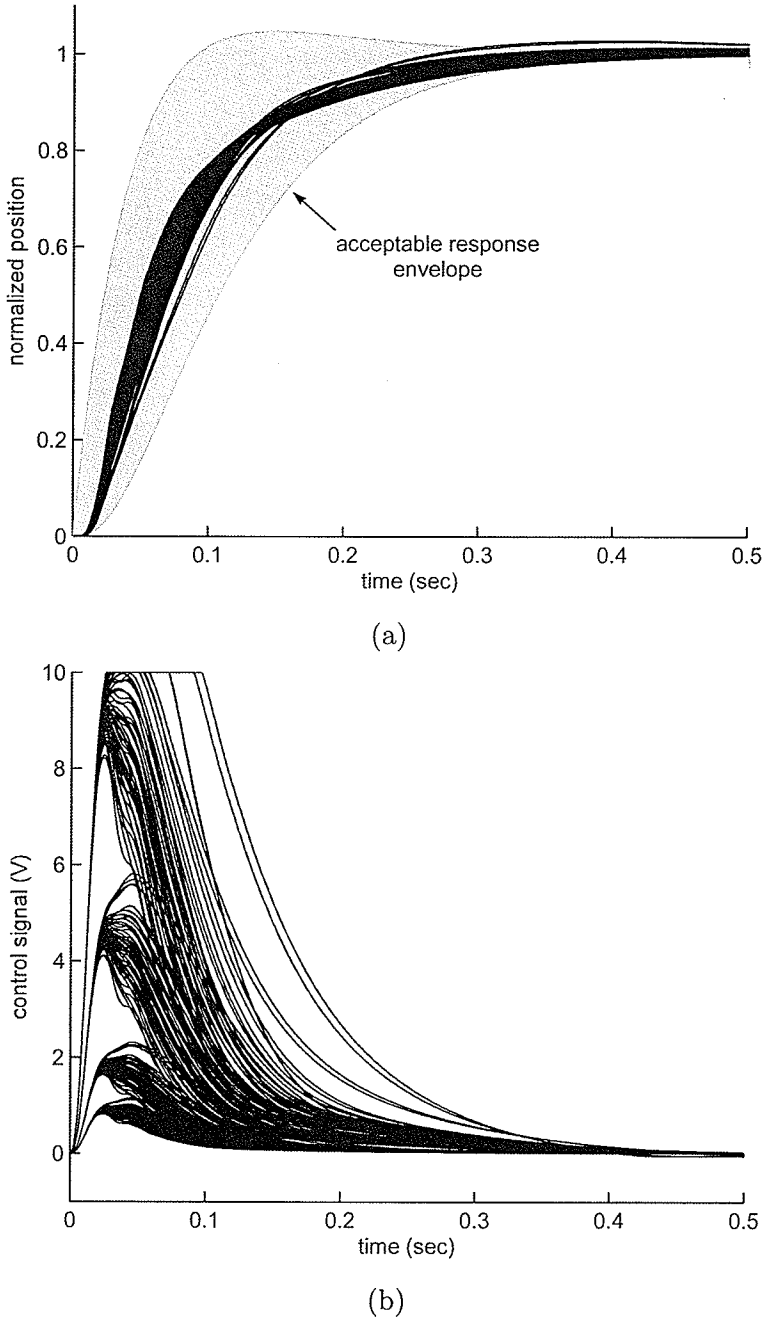

Figure 4.14: Representative normalized closed-loop step responses for integrating control system B (nonlinear simulations): (a) normalized positions; (b) control signals.

4.2.2 Experimental Results

Several experiments were performed to confirm the efficacy of control systems A and B when implemented on the hydraulic test bench. In the tests, the hydraulic actuator was operated against a spring rigidly fixed to the test bench base. This arrangement was used to create a position dependent load similar to the one considered in the control system design. The performance of the actuator was first tested for various step input commands from 5 to 40 mm against a 30 kN/m environment. The spring was not long enough to test 50 mm step commands. The results, using control system A, are shown in Figure 4.15. As can be seen, the experimental position responses, fall well within the design bounds for various step input commands. Moreover, the step responses and the corresponding control signals (see Figure 4.15b), are consistent with the nonlinear simulation results reported in section 4.2.1. The robustness of controller A against variations in the load was tested by operating the ram without any applied load and against a stiffer 80 kN/m spring. Typical results, shown in Figure 4.16, confirm that the control system can cope well with changes in the stiffness of the load. Only slight variations in the position responses are seen with the changes in the load.

Similar experiments were carried out using control system B. Figure 4.17 illustrates the performance of the actuator operating against the 30 kN/m environment. As predicted by the nonlinear simulations, the step responses fit accurately within the prescribed envelope. The robustness of control system B to changes in the stiffness of the environment is also very good, as evidenced by Figure 4.18. The position responses obtained, when operating the ram without any applied load and against 30 and 80 kN/m springs, are difficult to distinguish from one another due to the high gain of the controller.

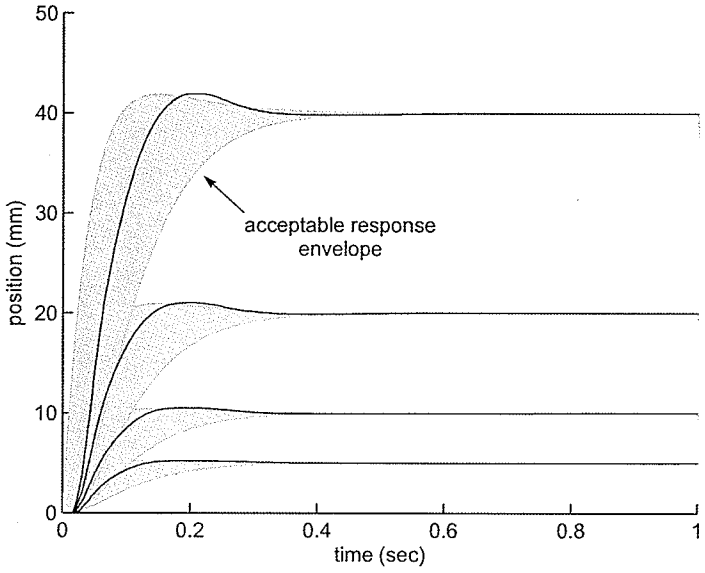

(a)

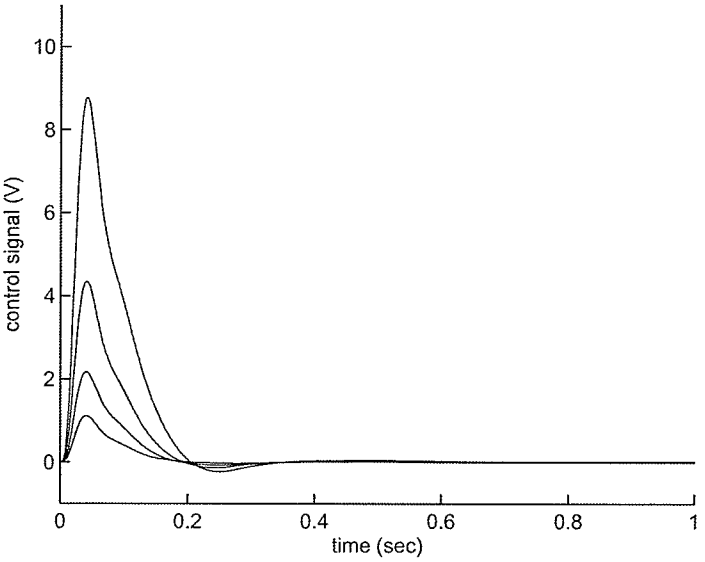

(b)

Figure 4.15: Experimental step responses against a 30 kN/m spring (control system A): (a) actuator position; (b) control signal.

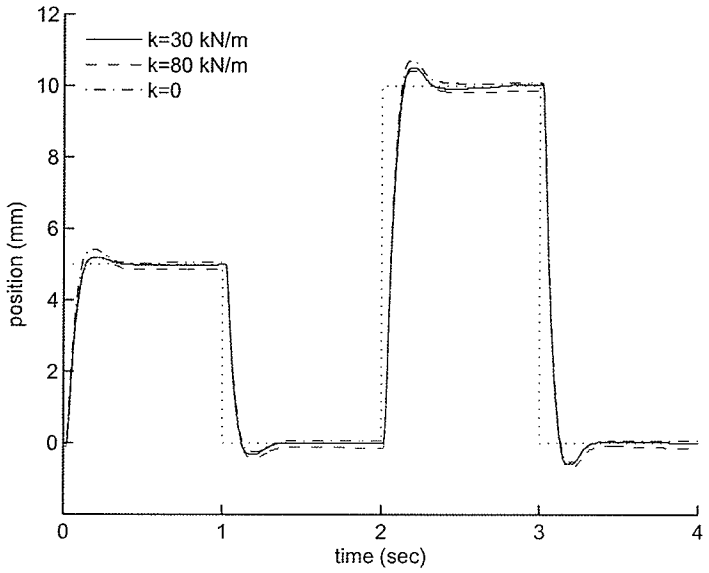

(a)

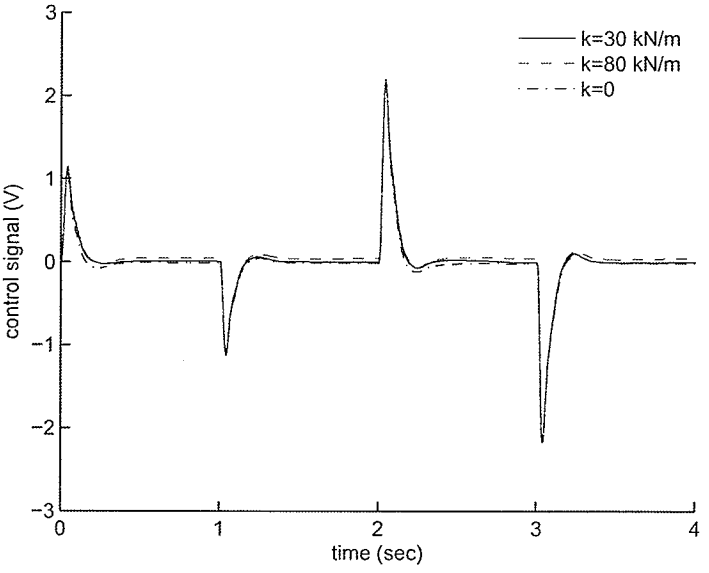

(b)

Figure 4.16: Experimental step responses with different environment stiffnesses (control system A): (a) actuator position; (b) control signal.

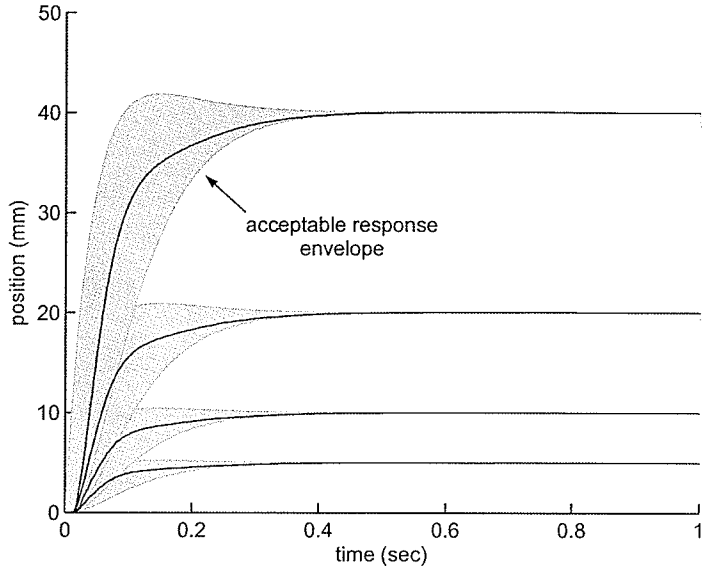

(a)

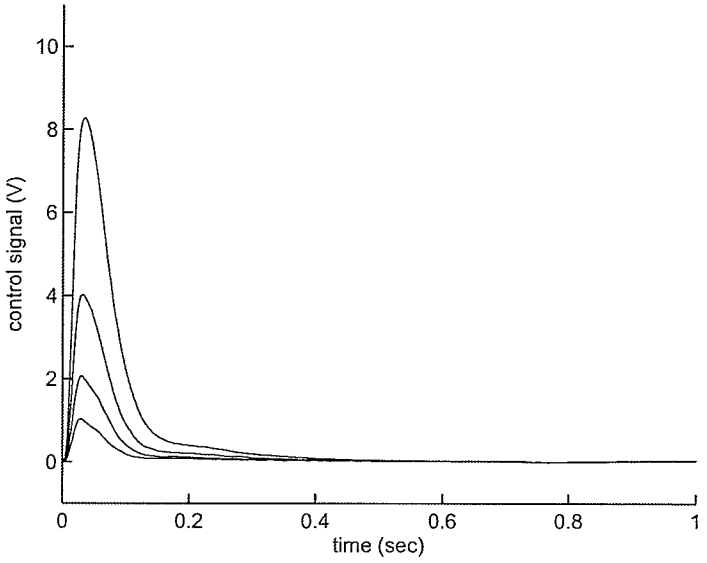

(b)

Figure 4.17: Experimental step responses against a 30 kN/m spring (control system B): (a) actuator position; (b) control signal.

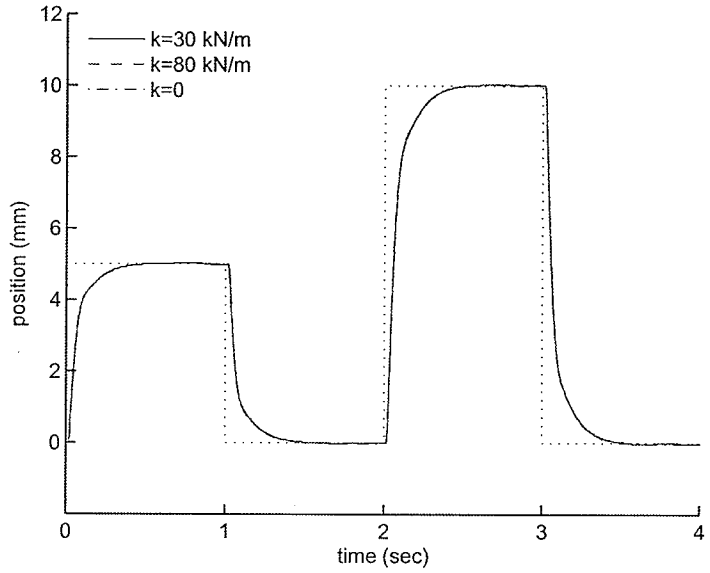

(a)

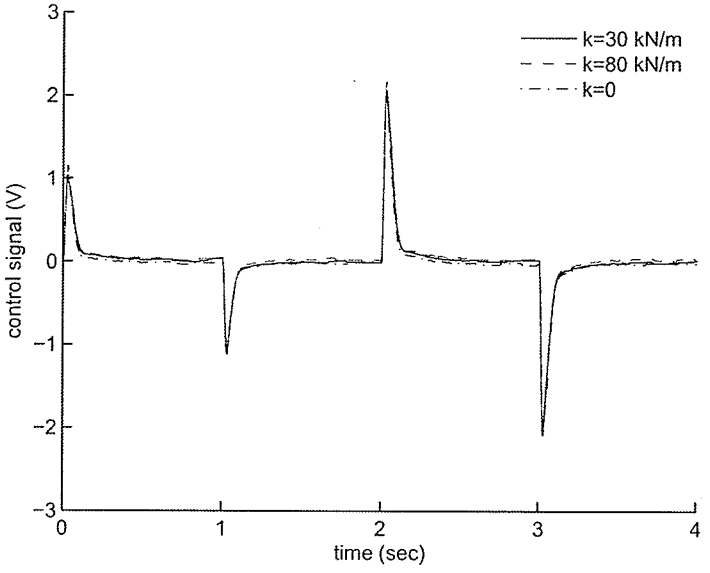

(b)

Figure 4.18: Experimental step responses with different environment stiffnesses (control system B): (a) actuator position; (b) control signal.

4.2.3 Performance in Presence of Internal Leakage Fault

Additional experiments were conducted to investigate the ability of the benchmark position control systems, designed only for normal operation of the actuator, to maintain the performance of the ram in the presence of an internal leakage fault. In the tests, the actuator was operated against a 30 kN/m spring for several different step input commands. The internal leakage fault was introduced by opening the ball valve that connects the two actuator cylinders and then adjusting the needle valve to control the intensity of the leakage flow. The actuator step response test was carried out for several different adjustments of the needle valve, in order to simulate a fault of increasing severity.

The operation of control system A, for various internal leakage rates from 0 to 5 L/min, is shown in Figure 4.19. Typical time-histories of the internal leakage flow are also given, for reference. As illustrated in Figure 4.19a, control system A cannot keep the step responses within the prescribed acceptable envelope when the internal leakage flow is introduced into the operation of the system. The steady-state positioning error is observed to increase in proportion to the severity of the fault. However, the control system is still able to maintain partial control over the load, because the position error signal keeps the servovalve open (see nonzero control signals in Figure 4.19b). Since a make-up flow of fluid is available to partially offset the amount that is bypassed due to the fault, the actuator can maintain a constant load pressure across the piston. However, the actuator force is limited to a magnitude smaller than is necessary to properly zero the position error.

The ability of control system B to cope with the internal leakage fault is demonstrated in Figure 4.20. In contrast to control system A, which gives large positioning errors in the presence of the internal leakage fault, control system B does a reasonable job of maintaining the positioning performance within the prescribed envelope. Only small excursions outside of the acceptable envelope are observed towards the

end of the transient response, despite the fact that the effects of the fault were not considered explicitly at the control system design stage. Part of the reason for the good performance of control system B in the presence of the fault lies in the fact that the control system contains an integrator that can automatically drive the servovalve spool to provide a make-up flow even when the position error is zero. Another factor that undoubtedly influenced the performance of control system B in the presence of the fault is the fact that the controller is overdesigned (see section 4.2.1). The high control law gain, which is necessary to reduce the sensitivity of the feedback system to the variations in the hydraulic actuator parameters, had the favorable effect of masking the effects of the internal leakage fault. Since benchmark controller B provides an inherent degree of robustness against the internal leakage fault, it can be used as a starting point for developing the fault tolerant controller. Design of the fault tolerant control law is the topic of the next section.

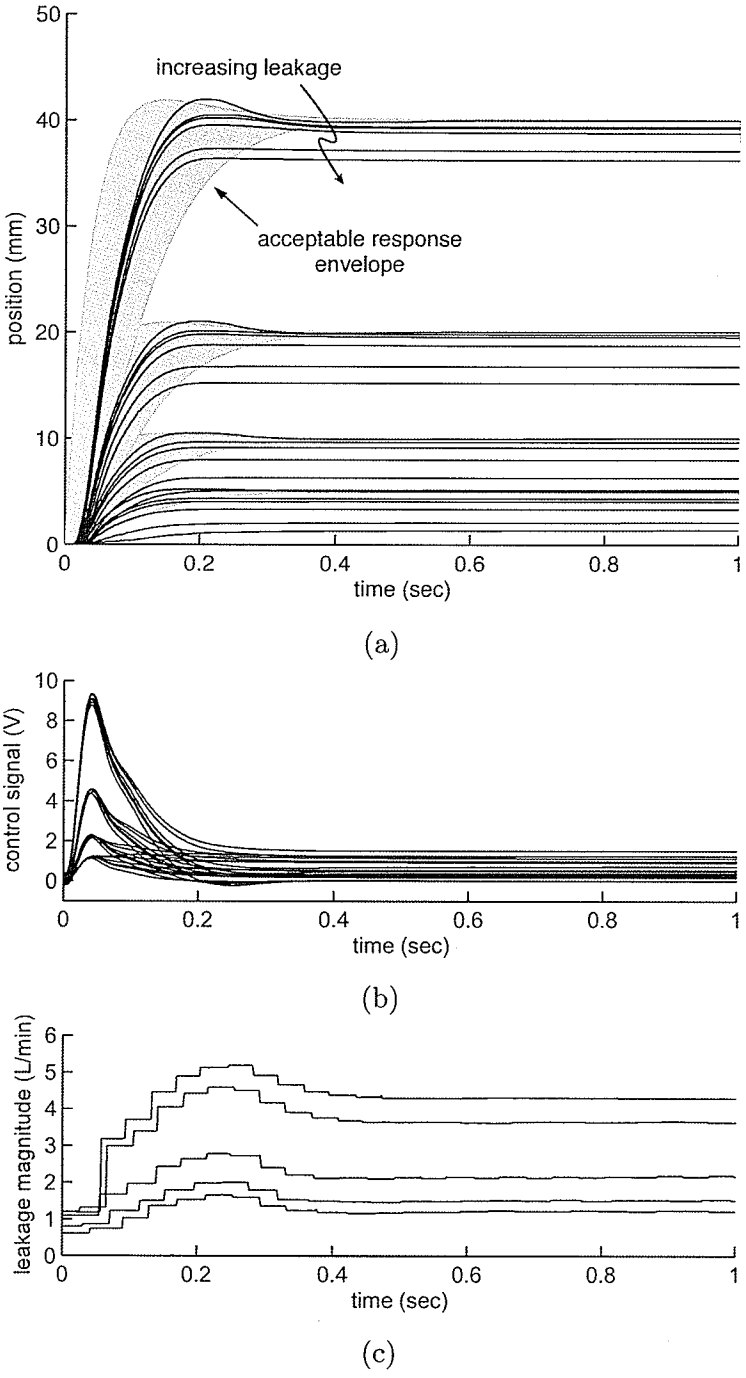

Figure 4.19: Experimental step responses against a 30 kN/m spring in the presence of internal leakage fault (control system A): (a) actuator position; (b) control signal; (c) typical internal leakage magnitudes corresponding to 40 mm step responses.

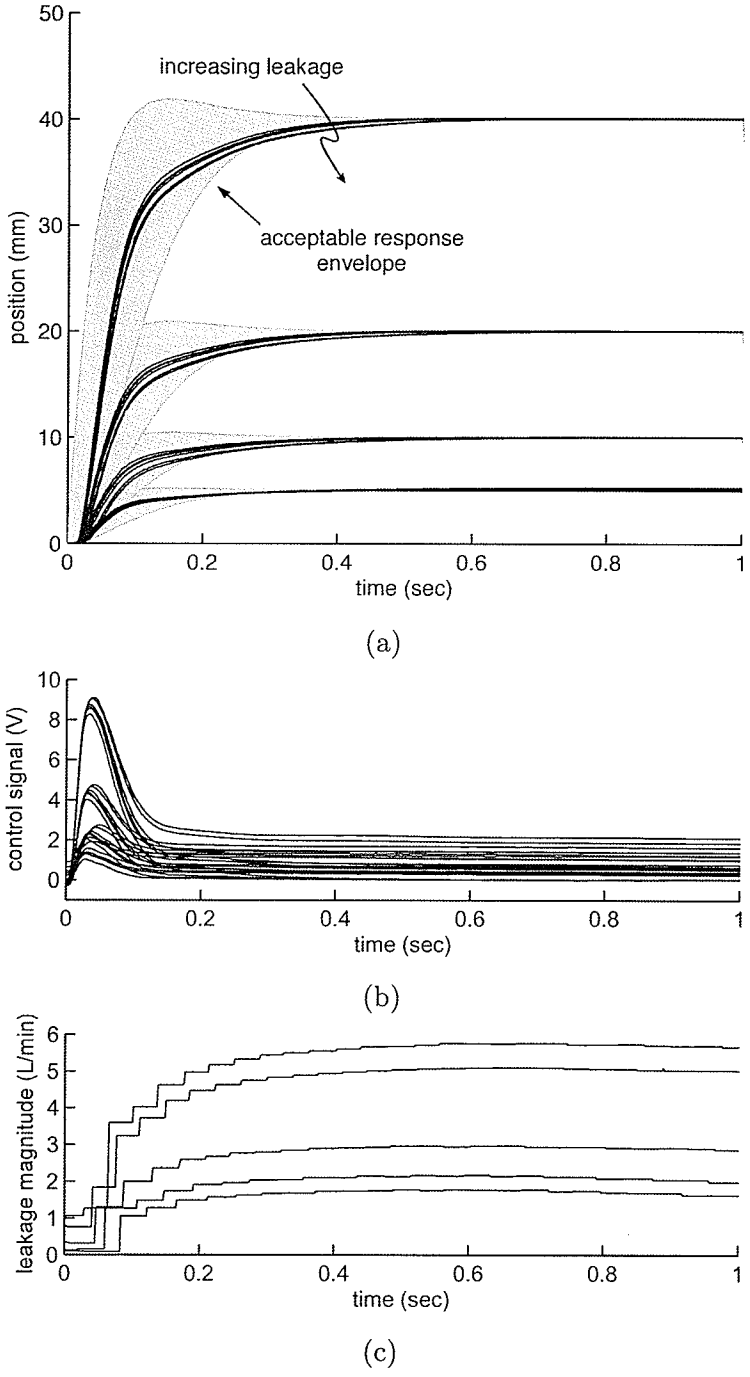

Figure 4.20: Experimental step responses against a 30 kN/m spring in the presence of internal leakage fault (control system B): (a) actuator position; (b) control signal; (c) typical internal leakage magnitudes corresponding to 40 mm step responses.

4.3 Design of Fault Tolerant Controller

This section presents the design of a fixed-gain control law that can compensate for the effects of the internal leakage fault and at the same time accommodate other parametric uncertainties. Specifics on the control system design, which includes expanding the LTIE plant templates to account for the effects of the internal leakage and re-shaping the nominal loop transmission, are given in section 4.3.1. The performance of the fault tolerant controller is verified by experiments in section 4.3.2.

4.3.1 Design Details

Step 1: LTI Equivalent Plant Set, $\mathcal{P}_e$

The fault tolerant controller was designed to generate the same family of acceptable closed-loop position responses as the benchmark control laws developed in section 4.2. The acceptable output set, $\mathcal{X}_p^a = \{X_p^c T\}$, is shown in Figure 4.21a, for the same set of command inputs. The servovalve spool displacements necessary to enable the hydraulic actuator to track the desired position responses were computed, as before, using the inverse model of the ram. The extreme ranges of the actuator parameter uncertainties listed in Table 4.1 were considered.

In the inverse model, coefficient K_{12} was varied in order to simulate the effects of the internal leakage fault. A maximum value of $K_{12} = 5.38 \times 10^{-8}$ m$^3/\sqrt{\text{Pa}}$·sec was selected by considering the available servovalve flow at the maximum nominal load pressure, $\frac{2}{3}P_s$ [2]. Setting $K_{12} = 5.83 \times 10^{-8}$ m$^3/\sqrt{\text{Pa}}$·sec allows approximately 40% of the rated servovalve flow to be bypassed across the actuator piston. However, when operating at the minimum supply pressure, 13.8 MPa (2000 psi), the available servovalve flow can become less than the amount consumed by the internal leakage fault. Consequently, the actuator was considered to operate under a slightly reduced load capacity for the fault tolerant control system design. This was accommodated in the inverse simulations by reducing the range of the actuator pre-load by about 30% from $F_o = [0, 4.4]$ kN to $F_o = [0, 2.8]$ kN.

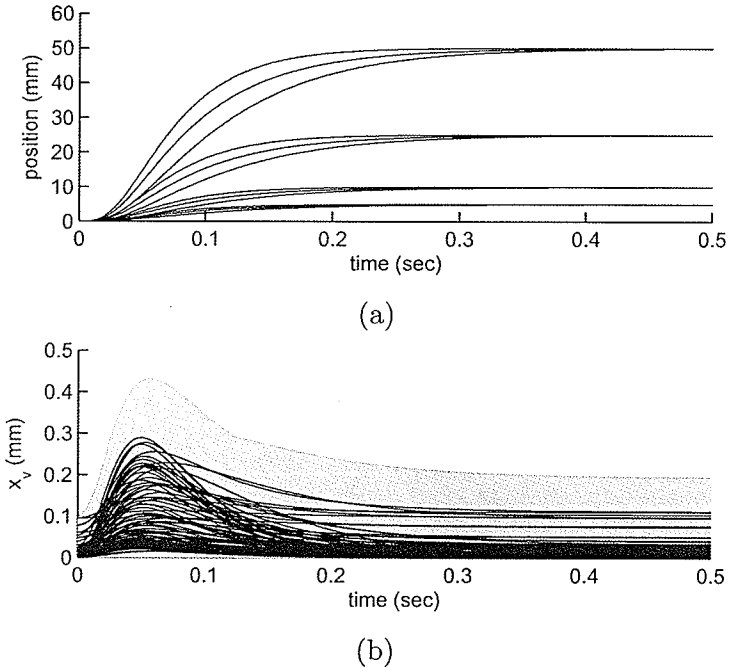

Figure 4.21: Time histories of acceptable plant input-output responses in presence of internal leakage fault: (a) acceptable position responses (output); (b) envelope (shaded area) and typical examples of valve spool displacements (input).

Figure 4.21b, shows the envelope (shaded area) and several examples of the valve spool displacements obtained from the inverse simulations. In all, about 21,000 different plant cases were evaluated. Referring to Figure 4.21b, it is seen that in order to compensate for the internal leakage fault, the acceptable plant input set now requires many signals to be non-zero in the steady-state. It is also observed that the peak value of the valve spool displacement envelope is $x_v = 0.43$ mm, which is larger than the saturation value of $x_{vm} = 0.28$ mm. Therefore, in the presence of the leakage fault, some plants in the uncertain set will require more capacity than the plant can deliver. Operation of the fault tolerant controller may be restricted in these cases. The total number of plants whose input signals would saturate the valve is, however, limited to about 5% of the total plant cases considered.

The envelope (shaded area) of the set of frequency response ratios, $\frac{\hat{X}_p(j\omega)}{\hat{X}_v(j\omega)}$, for operation of the hydraulic actuator in the presence of the internal leakage fault is shown in Figure 4.22. Some typical examples of the frequency response curves are also included for reference. A comparison of Figure 4.22 with Figure 4.5 clearly shows the effects of the leakage fault on the hydraulic actuator frequency response. In the low frequency range, $\omega < 10$ rad/sec, the actuator magnitude responses indicate that the internal leakage fault removes the integrating characteristic of the ram and causes a change in system type from 1 to 0. At frequencies above 10 rad/sec, the internal leakage fault greatly increases the damping of the hydraulic resonance, as evidenced by the curves pertaining to the actuator phase lag. The deviation in the actuator phase lag from the expected value of $-270°$ in the high frequency range $\omega > 3000$ rad/sec is a result of numerical artifacts arising during the Fourier transformation of some of the input-output signal pairs.

Some templates of the identified equivalent plant set $\mathcal{P}_e$, which now considers the effects of the internal leakage fault, are illustrated side-by-side in Figure 4.23. The template points were computed by multiplying ratios $\frac{\hat{X}_p(j\omega)}{\hat{X}_v(j\omega)}$ with the frequency response of the servovalve at the selected frequencies. For comparison, the template

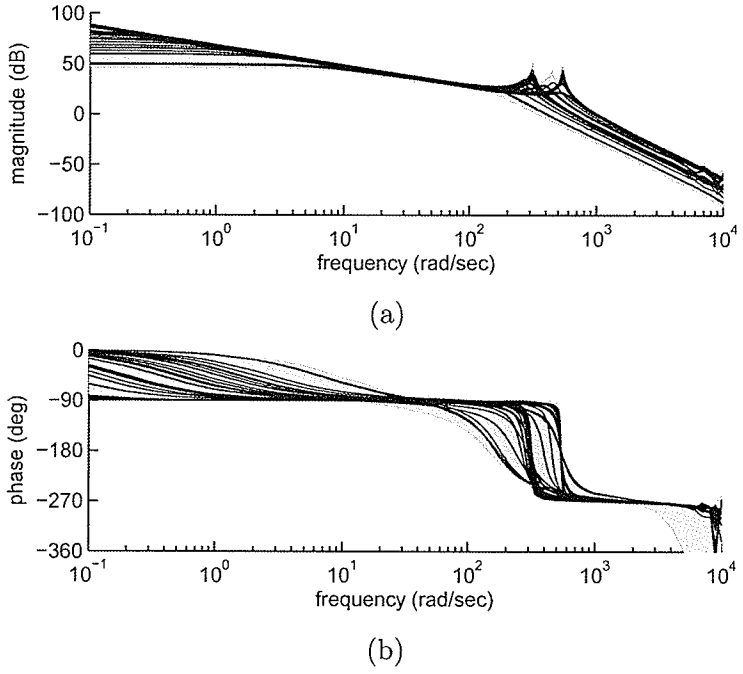

Figure 4.22: Envelope (shaded area) and examples of computed frequency response ratios, $\frac{\hat{X}_p(j\omega)}{\hat{X}_v(j\omega)}$, in presence of internal leakage fault.

boundaries of Figure 4.23 are shown along with the boundaries of the templates corresponding to normal actuator operation (shaded) in Figure 4.24.

The overall sizes of the templates have increased considerably, to account for the effects of the internal leakage fault on the dynamics of the actuator. It seems surprising, therefore, that benchmark control system B was able to do a reasonable job of maintaining the performance of the actuator in the presence of the internal leakage fault. However, as was shown, benchmark control system B is inherently conservative and the controller can, by chance, accommodate some of the uncertainty associated with the enlarged templates. Nonetheless, in order to properly compensate for the dynamic uncertainties associated with the fault, changes in the shapes of the QFT bounds and in the gains of the controller are expected.

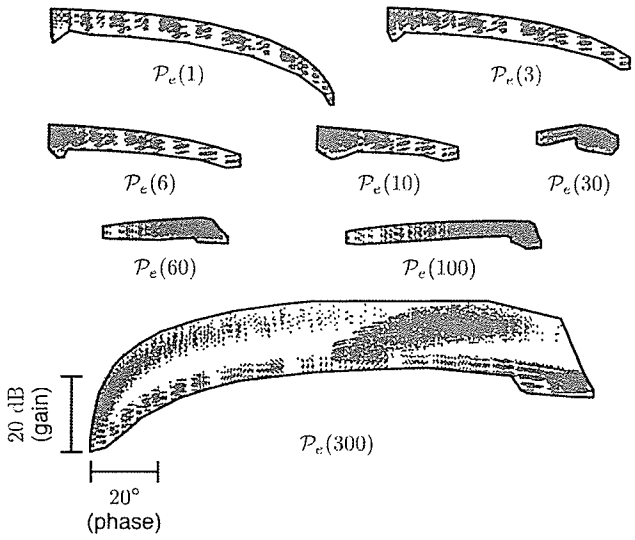

Figure 4.23: Templates of equivalent time invariant plant set, $\mathcal{P}_e$, in presence of internal leakage fault at selected frequencies, ω (rad/sec).

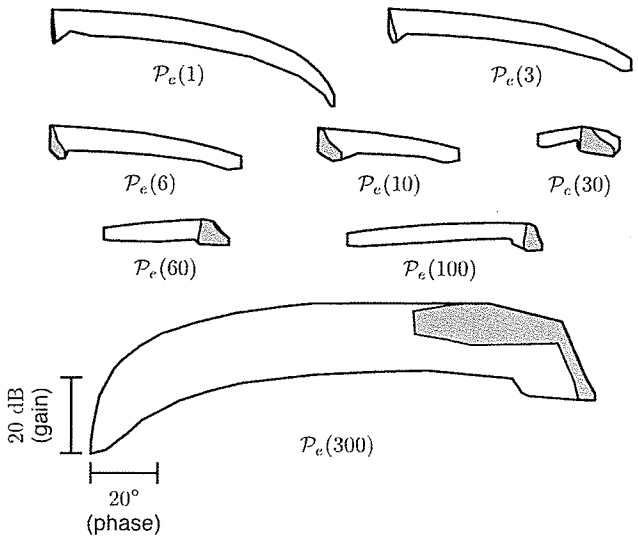

Figure 4.24: Comparison of plant template boundaries for normal operation of hydraulic actuator (shaded) and operation in presence of internal leakage fault.

Step 2: Nominal Loop Shaping a Prefilter Design

Several QFT bounds for design of the fault tolerant controller that correspond to the same closed-loop specifications used to synthesize the benchmark control laws are shown in Figure 4.25. The nominal loop transmission of each benchmark control system designed in section 4.2 is also shown, for reference. A number of changes in the QFT bounds, as compared to the bounds for normal operation (see Figure 4.9a), are apparent. First, the troughs in the low frequency bounds, $\mathcal{B}(0.1)$ through $\mathcal{B}(2)$, which were observed before around $-90°$ are now located at approximately $-180°$ on the Nichols chart. This indicates that the loop transmission which minimizes the controller gain will need to have a phase lag of 180° in the low-frequency range. The QFT bounds therefore dictate that the controller should contain an integrator. The second major difference in the QFT bounds for normal and fault tolerant operation is seen in the stability bounds $\mathcal{B}(20)$ through $\mathcal{B}(100)$. The large increase in the damping

of the hydraulic actuator resonance decreases the phase margin. Therefore, stability bounds $\mathcal{B}(20)$ through $\mathcal{B}(100)$ now extend much further to the right on the Nichols chart.

Due to the changes in the shapes of the QFT bounds, it is evident that neither benchmark loop transmission can properly solve the fault tolerant control problem. In particular, the benchmark control laws are observed to violate all of the bounds for $\omega < 10$. Thus, the specified sensitivity tolerances cannot be guaranteed in the presence of the internal leakage fault. However, the bound violations using benchmark control law B are less severe, which confirms quantitatively that benchmark controller B '*almost solves the fault tolerant control problem*'. Figure 4.25 also shows that the QFT bounds for fault tolerant control are satisfied for $\omega \geq 20$ using either benchmark control law. Therefore, the robust stability margins of the benchmark control systems are not impacted by the internal leakage fault.

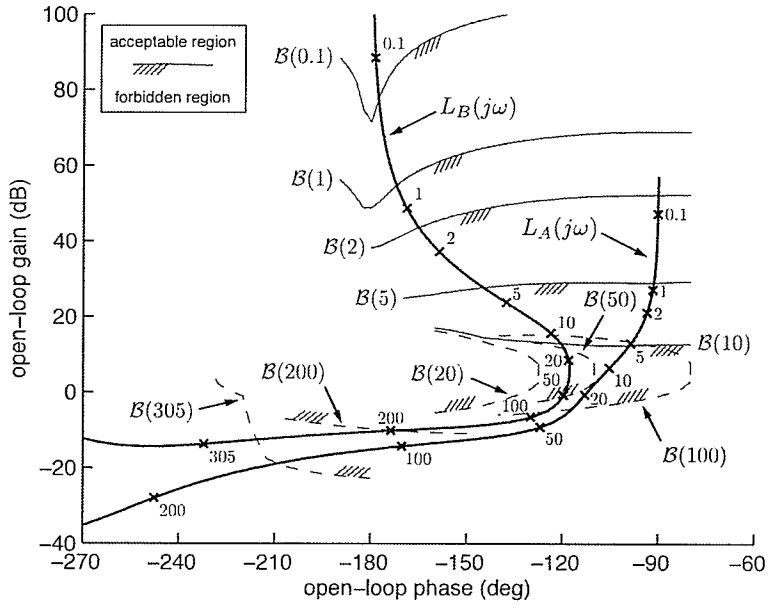

Figure 4.25: QFT bounds, $\mathcal{B}(\omega)$, for fault tolerant control. Benchmark loop transmissions shown for reference.

Two candidate loop transmissions for solution of the fault tolerant control design problem are shown in Figure 4.26. One approach to design the fault tolerant controller is to guide the loop transmission to the right of $\mathcal{B}(20)$ and underneath the more severe stability bounds, $\mathcal{B}(50)$ and $\mathcal{B}(100)$. This approach would minimize the amount of phase lead that must be provided by the controller and avoids the need for excessive controller gain in the high frequencies. Loop transmission $L_a(j\omega)$ represents an attempt made to meet this objective. However, due to the amount of integral gain required to satisfy tracking bounds $\mathcal{B}(0.1)$ through $\mathcal{B}(10)$, it was found to be extremely difficult to shape $L_a(j\omega)$ to satisfy $\mathcal{B}(20)$ and at the same time keep $L_a(j\omega)$ below $\mathcal{B}(50)$ and $\mathcal{B}(100)$. Bounds $\mathcal{B}(50)$ and $\mathcal{B}(100)$ are clearly violated by the design. Part of the reason for this difficulty is the Bode gain/phase relationship [89], which sets the maximum slope of $L(j\omega)$ on the Nichols chart. Because of the Bode gain/phase relationship, the introduction of phase lead to satisfy $\mathcal{B}(20)$ automatically reduces the gain margin and causes $\mathcal{B}(50)$ and $\mathcal{B}(100)$ to become violated.

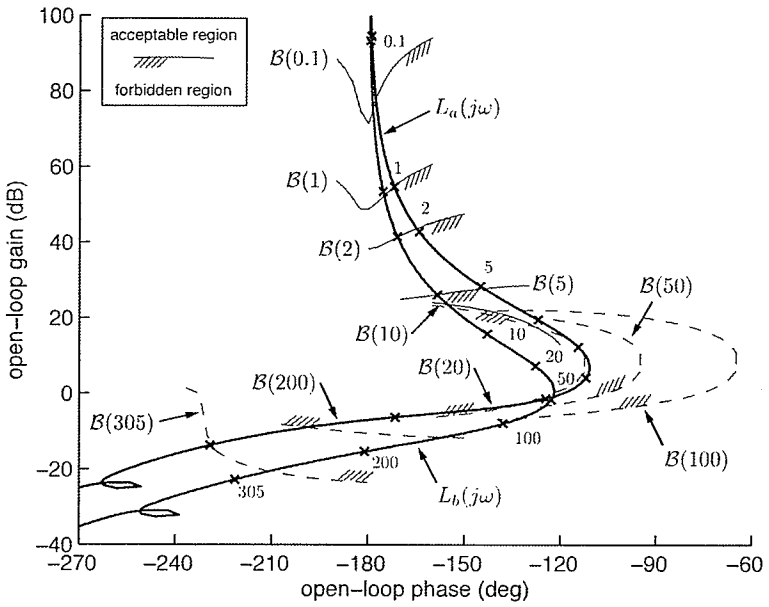

Figure 4.26: Two candidate loop transmissions illustrating tradeoff in achievable gain and phase margins.

Conversely, $\mathcal{B}(50)$ and $\mathcal{B}(100)$ can be satisfied by increasing the gain margin through a reduction in the gain of the controller in the mid-frequency band (see $L_b(j\omega)$ in Figure 4.26). However, doing so automatically impairs the phase margin and causes $\mathcal{B}(10)$ and $\mathcal{B}(20)$ to become violated. This tradeoff in achievable gain and phase margins represents a dilemma in shaping the gain and phase of $L(j\omega)$ whereby the frequency-domain specifications imposed by the combination of prescribed time-domain requirements and plant uncertainties cannot be easily satisfied by a linear control law. The use of a nonlinear controller, which is not bound by the Bode gain/phase relationship, may be the only way to achieve the desired closed-loop performance with a fixed-gain structure [115]. However, development of such a nonlinear control law is a nontrivial task and is outside the scope of this thesis.

Shaping the fault tolerant loop transmission to satisfy all the QFT bounds associated with the original design specifications is difficult, if not impossible, to accomplish. Therefore, the specification on closed-loop stability was relaxed so that the original tolerances on the closed-loop tracking performance could still be realized. The revised closed-loop stability specification is

$$\left|\frac{GP_e}{1+GP_e}\right| \leq 2.9 \text{ dB} \quad \forall P_e \in \mathcal{P}_e \tag{4.15}$$

which gives a 4.7 dB gain margin and a 40° phase margin[1]. The prefilter can be used to compensate the increase in overshoot resulting from the change in the closed-loop stability tolerance.

Figure 4.27 shows the re-computed QFT bounds and the finalized fault tolerant loop transmission. As can be seen, relaxing the closed-loop stability specification enables the loop transmission can be shaped to satisfy all of the QFT bounds. The overall heights of the mid-frequency stability bounds have been reduced by revised specification (4.15). It is now possible to place $L(50)$ and $L(100)$ below $\mathcal{B}(50)$ and

[1]The original specification set 5.4 dB/52° margins.

$\mathcal{B}(100)$ as required so that the prescribed gain margin can be robustly achieved by the design. The final loop transmission was shaped by re-tuning the elements of benchmark controller B to properly position the uncertainty templates on the Nichols chart. This included increasing the integral gain and relocating the controller zero from $s = -4.7$ to $s = -12$. As before, a complex pole was used to reposition the resonance peaks further to the region of low sensitivity on the inverted Nichols chart as shown in Figure 4.27b. The lag filter of controller B was not needed and was deleted. The fault tolerant controller, $G_{FTC}(s)$, has the following transfer function:

$$G_{FTC}(s) = \frac{3.18 \times 10^7 (s + 12)}{s(s^2 + 225s + 250^2)} \tag{4.16}$$

The prefilter that completes the design of the fault tolerant control system is

$$F_{FTC}(s) = \frac{22(s + 13.5)}{(s + 8.5)(s + 35)} \tag{4.17}$$

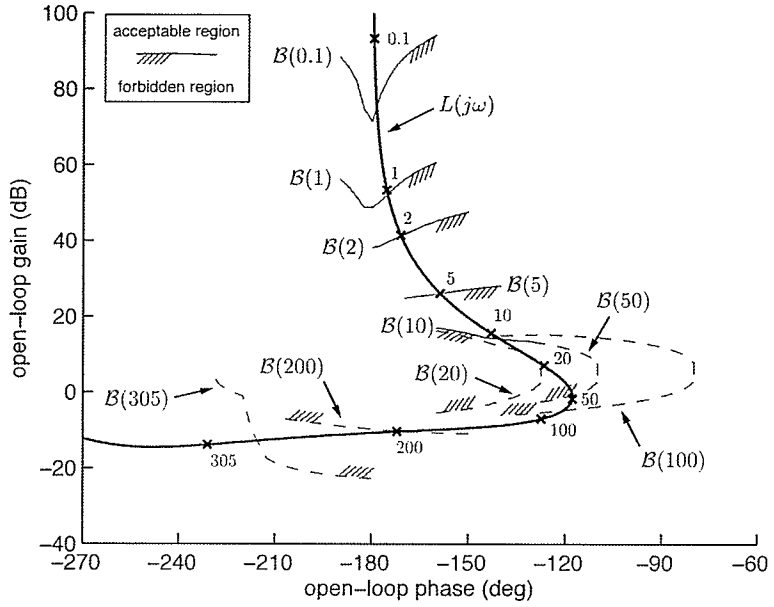

(a)

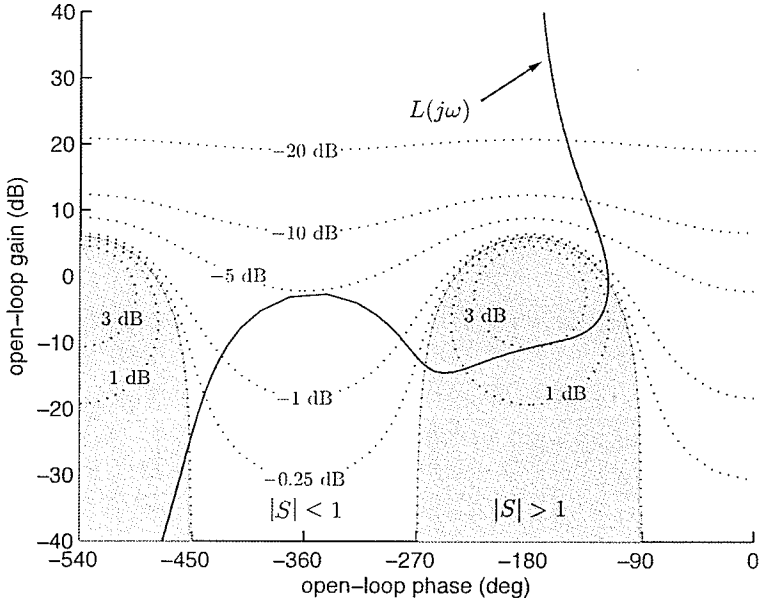

(b)

Figure 4.27: QFT bounds, $\mathcal{B}(\omega)$, with relaxed stability margins and the designed nominal fault tolerant loop transmission: (a) loop shape that satisfies the QFT bounds; (b) loop transmission on inverted Nichols chart.

Step 3: Controller Verification

The envelopes (shaded areas) of the closed-loop frequency responses, $\left|\frac{G\mathcal{P}_e}{1+G\mathcal{P}_e}\right|$, and of the closed-loop tracking responses, $\left|F\frac{G\mathcal{P}_e}{1+G\mathcal{P}_e}\right|$, are shown for the fault tolerant control system in Figure 4.28. Typical example curves are also included for several plants from set $\mathcal{P}_e$. The plots show clearly that none of the magnitude peaks in $\left|\frac{G\mathcal{P}_e}{1+G\mathcal{P}_e}\right|$ exceed the 2.9 dB design specification and that all of the transfer functions $\left|F\frac{G\mathcal{P}_e}{1+G\mathcal{P}_e}\right|$ lie within the prescribed lower and upper tracking bounds.

The time domain performance of the fault tolerant control system, under normal operation, is demonstrated in Figure 4.29 for several hundred plant cases. The results were obtained from the nonlinear simulation model of the hydraulic actuator using extreme combinations of the uncertain system parameters (see Table 4.1). Step commands ranging from 5 to 50 mm were considered for each combination of uncertain parameters. As shown in Figure 4.29a the normalized position responses generally fall within the acceptable response envelope. The overshoots of a small number of step responses slightly exceed the maximum acceptable value. This is the result of saturation of the servovalve input which occurred for some plant cases.

A second set of nonlinear simulations was carried out to evaluate the performance of the fault tolerant control system in the presence of the internal leakage fault. Typical position responses, for 20 mm step commands, are shown in Figure 4.30 for normal operation and for the case where the internal leakage coefficient is set to the maximum value of $K_{12} = 5.83 \times 10^{-8}$ m$^3/\sqrt{\text{Pa}}$·sec. Comparing Figures 4.30a and 4.30b, it is seen that the internal leakage fault causes only small changes in the individual actuator step response curves. Moreover, the designed fault tolerant controller can maintain all of the closed-loop step responses inside the acceptable response envelope, despite the occurrence of the fault.

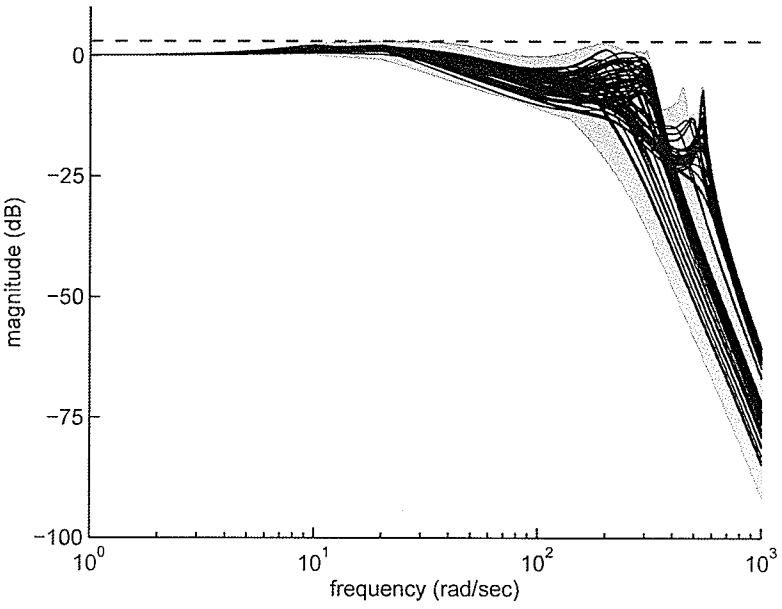

(a)

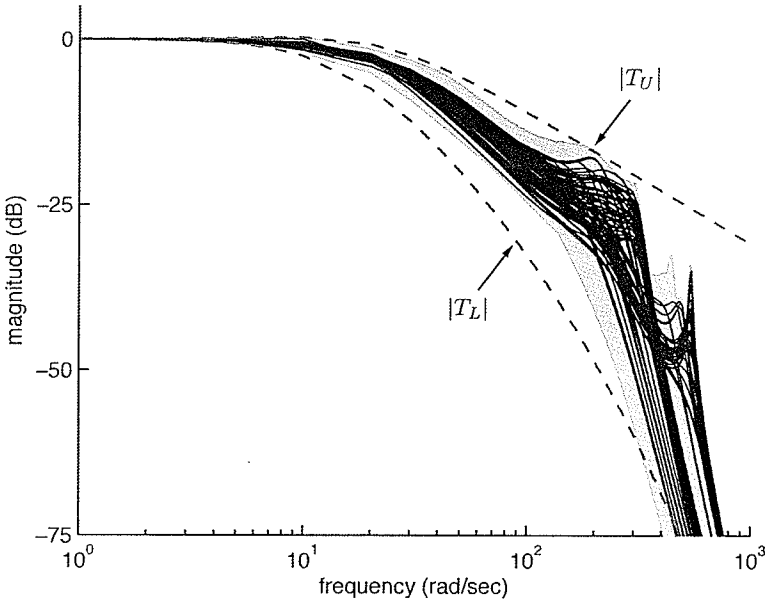

(b)

Figure 4.28: Envelope (shaded area) and examples of closed-loop frequency responses using fault tolerant controller over extreme range of parameter uncertainty: (a) magnitudes of $\frac{GP_e}{1+GP_e}$; (b) magnitudes of $F\frac{GP_e}{1+GP_e}$. Dashed lines indicate design specifications.

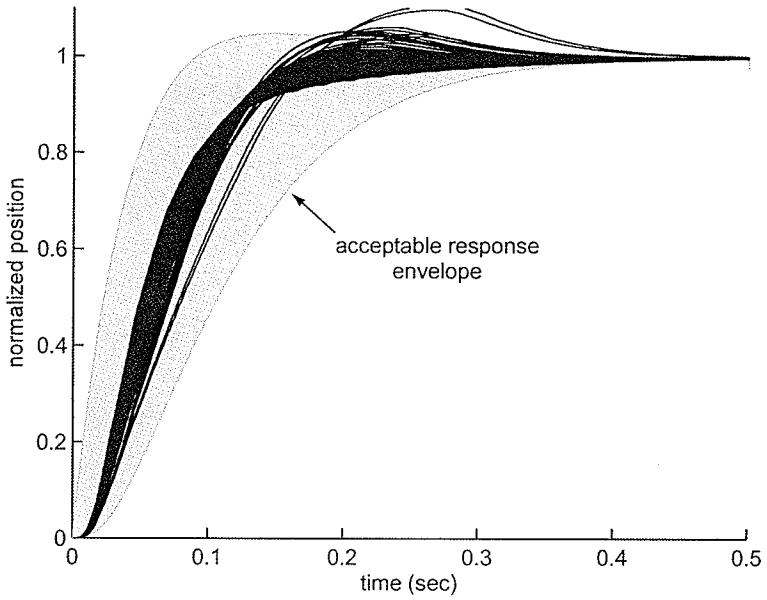

(a)

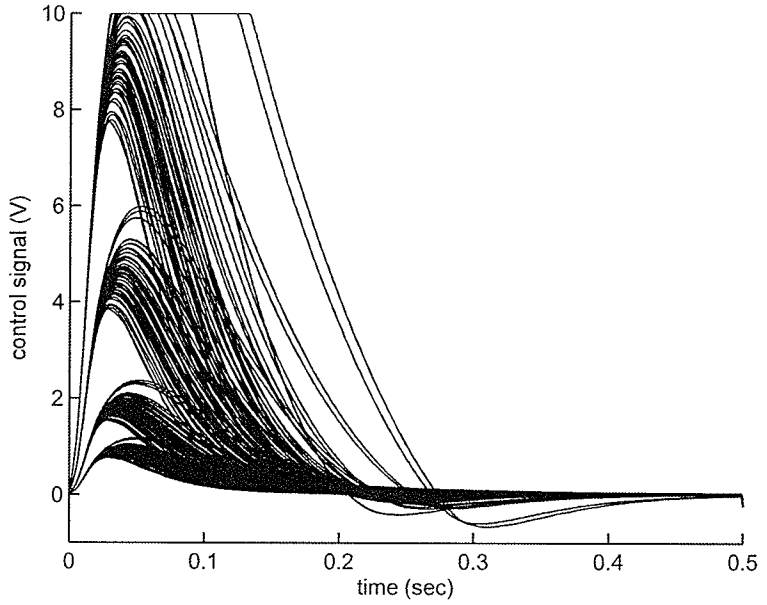

(b)

Figure 4.29: Representative normalized closed-loop step responses for fault tolerant control system under normal operation (nonlinear simulations): (a) normalized positions; (b) control signals.

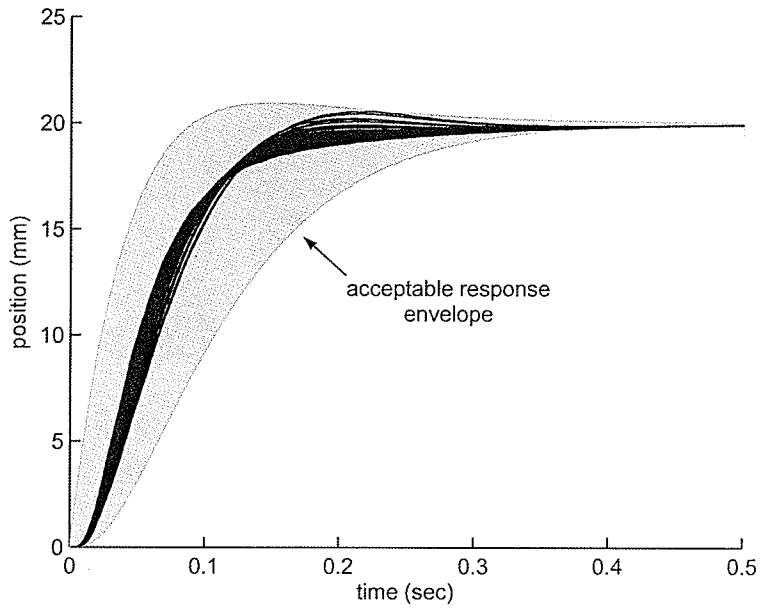

(a)

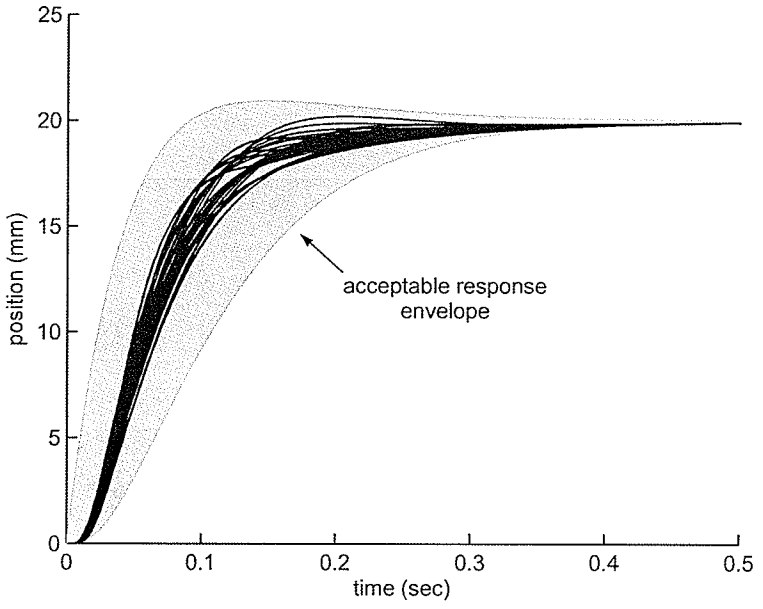

(b)

Figure 4.30: Closed-loop responses to 20 mm step command for extreme combinations of the uncertain system parameters (nonlinear simulations): (a) normal operation; (b) operation in presence of internal leakage fault with $K_{12} = 5.83 \times 10^{-8}$ m$^3/\sqrt{\text{Pa}}$·sec.

4.3.2 Experimental Results

The experimental performance of the fault tolerant control law was tested first, for normal operation of the actuator. Typical experimental step responses, obtained by operating the ram against a 30 kN/m spring, are shown in Figure 4.31. As predicted by the nonlinear simulations (see Figure 4.29), the experimental step responses are contained entirely within the prescribed bounds. The robustness of the fault tolerant controller against changes in the stiffness of the load is demonstrated by Figure 4.32. Very little difference is observed between the position response curves when the actuator operated without any applied load or against the 30 kN/m and 80 kN/m environments.

Figure 4.33 illustrates the experimental performance of the fault tolerant control system for various levels of the internal leakage fault and for different step input commands. With reference to Figure 4.33a it is seen that the fault tolerant controller can accurately keep actuator position responses within the acceptable envelope, despite internal fluid leakage rates ranging from 0 (normal operation) to 5.5 L/min in magnitude. The experimental results confirm that by considering the effects of the leakage fault at the control design stage, the positioning system can be designed to maintain tight control over the position response in the presence of the internal leakage fault.

The experimental performance of the fault tolerant controller is further demonstrated in Figure 4.34, which reports the results of a 20 mm square wave test. During the experiment, the needle valve that is used to control the flow of fluid between the actuator chambers was slowly opened to simulate an operating condition where the severity of the leakage increases progressively over time. Referring to Figure 4.34a, it is difficult to see any difference in the position response of the actuator as the internal leakage rate continues to increase. The fault tolerant controller does a good job of maintaining the performance of the experimental actuator by continuously adjusting the controller output, shown in Figure 4.34b, to properly compensate for the loss of hydraulic fluid across the actuator piston.

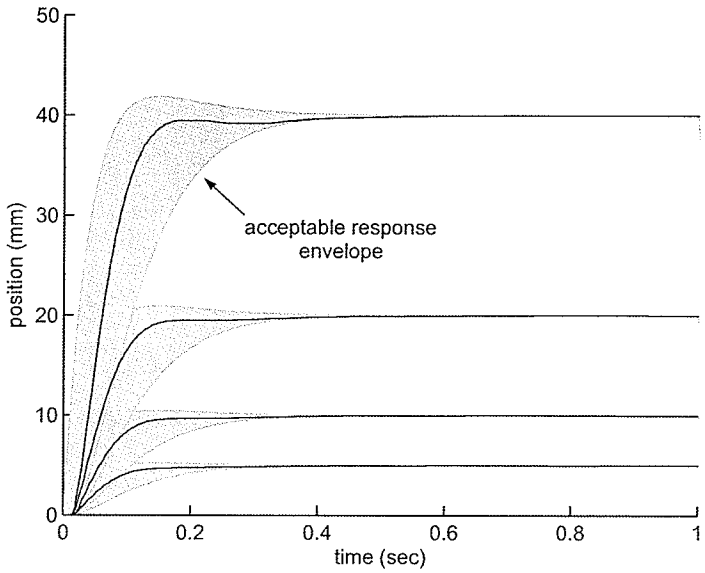

(a)

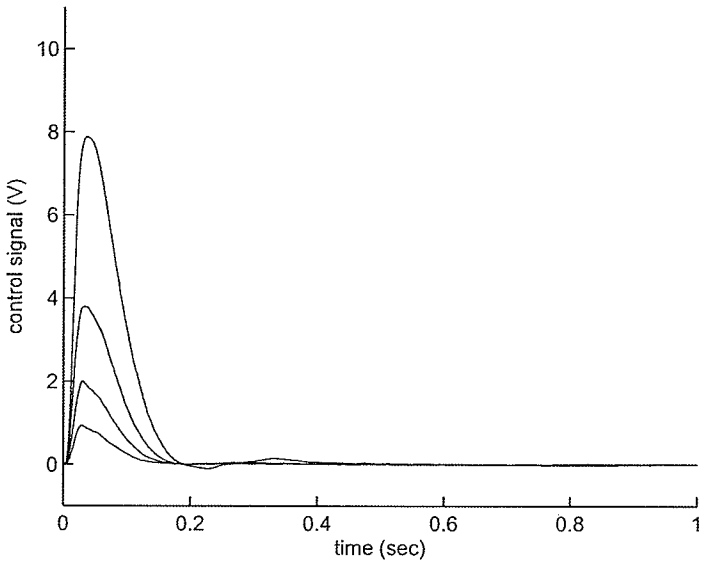

(b)

Figure 4.31: Experimental step responses against a 30 kN/m spring using fault tolerant controller under normal operation: (a) actuator position; (b) control signal.

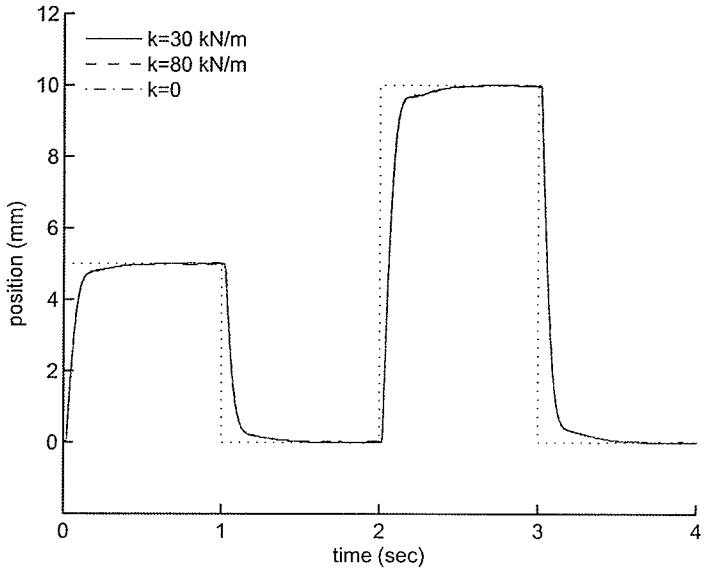

(a)

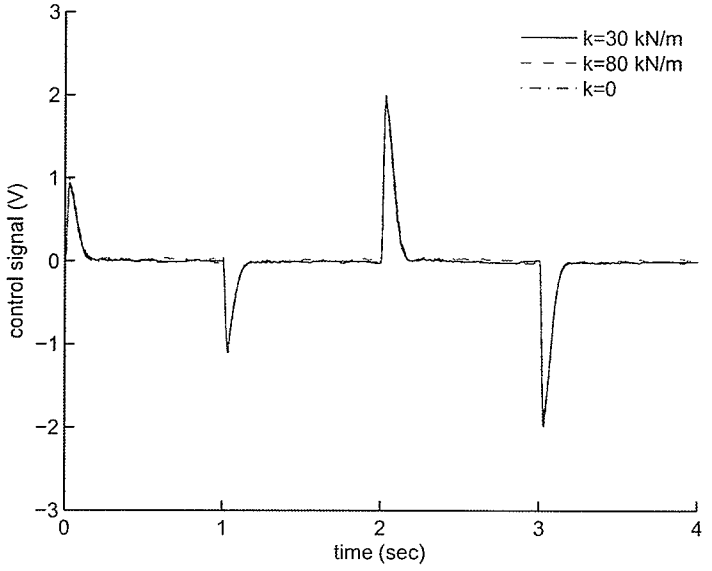

(b)

Figure 4.32: Experimental step responses with different environment stiffnesses using fault tolerant controller under normal operation: (a) actuator position; (b) control signal.

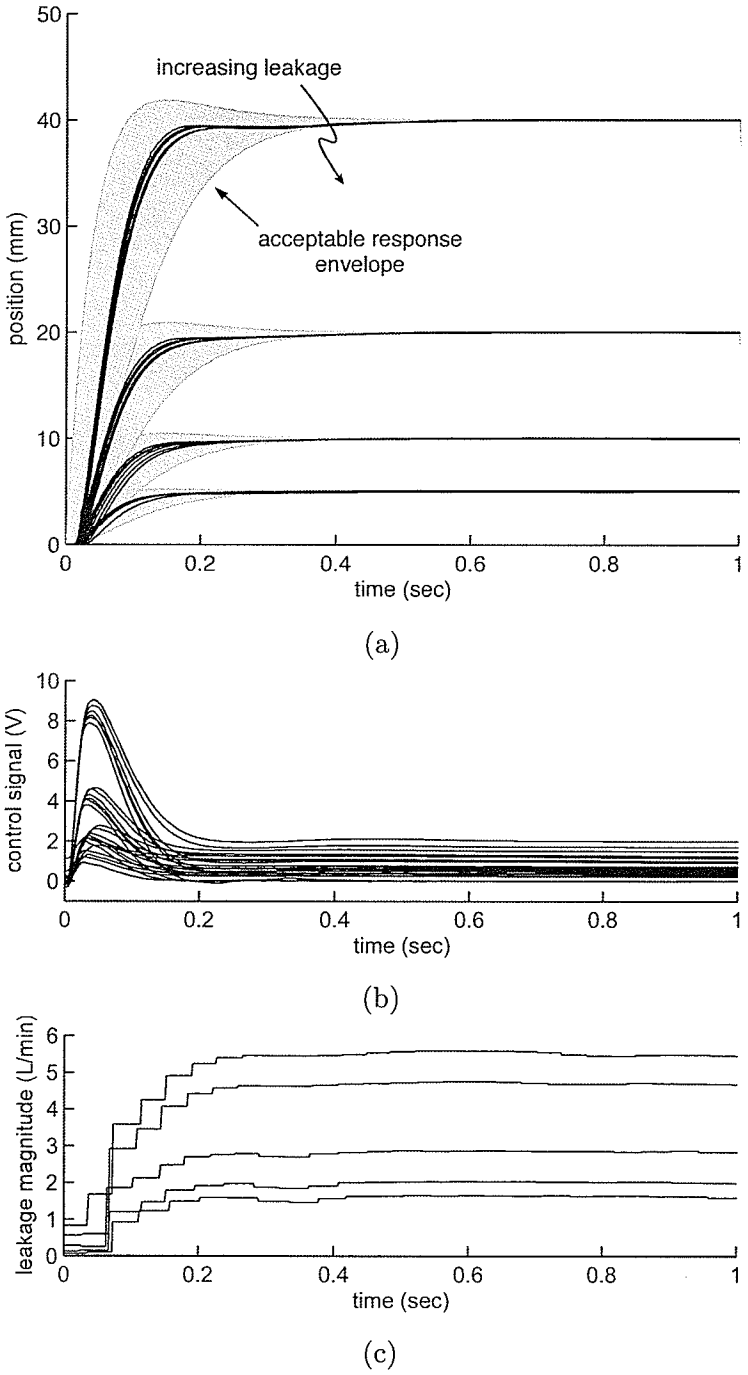

Figure 4.33: Experimental step responses against a 30 kN/m spring using fault tolerant controller in presence of internal leakage fault: (a) actuator position; (b) control signal; (c) typical internal leakage magnitudes corresponding to 40 mm step responses.

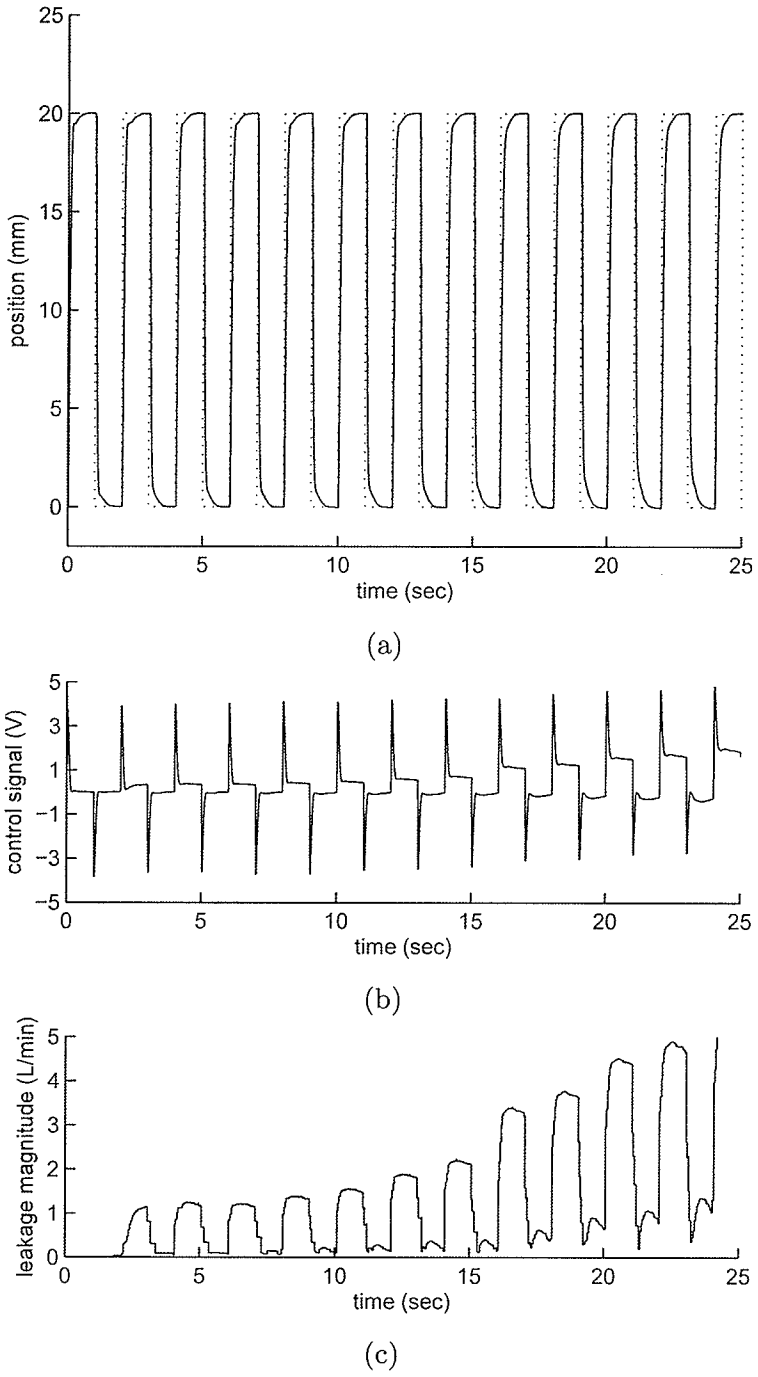

Figure 4.34: Experimental step responses against a 30 kN/m spring using fault tolerant controller in presence of slowly increasing internal leakage fault: (a) actuator position; (b) control signal; (c) internal leakage magnitude.

4.4 Summary

This chapter presented the development of a fixed-gain, fault tolerant, QFT control law for a hydraulic actuator that can compensate the effects of actuator internal leakage and at the same time accommodate typical system uncertainties. A benchmark control system, which considers only the normal operation of the hydraulic actuator, was designed first. Two different control structures could be used to solve the benchmark control problem. It was shown that the preferred control structure, in terms of minimizing the controller gain, is a non-integrating proportional type. A higher-gain integrating controller was designed and used as a basis for developing the fault tolerant controller. Despite a small, but necessary, tradeoff in the closed-loop stability specification, it was possible to synthesize a fixed-gain control law that can properly compensate for the effects of the internal leakage fault. Experiments demonstrated the improved performance of the fault tolerant control law, as compared to the low-gain benchmark design.

Chapter 5

Hardware-in-the-Loop Flight Simulator

This chapter describes a distributed hardware-in-the-loop (HIL) flight simulation framework that has been developed to allow the fault emulator actuator, operating as a flight control actuator, to be exercised against the numerical simulation of a modern high-performance jet aircraft. In the HIL simulation, a secondary loading actuator is used to recreate a wide range of in-flight operating conditions by replicating the aerodynamic load disturbance that is transmitted through the control surface hinge. Thus, the HIL flight simulator enables the performance of the fault tolerant QFT control system to be objectively tested under operating conditions that more closely resemble the intended application. An overview of the HIL simulation architecture, the implemented flight model, and some of the details related to the design of a robust force control system for the loading actuator are presented. The overall functionality of the HIL flight simulator is demonstrated by the results of several HIL simulation examples.

5.1 Simulator Architecture

Overview

A photograph of the HIL test facility and an overview of the HIL simulator architecture are shown in Figure 5.1. In the simulation shown, the experimental flight actuator (fault emulator ram) is being used to position the left horizontal tail half. The loading actuator is used to apply the aerodynamic disturbing load that arises due to the motions of the left tail half and of the aircraft. The remainder of the flight simulation, including the simulation of the remaining flight control actuators, is carried out in software. The entire HIL simulation is run on four desktop computers that have been networked together using a low-cost broadband router. This distributes the demanding computational load amongst a number of processors and allows real-time operation of the simulator to be realized.

Referring to Figure 5.1b, the first desktop computer (`PC1`) executes the numerical simulation model of the aircraft. This computer functions as a master processor and, in addition to performing integration of the aircraft dynamic equations, handles all human-computer interfacing. `PC1` also provides the commands that drive the remaining processors over ethernet. The software running on `PC1` has been implemented in a modular format and consists of the following main routines:

1. `hid()` - Human-interface routine that reads pilot commands from the joystick/keyboard or from a prepared data file.
2. `fcs()` - Implementation of realistic gain scheduled longitudinal, lateral and directional flight control laws.
3. `aerodyn()` - Nonlinear 6 degree of freedom model of the aircraft dynamics.
4. `cs-hydraulics()` - Nonlinear model for each hydraulically driven control surface.
5. `cs-loads()` - Nonlinear model of control surface aerodynamic disturbing forces.

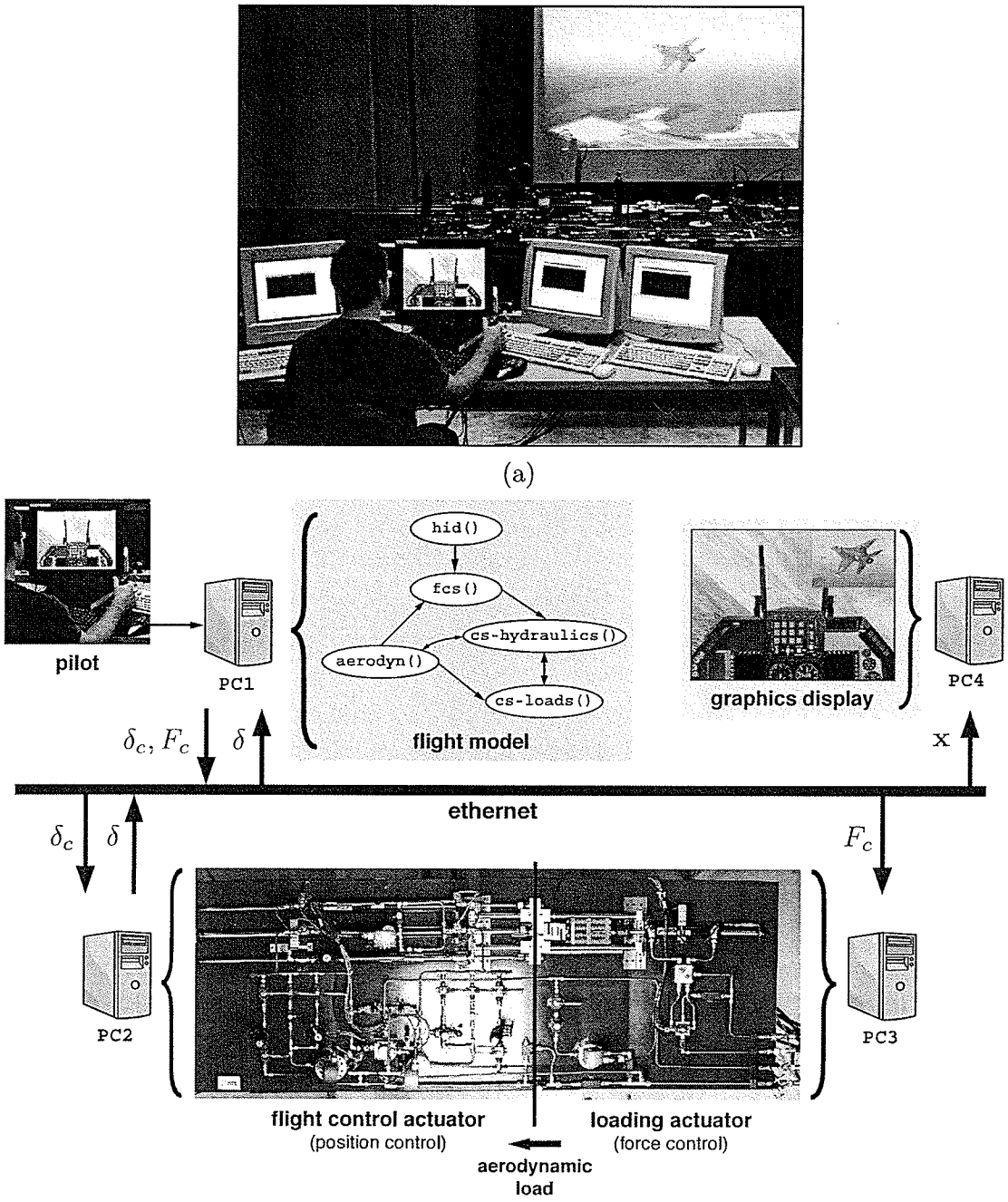

Figure 5.1: Hardware-in-the-loop flight simulator: (a) photograph of experimental facility; (b) schematic of simulator architecture illustrating UDP transmission of control data over ethernet. Legend: δ_c - commanded control surface deflection; δ - actual control surface deflection; F_c - commanded aerodynamic load; $\mathbf{x}$ - vector of aircraft states.

The listed software routines were coded in C++ using object oriented principles. Each routine can be compiled as a separate library to facilitate straightforward modification of the flight control laws, flight actuator models, and aerodynamic database. Thus, simulation of different flight controls or different aircraft types can be easily accommodated. The transmission of aircraft state, control and auxiliary data amongst the various software routines is indicated by the solid arrows within the flight model block.

The remaining desktop computers serve as slave processors. PC2 is used to control the experimental flight control actuator hardware via the software coded control law. The commanded deflection, δ_c, of the hardware emulated flight actuator is computed by routine `fcs()` on PC1 and is wrapped in a user datagram protocol (UDP) packet for transmission to PC2 over ethernet as indicated in Figure 5.1b. The deflection command is implemented by PC2 and the measured actuator displacement, δ, is communicated back to PC1, via a UDP packet, for use in updating the simulated aircraft states. UDP was selected for use since it is a quick, low-level protocol [116]. However, UDP does not guarantee the integrity of the received data, nor does the protocol ensure that individual packets will be received in order. Therefore, simple error-checking routines were implemented in the control software and out of order packets are discarded automatically since old data can be ignored if newer data has already been received. The loading actuator, which interacts with the flight actuator to impose the aerodynamic disturbing load, is controlled by PC3. The force commands, F_c, are computed from the flight model running on PC1 and are transmitted to PC3 over ethernet in the same way as the flight actuator deflection commands are communicated to PC2.

The final processor, PC4, is used to run a graphics engine to render the aircraft motion. The graphical visualization is necessary to provide the motion cues required for human-in-the-loop simulations. A graphical rendering is also useful to illustrate how aircraft motion changes in response to modifications of the flight control system,

or faults in the experimental flight actuator.

The particular graphics engine selected for use in the HIL simulation environment is the multi-platform open-source FlightGear package [117]. FlightGear is aimed at providing a basic simulator framework upon which other projects can be built for use in academic research [118]. In addition to providing several integrated flight dynamics models, FlightGear also allows externally developed flight dynamics models to drive the graphics engine via a network socket link. This functionality was used to interface the implemented flight simulation model to FlightGear. To update the graphics display, a vector, $\mathbf{x}$, of aircraft states (e.g. angle of attack, sideslip angle, roll, pitch and yaw angles) is transmitted periodically via UDP from `PC1` to the FlightGear rendering engine running on `PC4`.

Hydraulic Test Bench Setup

To properly reproduce in-flight control surface actuator operating conditions, three load effects need to be considered: the inertial effect caused by the mass of the control surface, the compliance of the actuator structural mounts in series with the stiffness of the actuator rods and the hydraulic oil in the cylinder, and the external load resulting from the control surface aerodynamics [119]. The inertial effect can be reproduced experimentally by operating the flight actuator against a mass, and the effects of structural compliance can be included by designing an appropriate actuator anchorage. In the HIL simulation environment, the actuator anchorage and linkage between the actuator and the flight control surface are, however, considered to be rigid. This assumption is reasonable since the natural frequency of a well designed hinge system is generally much greater than the bandwidth of the flight actuator [56]. Thus, the primary role of the loading actuator is to reproduce, as closely as possible, the external forces that are applied on the flight actuator as a result of the control surface aerodynamics.

To accomplish this goal, the hydraulic test bench has been configured as shown in Figure 5.2. Since the experimental actuators are rigidly mounted to the hydraulic test bench, the connection between the fault emulator and loading actuators is made using a flexible coupling (see Figure 5.2), which acts as nearly a pure stiffness. As discussed previously in chapter 2, reducing the stiffness of the joint between the two actuators lowers the gain of the force control loop that is implemented around the loading actuator. The resulting stabilizing effect simplifies the design of the force controller at the cost of a slight reduction in the achievable large force bandwidth of the actuator [82]. Thus, the joint stiffness was carefully selected to ensure that the external control surface aerodynamic load force can be properly replicated using the experimental hardware.

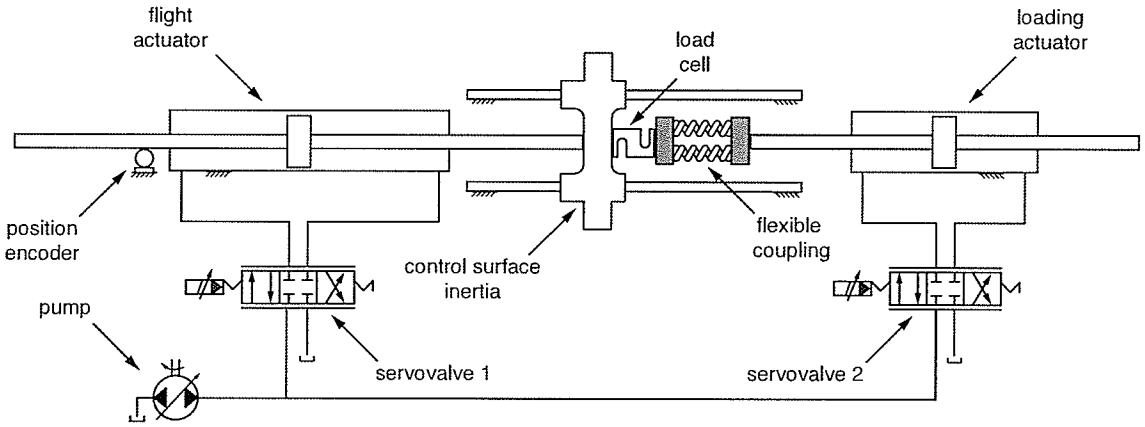

Figure 5.2: Hydraulic test bench configuration for HIL simulation.

Hydraulic Actuator Control Architecture

A block diagram of the control system architecture implemented around each hydraulic actuator is shown in Figure 5.3. The stiffness of the connection between the two rams is denoted by gain block, k_c. Controller, $G_P(s)$, and prefilter, $F_P(s)$, refer to the transfer functions of one of the QFT control systems developed in chapter 4.

However, any control law can be implemented to position the flight actuator. A two degree of freedom unity feedback control structure was also chosen to close the force loop around the loading actuator. Details related to the design of force controller, $G_F(s)$, and prefilter, $F_F(s)$, are given in section 5.3. Referring to Figure 5.3, the force control loop was also outfitted with a feedforward filter, $F_X(s)$, that generates an additional command signal. Using filter $F_X(s)$ improves the ability of the force control system to react to sudden changes in the measured force caused by the motion of the flight actuator.

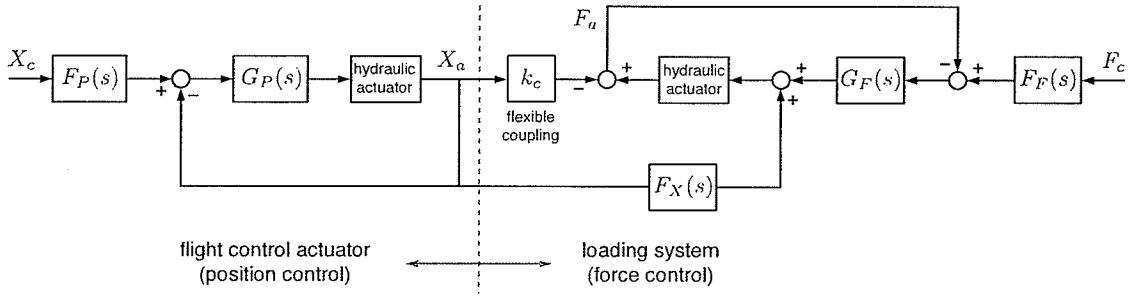

Figure 5.3: Block diagram of experimental hydraulic actuator control system implementation.

5.2 Description of Flight Model

The aerodynamic model implemented in the HIL simulation environment is based primarily upon the detailed nonlinear model of the F16 jet aircraft presented in [120]. To properly interface the aerodynamic model to the FlightGear graphics engine, the rotating oblate spherical earth model derived in [121] was considered to formulate the aircraft equations of motion. The equations of motion are referenced to the aircraft body axes system shown in Figure 5.4. To allow for continuity of the attitude motions, the angular orientations are determined using quarterions. A realistic gain scheduled full-envelope flight control system, detailed in [120], was implemented to

drive the aircraft flight actuators. The controlled flight variables are the aircraft normal acceleration and the body axis roll and yaw rates. The implemented flight control system also incorporates features typical to high-performance aircraft such as an angle of attack limiter on the commandable normal acceleration, a departure/spin prevention system and an aileron-rudder interconnect. A fixed-gain angle of attack controller, developed previously in [122], has also been implemented in the longitudinal channel. The influences of the engine power level as well as the momentum of the engine turbine have also been considered in the simulation model.

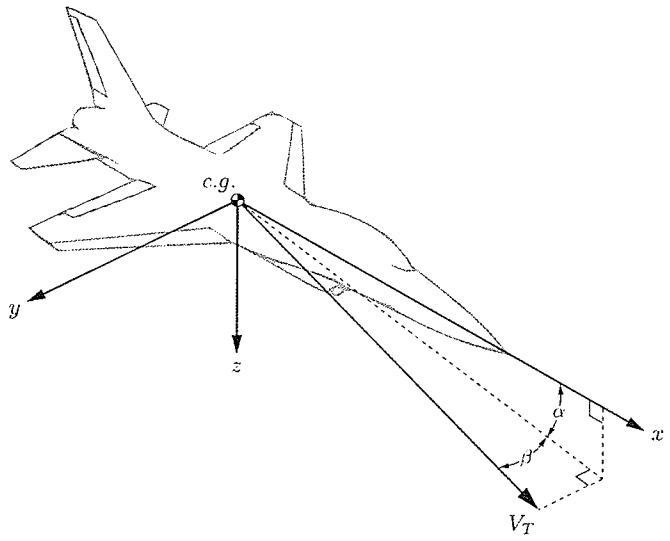

Figure 5.4: Aircraft body coordinate system, with origin at aircraft center of gravity, *c.g.*, and definition of angle of attack, α, and sideslip angle, β, with respect to aircraft velocity vector, V_T.

In the aircraft simulation model, the motion of the airplane is driven by the forces and moments acting at the center of gravity and aligned with the vehicle body axes. The forces are used to compute accelerations, which are numerically integrated using predictive and modified trapezoidal quadratures to obtain the velocity and position responses of the aircraft. The forces and moments acting at the center of gravity are defined in terms of a series of dimensionless aerodynamic coefficients that are

calculated, at each integration time step, by a *component buildup* scheme [74]. The particular values of the aerodynamic coefficients are highly nonlinear and depend primarily upon the aircraft angle of attack, α, sideslip angle, β (see Figure 5.4), and the deflections of the control surfaces. Readers are referred to [120] for details on the component buildup scheme and the tabulated data sets from which the aerodynamic coefficients are interpolated.

The experimental actuator hardware can only be used to position one of the primary flight control surfaces. Therefore, to complete the aircraft model, the dynamics of the flight actuators that position the remaining flight surfaces (horizontal tails, ailerons, and rudder) must be simulated numerically. Since primary control surface pairs are generally operated in tandem, a realistic nonlinear hydraulic actuator model was implemented for each simulated flight actuator in order to maintain consistency between the experimental and simulated actuator responses. The hydraulic actuator state equations (2.10) and the nominal values of the fault emulator parameters listed in Table 2.1 were used for this purpose. The unity feedback position loop around the simulated flight actuators is closed using the following control law, which was derived using a simple model-reference loop shaping approach (see [123] for details):

$$G(s) = \frac{13.2 \times 10^7}{(s + 153.7)(s^2 + 116.4s + 86.45^2)} \tag{5.1}$$

Control law (5.1) gives positioning performance similar to the QFT position control systems designed in chapter 4. The aircraft configuration implemented in the flight model also employs two leading edge flaps to increase lift at high angles of attack. The positioning dynamics of the leading edge flap actuators are described in the flight model as first-order lags with 0.14 sec time constants. Similar to the real airplane, the deflection of each flight surface was limited according the schedule given in Table 5.1.

Table 5.1: Control surface deflection limits implemented in flight model.

Control Surface	Deflection Limit
horizontal tails	±25°
ailerons	±20°
rudder	±30°
leading edge flaps	0°, +25°

In the flight simulation model, the aerodynamic disturbing load acting on each flight actuator is computed using the following equation:

$$F_L = \gamma \bar{q} C_h(\theta, \delta) \tag{5.2}$$

In (5.2), parameter $\gamma \propto \frac{S\bar{c}}{l_h} = 2500$ m^2 is a proportional scaling factor used to adjust the magnitude of the calculated aerodynamic load to a level that is compatible with the experimental hardware. The data pertaining to the nonlinear variation of C_h that are used to compute the load force are shown in Figure 5.5 as a function of the control surface angle of incidence[1], θ. The data in Figure 5.5 were adapted from [69] and do not represent the implemented aircraft configuration exactly. However, they are adequate to approximate the real aerodynamic loads acting on the various control surfaces. For reference, the full set of C_h data is tabulated in Appendix B.

5.3 Robust Force Control of Loading Actuator

This section presents some of the details related to the design of a robust force control system for the loading actuator. The controller was developed by following the same QFT design procedure that was used to synthesize the position control system

[1]The usual sign conventions with respect to the hinge moment coefficient have been followed in this work. The hinge moment coefficient is positive if it tends to drive the trailing edge of the control surface down in the direction of positive deflection [111].

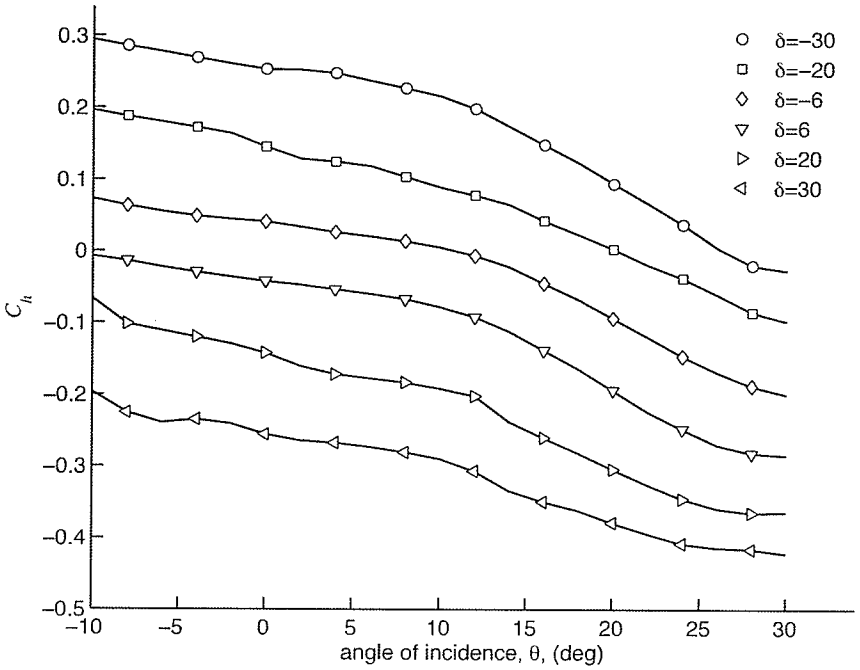

Figure 5.5: Variation of C_h as a function of angle of incidence, θ for several control surface displacements, δ. (Data adapted from Figure 13a of reference [69].)

around the flight control actuator in chapter 4. Therefore, emphasis is placed here on describing the aspects of the design process that are unique to the force controller development. Details that have already been covered are reviewed only briefly.

The QFT control system design was carried out based on the nonlinear model of the loading actuator given in chapter 2 with the nominal system parameters listed in Table 2.2. The applied force, F_a, which is the controlled actuator output, is computed from the auxiliary equation, $F_a = k_c(x_l - x_f)$, where k_c denotes the stiffness of the actuator coupling, x_l is the position of the loading actuator and x_f is the position of the flight actuator. With respect to the system state equations, variable x_f can be interpreted as a disturbance input. A block-diagram of the QFT control system

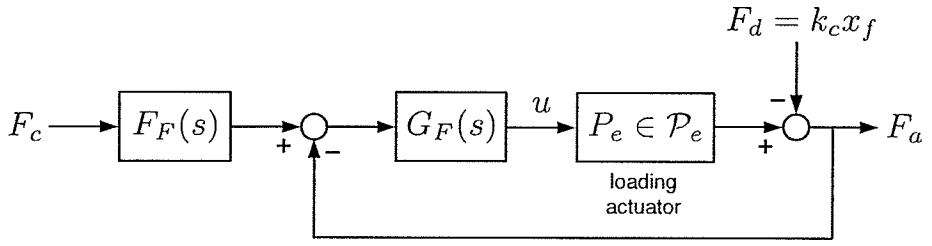

Figure 5.6: Block diagram of QFT control system around loading actuator relating commanded force, F_c, and disturbing force, F_d, to applied force, F_a.

which closes the force loop around the actuator is shown in Figure 5.6.

Step 1: LTIE Plant Set, $\mathcal{P}_e$

In section 4.1, it was shown that the relationship between the aerodynamic load force and hinge moment coefficient can be written in the following approximate transfer function form [111]:

$$F_L(s) \approx \frac{\bar{q}S\bar{c}}{l_h}\left\{C_{h,\alpha}\alpha(s) + C_{h,\delta_h}\delta_h(s)\right\} = \frac{\bar{q}S\bar{c}}{l_h}\left\{C_{h,\alpha}\frac{\alpha(s)}{\delta_h(s)} + C_{h,\delta_h}\right\}\delta_h(s) \qquad (5.3)$$

where $C_{h,\alpha}$ and C_{h,δ_h} are the components of the hinge moment coefficient related to the angle of attack, α, and the horizontal stabilator deflection, δ_h, respectively. It was also observed that the aerodynamic load has a slow component (5 rad/sec) due to input α that arises from the aircraft pitching response and a fast component (20 rad/sec) due to the motion of the flight control surface, δ_h.

It was assumed, as in [58], that if the loading system could be designed to be about 10 times faster than the dynamics of the disturbing load, then the load can be replicated with minimal distortion. Therefore, to properly reproduce the slow and fast components of the aerodynamic load force, the force control system should be designed to have a bandwidth of approximately 200 rad/sec.

The large force bandwidth, ω_o, of the loading system is approximately related to

the stiffness of the flexible coupling between the two hydraulic actuators [82]:

$$\omega_o = \frac{k_c Q_{\max}}{P_s A^2} \tag{5.4}$$

where k_c is the stiffness of the coupling, $Q_{\max}$ is the rated flow of the servovalve at supply pressure, P_s, and A is the annulus area of the actuator piston. Equation (5.4) assumes negligible motion of the flight actuator, and was derived independently from the control system by observing the fact that the open-loop characteristics of the actuator will dominate the dynamics of the force response when the control valve is operated around its limits [82].

In other words, (5.4) considers the maximum rate of change of the actuator force output to be equivalent to the product of the coupling stiffness and the maximum velocity of the ram with the control valve fully opened. However, the effects of piston inertia and damping as well as the dynamics of the control valve spool are neglected. Therefore, (5.4) is only reasonable if the frequency of the actuator resonant mode and the speed of the servovalve are both faster than the value of ω_o, which is the case here.

Using (5.4), along with the nominal values of the loading actuator parameters, it was found that to achieve $\omega_o = 200$ rad/sec, a coupling stiffness of $k_c = 3500$ kN/m is required. However, the maximum stiffness of the flexible coupling hardware is limited to 1500 kN/m. Thus, a force control loop cannot be designed to achieve the necessary 200 rad/sec bandwidth. Nonetheless, it is still possible to synthesize a force tracking system to properly reproduce the component of the aerodynamic load due to the aircraft motion. To meet the corresponding 50 rad/sec bandwidth requirement, a nominal coupling stiffness of $k_c \approx 1200$ kN/m was selected. However to ensure robustness, the controller will be designed to accommodate any value of k_c between 1000 and 1400 kN/m. With $k_c = 1200$ kN/m a nominal bandwidth specification of $\omega_o = 68$ rad/sec is obtained. This value of ω_o was used as a basis for constructing

the family of acceptable closed-loop force responses.

The acceptable family of closed-loop force responses is given by

$$\mathcal{F}_a(s) = \{F_c(s)T(s)\} = \left\{ F_c(s) \frac{\lambda\omega_n^2}{(s+\lambda)(s^2+2\zeta\omega_n s+\omega_n^2)} \right\} \tag{5.5}$$

with $w_n = 125$, $\zeta = 0.68$ and λ between 45 and 95. Using (5.5), the acceptable closed-loop bandwidth for step changes in the commanded force ranges between 45 and 88 rad/sec, which is compatible with the computed value of ω_o. Typical acceptable closed-loop responses are shown in Figure 5.7a for a set of command inputs, $\mathcal{F}_c$, consisting of steps from 1 to 7.5 kN in magnitude.

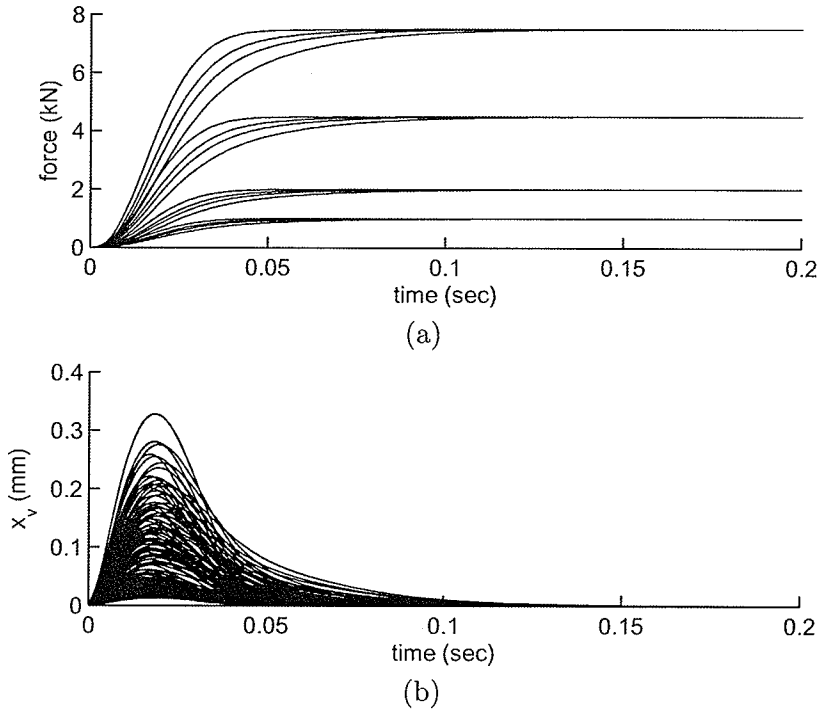

Figure 5.7: Time histories of acceptable plant input-output responses for design of robust force control system: (a) acceptable force responses (output); (b) corresponding valve spool displacements (input).

The plant drive signals required to generate the acceptable force outputs are shown in Figure 5.7b over the extreme ranges of the parameter uncertainties listed in Table 5.2. About 2000 plant cases were evaluated. The time histories for each input-output response pair were computed by first relating the acceptable actuator output force to the position of the actuator piston as follows:

$$x_l(t) = \frac{1}{k_c} F_a(t) \tag{5.6}$$

The time history of the control valve spool displacement that is necessary to ensure the actuator accurately tracks the acceptable position profile (5.6) was computed next, by simulating the inverse model of the nonlinear hydraulic actuator dynamics (see Appendix A). The accuracy of each inverse simulation was checked by integrating the relevant state equations forward in time. The time histories of the servovalve spool displacement computed from the inverse model, and the actuator output forces obtained from the forward simulation were then used together in order to identify the required LTIE frequency response ratios, $\frac{\hat{F}_a(j\omega)}{\hat{X}_v(j\omega)}$.

Table 5.2: Parametric uncertainty considered in force control system design.

Uncertain Parameter	Value		
	min	nominal	max
P_s (MPa)	13.8	17.2	18.6
m (kg)	3.4	3.8	4.2
d (N·sec/m)	200	250	300
β_h (MPa)	345	689	1030
k_v (m/mA) $\times 10^5$	2.84	3.15	3.47
ζ_v	0.5	0.9	1.0

Bode plots of the computed $\frac{\hat{F}_a(j\omega)}{\hat{X}_v(j\omega)}$ ratios are shown in Figure 5.8. With reference to Figure 5.8, it is observed that the identified frequency responses properly capture the important features of the loading actuator dynamics. Some templates of the identified set $\mathcal{P}_e(j\omega) = \left\{ P_V(j\omega)\frac{\hat{F}_a(j\omega)}{\hat{X}_v(j\omega)} \right\}$ are shown in Figure 5.9, at selected frequencies, ω.

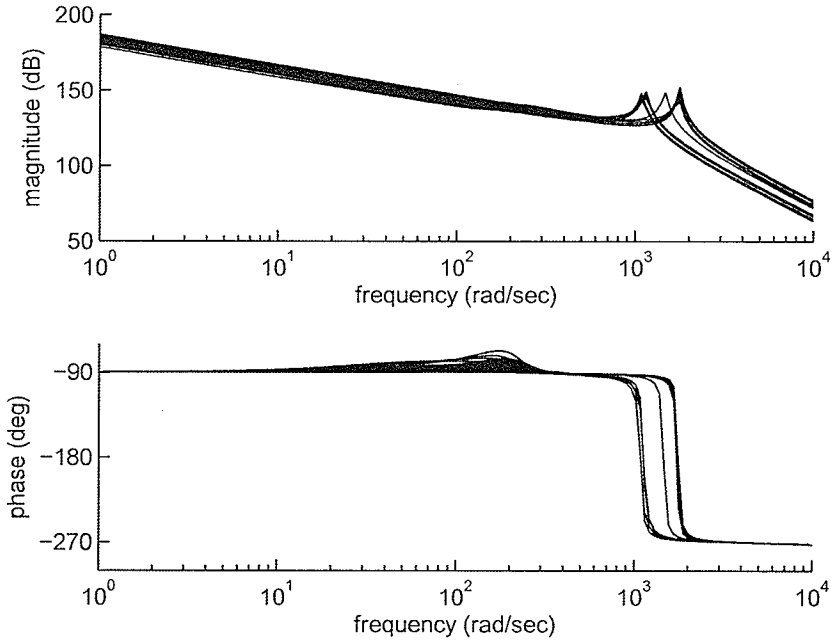

Figure 5.8: Bode plots of ratios $\frac{\hat{F}_a(j\omega)}{\hat{X}_v(j\omega)}$ for loading actuator.

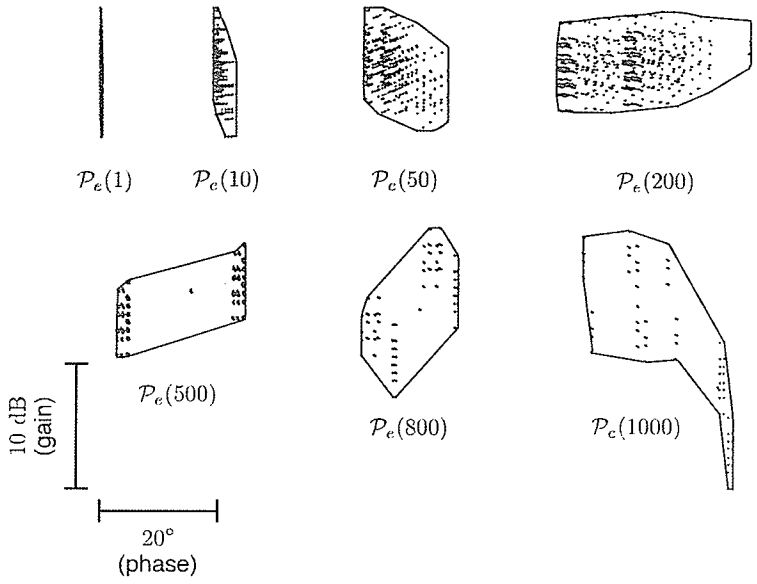

Figure 5.9: Templates of LTIE plant set, $\mathcal{P}_e$, at selected frequencies, ω rad/sec.

Step 2: Nominal Loop Shaping and Prefilter Design

The QFT design tolerances for synthesis of the force control system were derived to be compatible with the prescribed acceptable response envelope and are given below.

Closed-loop reference tracking:

$$\left|\frac{1.56\times 10^{10}}{(s+42.5)(s+2.34\times 10^4)(s^2+170s+1.56\times 10^4)}\right| \leq \left|F_F\frac{G_F P_e}{1+G_F P_e}\right| \leq \left|\frac{1.86\times 10^4(s+35)}{(s+40)(s+125)(s+130)}\right|, \quad \forall P_e \in \mathcal{P}_e \tag{5.7}$$

Closed-loop stability:

$$\left|\frac{G_F P_e}{1+G_F P_e}\right| \leq 1.9 \text{ dB}, \quad \forall P_e \in \mathcal{P}_e \tag{5.8}$$

Specifications (5.7) and (5.8) were used together with the templates of $\mathcal{P}_e$ to compute the point-wise QFT design bounds on the nominal system loop transmission.

The QFT bounds are shown in Figure 5.10 along with the designed nominal loop transmission. $L(j\omega)$ was shaped by first adjusting the proportional loop gain so that the low-frequency bound, $\mathcal{B}(1)$, was satisfied. Then, a lag filter formed by the pole-zero pair, $\frac{(s+48)}{(s+35)}$, was implemented to bring the $L(j\omega)$ locus closer to the mid-frequency bounds $\mathcal{B}(50)$ and $\mathcal{B}(100)$ in order to reduce design conservatism. Finally, a real zero at $s = -500$ and an underdamped complex pole-pair were added to roll off the high frequency controller gain and low-pass filter the noise originating from the load cell. The phase lag introduced by the complex pole allowed the resonance peaks to be moved into the region of low sensitivity on the Nichols chart as shown in Figure 5.10b. Robust compensator G_F has the following transfer function:

$$G_F(s) = \frac{1.22(s+48)(s+500)}{(s+35)(s^2+700s+2.5\times 10^5)} \tag{5.9}$$

The transfer function of the prefilter which completes the QFT control system design is

$$F_F(s) = \frac{1.75\times 10^4}{(s+100)(s+175)} \tag{5.10}$$

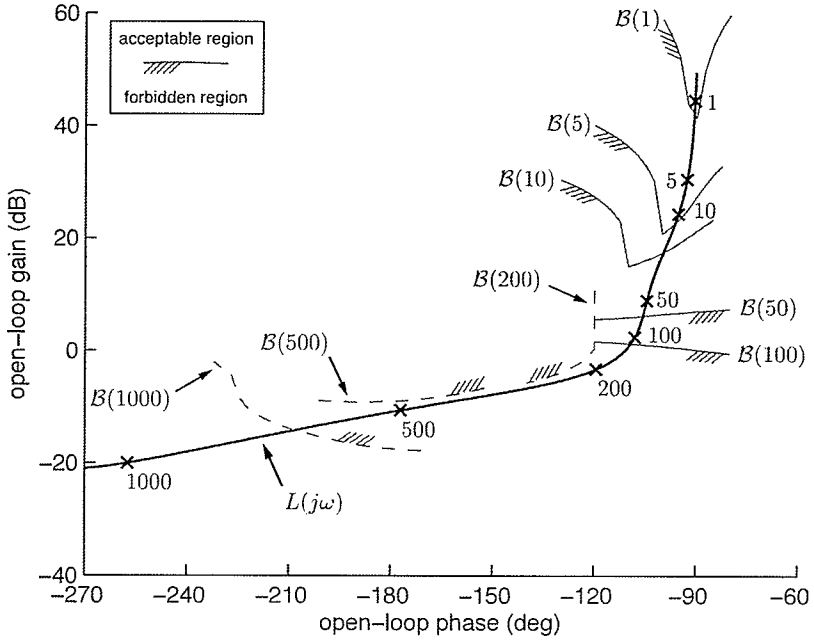

(a)

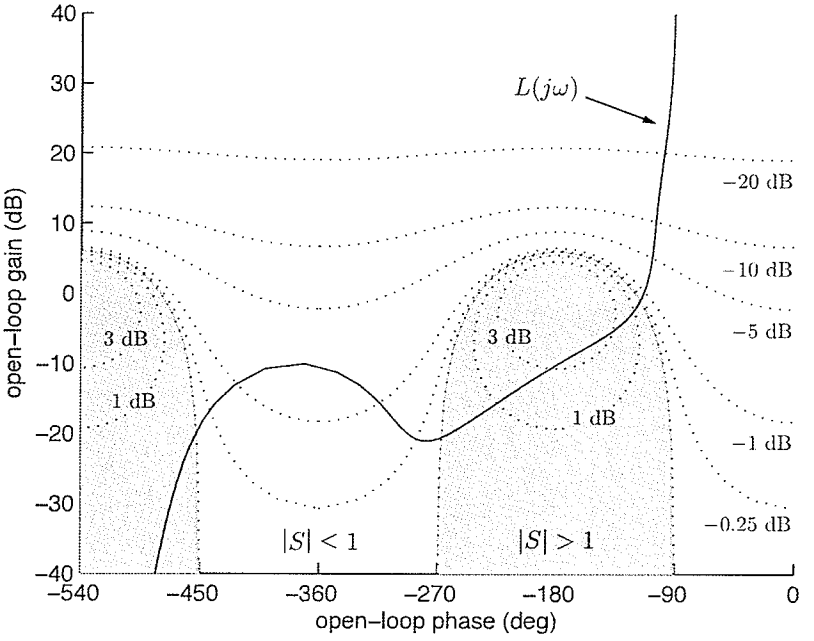

(b)

Figure 5.10: QFT bounds, $B(\omega)$, for force control system and the designed nominal loop transmission, $L(j\omega)$: (a) loop shape and QFT bounds; (b) loop transmission on inverted Nichols chart.

Step 3: Control Augmentation

The two degree of freedom control structure of Figure 5.6 is now augmented with a filter that generates a secondary command input to drive the servovalve based on the position of the flight actuator. This is done to improve the ability of the force control system to attenuate force errors arising from the flight actuator motion. A block diagram of the augmented QFT control system with filter, $F_X(s)$, is shown in Figure 5.11a. By considering the principle of superposition, changes in the applied force, F_a, can be related to the commanded force, F_c, and the position of the load, x_l, as follows:

$$F_a = F_F \frac{G_F P_e}{1 + G_F P_e} F_c + \left[F_X \frac{P_e}{1 + G_F P_e} - \frac{k_c}{1 + G_F P_e} \right] X_l \tag{5.11}$$

Assuming the actuator has reached the steady-state, i.e. $F_a = F_c$, zeroing the force error, $F_e = F_a - F_c$, that is caused by force disturbance, $F_d = k_c x_l$, requires that

$$F_e = F_X \frac{P_e}{1 + G_F P_e} X_l - \frac{k_c}{1 + G_F P_e} X_l = 0 \tag{5.12}$$

Equation (5.12) can be further simplified to give

$$F_e = F_X P_e - k_c = 0 \tag{5.13}$$

where product $F_X P_e$ is the transfer function of the compensation used to reduce force errors caused by the moving load (see Figure 5.11b).

Considering the effects of uncertainty in the hydraulic actuator dynamics, (5.13) can be manipulated to give the following inequality that is used to guide the design of F_X

$$\left| \frac{k_c}{\mathcal{P}_e(j\omega)} \right|_{\min} \leq |F_X(j\omega)| \leq \left| \frac{k_c}{\mathcal{P}_e(j\omega)} \right|_{\max} \tag{5.14}$$

A plot of the set of $\frac{k_c}{\mathcal{P}_e(j\omega)}$ magnitudes is shown in Figure 5.12 along with the

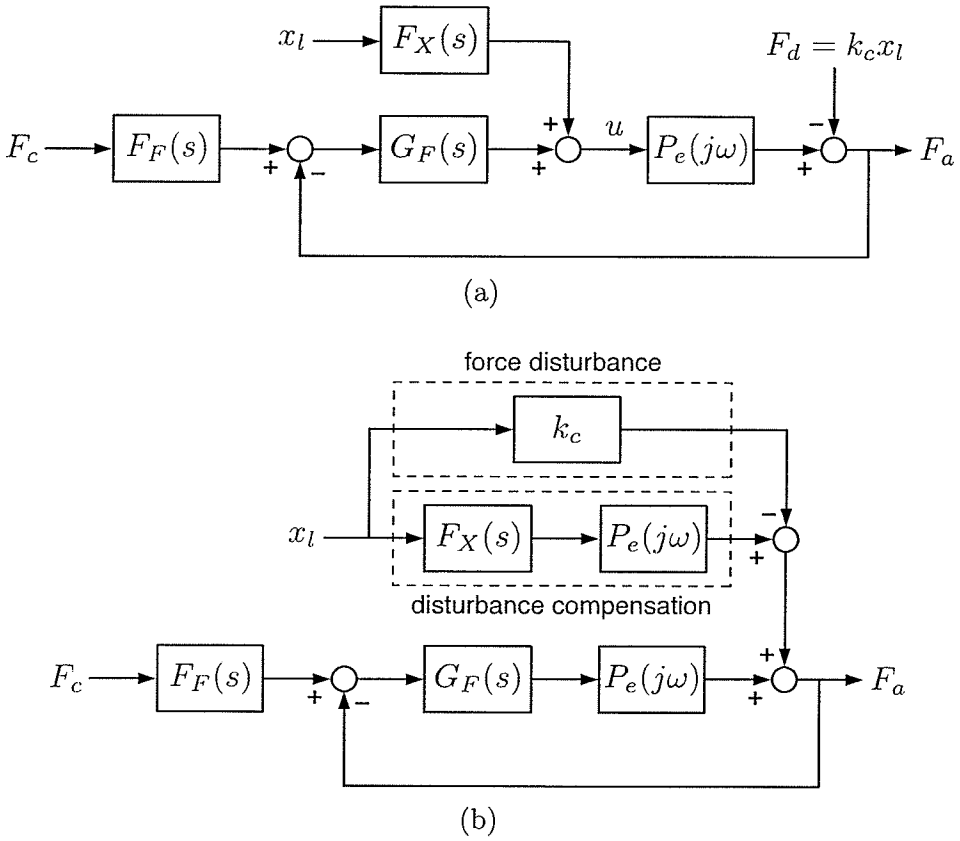

Figure 5.11: Schematic of augmented force control system: (a) block diagram with added filter, $F_X(s)$; (b) equivalent block diagram illustrating force disturbance compensation.

magnitude plot of the designed $F_X(j\omega)$, which has transfer function

$$F_X(s) = \frac{1.6 \times 10^4 s}{s + 1000} \tag{5.15}$$

Referring to Figure 5.12, filter $F_X(s)$ was designed to closely follow the locus of $\left|\frac{k_c}{\mathcal{P}_e(j\omega)}\right|_{\min}$ up to $\omega \approx 1000$ rad/sec. Selecting $|F_X(j\omega)| \approx \left|\frac{k_c}{\mathcal{P}_e(j\omega)}\right|_{\min}$ gives a well damped regulating response to changes in the position of the flight actuator.

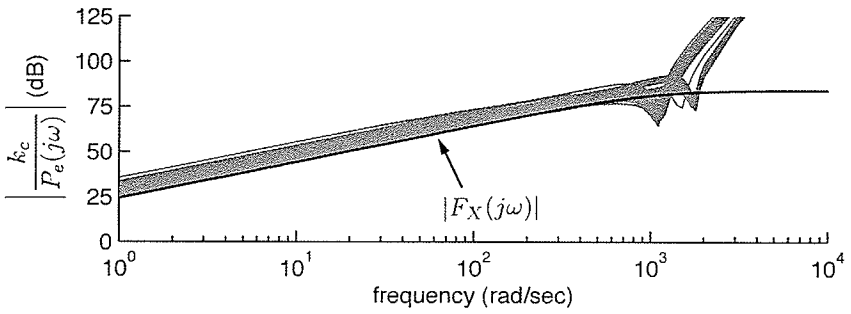

Figure 5.12: Magnitude plots of set $\frac{k_c}{\mathcal{P}_e(j\omega)}$ and designed filter, $F_X(j\omega)$.

Step 4: Controller Verification

To evaluate the performance of the designed force control system prior to implementation on the experimental hydraulic test bench, the closed-loop system was simulated. Several hundred nonlinear simulations were performed using the extreme combinations of the uncertain system parameter values given in Table 5.2 and for different step command inputs ranging from 1 to 7.5 kN. Normalized step responses for $x_f = 0$ are shown in Figure 5.13a along with the acceptable step response envelope defined by the closed-loop tracking specifications, for reference. The corresponding control signals are shown in Figure 5.13b. The step responses are observed to fall well within the specified acceptable response envelope, which confirms the validity of the control system design. Moreover, since the servovalve control signals always remain below

the 10 mA saturation level, large changes in the actuator force output can be accomplished without exhausting the capacity of the uncertain plant.

The simulated response of the force control system to flight actuator motion was examined next. The position of the flight actuator was varied using profile $x_f(t) \approx 5(1-e^{-20t})$ mm, which is similar to the closed-loop step response of the experimental flight actuator. Simulated force errors, $F_e = F_a - F_c$, are shown in Figure 5.14, for various combinations of the uncertain model parameters and for different initial steady-state forces. Figure 5.14a shows the simulation results using the base QFT force control system, without filter $F_X(s)$. The simulation results with filter $F_X(s)$ active in the control loop are shown in Figure 5.14b. With reference to Figure 5.14, it is observed that by using the filtered changes in the flight actuator position as a secondary control input, the peak values of the force error are reduced by about 50%. The 2% settling time is also improved by more than 30% over the base control system. Thus, the implementation of filter $F_X(s)$ greatly improves the ability of the force control system to accommodate motion of the flight actuator.

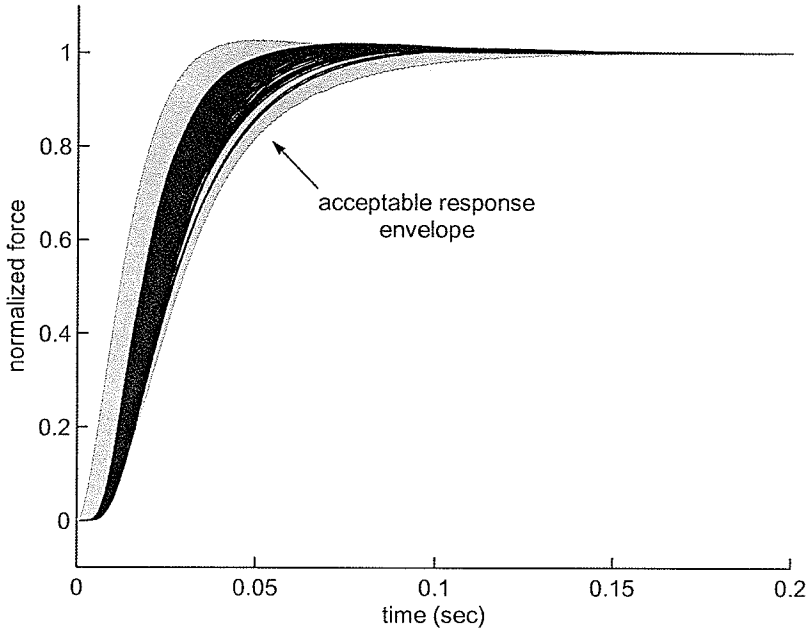

(a)

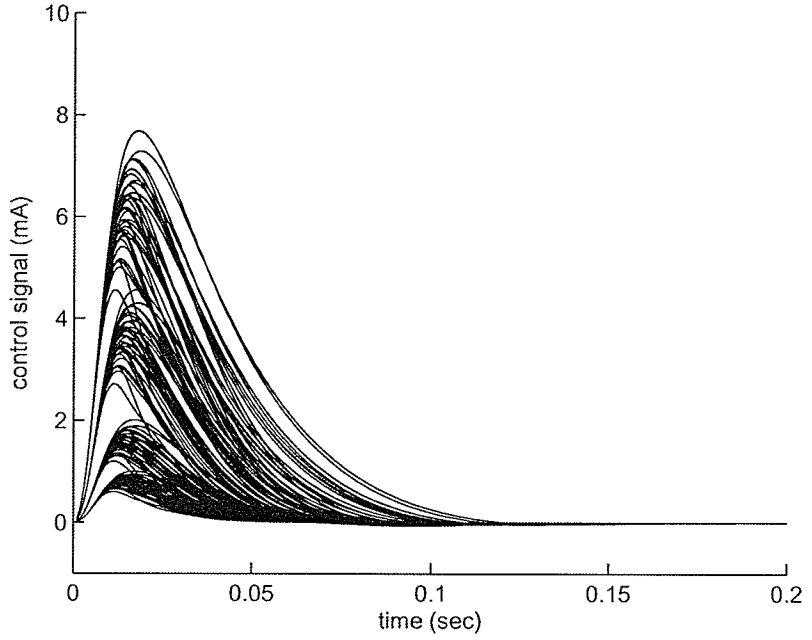

(b)

Figure 5.13: Representative normalized step responses of closed-loop force control system for $x_f = 0$ (nonlinear simulations): (a) normalized force; (b) control signal.

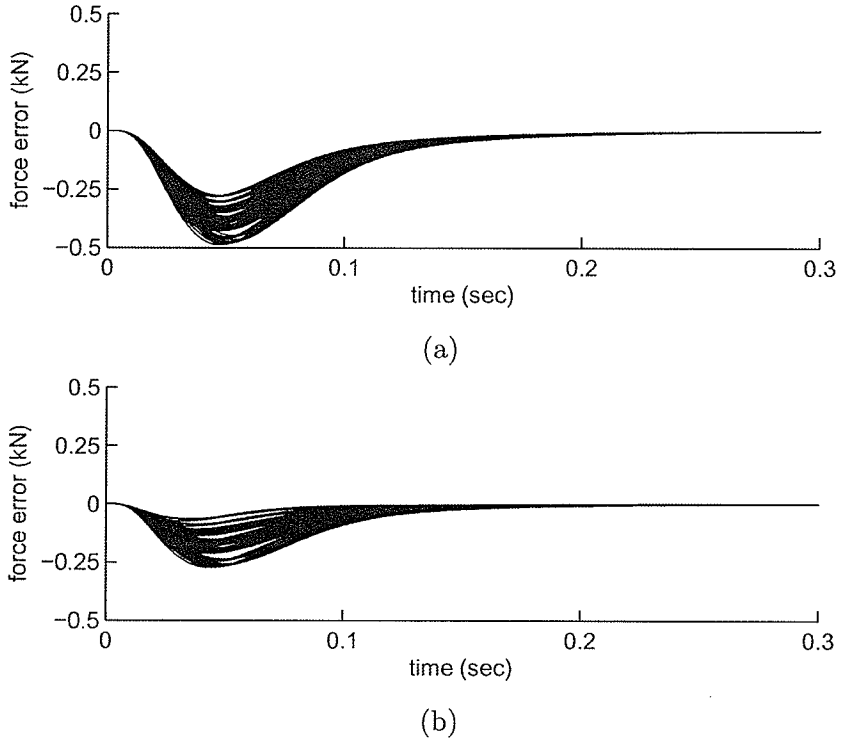

Figure 5.14: Typical closed-loop force regulating errors resulting from flight actuator movement (nonlinear simulations): (a) base control system without filter $F_X(s)$; (b) augmented control system with filter $F_X(s)$.

Step 5: Experiments

The experimental performance of the force control system against a rigid environment is illustrated in Figure 5.15 for different force step commands covering the entire 7.5 kN operational range of the actuator. The results have been normalized to facilitate comparison with the acceptable response envelope. As can be seen, the experimental step responses fit accurately within the design bounds. The force responses and corresponding control signals, shown in Figure 5.15b, are also observed to be consistent with the nonlinear simulation results. Figure 5.16 demonstrates the performance of the force control system operating against the moveable flight actuator for various force setpoints. For each experiment, a 5 mm step command was applied to the flight actuator at $t = 2$ sec so that the closed-loop regulating response could be evaluated. Experimental responses are shown for the augmented force control system that uses filter $F_X(s)$ (solid line), and for the base QFT control system (dashed line). With reference to the system step responses, it is observed that the measured force remains properly located within the acceptable response envelope. In addition, Figure 5.16 shows that the augmented force control system is able to keep the force disturbance to within about ± 350 N of the setpoint and zero the error in less than 0.08 sec. This is in contrast to the nearly two-fold increase in the peak values of the force error and the significantly longer settling times which are observed in the case where only the base QFT force control system is implemented.

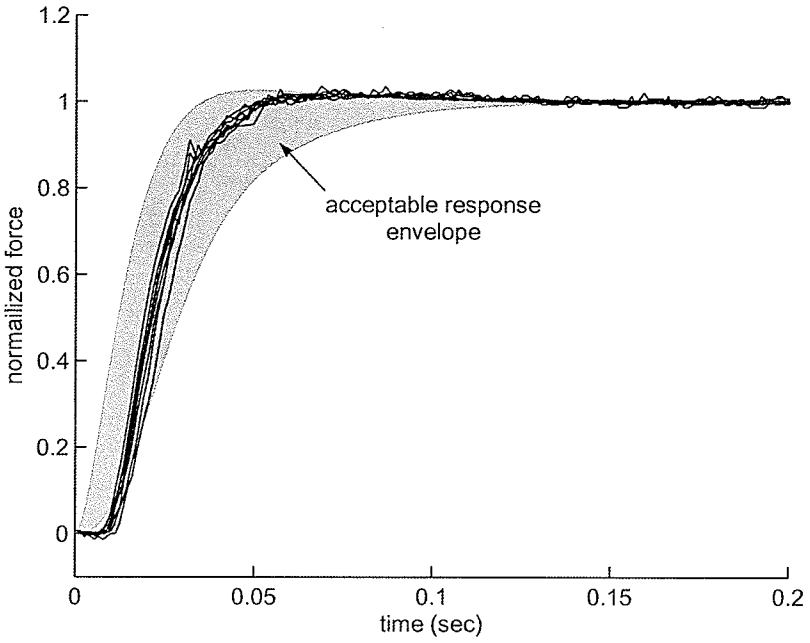

(a)

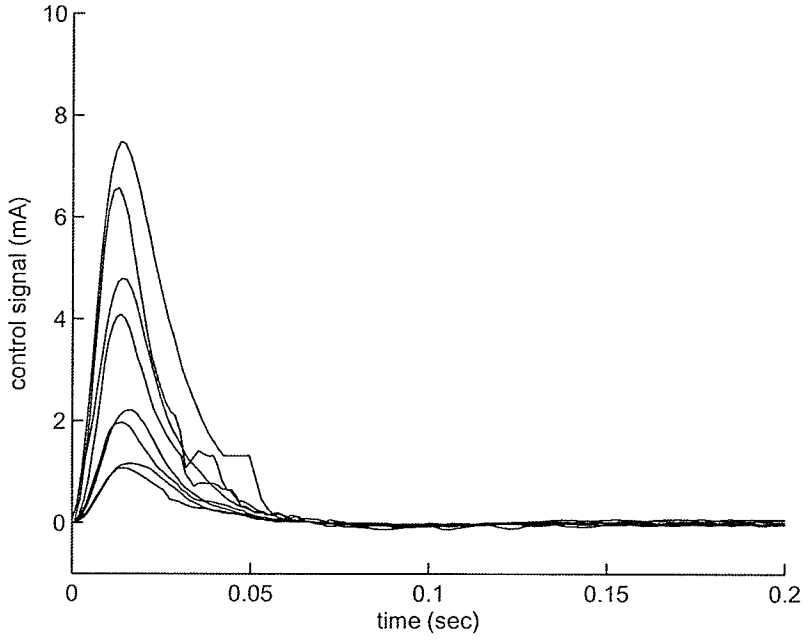

(b)

Figure 5.15: Typical experimental performance of force control system operating against a fixed environment: (a) normalized force; (b) control signal.

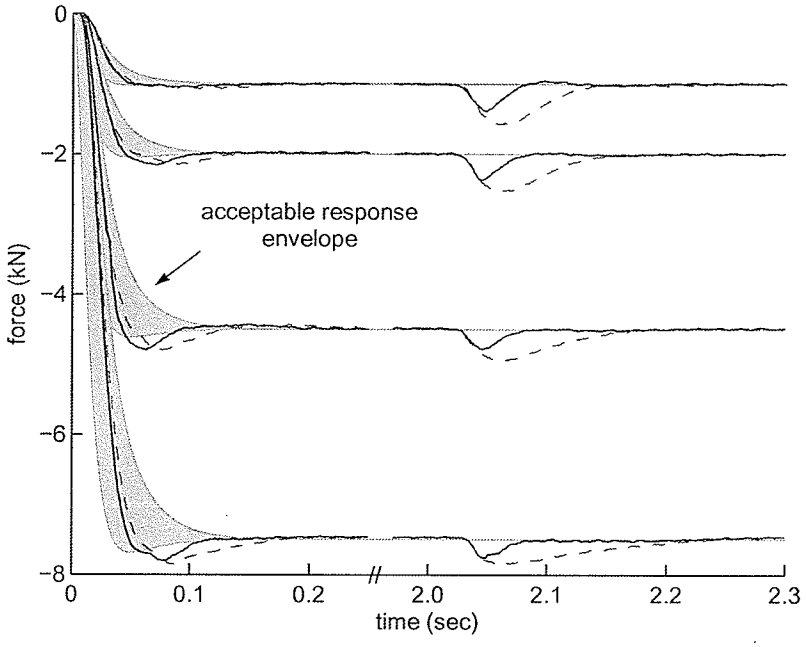

Figure 5.16: Typical experimental performance of augmented force control system with filter $F_X(s)$ operating against a moveable environment (solid lines). Performance of base control system, without $F_X(s)$ included for reference (dashed lines).

5.4 Demonstration of HIL Simulator

In this section, the experimental results of two case studies are presented to illustrate the applicability of the HIL flight simulator towards evaluating the performance of the experimental flight actuator. The first case study is an angle of attack control experiment that demonstrates the ability of the electrohydraulic loading system to properly replicate the commanded aerodynamic load disturbance. Case study 2 shows the results of a piloted HIL simulation with a human operator in the loop and confirms the correct implementation of the aircraft dynamic model and tests the functionality of the longitudinal and lateral/directional flight control systems.

Case Study 1:

In this HIL simulation example, a typical angle of attack (α-) control experiment was performed. To perform the test, a fixed-gain α-controller, previously developed in [122], was activated in the longitudinal channel of the flight control system. The aircraft was trimmed[2] for steady 1g flight at 12000 m altitude and 156 m/sec airspeed. A 20° α pull-up was commanded and held for 5 sec, after which trim α was resumed. Figure 5.17a shows the resulting aircraft α response. The deflections of each horizontal stabilator half are shown in Figure 5.17b. The measured aerodynamic disturbing load that was applied to the experimental flight actuator is shown in Figure 5.17c, along with the commanded load profile. Figure 5.17d reports the force error associated with the experiment.

Referring to Figure 5.17b, it is observed that the left (experimental hardware) and right (simulated) horizontal tail halves move symmetrically and synchronously, as commanded by the α-controller. The similarity between the two traces indicates that the model used to compute the dynamics of the flight actuators in the air-

[2]In the flight control literature, *trimming* refers to finding an equilibrium flight condition. To trim the aircraft at a particular flight condition, it is necessary to determine the control inputs, i.e. the deflections of the control surfaces and the throttle setting, that balance the forces and moments acting at the aircraft center of gravity [1].

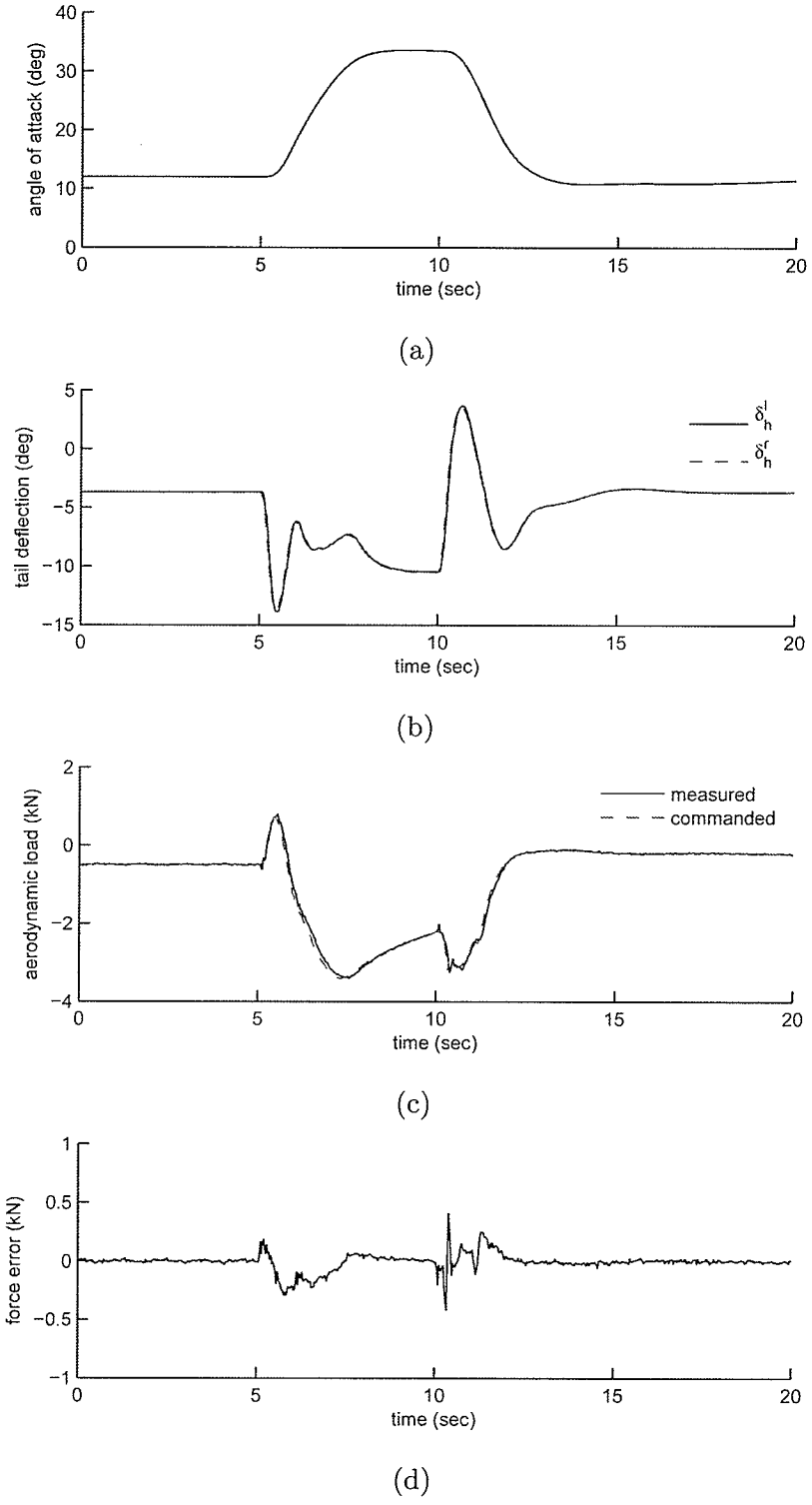

Figure 5.17: Results of angle of attack control experiment: (a) angle of attack; (b) horizontal stabilator deflections: δ_h^l - experimental; δ_h^r - simulated; (c) aerodynamic disturbing load; (d) force error.

craft simulation is an accurate representation of the experimental hardware. The synchronous motion of the two horizontal tail halves confirms that no significant delays are introduced by transmitting control data between the PCs over the network connection. The efficacy of the hydraulic loading system to accurately replicate the commanded aerodynamic disturbing load is verified in Figure 5.17c. As is seen, the load disturbance applied to the experimental flight actuator during the α-control experiment very closely resembles the commanded profile, even in the presence of significant flight actuator motion. A plot of the force error pertaining to the experiment (see Figure 5.17d) confirms that the peak force tracking error is less than 10% over the entire HIL simulation. Thus, the designed force control system is adequate to reproduce the necessary in-flight actuator operating conditions.

During the HIL experiment, the CPU time (real time) elapsed since the beginning of the test was determined by querying a high-resolution performance counter on the workstation running the aircraft simulation model at each instant the aircraft states were advanced forward in time. The measured CPU time is plotted against the simulation time in Figure 5.18. As can be seen, the curve is linear with a unity slope. This indicates that the amount of time required to query the experimental hardware, perform the numerical integration of the aircraft states and compute the command signals that need to be applied at the next integration step can be kept smaller than the integration time step used in the numerical simulation model. Thus, the HIL simulator is capable of operating in real-time.

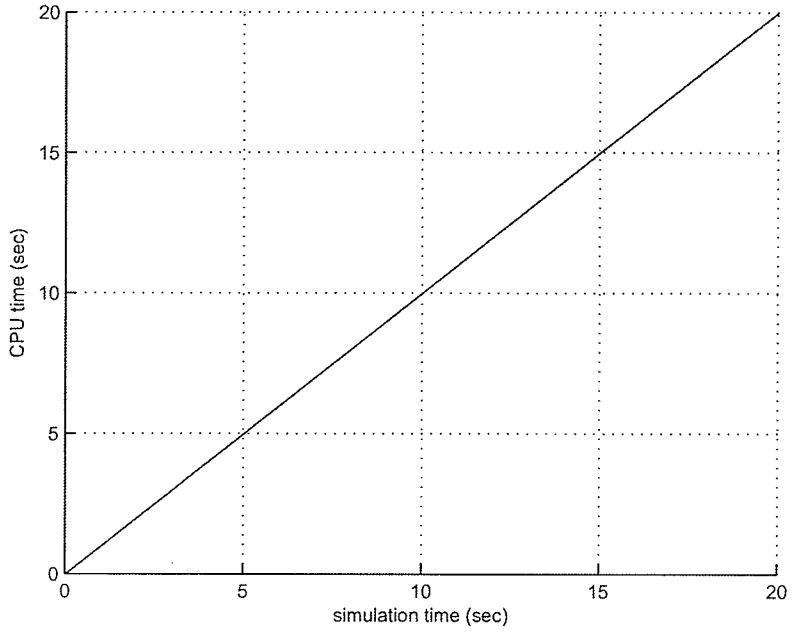

Figure 5.18: Elapsed CPU time versus simulation time pertaining to angle of attack pull-up experiment.

Case Study 2:

This case study was performed in order to verify the proper functionality of the longitudinal and lateral/directional flight control systems and to validate the correct implementation of the aircraft dynamic model. A secondary objective was to demonstrate the ability of the HIL simulator to support human-in-the-loop testing. In the HIL simulation, a human operator attempted to complete a 360° roll from steady 1g flight at 9144 m altitude and a high angle of attack ($\alpha = 25°$) by applying a full lateral stick command. The experimental results are shown in Figure 5.19.

Upon application of the lateral stick input (see time history of normalized pilot commands in Figure 5.19a), the aileron deflection, δ_a, reached its limit and the proper operation of the aileron-rudder interconnect caused a coordinated deflection of the rudder, δ_r, as shown in Figure 5.19b. Figure 5.19b also shows that a maximum nose-down stabilator deflection, $\delta_h = +25°$, is commanded by the angle of attack

limiter at $t \approx 6$ sec in an attempt to prevent a pitch out departure ($\alpha > 30°$ in Figure 5.19c). Large adverse sideslip excursions, indicated by the variation of the sideslip angle, β, between $\pm$ 20° in Figure 5.19c are also observed. After regaining control over the aircraft at $t \approx 13$ sec, the human operator completed the roll, as shown in Figure 5.19d, by finely manipulating the pilot stick. The features of the F16 response and the control surface deflections that were recorded during the piloted HIL experiment very closely resemble results in other references, i.e. Figure 22 of reference [120], thus confirming the correct implementation of the flight model.

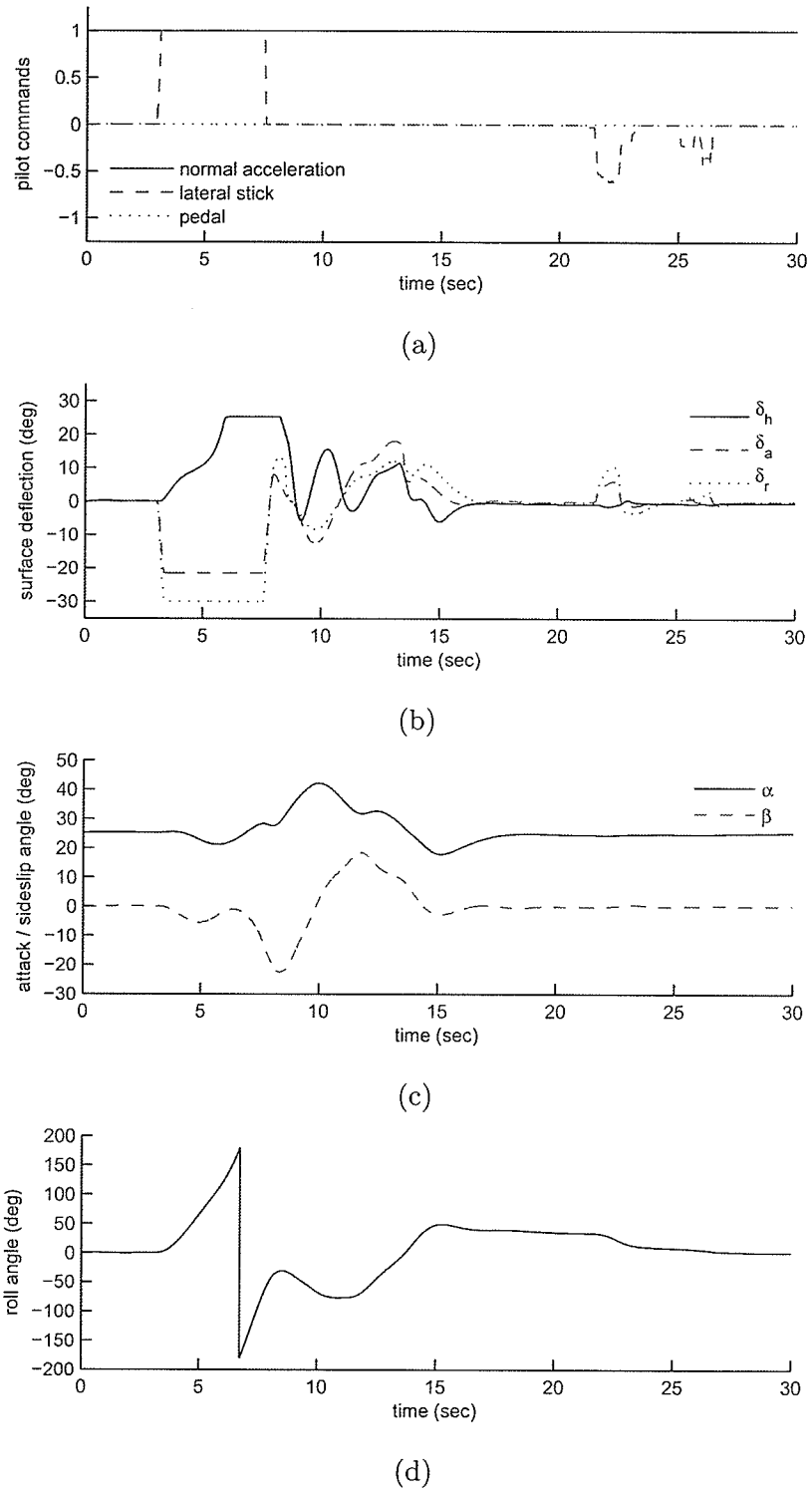

Figure 5.19: Results of 360° roll experiment with human-in-the-loop: (a) normalized pilot commands; (b) control surface deflections; (c) angle of attack and sideslip angle; (d) roll angle.

5.5 Summary

This chapter described the details of a hardware-in-the-loop (HIL) flight simulation environment that was developed in order to further test the efficacy of the fault tolerant controller designed in chapter 4. The HIL simulation framework enables the fault emulator actuator on the hydraulic test bench to be employed as a flight control actuator in the numerical simulation of a high-performance F16 aircraft. The hydraulic test bench has also been configured so that a secondary ram can be used to interact with the flight actuator and replicate the aerodynamic load disturbance that would normally be transmitted through the control surface hinge during flight. Thus, the HIL simulator facilitates control system verification under an extended range of operating conditions. QFT was applied to synthesize a robust force control system around the loading actuator. Then, the robust control structure was further augmented by the design of a filter that enables the loading system to better accommodate changes in the flight actuator position. The results of two HIL simulation case studies demonstrated the overall functionality of the simulator and confirmed the ability of the electrohydraulic loading system to properly recreate the commanded force profile.

Chapter 6

Hardware-in-the-Loop Experiments

This chapter documents the results of several hardware-in-the-loop (HIL) experiments that were carried out using the developed flight simulation framework. The objectives of this testing are two-fold. First, it is desired to further evaluate the performance of the fault tolerant position control law under operating conditions that more closely resemble the intended flight control application. A secondary goal of the HIL testing is to investigate the interaction between the functionality of the experimental flight actuator and the flight performance of the aircraft, which represents a complex dynamic system. It is of particular interest to examine whether the internal leakage fault, if not properly compensated at the actuator level, can cause the airplane to exhibit undesirable flying qualities. Two realistic flight maneuvers are studied in order to explore these objectives. The flight maneuvers are described in section 6.1, while section 6.2 presents the HIL simulation results and their interpretation.

6.1 Description of Tests

In the HIL experiments, the experimental flight actuator is used to position the left horizontal tail half of the simulated aircraft. The experimental ram is primarily responsible for controlling the longitudinal (pitching) motion of the airplane. Several

relevant points from reference [120], which describe the longitudinal stability and control characteristics of the simulated aircraft configuration, have therefore been summarized below:

1. The aircraft is longitudinally unstable at low angles of attack with a negative static margin[1]. Angle of attack feedback is used to drive the horizontal tail in order to provide artificial pitch stability. Therefore, the horizontal tail plays an important role in maintaining satisfactory flying qualities.

2. It is possible for the aircraft to enter a stable deep-stall trim condition at an extreme angle of attack ($\alpha \approx 60°$). However, the effectiveness of the horizontal tail is poor for $\alpha > 25°$, which makes it difficult to recover the aircraft after it has entered deep-stall trim. To inhibit excursions into the deep-stall regime, an α-limiting system is used to drive the horizontal tail in a way that attempts to keep $\alpha \leq 25°$.

3. A sharp loss in horizontal tail effectiveness is observed for sideslip (β) magnitudes greater than 10°. Therefore large sideslip excursions, such as those generated during rolling maneuvers, can degrade the effectiveness of the angle of attack limiting system.

In light of the above discussion, two different flight maneuvers were selected that rely on the performance of the horizontal tail actuators in order to maintain control over the motion of the aircraft. The first flight maneuver is a bank-to-bank reversal in which the aircraft is rolled through a series of bank angle changes using maximum lateral stick input and maximum commanded normal acceleration. Figure 6.1 shows the time history of the lateral stick input commands used in the bank-to-bank maneuver as well as a typical bank angle response obtained from the HIL flight simulator. Referring to Figure 6.1b, the selected sequence of lateral stick inputs gives maximum bank angles of about 80°. The second flight maneuver is a 360° roll in which full

[1]A detailed description of the static margin concept can be found in §3.3.7 of [1]. For the purpose of the discussion presented here, however, it is sufficient to define the static margin as a quantity that relates the buildup of nose-down pitching moment to an increase in the angle of attack, α. A positive static margin produces a pitching moment that opposes increasing α, giving a stable longitudinal response. A negative static margin, on the other hand, produces a pitching moment that causes the aircraft to rotate in the direction of increasing α. This results in an unstable longitudinal response.

lateral stick input is applied in an effort to roll the aircraft 360° about the velocity vector. The time history of the lateral stick input is shown in Figure 6.2 along with a typical roll response. Both flight maneuvers are conducted from 1g trim at $\alpha = 25°$.

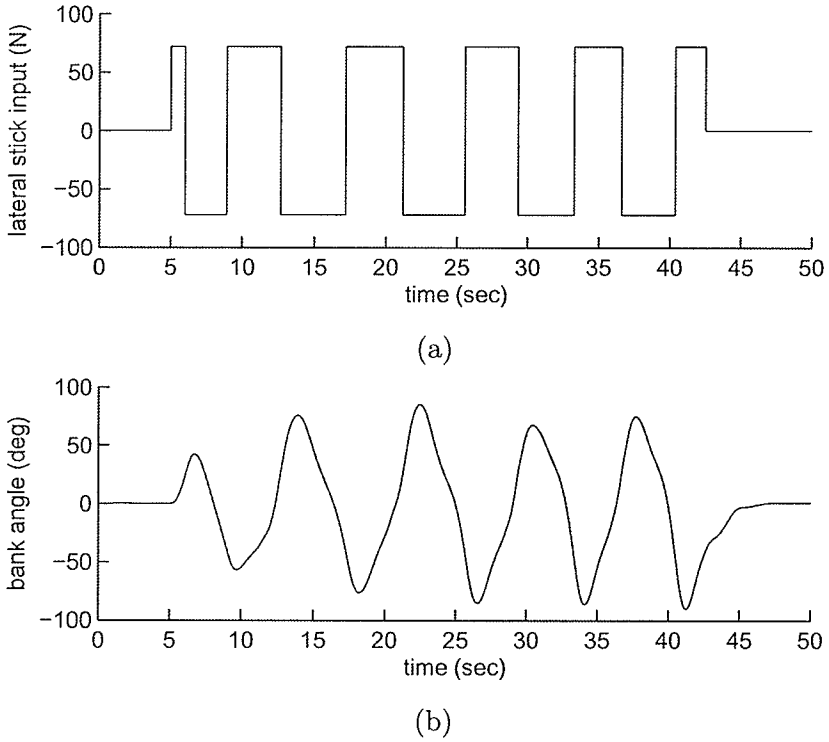

Figure 6.1: Input command and typical bank angle response for bank-to-bank reversal maneuver: (a) lateral stick input; (b) bank angle.

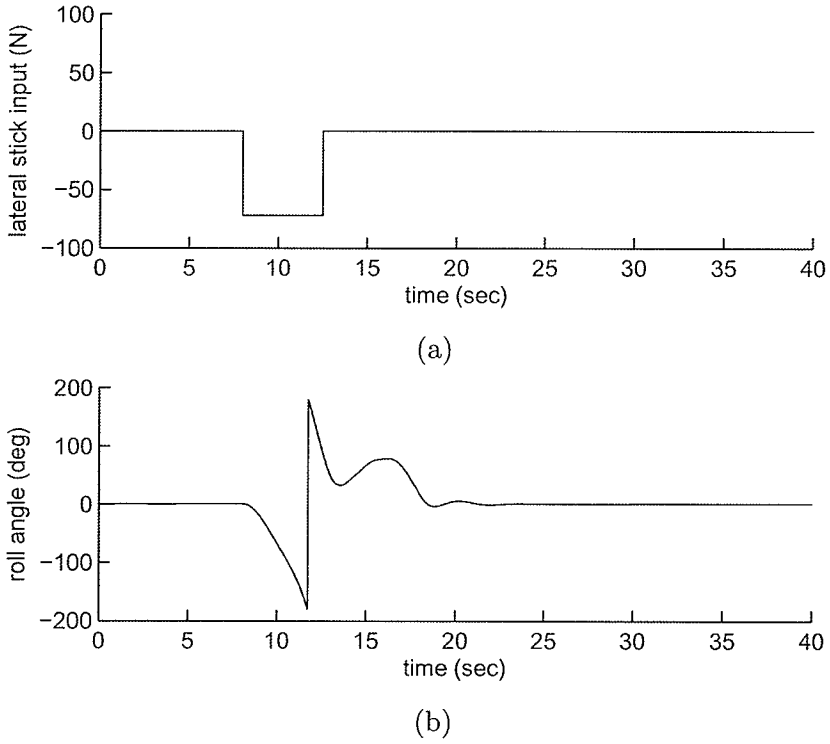

Figure 6.2: Input command and typical roll response for 360° roll maneuver: (a) lateral stick input; (b) roll angle.

6.2 Results

This section presents the HIL simulation results obtained for each flight maneuver as well as their interpretation. The performance of benchmark control system A (see chapter 4) and the fault tolerant controller is tested for normal actuator operation and in the presence of an internal leakage fault whose severity increases progressively over time. The HIL simulation results therefore further substantiate the functionality of the designed fault tolerant controller and show how the performance of the benchmark control system is inadequate, in the presence of the internal leakage fault. The potential for the aircraft to enter an undesirable deep stall flight condition, when the internal leakage fault is not properly compensated by flight actuator control system, is also illustrated.

6.2.1 Bank-to-Bank Reversals

Benchmark Control System A

The results of the bank-to-bank reversal maneuver using benchmark control system A are shown in Figure 6.3, for normal operation of the experimental flight actuator. The deflection of the left (experimental) horizontal tail is shown in Figure 6.3a, along with the time history of the control signal applied to the servovalve in Figure 6.3b. Referring to Figure 6.3a, the activity level of the horizontal tail is observed to be quite high. The flight actuator traverses nearly the entire range of control surface motion and reaches saturation ($\delta_h = +25°$) during each bank angle reversal. Nonetheless, using the benchmark controller, the flight actuator is able to properly track the commanded surface deflection profile, even under the influence of the aerodynamic load force (see Figure 6.3c) applied by the electrohydraulic loading system.

The aircraft response histories are illustrated in Figures 6.3d and Figure 6.3e, which show the bank angle and the attack/sideslip angles, respectively. With reference to Figure 6.3d, the maximum bank angles observed during the test were about 80°,

as expected. Figure 6.3e shows small excursions of the angle of attack from $\alpha = 25°$ during the flight maneuver. However, due to the action of the horizontal tail, the angle of attack never exceeded 33°. Figure 6.3e also shows that the sideslip excursions induced by the rolling motion of the aircraft remained within $\pm 10°$.

Figure 6.4 shows the results of the bank-to-bank reversals using benchmark controller A, but this time in the presence of the internal leakage fault. During the test, the severity of the internal leakage fault was increased gradually by slowly opening the needle valve connecting the two actuator cylinders. Figure 6.4a confirms that, in the presence of the fault, the experimental flight actuator cannot properly track the commanded deflection profile. Although the control signal applied to the servovalve, shown in Figure 6.4c, increases in proportion to the tracking error, the controller simply cannot provide enough effort to maintain the performance of the flight actuator against the aerodynamic load (see Figure 6.4d). The aerodynamic load force, which is computed in real-time from the aerodynamics model, is also observed to change slightly as compared to Figure 6.3c, due to changes in the flight actuator response.

The aircraft response histories in the presence of the internal leakage fault are shown in Figures 6.4e and Figure 6.4f. The attack, sideslip and bank angles do not appear to be affected much by the flight actuator fault. In the presence of the fault, the aircraft could still be rolled to bank angles around 80°. Moreover, the peak value of α remained below 33° and the sideslip excursions were less than $\pm 10°$, as before. Therefore, for the particular flight condition and maneuver studied, it is apparent that the reduction in effectiveness of the horizontal tail caused by the flight actuator fault is not large enough to noticeably impact the flight performance of the aircraft. This result shows that the problem with the aircraft flight control actuator may go unnoticed by the pilot, and justifies the need for fault tolerant control algorithms that can automatically compensate hydraulic system faults until they can be diagnosed and corrected.

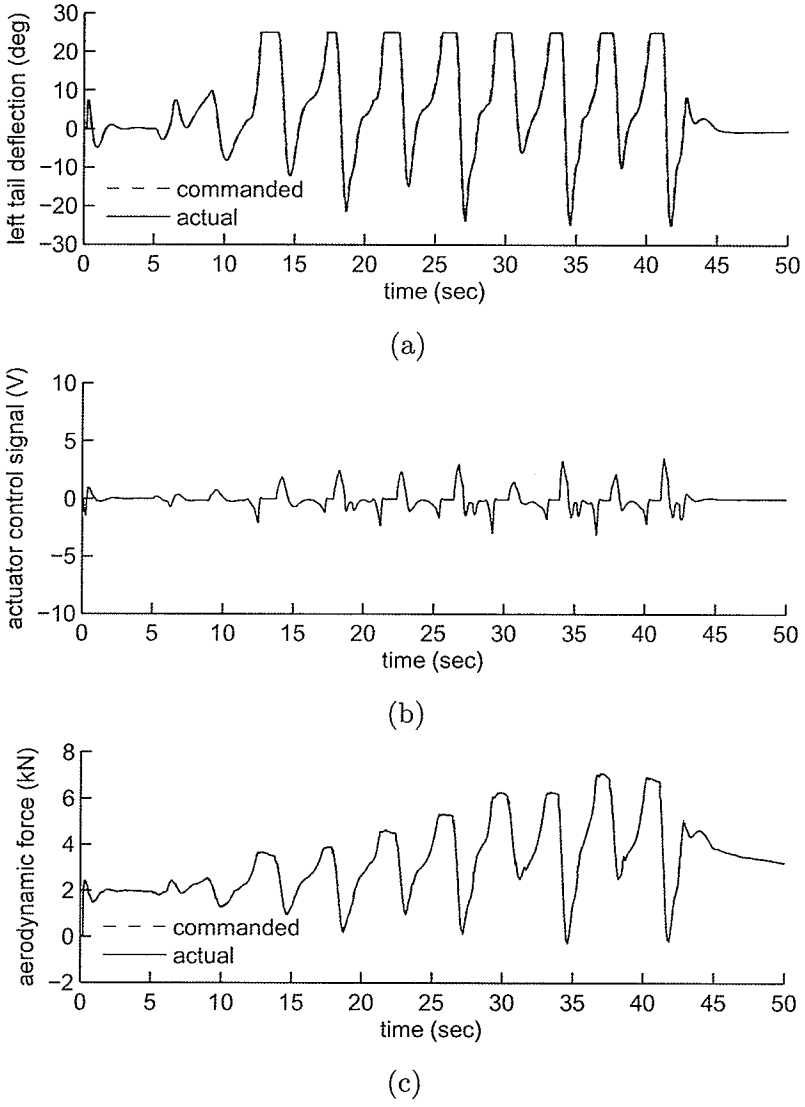

Figure 6.3: Bank-to-bank reversals using benchmark controller A under normal operation: (a) left tail deflection; (b) actuator control signal; (c) applied aerodynamic load; (d) bank angle; (e) attack and sideslip angles.

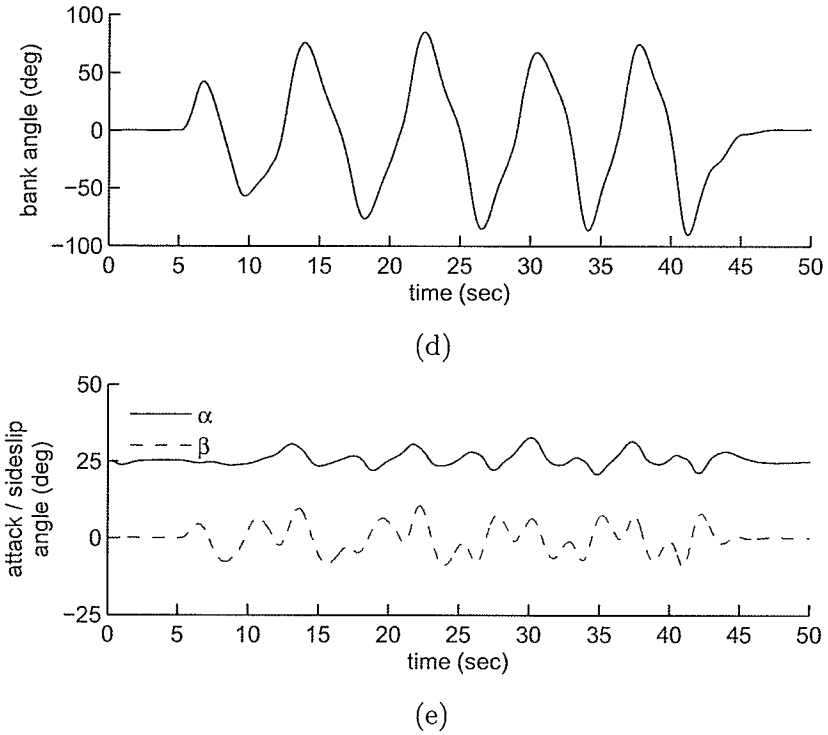

Figure 6.3 – concluded: Bank-to-bank reversals using benchmark controller A under normal operation: (a) left tail deflection; (b) actuator control signal; (c) applied aerodynamic load; (d) bank angle; (e) attack and sideslip angles.

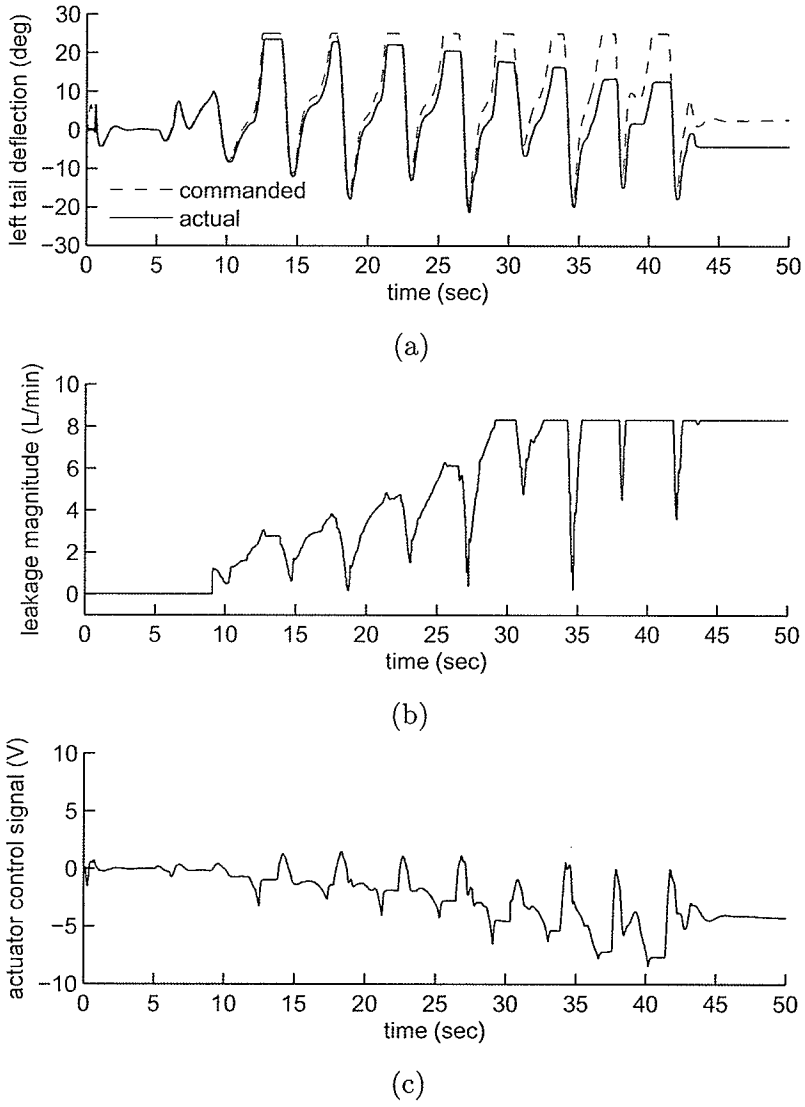

Figure 6.4: Bank-to-bank reversals using benchmark controller A for increasing internal leakage: (a) left tail deflection; (b) internal leakage magnitude; (c) actuator control signal; (d) applied aerodynamic load; (e) bank angle; (f) attack and sideslip angles.

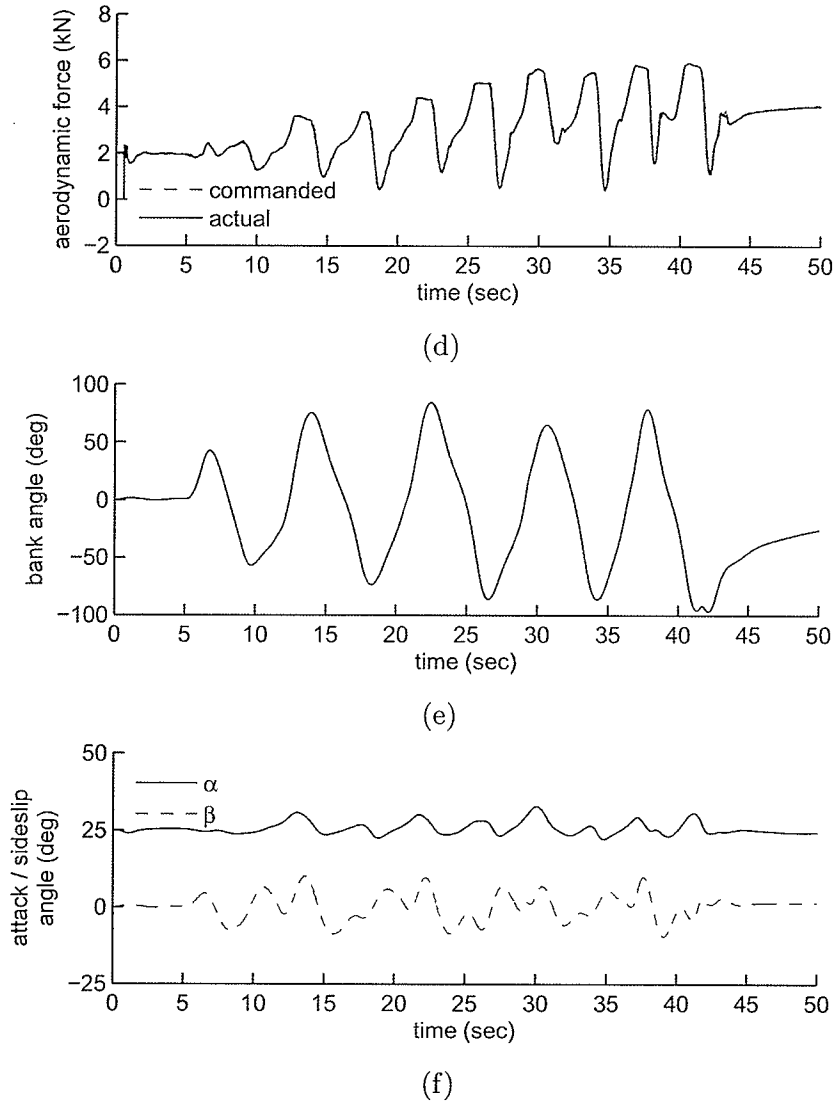

Figure 6.4 – concluded: Bank-to-bank reversals using benchmark controller A for increasing internal leakage: (a) left tail deflection; (b) internal leakage magnitude; (c) actuator control signal; (d) applied aerodynamic load; (e) bank angle; (f) attack and sideslip angles.

Fault Tolerant Controller

The bank-to-bank reversal maneuver was repeated using the fault tolerant controller to position the experimental flight actuator. For normal operation of the hydraulic system, the experimental results were similar to those obtained using the benchmark controller, and are therefore omitted. However, as illustrated by Figure 6.5, which shows the HIL simulation results in the presence of increasing internal leakage, the fault tolerant controller enables the flight actuator to properly track the commanded deflection profile against the aerodynamic load, despite the fault. The fault tolerant controller maintains the positioning performance of the actuator by exploiting the action of the control law integrator, which keeps the servovalve open to provide a makeup flow of hydraulic fluid even when the tracking error is small.

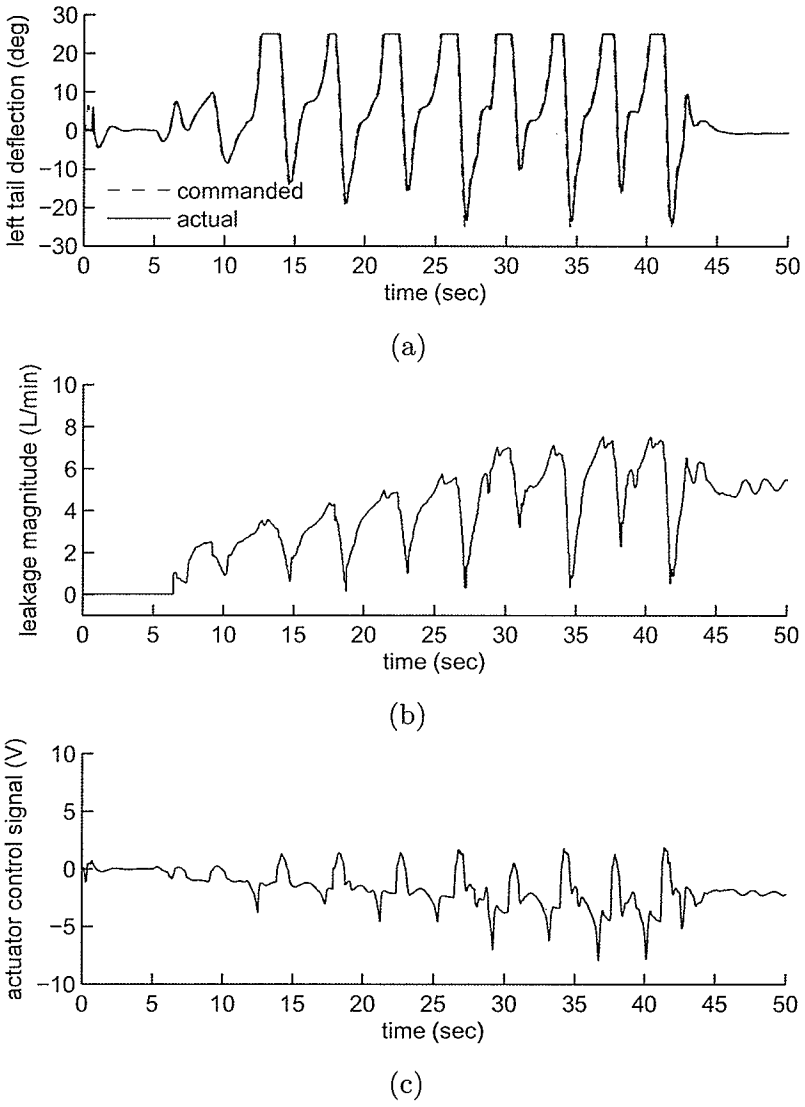

Figure 6.5: Bank-to-bank reversals using fault tolerant controller for increasing internal leakage: (a) left tail deflection; (b) internal leakage magnitude; (c) actuator control signal; (d) applied aerodynamic load; (e) bank angle; (f) attack and sideslip angles.

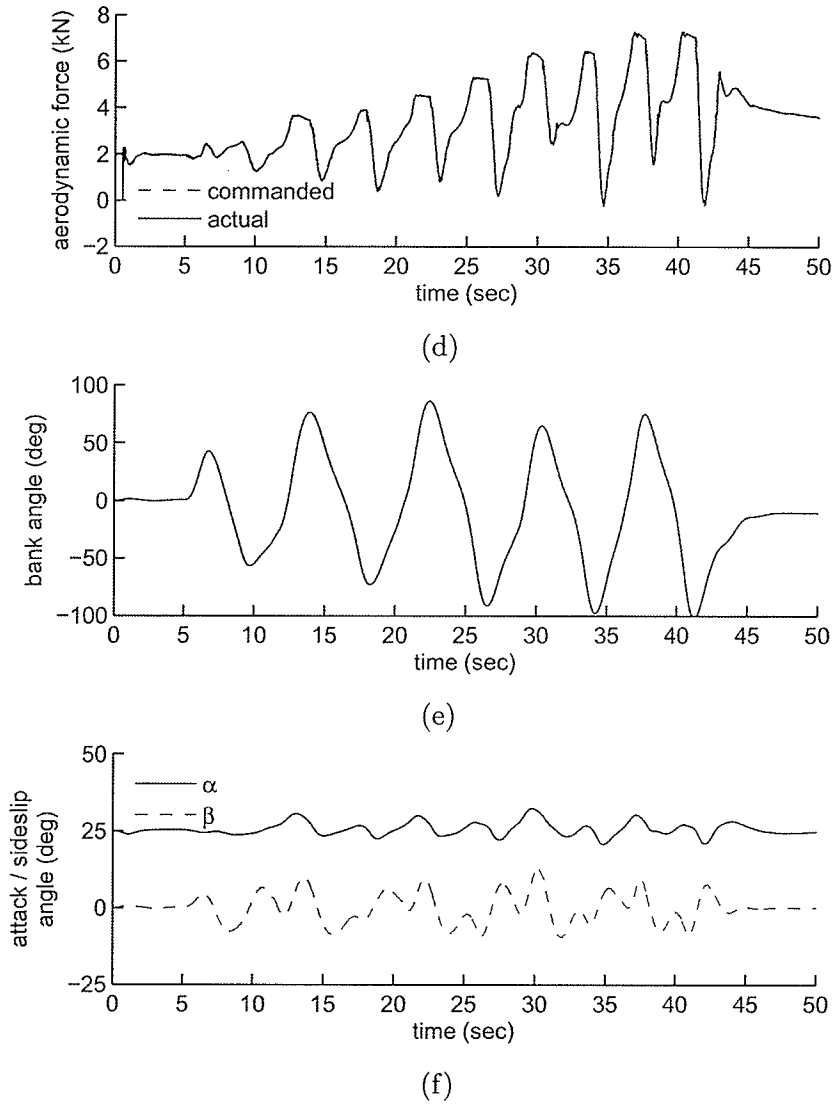

Figure 6.5 – concluded: Bank-to-bank reversals using fault tolerant controller for increasing internal leakage: (a) left tail deflection; (b) internal leakage magnitude; (c) actuator control signal; (d) applied aerodynamic load; (e) bank angle; (f) attack and sideslip angles.

6.2.2 Roll Maneuver

Benchmark Control System A

The roll maneuver was simulated next using the HIL framework to further examine the flight performance of the aircraft in the presence of the flight actuator internal leakage fault. Figure 6.6 shows the results obtained using the benchmark control law for normal operation of the experimental flight actuator. The deflection of the left horizontal tail and the control signal applied to the flight actuator servovalve are shown in Figures 6.6a and 6.6b, respectively. Referring to Figure 6.6a, it is seen that the control surface reaches its travel limit at $t \approx 11$ sec. The horizontal tail deflection was saturated by the α-limiting system in an attempt to counteract the increase in angle of attack that arises due to the large inertia-coupling moment, induced by the lateral-directional motion of the aircraft [120]. However, since the horizontal tails begin to lose effectiveness for $\alpha > 25°$, the angle of attack increased to a value of $42°$ at $t \approx 15$ sec (see Figure 6.6d). Large sideslip excursions $\beta \approx \pm 20°$, which further reduce the effectiveness of the horizontal tail, were also recorded during the test. When the lateral stick input was released at $t = 12.5$ sec, the roll and yaw rates were observed to quickly decrease. This, in turn, reduced the magnitude of the inertia-coupling moment and allowed the control forces produced by the horizontal tail to suppress any further α increase. Consequently, the angle of attack excursion could be corrected and trim α regained as the aircraft completed the roll between $t = 15$ and 20 sec.

Figure 6.7 reports the results of the same roll maneuver attempted in the presence of an increasing internal leakage fault. As shown in Figure 6.7a, the experimental flight actuator cannot track the control surface deflection profile commanded by the longitudinal flight control law. The interaction between the faulty flight actuator and the applied aerodynamic load prevented the left horizontal tail from being deflected to its travel limit, resulting in a pitch-out departure ($\alpha \gg 30°$) at $t \approx 15$ sec. The

airplane then flew into a deep-stall flight condition as indicated in Figure 6.7f by the oscillation of α in the vicinity of 60° and by the large variation in the sideslip angle. Deep-stall is an undesirable flight condition since there is no way of recovering using the normal flight control system [120]. Therefore, when the aircraft enters deep-stall, the pilot essentially loses the ability to control the aircraft [124]. The results of this HIL simulation example represent one scenario where an uncompensated flight actuator failure can negatively impact the flight performance of the simulated aircraft configuration.

Fault Tolerant Controller

The roll maneuver was repeated again using the fault tolerant controller to drive the experimental flight actuator. Figure 6.8 shows clearly that the fault tolerant controller is capable of providing sufficient control effort to maintain the tracking performance of the flight actuator under increasing internal leakage. Since the experimental flight actuator could properly position the flight surface against the aerodynamic load, the motion of the horizontal tail suppressed the angle of attack buildup allowing the aircraft to complete the roll. By using the fault tolerant hydraulic actuator control law, it was possible to compensate for the effects of the internal leakage fault and keep the aircraft from flying into a potentially unsafe deep stall flight condition. Fault tolerant control at the flight actuator level can therefore maintain the flight performance of the aircraft despite actuator faults.

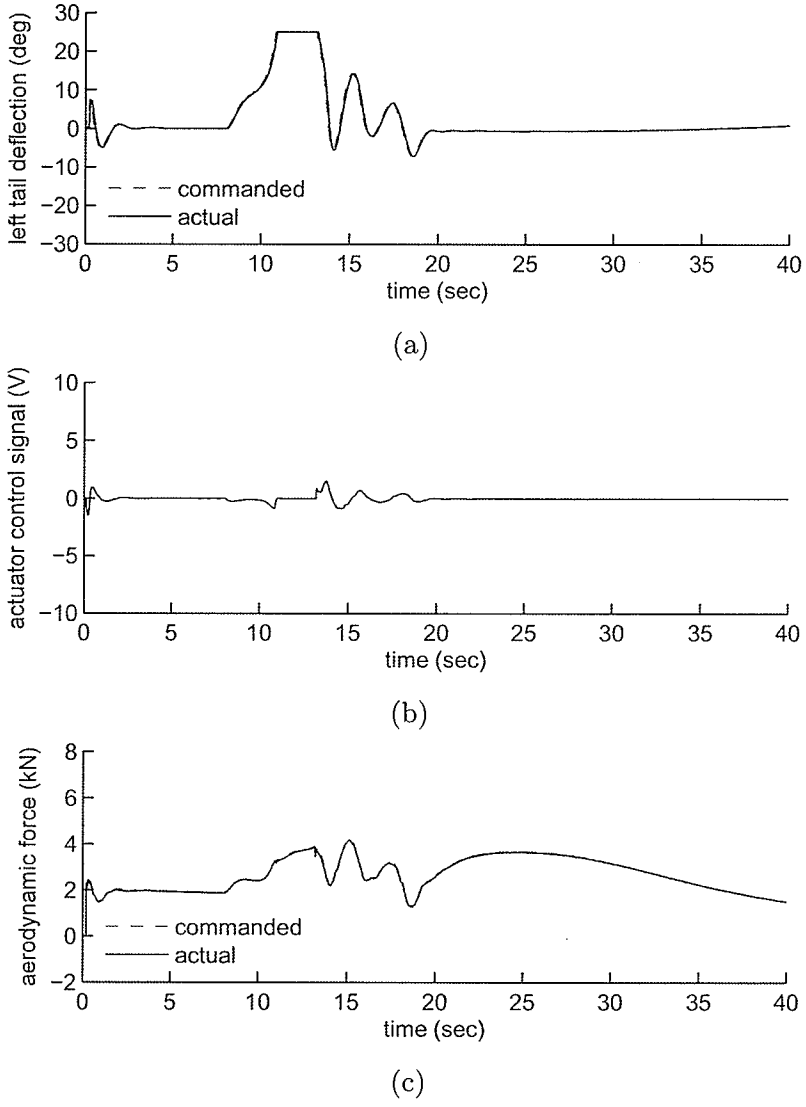

Figure 6.6: Roll maneuver using benchmark controller A under normal operation: (a) left tail deflection; (b) actuator control signal; (c) applied aerodynamic load; (d) roll angle; (e) attack and sideslip angles.

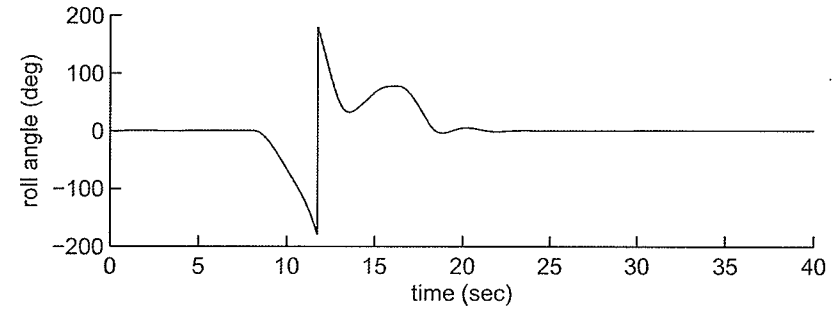

(d)

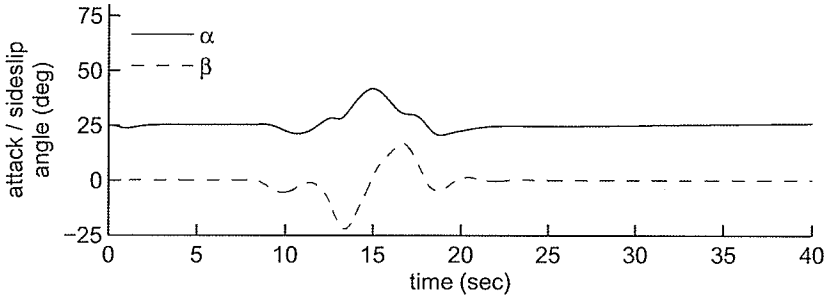

(e)

Figure 6.6 – concluded: Roll maneuver using benchmark controller A under normal operation: (a) left tail deflection; (b) actuator control signal; (c) applied aerodynamic load; (d) roll angle; (e) attack and sideslip angles.

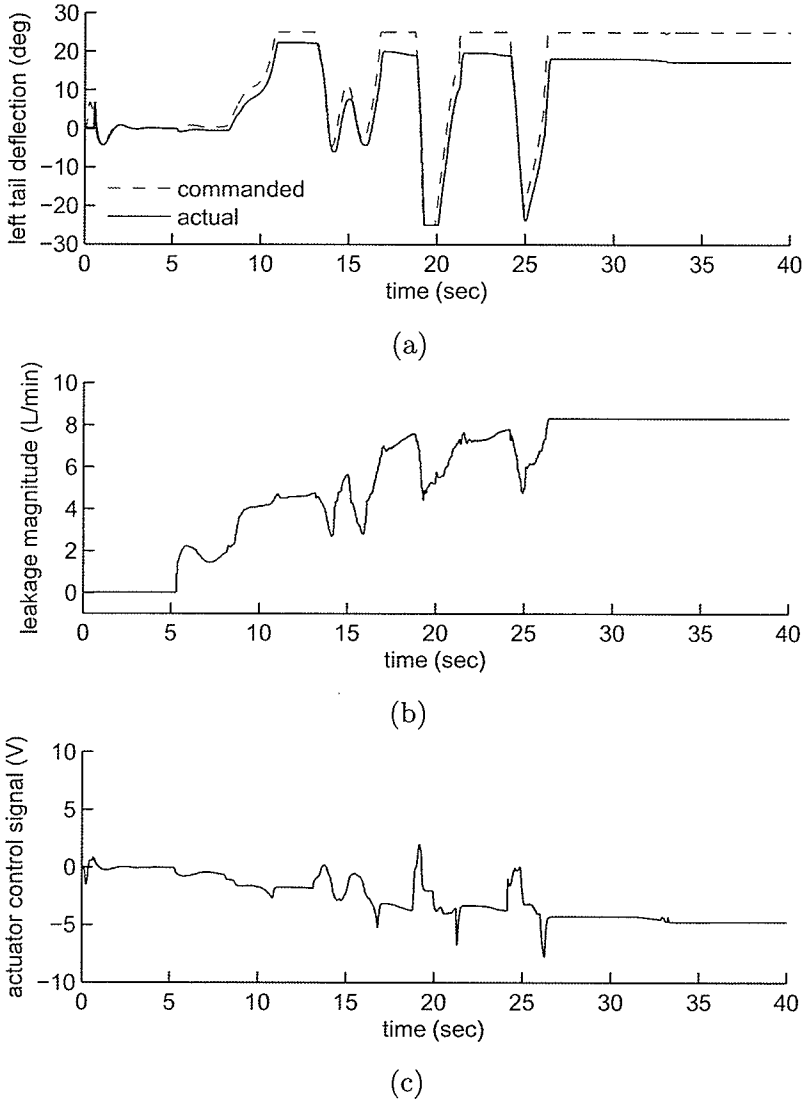

Figure 6.7: Roll maneuver using benchmark controller A for increasing internal leakage: (a) left tail deflection; (b) internal leakage magnitude; (c) actuator control signal; (d) applied aerodynamic load; (e) roll angle; (f) attack and sideslip angles.

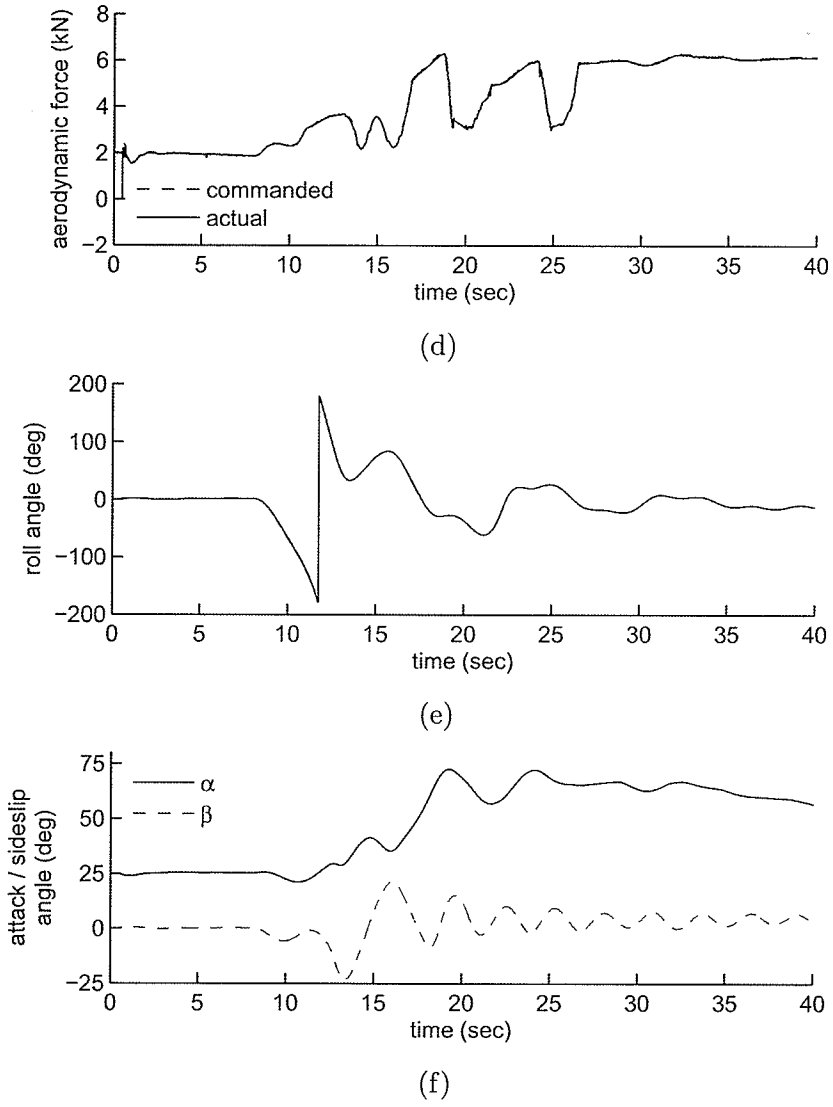

Figure 6.7 – concluded: Roll maneuver using benchmark controller A for increasing internal leakage: (a) left tail deflection; (b) internal leakage magnitude; (c) actuator control signal; (d) applied aerodynamic load; (e) roll angle; (f) attack and sideslip angles.

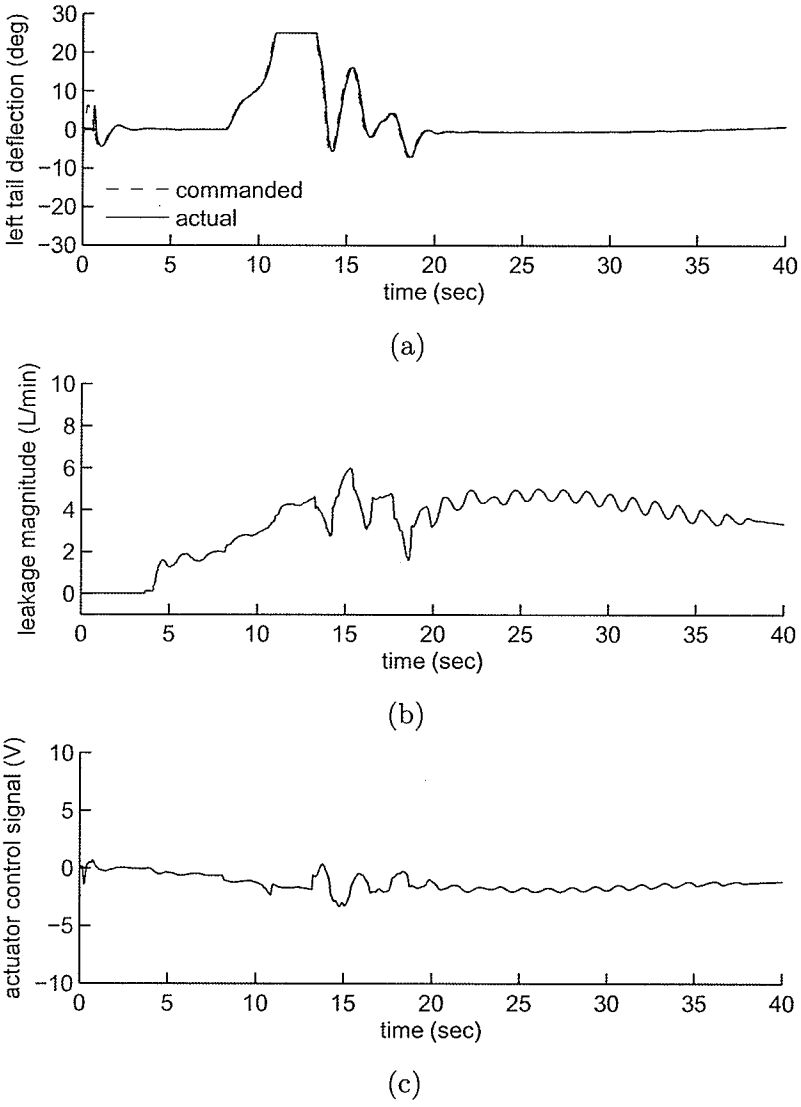

Figure 6.8: Roll maneuver using fault tolerant controller for increasing internal leakage: (a) left tail deflection; (b) internal leakage magnitude; (c) actuator control signal; (d) applied aerodynamic load; (e) roll angle; (f) attack and sideslip angles.

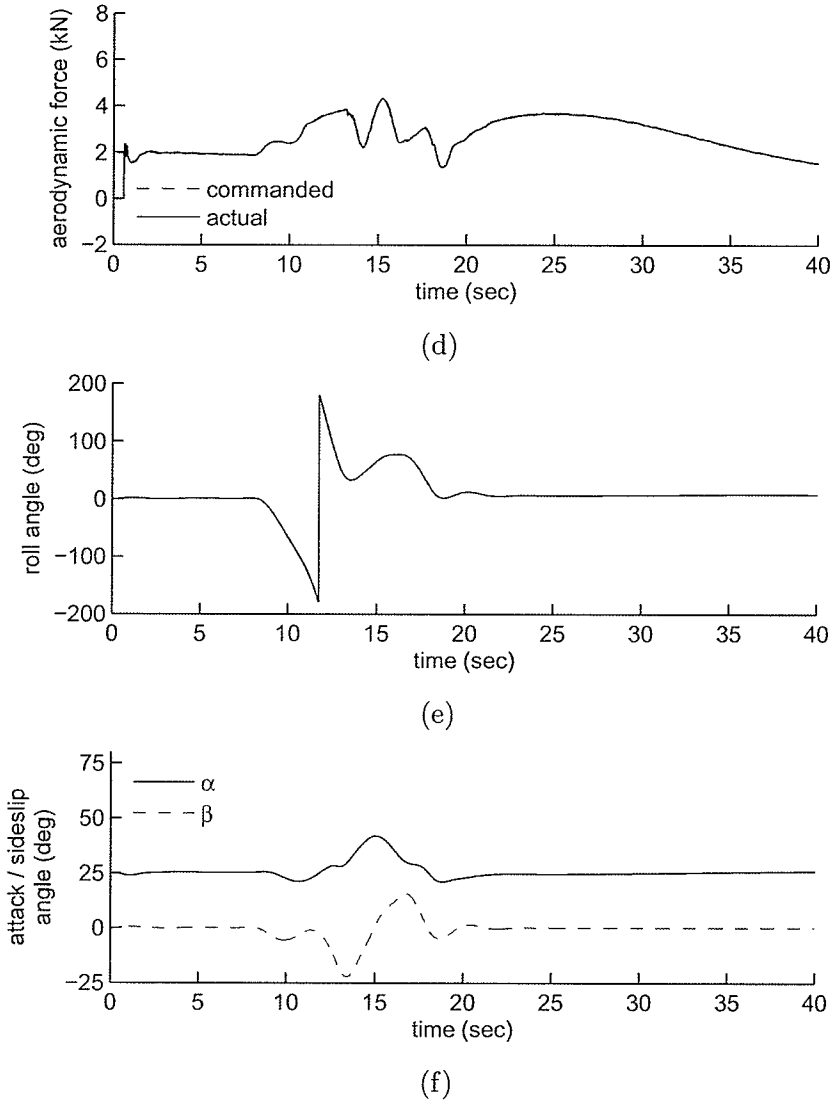

Figure 6.8 – concluded: Roll maneuver using fault tolerant controller for increasing internal leakage: (a) left tail deflection; (b) internal leakage magnitude; (c) actuator control signal; (d) applied aerodynamic load; (e) roll angle; (f) attack and sideslip angles.

6.3 Summary

This chapter further substantiated the performance of the fault tolerant control system by operating the faulty experimental hydraulic actuator as a flight actuator under realistic in-flight conditions. The interaction between the functionality of the flight actuator and the flight performance of the simulated aircraft configuration was also investigated. Two different flight maneuvers were studied, both of which placed considerable demands on the performance of the experimental flight actuator. The HIL simulation results showed that in the presence of the internal leakage fault, the non-integrating benchmark control system could not properly track the commanded surface deflection profile. The aerodynamic load caused a control surface deflection error, which in turn decreased the horizontal tail effectiveness. Despite the control surface deflection error, the influence of the internal leakage fault had little effect on the aircraft response in the bank-to-bank reversal maneuver. However, for a more extreme roll maneuver, the decreased effectiveness of the horizontal tail caused a pitch-out departure. The airplane then entered an undesirable deep-stall flight condition, from which it is difficult to recover. On the other hand, the HIL simulation results confirmed that the designed fault tolerant controller could maintain small control surface deflection errors by properly compensating the effects of the internal leakage fault, even in the presence of the aerodynamic load disturbance. Consequently, by accommodating the hydraulic system fault at the actuator level, the fault tolerant controller could keep the airplane from entering the deep-stall regime during the roll maneuver in spite of the flight actuator failure.

Chapter 7

Concluding Remarks

7.1 Contributions

Despite a substantial body of literature pertaining to feedback control of hydraulic actuators, fault tolerant control design for such systems is only emerging as an active area of fluid power research. This thesis presents the most comprehensive work to date on control system design for hydraulic actuators in the presence of significant actuator internal leakage. The contributions of this thesis are three-fold. First, a new numerical approach for identifying the LTIE frequency response of hydraulic actuators was developed. The proposed approach can properly identify the features of the hydraulic actuator frequency response that are important for control system design. A further advantage of the approach over existing LTIE identification techniques, such as Golubev's least-squares method, is that no prior knowledge about the asymptotic behavior or structure of the LTIE transfer function is required. Second, a passive fault tolerant control law that can compensate the effects of an actuator internal leakage fault and at the same time retain robustness against parametric uncertainties typical to fluid power systems was designed and experimentally tested. No other research work, prior to this study, has documented the development of a single, fixed-gain, controller that can simultaneously achieve these two objectives. Third, a hardware-in-the-loop (HIL) simulation platform, appropriate for objective

testing of fault tolerant fluid power systems, has been developed that incorporates experimental hydraulic actuator hardware into the numerical simulation of complex dynamic systems, for example aircraft flight control. Implementation of the (HIL) framework required integration of various hardware elements to emulate the effects of different hydraulic actuator faults, design of a robust electrohydraulic loading system to recreate complex load disturbances, and development of a distributed simulator architecture to ensure real-time operation of the system. In the considered flight control application, HIL simulation experiments demonstrated the importance of using a fault tolerant controller to compensate the internal leakage fault at the actuator level. The dynamics of the systems in which hydraulic actuators are embedded should therefore be incorporated into the development of fault tolerant fluid power systems. The detailed contributions of this thesis are outlined below:

1. Equivalent LTI Modeling of Hydraulic Actuators

Various approaches for deriving equivalent LTI models for electrohydraulic actuators were investigated, from a robust control perspective. It was shown that small-signal transfer functions, which are commonly used to model fluid power actuators, are generally inadequate to describe the transient response and that an alternative description of the hydraulic actuator dynamics known as the LTIE is a more appropriate choice for fluid power control system development. LTIE functions are derived by transforming acceptable actuator input-output responses and can therefore accurately characterize both small and large signal responses using a fixed-gain structure, one of the assumptions underlying many robust control techniques including QFT. Owing to the complexity of the hydraulic actuator dynamics, the LTIE functions can only be computed numerically. Therefore, a simple model-based approach for evaluating the LTIE frequency response of hydraulic actuators directly from acceptable input-output data was developed. The proposed approach eliminates the need to solve a rational transfer function and therefore improves the efficiency of the LTIE

modeling stage, which can be one of the most time consuming aspects of the QFT design process.

2. Fault Tolerant Control System Design

Having established a suitable model-based procedure for evaluating the LTIE dynamics of electrohydraulic actuators, QFT was applied next towards the design of a fault tolerant position control law that can compensate the effects of an actuator internal leakage fault. The position control problem was formulated to achieve closed-loop performance similar to a typical electrohydraulic flight actuator. Design of a benchmark control system that considers only the normal operation of the hydraulic actuator was considered first. It was shown that two different control structures can be used to solve the benchmark control problem and that the near optimal control structure, in terms of minimizing the controller gain is a non-integrating proportional type.

The position control problem could also be solved using a controller with an integrating structure and it was demonstrated that the over-design inherent in the integrating control system gave the controller some ability to compensate the internal leakage fault. However, to properly account for the dynamic uncertainty introduced by the internal leakage fault, the fault tolerant controller had to be developed next. The designed low-order, fixed-gain, fault tolerant control law can: (*i*) properly maintain the positioning performance of the hydraulic actuator within the prescribed specifications despite an internal leakage fault that can bypass approximately 40% of the rated steady-state servovalve flow across the piston, and (*ii*) maintain robustness against typical uncertainties in hydraulic system parameters including a 20% reduction in the hydraulic supply pressure, and $\pm 50\%$ variation in the hydraulic bulk modulus. Experiments demonstrated the individual performance of the developed controllers under normal and faulty operating conditions.

3. HIL Testing of Fault Tolerant Control Law

To further evaluate the performance of the fault tolerant controller, a distributed HIL simulation architecture was developed and implemented that enables an experimental hydraulic actuator, operating as a flight actuator, to be exercised against the real-time numerical simulation of a high-performance jet aircraft. The HIL test facility employs a secondary loading actuator to enable a variety of in-flight operating conditions to be replicated experimentally. Another contribution arising from the implementation of the HIL simulation environment was the development of a systematic approach for robust electrohydraulic force control against a non-stationary environment, within the framework of QFT.

The efficacy of the fault tolerant controller was further substantiated by using the HIL simulator to study two different flight maneuvers, which place considerable demands on the performance of the experimental flight actuator. The HIL experiments showed that if the internal leakage fault is not properly compensated by the hydraulic control system, the flight actuator cannot track the commanded deflection profile, resulting in decreased control surface effectiveness. In one HIL test, the control surface deflection error resulting from the actuator internal leakage fault caused the airplane to enter into an undesirable deep-stall flight condition, from which it is difficult to recover. The fault tolerant controller, on the other hand, could keep the airplane from departing into the deep-stall regime, despite a similar actuator failure. The results of the HIL experiments have clearly demonstrated the importance of continued research and development on fault tolerant fluid power systems.

7.2 Future Work

This work can be extended in several different directions:

1. The model-based robust control design approach used here can be applied to develop fault tolerant control systems that can compensate other fault classes, for example external leakage faults. An important question to be addressed in this area is whether or not a fixed-gain structure can be used to compensate different faults simultaneously.

2. The sensitivity of the closed-loop control systems developed in this work should be investigated with respect to the effects of other fault types. Since the QFT design methodology compensates the dynamic uncertainties introduced from faults by using the controller gain to reduce the sensitivity of the feedback loop, it is possible that the designed control systems may perform well for fault classes not explicitly considered in the design. Such an analysis may also provide further insight into appropriate methodologies for fault tolerant control development around fluid power systems.

3. The HIL simulator can be used as a platform for testing fault tolerant control as well as diagnostics and condition monitoring algorithms developed independently of this thesis. One could compare fixed-gain fault tolerant controls against adaptive systems using similar flight maneuvers to the ones studied here. An important question is whether or not adaptive or active systems can reconfigure the controller quickly enough to prevent the aircraft from entering undesirable modes of operation.

References

[1] D. McLean, *Automatic Flight Control Systems.* Englewood Cliffs, NJ: Prentice-Hall, 1990.

[2] H. E. Merritt, *Hydraulic Control Systems.* New York: Wiley, 1967.

[3] W. J. Crowther, K. A. Edge, C. R. Burrows, R. M. Atkinson, and D. J. Wollons, "Fault diagnosis of a hydraulic actuator circuit using neural networks–An output vector space classification approach," *Proceedings of the Institution of Mechanical Engineers Part I: Journal of Systems and Control Engineering*, vol. 212, no. 11, pp. 57–68, 1998.

[4] L. An and N. Sepehri, "Hydraulic actuator circuit fault detection using extended Kalman filter," *International Journal of Fluid Power*, vol. 6, no. 1, pp. 41–51, March 2005.

[5] V. A. Skormin, J. Apone, and J. J. Dunphy, "On-line diagnostics of a self-contained flight actuator," *IEEE Transactions on Aerospace and Electronic Systems*, vol. 30, no. 1, pp. 186–195, 1994.

[6] H. Tan and N. Sepehri, "Parametric fault diagnosis for electrohydraulic cylinder drive units," *IEEE Transactions on Industrial Electronics*, vol. 49, no. 1, pp. 96–106, 2002.

[7] M. Khoshzaban-Zavarehi, "On-line condition monitoring and fault diagnosis in hydraulic system components using parameter estimation and pattern classification," Ph.D. dissertation, University of British Columbia, 1997.

[8] D. Yu, D. N. Shields, and J. L. Mahtani, "Fault detection for bilinear systems with application to a hydraulic system," in *Proceedings of the 1994 IEEE Conference on Control Applications*, 1994, pp. 1379–1384.

[9] V. A. Skormin and J. Apone, "On-line diagnostics of a variable displacement pump of a flight actuation system," in *Proceedings of the 1995 IEEE National Aerospace and Electronics Conference*, 1995, pp. 503–510.

[10] P. Garimella and B. Yao, "Model based fault detection of an electro-hydraulic cylinder," in *Proceedings of the 2005 American Control Conference*, Portland, OR, June 8-10 2005, pp. 484–489.

[11] Z. Shi, F. Gu, B. Lennox, and A. D. Ball, "The development of an adaptive threshold for model-based fault detection of a nonlinear electro-hydraulic system," *Control Engineering Practice*, vol. 13, pp. 1357–1367, 2005.

[12] Y. Chinniah, R. Burton, and S. Habibi, "Failure monitoring in a high performance hydrostatic actuation system using the extended Kalman filter," *Mechatronics*, vol. 16, pp. 643–653, 2006.

[13] H. Huang, K.-S. Chen, and L.-C. Zeng, "BP neural network-based fault diagnosis of hydraulic servo-valves," in *Proceedings of the 4th International Conference on Machine Learning and Cybernetics*, Guangzhou, August 18-21 2005.

[14] C. Lurette and S. Lecoeuche, "Unsupervised and auto-adaptive neural architecture for on-line monitoring–Application to a hydraulic process," *Control Engineering Practice*, vol. 16, pp. 441–451, 2003.

[15] T. T. Le, J. Watton, and D. T. Pham, "An artificial neural network based approach to fault diagnosis and classification of fluid power systems," *Proceedings of the Institution of Mechanical Engineers Part I: Journal of Systems and Control Engineering*, vol. 211, pp. 307–317, 1997.

[16] T. T. Le, J. Watton, and D. T. Pham, "Fault classification of fluid power systems using a dynamics feature extraction technique and neural networks," *Proceedings of the Institution of Mechanical Engineers Part I: Journal of Systems and Control Engineering*, vol. 212, pp. 87–97, 1998.

[17] K. A. Edge, O. P. Boston, C. R. Burrows, J. Darling, D. J. Wollons, R. M. Atkinson, and P. G. Hawkins, "An approach to automated fault diagnosis of hydraulic circuits using neural networks," in *ASME Fluid Power Systems and Technology Conference*, 1995, pp. 37–42.

[18] P. A. Hogan, C. R. Burrows, K. A. Edge, D. J. Wollons, and R. M. Atkinson, "A system for diagnosing faults in hydraulic circuits based on qualitative models of component behavior," in *Proceedings of the IFAC/IMACS Symposium on Fault Detection, Supervision and Safety for Technical Processes*, 1991, pp. 377–382.

[19] D. J. Creber and J. Watton, "Development of a low cost expert system shell for condition monitoring of fluid power systems," in *Proceedings of the 9th International Fluid Power Symposium*, Cambridge, 1990, pp. 281–291.

[20] J. C. Stewart and J. Watton, "Some aspects of rule-based expert system design for on-line fault diagnosis of fluid power systems," in *ASME Engineering Systems Design and Analysis Conference*, vol. 8 Part B, 1994, pp. 457–465.

[21] J. Watton, O. Lucca-Negro, and J. C. Stewart, "An on-line approach to fault diagnosis of fluid power cylinder drive units," *Proceedings of the Institution of Mechanical Engineers Part I: Journal of Systems and Control Engineering*, vol. 208, pp. 249–262, 1994.

[22] C. Angeli and D. Atherton, "A model-based method for an online diagnostic knowledge-based system," *Expert Systems*, vol. 18, no. 3, pp. 150–158, 2001.

[23] A. Chatzinikolaou and C. Angeli, "Modelling for an expert system and a parameter validation method," *Expert Systems*, vol. 19, no. 5, pp. 285–294, 2002.

[24] N. Sepehri, M. Karpenko, L. An, and S. Karam, "A test bed for experimental validation of fault tolerant control and condition monitoring algorithms in fluid power systems: From design through implementation," *Transactions of the CSME*, vol. 29, no. 3, pp. 441–458, 2005.

[25] N. Niksefat and N. Sepehri, "A QFT fault-tolerant control for electrohydraulic positioning systems," *IEEE Transactions on Control Systems Technology*, vol. 10, no. 4, pp. 626–632, 2002.

[26] M. Karpenko and N. Sepehri, "Robust position control of an electrohydraulic actuator with a faulty actuator piston seal," *ASME Journal of Dynamic Systems, Measurement, and Control*, vol. 125, no. 3, pp. 413–423, 2003.

[27] M. Karpenko and N. Sepehri, "Fault-tolerant control of a servohydraulic positioning system with corssport leakage," *IEEE Transactions on Control Systems Technology*, vol. 13, no. 1, pp. 155–161, 2005.

[28] P. N. Nikiforuk and D. R. Westlund, "The large signal response of a loaded high-pressure hydraulic servomechanism," *Proceedings of the Institution of Mechanical Engineers*, vol. 180, no. 32, pp. 757–775, 1965.

[29] J. L. Shearer, "Dynamic characteristics of valve-controller hydraulic servomotors," *Transactions of the ASME*, vol. 76, no. 6, pp. 895–903, 1954.

[30] T. R. Welch, "The use of derivative pressure feedback in high performance hydraulic servomechanisms," *ASME Journal of Engineering for Industry*, vol. 84, pp. 8–14, 1962.

[31] C. Canadus de Wit, P. Noel, A. Aubin, and B. Brogliato, "Adaptive friction compensation in robot manipulators: Low velocities," *International Journal of Robotics Research*, vol. 10, no. 3, pp. 189–199, 1991.

[32] S. Tafazoli, C. W. de Silva, and P. D. Lawrence, "Tracking control of an electrohydraulic manipulator in the presence of friction," *IEEE Transactions on Control Systems Technology*, vol. 6, no. 3, pp. 401–411, 1998.

[33] N. Sepehri, A. A. Khayyat, and B. Heinrichs, "Development of a nonlinear PI controller for accurate positioning of an industrial hydraulic manipulator," *Mechatronics*, vol. 7, no. 8, pp. 683–700, 1997.

[34] A. Bonchis, P. I. Corke, and D. C. Rye, "Experimental evaluation of position control methods for hydraulic systems," *IEEE Transactions on Control Systems Technology*, vol. 10, no. 6, pp. 876–882, 2002.

[35] J. Yu, Z. Chen, and Y. Lu, "The variation of oil effective bulk modulus with pressure in hydraulic systems," *ASME Journal of Dynamic Systems, Measurement, and Control*, vol. 116, pp. 146–150, 1994.

[36] B. Porter and M. L. Tatnall, "Performance characteristics of an adaptive hydraulic servo-mechanism," *International Journal of Control*, vol. 11, no. 5, pp. 741–757, 1970.

[37] J. M. Finney, A. de Pennington, M. S. Bloor, and G. S. Gill, "A pole-assignment controller for an electrohydraulic cylinder drive," *ASME Journal of Dynamic Systems, Measurement, and Control*, vol. 107, pp. 145–150, 1985.

[38] J. S. Yun and H. S. Cho, "Application of an adaptive model following control technique to a hydraulic servo system subjected to unknown disturbances," *ASME Journal of Dynamic Systems, Measurement, and Control*, vol. 113, pp. 479–486, 1991.

[39] A. R. Plummer and N. D. Vaughan, "Robust adaptive control for hydraulic servosystems," *ASME Journal of Dynamic Systems, Measurement, and Control*, vol. 118, pp. 237–244, 1996.

[40] J. E. Bobrow and K. Lum, "Adaptive, high bandwidth control of a hydraulic actuator," *ASME Journal of Dynamic Systems, Measurement, and Control*, vol. 118, pp. 714–720, 1996.

[41] A. Alleyne, "Nonlinear force control of an electro-hydraulic actuator," in *Proceedings of the Japan/USA Symposium on Flexible Automation*, 1996, pp. 193–200.

[42] G. A. Sohl and J. E. Bobrow, "Experiments and simulations on the nonlinear control of a hydraulic servosystem," *IEEE Transactions on Control Systems Technology*, vol. 7, no. 2, pp. 238–247, 1999.

[43] A. Alleyne and R. Liu, "A simplified approach to force control for electro-hydraulic systems," *Control Engineering Practice*, vol. 8, pp. 1347–1356, 2000.

[44] N. Niksefat, C. Q. Wu, and N. Sepehri, "Design of a Lyapunov controller for an electro-hydraulic actuator during contact tasks," *ASME Journal of Dynamic Systems, Measurement, and Control*, vol. 123, pp. 299–307, 2001.

[45] B. Yao, F. Bu, and G. T. C. Chiu, "Non-linear adaptive robust control of electro-hydraulic systems driven by double-rod actuators," *International Journal of Control*, vol. 74, no. 8, pp. 761–775, 2001.

[46] H. S. Kim, K. Lee, and Y. M. Cho, "Robust two-stage non-linear control of a hydraulic servo-system," *International Journal of Control*, vol. 75, no. 7, pp. 502–516, 2002.

[47] P. Sekhavat, Q. Wu, and N. Sepehri, "Impact control in hydraulic actuators," *ASME Journal of Dynamic Systems, Measurement, and Control*, vol. 127, pp. 197–205, 2005.

[48] R. N. Banavar and V. Aggarwal, "A loop transfer recovery approach to the control of an electro-hydraulic actuator," *Control Engineering Practice*, vol. 6, pp. 837–845, 1998.

[49] A. L. D. Franco, E. R. De Pieri, E. B. Castelan, R. Gunether, and A. C. Valdiero, "Design and experimental evaluation of position controllers for hydraulic actuators: Backstepping and LQR-2DOF controllers," *International Journal of Fluid Power*, vol. 5, no. 3, pp. 39–48, 2004.

[50] R. Piche, S. Pohjolainen, and T. Virvalo, "Design of robust controllers for position servos using the H_∞ theory," *Proceedings of the Institution of Mechanical Engineers Part I: Journal of Systems and Control Engineering*, vol. 205, no. 4, pp. 299–306, 1991.

[51] R. Piche, S. Pohjolainen, and T. Virvalo, "Design of robust two-degree-of-freedom controllers for position servos using H_∞ theory," *Proceedings of the Institution of Mechanical Engineers Part I: Journal of Systems and Control Engineering*, vol. 206, no. 2, pp. 135–142, 1992.

[52] L. Laval, N. K. M'Sirdi, and J. Cadiou, "H_∞ force control of a hydraulic servo-actuator with environmental uncertainties," in *Proceedings of the 1996 IEEE International Conference on Robotics and Automation*, Minneapolis, MN, 1996, pp. 1566–1571.

[53] T. Sugiyama and K. Uchida, "Gain scheduled velocity and force controllers for the electro-hydraulic servosystem," in *Proceedings of the 2002 American Control Conference*, Anchorage, AK, 2002, pp. 4433–4438.

[54] M. Namvar and F. Aghili, "A combined scheme for identification and robust control of hydraulic actuators," *ASME Journal of Dynamic Systems, Measurement, and Control*, vol. 125, pp. 595–606, 2003.

[55] M. J. Ashworth, "Robust design of sampled-data systems with application to an electro-hydraulic position controller," *Radio and Electronics Engineer*, vol. 54, no. 9, pp. 377–385, 1984.

[56] M. Pachter, C. H. Houpis, and K. Kang, "Modeling and control of an electrohydrostatic actuator," *International Journal of Robust and Nonlinear Control*, vol. 7, pp. 591–608, 1997.

[57] D. F. Thompson, J. S. Pruyn, and A. Shukla, "Feedback design for robust tracking and robust stiffness in flight control actuators using a modified QFT technique," *International Journal of Control*, vol. 72, no. 16, pp. 1480–1497, 1999.

[58] Y. Nam and S. K. Hong, "Force control system design of aerodynamic load simulator," *Control Engineering Practice*, vol. 10, pp. 549–558, 2002.

[59] N. Niksefat and N. Sepehri, "Design and experimental evaluation of a robust force controller for an electro-hydraulic actuator via quantitative feedback theory," *Control Engineering Practice*, vol. 8, no. 12, pp. 1335–1345, 2000.

[60] C. G. Tzafestas, G. G. Rigatos, and S. G. Tzafestas, "Design of fault-tolerant control systems: Passive and active approaches," *Systems Science*, vol. 24, no. 4, pp. 5–28, 1998.

[61] K. A. Edge, "The control of fluid power systems – responding to the challenges," *Proceedings of the Institution of Mechanical Engineers Part I: Journal of Systems and Control Engineering*, vol. 211, pp. 91–110, 1997.

[62] N. Niksefat, N. Sepehri, and Q. Wu, "Design and experimental evaluation of a QFT contact task controller for electro-hydraulic actuators," *International Journal of Robust and Nonlinear Control*, vol. 17, no. 2-3, pp. 225–250, 2007.

[63] I. M. Horowitz, *Quantitative Feedback Design Theory - QFT.* Boulder, CO: QFT Publications, 1993, vol. 1.

[64] A. E. Bentley, "Quantitative feedback theory with applications in welding," *International Journal of Robust and Nonlinear Control*, vol. 4, pp. 119–160, 1994.

[65] O. R. Reynolds, M. Pachter, and C. H. Houpis, "Full envelope flight control system design using QFT," in *Proceedings of the 1994 IEEE Conference on Control Applications*, 1994, pp. 350–354.

[66] I. Horowitz and M. Sidi, "Synthesis of feedback systems with large plant ignorance for prescribed time domain tolerances," *International Journal of Control*, vol. 16, no. 2, pp. 287–309, 1972.

[67] I. Horowitz, "Synthesis of feedback systems with nonlinear time-varying uncertain plants to satisfy quantitative performance specifications," *IEEE Proceedings*, vol. 64, pp. 123–130, 1976.

[68] I. Horowitz, "Feedback systems with nonlinear uncertain plants," *International Journal of Control*, vol. 36, pp. 155–171, 1982.

[69] J. B. Dods and B. E. Tinling, "Summary of results of a wind-tunnel investigation of nine related horizontal tails," National Advisory Committee for Aeronautics, Tech. Rep. TN-3497, 1955.

[70] R. C. Dorf and R. H. Bishop, *Modern Control Systems*, 8th ed. Menlo Park, CA: Addison Wesley, 1998.

[71] J. J. Pippenger, *Fluid Power – The Hidden Giant.* New York: Amalgam Publishing, 1992.

[72] J. F. Blackburn, G. Reethof, and J. L. Shearer, Eds., *Fluid Power Control.* MIT Press, 1960.

[73] N. Acherkan, *Machine Tool Design.* Moscow: MIR Publishers, 1982.

[74] B. L. Stevens and F. L. Lewis, *Aircraft Control and Simulation.* New York: John Wiley & Sons, 1992.

[75] D. Wu, R. Burton, G. Schoenau, and D. Bitner, "Establishing operating points for a linearized model of a load sensing system," *International Journal of Fluid Power*, vol. 3, no. 2, pp. 47–54, 2002.

[76] N. D. Manring, *Hydraulic Control Systems.* Hoboken, NJ: Wiley, 2005.

[77] J. W. Edwards, "Analysis of an electrohydraulic aircraft control-surface servo and comparison with test results," NASA Edwards Flight Research Center, Edwards, CA, NASA Technical Note TN-D-6928, 1972.

[78] G. J. Schoenau, R. T. Burton, and G. P. Kavanagh, "Dynamic analysis of a variable displacement pump," *ASME Journal of Dynamic Systems, Measurement, and Control*, vol. 112, no. 1, pp. 122–132, 1990.

[79] M. Guillon, *Hydraulic Servo Systems: Analysis and Design.* London: Butterworths, 1969.

[80] M. Khoshzaban-Zavarehi, P. D. Lawrence, and F. Sassani, "Nonlinear modeling and validation of solenoid-controlled pilot-operated servovalves," *IEEE/ASME Transactions on Mechatronics,*, vol. 4, pp. 324–334, 1999.

[81] A. R. Plummer, "Robust electrohydraulic force control," *Proceedings of the Institution of Mechanical Engineers Part I: Journal of Systems and Control Engineering*, vol. 221, pp. 717–731, 2007.

[82] D. W. Robinson and G. A. Pratt, "Force controllable hydro-elastic actuator," in *Proceedings of the 2000 IEEE International Conference on Robotics and Automation*, San Francisco, CA, 2000, pp. 1321–1327.

[83] W. J. Thayer, "Transfer functions for Moog servovalves," Moog Inc., East Aurora, NY, January 1965.

[84] Hercules Sealing Products, "2007 Hercules seal catalog."

[85] C. Canadus de Wit, H. Olsson, K. J. Aström, and P. Lischinsky, "A new model for control of systems with friction," *IEEE Transactions on Automatic Control*, vol. 40, pp. 419–425, 1995.

[86] B. Golubev and I. Horowitz, "Plant rational transfer approximation from input-output data," *International Journal of Control*, vol. 36, no. 4, pp. 711–723, 1982.

[87] I. Horowitz, "Improvement in quantitative nonlinear feedback design by cancellation," *International Journal of Control*, vol. 34, pp. 547–560, 1981.

[88] I. M. Horowitz, *Synthesis of Feedback Systems.* New York: Academic Press, 1963.

[89] H. W. Bode, *Network Analysis and Feedback Amplifier Design.* New York: D. Van Nostrand Company, 1945.

[90] G. Stein, "Respect the unstable," *IEEE Control Systems Magazine*, vol. 23, no. 4, pp. 12–25, 2003.

[91] M. Sidi, *Design of Robust Control Systems.* Malabar, FL: Krieger, 2001.

[92] C. H. Houpis, S. J. Rasmussen, and M. Garcia-Sanz, *Quantitative Feedback Theory: Fundamentals and Applications*, 2nd ed. Boca Raton, FL: CRC Press, 2006.

[93] O. Yaniv, *Quantitative Feedback Design of Linear and Nonlinear Control Systems.* Norwell, MA: Kluwer Academic Publishers, 1999.

[94] J. J. D'Azzo and C. H. Houpis, *Linear Control System Analysis and Design: Conventional and Modern*, 3rd ed. New York: McGraw-Hill, 1988.

[95] Y. Chait and O. Yaniv, "Multiple-input/single-output computer-aided control design using the quantitative feedback theory," *International Journal of Robust and Nonlinear Control*, vol. 3, pp. 47–54, 1993.

[96] D. F. Thompson and O. D. I. Nwokah, "Analytical loop shaping methods in quantitative feedback theory," *ASME Journal of Dynamic Systems, Measurement, and Control*, vol. 116, no. 2, pp. 169–177, 1994.

[97] G. F. Bryant and G. D. Halikias, "Optimal loop-shaping for systems with large parameter uncertainty via linear programming," *International Journal of Control*, vol. 62, no. 3, pp. 557–568, 1995.

[98] Y. Chait, Q. Chen, and C. V. Hollot, "Automatic loop-shaping of QFT controllers via linear programming," *ASME Journal of Dynamic Systems, Measurement, and Control*, vol. 121, pp. 351–357, 1999.

[99] P. S. V. Nataraj and N. Kubal, "Automatic loop shaping in QFT using hybrid optimization and constraint propagation techniques," *International Journal of Robust and Nonlinear Control*, vol. 17, pp. 251–264, 2007.

[100] R. L. Cosgriff, *Nonlinear Control Systems.* New York: McGraw-Hill, 1958.

[101] S. F. Wu, M. J. Grimble, and W. Wei, "QFT-based robust/fault-tolerant flight control design for a remote pilotless vehicle," *IEEE Transactions on Control Systems Technology*, vol. 8, no. 6, pp. 1010–1016, 2000.

[102] M. Karpenko and N. Sepehri, "Development and experimental evaluation of a fixed-gain nonlinear control for a low-cost pneumatic actuator," *Proceedings of the IEE Part D: Control Theory and Applications*, vol. 153, no. 6, pp. 629–640, 2006.

[103] A. H. Whitfield and N. Messali, "Integral-equation approach to system identification," *International Journal of Control*, vol. 45, no. 4, pp. 1431–1445, 1987.

[104] H. Garnier, M. Mensler, and A. Richard, "Continuous-time model identification from sampled data: Implementation issues and performance evaluation," *International Journal of Control*, vol. 76, no. 13, pp. 1337–1357, 2003.

[105] F. I. Mopsik, "The transformation of time-domain relaxation data into the frequency domain," *IEEE Transactions on Electrical Insulation*, vol. 20, no. 6, pp. 957–964, 1985.

[106] C. J. Tranter, *Integral Transforms in Mathematical Physics.* New York: John Wiley & Sons, 1951.

[107] L. N. G. Filon, "On a quadrature formula for trigonometric integrals," *Proceedings of the Royal Society of Edinburgh*, vol. 49, pp. 38–47, 1929.

[108] D. H. Bailey and P. N. Swarztrauber, "A fast method for the numerical evaluation of continuous Fourier and Laplace transforms," *SIAM Journal on Scientific Computing*, vol. 15, no. 5, pp. 1105–1110, 1994.

[109] E. C. Levy, "Complex curve fitting," *IRE Transactions on Automatic Control*, pp. 37–43, 1959.

[110] B. Etkin, *Dynamics of Atmospheric Flight.* New York: Wiley, 1972.

[111] J. Roskam, *Airplane Flight Dynamics and Automatic Flight Controls: Part I.* Lawrence, KS: DAR Corporation, 2003.

[112] Y. Chait, C. Borghesani, and Y. Zheng, "Single-loop QFT design for robust performance in the presence of non-parametric uncertainties," *ASME Journal of Dynamic Systems, Measurement, and Control*, vol. 117, no. 3, pp. 420–425, 1995.

[113] J. Heintze, "Design and control of a hydraulically actuated industrial brick laying robot," Ph.D. dissertation, Delft University of Technology, Netherlands, 1997.

[114] A. W. Osburn and M. A. Franchek, "Reducing engine idle speed deviations using the internal model principle," *ASME Journal of Dynamic Systems, Measurement, and Control*, vol. 128, no. 4, pp. 869–877, 2006.

[115] J. W. Glass and M. A. Franchek, "Frequency-based nonlinear controller design for regulating frequency-based nonlinear controller design for regulating systems subjected to time-domain constraints," *International Journal of Robust and Nonlinear Control*, vol. 10, pp. 39–57, 2000.

[116] K. Goldberg and R. Siegwart, Eds., *Beyond Webcams: An Introduction to Online Robots.* Cambridge, MA: The MIT Press, 2002, ch. Toward Bilateral Teleoperation, pp. 193–214.

[117] [Online]. Available: http://www.flightgear.org

[118] B. Sehgal, R. W. Deters, and M. S. Selig, "Icing encounter flight simulator," in *AIAA Aerospace Sciences Meeting and Exhibit*, 2002.

[119] J.-C. Mare, "Dynamic loading systems for ground testing of high speed aerospace actuators," *Aircraft Engineering and Aerospace Technology: An International Journal*, vol. 78, no. 4, pp. 275–282, 2006.

[120] L. T. Nguyen, M. E. Ogburn, W. P. Gilbert, K. S. Kibler, P. W. Brown, and P. L. Deal, "Simulator study of stall/post-stall characteristics of a fighter airplane with relaxed static stability," NASA Langley Research Center, Hampton, VA, Tech. Rep. NASA-TP-1538, December 1979.

[121] B. E. Jackson, "Manual for a workstation-based generic flight simulator program (LaRCSim) version 1.4," NASA Langley Research Center, Hampton, VA, Tech. Rep. NASA-TM-110164, 1995.

[122] S. A. Snell and P. W. Stout, "Quantitative feedback theory with a scheduled gain for full envelope longitudinal control," *Journal of Guidance, Control, and Dynamics*, vol. 19, no. 5, pp. 1095–1101, 1996.

[123] M. Karpenko and N. Sepehri, "Hardware-in-the-loop simulator for research on fault tolerant control of electrohydraulic flight control systems," in *Proceedings of the 2006 American Control Conference*, Minneapolis, MN, June 14-16 2006, pp. 4645–4651.

[124] F. Ahmed-Zaid, P. Ioannou, K. Gousman, and R. Rooney, "Accommodation of failures in the F16 aircraft using adaptive control," *IEEE Control Systems Magazine*, vol. 11, no. 1, pp. 73–78, 1991.

Appendix A

Hydraulic Actuator Inverse Model

Consider the nonlinear hydraulic actuator state equations given by (2.10). The input, x_v, is related to output, x_p, by state equations (2.10a) through (2.10d). To determine the equivalent linear time invariant representation of the nonlinear hydraulic actuator dynamics between x_v and x_p, a necessary step is to invert the plant dynamics so that the acceptable plant drive signals, $x_v(t)$, can be solved from the acceptable piston trajectory, $x_p(t)$. However, the complexity of the nonlinear equations describing the motion of actuator, in particular equations (2.10c) and (2.10d), precludes the derivation of analytic expressions for $x_v(t)$. Therefore, the acceptable $x_v(t)$ time histories are computed numerically using the approach described previously in [62]. The inverse model has, however, been modified here to include the effects of actuator internal and external leakage faults.

To invert the plant dynamics, first differentiate and manipulate equation (2.10b), which describes the dynamics of the piston as follows:

$$A(\dot{P}_1 - \dot{P}_2) = m\dddot{x}_p + d\ddot{x}_p + \dot{F}_d \tag{A.1}$$

Next use (2.10c) and (2.10d) along with (A.1) to assemble a system of linear equations $\mathbf{Ax} = \mathbf{b}$, having solution vector $\mathbf{x} = [\dot{P}_1, \dot{P}_2, x_v]^T$, and coefficient matrix

$$\mathbf{A} = \begin{bmatrix} A & -A & 0 \\ 1 & 0 & \dfrac{-K_v w \beta_h}{A x_p + \bar{V}_1}\sqrt{\dfrac{P_s - P_r}{2} + \dfrac{x_v}{|x_v|}\left(\dfrac{P_s + P_r}{2} - P_1\right)} \\ 0 & 1 & \dfrac{K_v w \beta_h}{A(L - x_p) + \bar{V}_2}\sqrt{\dfrac{P_s - P_r}{2} + \dfrac{x_v}{|x_v|}\left(P_2 - \dfrac{P_s + P_r}{2}\right)} \end{bmatrix} \tag{A.2}$$

Vector $\mathbf{b}$ is given by

$$\mathbf{b} = \begin{Bmatrix} m\dddot{x}_p + d\ddot{x}_p + \dot{F}_d \\ -\dfrac{\beta_h}{A x_p + \bar{V}_1}\left[-K_1\sqrt{P_1} - K_{12}\sqrt{|P_1 - P_2|}\,\mathrm{sgn}(P_1 - P_2) - A\dot{x}_p\right] \\ \dfrac{\beta_h}{A(L - x_p) + \bar{V}_2}\left[-K_2\sqrt{P_2} + K_{12}\sqrt{|P_1 - P_2|}\,\mathrm{sgn}(P_1 - P_2) + A\dot{x}_p\right] \end{Bmatrix} \tag{A.3}$$

Using the time derivatives of the acceptable piston displacement and the load force, the linear system formed by (A.2) and (A.3) is recursively solved for the values of variables x_v, $\dot{P}_1$, and $\dot{P}_2$. To propagate the inverse model forward in time, the previously solved pressure derivatives, $\dot{P}_1(t_i)$ and $\dot{P}_2(t_i)$, are integrated using Euler's forward method. The results of the numerical integration are the values $P_1(t_{i+1})$ and $P_2(t_{i+1})$, which are used to solve the system of equations at the next integration interval. The accuracy and uniqueness of the inverse simulation can be checked by integrating state equations (2.10a) through (2.10d) forward in time, using the values of input signal x_v obtained from the inverse model.

Appendix B

Table of Hinge Moment Coefficients

The tabular data used to compute the aerodynamic force acting on the hydraulic flight control actuator are given in Table B.1. The data were adapted from Figure 13a of reference [69]. The dimensionless hinge moment coefficient, $C_h(\theta, \delta)$ is interpolated from Table B.1 based on the given control surface angle of incidence, θ, and the control surface deflection, δ. In [69], the hinge moment coefficient data were only available for $-10° \leq \theta \leq 30°$. In the aircraft simulation model, the range of the available data is extended smaller or larger values of θ by linear extrapolation. This was done in order to maintain consistency with the aircraft aerodynamic database.

Table B.1: Table of hinge moment coefficients, $C_h(\theta, \delta)$.

	Control Surface Deflection, δ (deg)						
Angle of	-30	-25	-20	-15	-10	-6	-4
Incidence, θ (deg)	-2	0	2	4	6	20	30
-10	0.2948	0.2474	0.1966	0.1449	0.1015	0.0732	0.0600
	0.0458	0.0357	0.0197	0.0061	-0.0073	-0.0661	-0.1966
-8	0.2860	0.2381	0.1877	0.1334	0.0902	0.0630	0.0495
	0.0359	0.0263	0.0109	-0.0018	-0.0137	-0.1016	-0.2254
-6	0.2780	0.2308	0.1799	0.1234	0.0805	0.0548	0.0420
	0.0288	0.0172	0.0034	-0.0084	-0.0225	-0.1114	-0.2394
-4	0.2695	0.2222	0.1722	0.1120	0.0725	0.0486	0.0356
	0.0231	0.0111	-0.0027	-0.0144	-0.0295	-0.1200	-0.2350

continued on next page...

Angle of Incidence, θ (deg)	Control Surface Deflection, δ (deg)						
	-30	-25	-20	-15	-10	-6	-4
	-2	0	2	4	6	20	30
-2	0.2610	0.2159	0.1635	0.1028	0.0697	0.0444	0.0300
	0.0177	0.0051	-0.0089	-0.0208	-0.0364	-0.1293	-0.2410
0	0.2533	0.2021	0.1451	0.0988	0.0694	0.0406	0.0254
	0.0120	-0.0003	-0.0142	-0.0277	-0.0426	-0.1423	-0.2556
2	0.2525	0.1794	0.1284	0.0932	0.0614	0.0338	0.0192
	0.0053	-0.0063	-0.0205	-0.0326	-0.0477	-0.1609	-0.2647
4	0.2476	0.1841	0.1243	0.0805	0.0511	0.0258	0.0129
	-0.0008	-0.0121	-0.0265	-0.0390	-0.0538	-0.1719	-0.2675
6	0.2370	0.1884	0.1181	0.0715	0.0446	0.0199	0.0059
	-0.0061	-0.0204	-0.0327	-0.0456	-0.0600	-0.1780	-0.2737
8	0.2270	0.1776	0.1031	0.0656	0.0394	0.0134	0.0000
	-0.0118	-0.0261	-0.0398	-0.0528	-0.0675	-0.1835	-0.2808
10	0.2157	0.1630	0.0887	0.0573	0.0294	0.0047	-0.0115
	-0.0216	-0.0342	-0.0481	-0.0634	-0.0782	-0.1921	-0.2902
12	0.1984	0.1444	0.0774	0.0476	0.0165	-0.0070	-0.0212
	-0.0332	-0.0461	-0.0605	-0.0773	-0.0924	-0.2025	-0.3069
14	0.1732	0.1197	0.0644	0.0328	0.0005	-0.0225	-0.0369
	-0.0517	-0.0648	-0.0795	-0.0970	-0.1124	-0.2381	-0.3344
16	0.1483	0.0879	0.0422	0.0112	-0.0235	-0.0455	-0.0611
	-0.0777	-0.0918	-0.1068	-0.1236	-0.1386	-0.2606	-0.3498
18	0.1231	0.0624	0.0229	-0.0093	-0.0479	-0.0678	-0.0837
	-0.0995	-0.1151	-0.1304	-0.1496	-0.1645	-0.2814	-0.3618
20	0.0937	0.0374	0.0027	-0.0286	-0.0723	-0.0940	-0.1104
	-0.1264	-0.1416	-0.1588	-0.1786	-0.1941	-0.3047	-0.3792
22	0.0663	0.0169	-0.0198	-0.0503	-0.0993	-0.1202	-0.1374
	-0.1547	-0.1698	-0.1882	-0.2078	-0.2242	-0.3260	-0.3945
24	0.0369	-0.0050	-0.0381	-0.0752	-0.1281	-0.1470	-0.1641
	-0.1816	-0.1942	-0.2143	-0.2352	-0.2484	-0.3457	-0.4081
26	0.0041	-0.0281	-0.0615	-0.1015	-0.1515	-0.1696	-0.1869
	-0.2043	-0.2161	-0.2358	-0.2561	-0.2707	-0.3594	-0.4140
28	-0.0202	-0.0491	-0.0856	-0.1210	-0.1697	-0.1884	-0.2057
	-0.2211	-0.2323	-0.2519	-0.2706	-0.2823	-0.3653	-0.4161
30	-0.0271	-0.0583	-0.0983	-0.1344	-0.1808	-0.2002	-0.2137
	-0.2278	-0.2392	-0.2568	-0.2741	-0.2853	-0.3643	-0.4224

Table B.1 Completed.